



POLITECNICO DI MILANO
DIPARTIMENTO DI MATEMATICA
DOCTORAL PROGRAM IN MATHEMATICAL MODELS AND
METHODS IN ENGINEERING

A HIGH ORDER ACOUSTIC SOLVER FOR
AEROACOUSTIC PROBLEMS

Supervisor:

Prof. Nicola Parolini

Co-supervisor:

Prof. Daniele Rocchi

The Chair of the Doctoral Program:

Prof. Michele Correggi

Doctoral Dissertation of:
Alberto Artoni

XXXVI Cycle

Abstract

We introduce a high fidelity high order Discontinuous Galerkin Spectral Element Method (DGSEM) to solve the segregated aeroacoustic problem. The segregated strategy first solves the flow problem based on employing Finite Volume (FV) methods. Then, the flow solution is employed to compute the sound source for the acoustic problem via a suitable post processing approach. This requires suitable projection operations between the non-nested three-dimensional meshes that preserve the overall accuracy of the segregated approach. Finally, we solve an inhomogeneous wave equation to propagate the noise generated by the flow based on employing a high order Discontinuous Galerkin Spectral Element method. The problem is coupled through a novel intergrid projection method that computes explicitly the intersection between the two (non nested) computational grids of the flow and acoustic problems. We prove and demonstrate through extensive testing the accuracy of the intersection algorithm, and we verify the scalability of our implementation. The fully discrete acoustic problem has been analysed by taking into account the presence of the projected source term. We first analyse the projection error proving and verifying a priori estimates in the case of piecewise constant flow solution and we generalise it by considering high order reconstruction of the finite volume flow solution. Then, an a priori error analysis is carried out and verified for the fully discrete acoustic problem where the source term is a given projected piecewise constant or linearly reconstructed function. We apply our computational strategy to a wide number of benchmarks. First, we assess the capabilities of our acoustic solver that leads to remarkable performance with respect to commercial software in terms of speed and accuracy. We also simulate a real test case that generates a monopole sound source. The numerical solution has been compared with the experimental data. Finally, the proposed computational framework is applied to aeroacoustic benchmarks. We considered flow problems where the solution was given, computed from

a laminar problem or computed from turbulent problems. We conclude by showing the three dimensional capabilities of the solver by solving the aeroacoustic noise around a side view mirror of a vehicle. Our results have been validated with the benchmark results available in the literature.

Sommario

Consideriamo un metodo ad alto ordine basato su Discontinuous Galerkin Spectral Element Method (DGSEM) per risolvere il problema aeroacustico in maniera segregata. La strategia segregata risolve prima il problema fluidodinamico utilizzando un metodo a Volumi Finiti (FV). Successivamente, la soluzione del campo fluidodinamico è utilizzata per calcolare il termine di sorgente per il problema acustico. Per fare ciò, occorre un opportuno metodo di proiezione tra le generiche griglie tridimensionali che preservi l'accuratezza globale dell'approccio segregato. Risolviamo, per finire, un'equazione delle onde non omogenea per propagare il rumore generato dal flusso, utilizzando il metodo ad alto ordine DGSEM. Il problema è accoppiato tramite una strategia di proiezione innovativa che calcola in maniera esplicita le intersezioni delle due griglie computazionali del problema fluidodinamico e del problema acustico. Verifichiamo l'accuratezza dell'algoritmo di intersezione e verifichiamo la scalabilità dell'implementazione. Abbiamo analizzato il problema acustico discretizzato in tempo e spazio considerando anche l'effetto dell'errore introdotto dal termine di proiezione. L'errore di proiezione è stato analizzato, producendo una stima a priori. Verifiche delle stime a priori sono state ottenute nel caso di sorgente costante a tratti e lineare a tratti. Abbiamo generalizzato il risultato teorico al caso in cui la sorgente FV sia ricostruita ad alto ordine. Successivamente, abbiamo applicato la nostra strategia computazionale ad un ampio insieme di casi test. Il risolutore acustico è stato confrontato con un software commerciale in termini di velocità e precisione, mostrando ottimi risultati. Il risolutore acustico è stato inoltre utilizzato per caratterizzare una prova sperimentale dove si è utilizzata una sorgente modellizzata come monopolio. I dati numerici sono stati confrontati con i dati sperimentali. Per concludere, il risolutore aeroacustico è stato utilizzato in benchmark per problemi di aeroacustica. Abbiamo prima risolto casi più semplici di problemi dove la soluzione fluidodinamica era un dato, per poi risolvere problemi lami-

nari ed infine problemi più complessi con flussi turbolenti. Concludiamo la tesi mostrando le capacità della strategia aeroacustica andando ad affrontare il rumore generato da uno specchietto. I risultati sono stati validati con la letteratura.

Ringraziamenti

Ci fu un vento impetuoso e gagliardo da spaccare i monti e spezzare le rocce davanti al Signore, ma il Signore non era nel vento.

Dopo il vento, un terremoto, ma il Signore non era nel terremoto.

Dopo il terremoto, un fuoco, ma il Signore non era nel fuoco.

Dopo il fuoco, il sussurro di una brezza leggera.

Incredibile come una brezza leggera faccia tanto rumore.

E' un rumore che ti incuriosce, ti interroga e che vuoi provare a comprendere.

Ed è un rumore che oggi mi fa dire grazie a tutte le persone che mi hanno accompagnato nel progetto di dottorato. A partire dal mio relatore il prof. Parolini, attento nel supervisionarmi e nel guidarmi in questi anni di dottorato. Al prof. Mazzieri per avermi seguito e supportato con costanza ed alla prof. Antonietti per le attente revisioni. Ai colleghi di meccanica i prof. Corradi, prof. Schito ed prof. Rocchi per lo sguardo fisico molto concreto.

Infine grazie a tutti i gli amici nel Tender. Il "fratelli" Giovanni e Giorgio con i quali abbiamo condiviso più di un relatore, a Giuseppe continuo esempio di dedizione e ad Anna, maestra di cura. E poi Emilia, Beatrice, Mattia, Matteo, Dario, Marco, Enrico anche se va a Bergen, Paolo, Giulia, Fede. Grazie a tutti quanti, a vostro modo, avete reso l'ambiente di lavoro sereno. Vabbé, grazie Manu. Ricordati: Troy, Alessandro, Edoardo, Ninjaran, ottimi coinquilini, troy in particolare.

Contents

1	Introduction	3
1.1	Motivation	3
1.2	Computational Aeroacoustics	5
1.3	High Order Numerical Methods for Aeroacoustics	7
1.4	Research Gap and Thesis Novelties	8
1.5	Thesis Outline	9
2	Physical Model	11
2.1	Compressible Fluid Dynamics	11
2.1.1	Basic Kinematics	12
2.1.2	Mass Balance	12
2.1.3	Momentum Balance	13
2.1.4	Constitutive Laws for Newtonian Fluids	13
2.1.5	Energy Balance	14
2.1.6	Compressible Navier Stokes Equations	15
2.1.7	Entropy	15
2.1.8	Adimensional Quantities	16
2.2	Incompressible Fluid Dynamics	17
2.2.1	Incompressible Flow Equations	17
2.2.2	Reynolds Averaged Navier Stokes (RANS)	18
2.2.3	Large Eddy Simulation (LES)	22
2.3	Acoustics	29
2.3.1	Acoustic Wave Equation	29
2.3.2	Analytical Methods for the Wave Equation	31
2.3.3	Boundary Conditions	37
2.4	Aeroacoustic Model	45
2.4.1	Motivations	46
2.4.2	Lighthill's Wave Equation	46
2.4.3	The Hybrid Aeroacoustic Model	48
2.4.4	Semi Analytical Models	50

2.5	Notations	52
2.6	Discretization of the Acoustic Problem	53
2.6.1	SEM Discretization of the Acoustic Wave Equation	53
2.6.2	Fully Discretization of the Acoustic Wave Equation	55
2.6.3	SEM Discretization of Lighthill's Wave Equation	56
2.6.4	DGSEM Discretization of Lighthill's Wave Equation	57
2.6.5	Robust DGSEM	61
2.7	Discretization of the Flow Problem	62
2.7.1	Time Discretization of the Flow Problem	62
2.7.2	Finite Volume Discretization of the Flow Problem	62
2.7.3	Velocity Pressure Coupling for the Flow Problem	67
2.8	Intergrid Projection Method	68
2.9	Intergrid Geometrical Coupling	70
2.9.1	Grid Intersection Algorithm	70
2.9.2	Accuracy of the Intergrid Intersection Algorithm	74
2.9.3	Scalability of the Intergrid Intersection Algorithm	77
2.10	Implementation Remarks	78
2.10.1	A Quadrature-Free Method for Integral Evaluation	78
2.10.2	Source Time Storage	80
2.10.3	Parallel Decomposition	80
2.10.4	Source Time File Reading	81
3	Theoretical Analysis	85
3.1	Preliminaries	85
3.2	A Priori Error Estimate	89
3.3	Approximation Properties of the Intergrid Projection Operator	91
3.3.1	Piecewise Constant Flow Source Term	91
3.3.2	High Order Reconstruction of the Flow Source Term	94
3.4	Numerical Results: Verification of the a Priori Projection Error	97
3.4.1	Piecewise Constant Flow Source Term	97
3.4.2	Piecewise Linear Flow Source Term	100
3.4.3	On High Order Reconstruction of the Flow Source Terms	101
3.5	A Priori Error Estimate with Projected Right Hand Side	102
3.5.1	Preliminary Results	103

3.5.2	Main Results of the Acoustic Problem with Projected Source Term	121
3.6	Verification of the a Priori Error Estimate	128
4	Numerical Results on Acoustics Problems	135
4.1	Manufactured Solution	135
4.2	One-dimensional Bar: Impedance Boundary Conditions	136
4.3	One-dimensional Bar: Absorbing Conditions	139
4.4	Monopole Sound Source	143
4.5	Anechoic Chamber	146
4.5.1	Experimental Setup	147
4.5.2	Sound Source	148
4.5.3	Analytical Model	149
4.5.4	Computational Setup	151
4.5.5	Acoustic Results	151
4.6	Noise Box	152
4.7	Conclusions	154
5	Numerical Results on Aeroacoustic Problems	155
5.1	Potential Flow with Corotating Vortex Pair	156
5.2	Laminar Flow Around a Square Cylinder	160
5.3	Turbulent Flow Around a Tandem Cylinder	165
5.4	Wall Mounted Side View Mirror	172
6	Conclusions and Future Perspectives	185
6.1	Main Outcomes	186
6.2	Perspective and Future Developments	187

List of Figures

1.1	Information on the number of people estimated to be highly annoyed and highly sleep disturbed due to noise from road, railway and aircraft. The data report also the information on the estimated number of cases per year of ischaemic heart disease and estimated premature deaths in 2017 in the EU. The values reported in the graphics are employed to estimate the Burden of Disease (BoD) in Disability Adjusted Life Years (DALYs). Source data: [3].	4
1.2	Engine with serrations. The effects of serrection is to reduce the noise emitted by the nozzle.	4
1.3	Car noise different contributions depending on the vehicle speed. Source: [70].	5
2.1	Ω is divided by the surface Σ in two regions Ω_{IN} , Ω_{OUT}	35
2.2	Transmission acoustic problem. The blue wave p'_{inc} is the incident wave, the red wave p'_{re} is the reflected wave and the green wave p'_{tr} is the transmitted wave.	39
2.3	Example of a domain where we employ the PML conditions.	42
2.4	Computational domain for the aeroacoustic problem and sketch of the hybrid numerical strategy. First, the fluid problem is solved on Ω_f . Then the acoustic source term is computed from the flow velocity. Finally, an inhomogeneous acoustic wave equation is solved on Ω_a	48
2.5	Domain for the Curle's analogy. The pressure fluctuations generated by the flow in V on the body B are evaluated in \mathbf{x} at time t	50

2.6 (a) Discretization employing $r = 1$ elements. (b) Discretization employing $r = 2$ elements. (c) Discretization employing $r = 4$ elements. (d) Discretization employing $r = 8$ elements. In black, edges of the mesh elements. In blue, edges connecting the degrees of freedom. The number of degrees of freedom of the discretized geometry are the same, but the low order approximation is able to better capture the rounded geometrical feature of the object.	58
2.7 Example of a DG decomposition.	59
2.8 Sketch of the geometrical notation for the finite volume discretization. The polyhedral cells K_+ and K_- have barycentre \mathbf{x}_+ , \mathbf{x}_- , that is connected through the segment \mathbf{h} . The segment \mathbf{h} intersects the face F , shared by both elements K_- and K_+ in \mathbf{x}_\cap . We denote with \mathbf{x}_F the face F barycentre, and with \mathbf{h}_- and \mathbf{h}_+ the segments that connect the barycenters \mathbf{x}_- , \mathbf{x}_+ to the face barycentre \mathbf{x}_F	66
2.9 Schematic representation of Algorithm 2. (●) Acoustic element K_a . (●) Example of a fluid element $K_f \in \mathcal{I}_a$. (●) Example of a fluid element $K_f \in \mathcal{K}_a$ but not intersecting with the selected element K_a . (●) Example of a fluid element $K_f \in \mathcal{C}_a$	71
2.10 Schematic representation of Algorithm 2. (●) Acoustic element K_a . (●) Example of a fluid element $K_f \in \mathcal{I}_a$. (●) Example of a fluid element $K_f \in \mathcal{K}_a$ but not intersecting with the selected element K_a . (●) Example of a fluid element $K_f \in \mathcal{C}_a$	72
2.11 (a) Distorted acoustic grid \mathcal{T}_a^1 . (b) Generic polyhedral fluid grid \mathcal{T}_a^2 . (c) Two-dimensional view of the computed intersections between \mathcal{T}_a^1 and \mathcal{T}_f^1 . The considered computational grids are first generated in two dimensions and then extruded in the third dimension, with only one element in the vertical direction. All the intersections between elements in \mathcal{T}_f^1 and a single element in \mathcal{T}_a^1 have the same colour.	76

2.12 (a) Cartesian acoustic grid \mathcal{T}_a^2 . (b) Voroinoi fluid grid \mathcal{T}_f^2 . (c) Intersection between \mathcal{T}_a^2 and \mathcal{T}_f^2 . The fluid grid is made of polyhedral elements, while the acoustic grid is made of hexahedral elements. All the intersections between elements in \mathcal{T}_f^2 and a single element in \mathcal{T}_a^2 have the same color.	76
2.13 Scalability test. The speed-up is computed with respect to the test performed on 8 cores. The coarse mesh has 884736 intersections, while the fine mesh has 7077888 intersections.	77
2.14 Decomposition of a computational grid employing DGSEM. The domain Ω_1 has $r = 1$ and 225000 elements, Ω_2 has $r = 2$ and 90000 elements, and the remaing Ω_3 has $r = 3$ and 300000 elements. We decompose the whole domain employing 512 cores. We notice that introducing the weighting improves the decomposition.	82
2.15 Geometrical decomposition and algebraic decomposition employing 8 cores. During the assembly phase the PETSc wrapper is called assembling the matrices with the new algebraic decomposition.	83
2.16 The scheme represents the reading scratety of the vectors b for the times t_1, \dots, t_n with n cores c_1, \dots, c_n . At time t_1 , each core c_i reads the source $b(t_i)$. Hence, the source $b(t_i)$ is known only by the core c_i . At the time t_j the core c_j communicates each piece of the vector $b(t_j)$ to all the respective core, using the decomposition required by the algebraic solver.	83
3.1 Schematic representation of the computational grids and the correspnding projection operators. For a given function $f \in L^2(\Omega)$, f_f is the projection $\Pi_{0,h_f}f$, f_a is the projection $\Pi_{r,h_a}f_f$ and f_p is the projection $\Pi_{r,h_a}f$. The computational grids \mathcal{T}_a and \mathcal{T}_f are assumed to be nested.	92
3.2 Computed errors $\ f - f_a\ _{L^2(\Omega)}$ versus h_f , for different polynomial degrees $r = 1, 2, 3, 4$ and different choices of $h_a = 0.25, 0.125, 0.0625$	98
3.3 Computed errors $\ f_p - f_a\ _{L^2(\Omega)}$ versus h_f , for different polynomial degrees $r = 1, 2, 3, 4$ and different choices of $h_a = 0.25, 0.125, 0.0625$	99

3.4 Computed errors $\ f - f_p\ _{L^2(\Omega)}$ versus h_a (a) and r (b), for different choices of $r = 1, 2, 3, 4$ and $h_a = 0.25, 0.125, 0.0625$	99
3.5 Computed errors $\ f_p - f_a\ _{L^2(\Omega)}$ versus h_f , for different polynomial degrees $r = 1, 2, 3, 4$ and different choices of $h_a = 0.25, 0.125, 0.0625$ comparing our proposed projection method and mid point projection method, [128].	100
3.6 Computed errors $\ f - f_a\ _{L^2(\Omega)}$ versus h_f , for different polynomial degrees $r = 1, 2, 3, 4$ and different choices of $h_a = 0.25, 0.125, 0.0625$.	102
3.7 Computed errors $\ f_p - f_a\ _{L^2(\Omega)}$ versus h_f , for different polynomial degrees $r = 1, 2, 3, 4$ and different choices of $h_a = 0.25, 0.125, 0.0625$.	103
3.8 Computed errors $\ f_p - f_a\ _{L^2(\Omega)}$ versus h_f , for different polynomial degrees $r = 2, 3, 4$ and different choices of $h_a = 0.25, 0.125, 0.0625$, with a linear flow reconstruction.	104
3.9 Computed errors $\ f_p - f_a\ _{L^2(\Omega)}$ versus h_f , for different polynomial degrees $r = 3, 4$ and different choices of $h_a = 0.25, 0.125, 0.0625$, with a quadratic reconstruction.	105
3.10 Computed errors $\ f - f_a\ _{L^2}$ versus h_f , for different polynomial degrees $r = 1, 2, 3$ and different choices of $h_a = 0.25, 0.125, 0.0625, 0.03125$.	131
3.11 Computed errors $\ \rho(t^N) - \rho_h^n\ _{H^1}$ versus h_f , for different polynomial degrees $r = 1, 2, 3, 4$ and different choices of $h_a = 0.25, 0.125, 0.0625, 0.03125$.	132
3.12 Computed errors $\ \rho(t^N) - \rho_h^n\ _{H^1}$ versus h_a , for different polynomial degrees $r = 1, 2, 3$ and different choices of $h_f = 0.125, 0.0625, 0.03125, 0.015625, 0.0078125, 0.00390625$.	133
4.1 Comparison between the SEM solver AeroSPEED and the Lagrangian FEM solver COMSOL. (a) Computed errors vs number of degrees of freedom (ndof). (b) Computed error versus CPU time. The computational tests were performed on 4 cores Intel(R) Xeon(R) Gold 6226 CPU at 2.70GHz.	137

4.2	(a) Computational domain for the transmission problem. (b) Computational domain for the problem with impedance conditions. (c) Example of the computational grid. The grid elements have black edges, while in blue we represented the edges connecting the internal nodes of the spectral grid.	137
4.3	Comparison of the computed numerical solution for the transmission problem and impedance problem with the exact solution computed at $P1 = (0, 0, -0.2L_\ell)$, $P2 = (0, 0, -0.1L_\ell)$, $P3 = (0, 0, 0.5L_r)$, where $L_\ell = 1\text{ m}$ and $L_r = 0.2\text{ m}$	140
4.4	(a) Setup with Absorbing conditions. (b) Setup with PML conditions.	141
4.5	Computed numerical solutions at the probes $P1$, $P2$, $P3$ computed with the PML with a length of $L_{PML} = 0.15\text{ m}$, $L_{PML} = 0.2\text{ m}$, the absorbing condition and the exact solution.	142
4.6	(a) Computational domain for the case with the absorbing boundary conditions. On the whole external boundary domain $\partial\Omega_a$ the characteristic impedance is imposed. (b) Computational domain for the case with the perfectly matched layer. In blue, the domain of the Ω_{PML} surrounding the whole acoustic domain.	143
4.7	Computed numerical solutions for the case with absorbing boundary conditions and the PML compared with the analytical solution in three probes of interest.	145
4.8	Snapshot for $T = 0.1\text{ s}$ cut with a plane $\mathbf{n} = (-1, 1, 0)$. On the left, solution obtained with the absorbing condition. On the right, solution obtained with the PML. Notice on the corner of the slice the different behaviours of the computend numerical solutions.	145
4.9	(a) Snapshot of the numerical solution computed employing the absorbing boundary conditions. (b) Snapshot of the numerical solution computed employing the PML. For both the snapshots, the shown contour levels are $p' = -0.5, -0.375, -0.25, -0.125, 0.125, 0.25, 0.375, 0.5$ (acoustic pressure in Pa). Notice at the corner of the domains the differences between the computed numerical solutions.	146

4.10 (a) Q-source placed inside the anechoic room, alongside the employed microphones. (b) Schematic representation of the experimental setup. (c) The employed sound generator, the q-source.	148
4.11 Scheme of the processing of the voltage input measured from the q-source. The final employed signal is $\hat{Q}(\mathbf{x}, t)$	150
4.12 (a) Extract of the input source $q(t)$. (b) Comparison between the source spectra before and after the application of a low pass filter. (c) Extract of the input source after the filtering operation $\hat{Q}(t)$	150
4.13 Sketch of the mirroring strategy. We added a specular source and we employ it to compute the effect of the floor Γ_b	150
4.14 Computational model of the anechoic chamber. (a) Sketch of the computational domain with the boundary conditions. In red, the Neumann boundary. In blue, the hull of the PML. (b) Discretization of the computational domain. On the clip xz we show the computational grid with the degrees of freedom. On the clip yz we show the elements of the grid.	151
4.15 Comparison of the computed numerical data with SPEED, the measured data and the analytical frequency response function. (a) Amplitude of the frequency response function computed at microphone M1. (b) Amplitude of the frequency response function computed at microphone M2. (c) Phase of the frequency response function computed at microphone M1. (d) Phase of the frequency response function computed at microphone M2.	152
4.16 (a) Three-dimensional view of the domain of the Noise Box. A and B are the positions of the selected microphones, where $A = (0.424 \text{ m}, 0.595 \text{ m}, 0.151 \text{ m})$ and $B = (0.9 \text{ m}, 0.224 \text{ m}, 0.528 \text{ m})$. (b) Quoted computational domain of the Noise Box. The spanwise length is 0.825 m. In the figure, units are expressed in millimeters.	153
4.17 Computed acoustic pressure measured by microphone A and B with both AeroSPEED and COMSOL.	154
4.18 Snapshots of the computed pressure fluctuations $p' = p - \bar{p}$, where \bar{p} is the average pressure, inside the Noise Box, for $t = 0.495, 0.496, 0.497 \text{ s}$. The selected contour levels are from -7.5 Pa to 7.5 Pa with a step of 1.5 Pa	154

5.1	Sketch of the domain for the corotating vortex pair problem. The model is not to scale.	157
5.2	Comparison between the analytical far field solution and the computed numerical solution obtained with the hybrid approach and by employing the vortex core model. The results have been normalized with respect to $p_{ref} = \max(p - \bar{p})$ to take into account the energy disparity introduced by the vortex model.	158
5.3	Snapshots of the computed numerical solution for the corotating vortex pair for $t = 365, 370, 375, 380$ s.	159
5.4	Computational domain for the flow problem. Here Γ_{in} denotes the inlet boundary condition, Γ_{out} denotes the outlet boundary condition, Γ_n is the Neumann boundary on the square cylinder and Γ_{sym} is the symmetric boundary.	160
5.5	Computational domain of the flow problem and the acoustic problem. The square cylinder has a diameter $D = 3.28 \times 10^{-5}$ m and the fluid domain is a rectangle of size $121D \times 41D$. The acoustic domain is a circle of radius $150D$, centered at the centre of the square. The dotted line represent the sampled probes in the acoustic domain employed to compute the directivity, see Fig. 5.9.	161
5.6	Detail of the acoustic (green) and fluid (blue) computational grids around the square cylinder for the aeroacoustic test case. A structured o-grid is employed for the acoustic problem and a structured h-grid is employed for the flow problem.	161
5.7	Computed lift C_L and drag C_D force coefficients.	164
5.8	Snapshot of the computed acoustic pressure field at $t = 1.47 \times 10^{-4}$ s, 1.48×10^{-4} s, 1.49×10^{-4} s, 1.5×10^{-4} s.	164
5.9	Directivity pattern. The adimensionalized p'_{rms} is sampled on a circumference of radius $75D$, see Fig. 5.5. Comparison with the DNS in [74] and the Curle computations of [140].	165
5.10	Computational domain for the flow problem. Γ_{in} denotes the inlet boundary. Γ_{out} denotes the outlet boundary. Γ_{C1} and Γ_{C2} are the front and rear cylinder's surface, respectively. Γ_{sym} denotes the remaining boundary.	166

5.11 Aeroacoustics computational domain. The center of the computational domain is set at the center of the front cylinder. Microphone probes are located at A = (-8.33D,27.82D), and B = (9.11D, 32.49D), with $D = 0.057\text{ m}$. We denote with Ω_a the acoustic domain, with Ω_f the fluid domain contained in Ω_a . We denote with Γ_{abso} the boundary of the external domain and with Γ_n the wall boundary of the tandem.	167
5.12 Average velocity magnitude $ \mathbf{u} $ on the xy plane with streamlines.	168
5.13 Different snapshots of the flow solution, with isosurfaces of $Q = 1000$ and colored with velocity magnitude.	169
5.14 Comparison of the average drag forces and the <i>rms</i> for lift and drag of the two cylinders. With “Workshop” we denote the data taken from [90]. The lift frequency is common between the two cylinders. The bar is centred on the mean value of the available literature data, and the length of the bar is one standard deviation.	170
5.15 Average C_P distribution on the surface of the front and rear cylinders, where $C_P = \frac{\bar{p} - p_{\text{ref}}}{\frac{1}{2}\rho_0 U_\infty^2}$. With QFF we denote the data measured at the Quite Flow Facility [105], while BART denotes the Basic Aerodynamic Research Tunnel see [105] and with DDES we refer to the computed data in [62].	170
5.16 Snapshot of the fluctuating pressure (from the acoustic computations), and Q criterion colored with the velocity magnitude (from the flow computations).	171
5.17 Comparison of the sound spectra at microphone A=(-8.33D,27.82D) and B=(9.11D, 32.49D). Curle and Curle-Corr denote the data computed in [148], while QFF denotes the experiment in [105].	172
5.18 Geometry of the Side View Mirror.	173
5.19 (a) Computational domain for the flow problem. (b) Geometry of the plate.	174
5.20 Computational support of the aeroacoustic source for the acoustic problem.	174
5.21 Close-up of the side-view mirror with the discretization of the flow problem.	174

5.22	Acoustic domain. The microphones M1, M2, M3, M4, M5 are employed for the acoustic validation.	175
5.23	Slice of the acoustic domain at the yz mid plane. (●) Inner region. (●) Downstream near field region. (●) Transition region (●) Free field region. (a) Description of the discretization strategy. Only the elements are shown. (b) Close up to the mirror geometry. Only the elements are shown. (c) Close up to the mirror geometry. Elements and degrees of freedom are shown.	176
5.24	(a) Id of each measurements probes vs pressure coefficient C_p . DDES refers to [154], Exp denotes the experiments performed in [72], LES denotes the computations in [19]. (b) Position of the probes on the geometry of the SVM.	177
5.25	Snapshot of the averaged field on the zy mid plane.	178
5.26	Snapshots of the instantaneous flow field on the zy mid plane.	179
5.27	Snapshots of the instantaneous flow field, Q criterion.	179
5.28	Near field probes from the CFD computation. DDES refers to the computation performed in [154], LES refers to the computation perfomed in [19], while Exp refers to the experiment in [72].	180
5.29	Countour plot of the acoustic field.	180
5.30	Computed pressure fluctuations acquired at the microphone M1, M2, M3, M4, M5 see Table 5.8, compared from the reference values of the experimental data in [72].	181

List of Tables

2.1	Computed $E_{rel}(f)$, for different meshes: acoustic grid \mathcal{T}_a^1 , fluid grid \mathcal{T}_f^1 and their intersection $\mathcal{T}_a^1 \cap \mathcal{T}_f^1$. Here, $\Omega = (-2, 2) \times (-2, 2) \times (-0.05, 0.05)$	75
2.2	Computed error $E_{rel}(f)$ for different meshes: acoustic grid \mathcal{T}_a^2 , fluid grid \mathcal{T}_f^2 and their intersection $\mathcal{T}_a^2 \cap \mathcal{T}_f^2$. Here, $\Omega = (-0.5, 0.5)^3$	75
5.1	Parameters employed for the rotating vortex pair test case.	157
5.2	Boundary conditions for the laminar flow around a square cylinder. The boundary definitions are detailed in Figure 5.4.	160
5.3	Comparison of the results on the laminar flow around the cylinder with analogous results available in the literature, at $Re = 150$	163
5.4	Boundary conditions for the flow around the tandem cylinder. On the walls of the front and the rear cylinder wall functions (WF) are applied. ω WF is the wall function denoted as <code>omegaWallFunction</code> in OpenFOAM, see [115]. $kqRWF$ is the wall function denoted as <code>kqRWallFunction</code> in OpenFOAM.	166
5.5	Boundary condition for the flow around a side view mirror problem. ω WF is the wall function denoted as <code>omegaWallFunction</code> in OpenFOAM, see [115]. $kqRWF$ is the wall function denoted as <code>kqRWallFunction</code> in OpenFOAM. The boundary are defined in Figure 5.19a.	173
5.6	Position of the probes for the computation of the pressure coefficient C_p . The microphone positions are taken from [72].	182

5.7	Position of the probes for the computation of the flow spectra. The microphone positions are taken from [72].	183
5.8	Microphone positions for the acoustic computations. The microphone positions are taken from [72].	183

Chapter 1

Introduction

1.1 Motivation

Aeroacoustics is the field of acoustics that studies the noise induced by air flows. Aeroacoustic noise is relevant in common situations like air and ground transportation, ventilation systems, wind-energy production and buildings. Reducing the aeroacoustic noise plays an important role on the well-being and positively impacts human health. Indeed, chronic noise exposure has been associated to tinnitus, sleep deprivation and cardiovascular diseases [67, 68] as it has been also reported by the European Environment Agency, see Figure 1.1. The European Commission outlined the vision for the future of aviation highlighting the importance of reducing noise pollution in the aeronautic industry [38]. The program sets a challenging goal of achieving a 65% reduction in the effective perceived noise (EPN) emissions from flying aircraft by the year 2050 by suggesting policies and strategies to reduce the noise. Aircraft and engine manufacturers are investigating strategies to reduce the *noise at source*. New reducing noise solutions have been largely explored and introduced, like for instance the presence of serrations at the back of the engines [113, 150], see Figure 1.2. The next generation aircraft engines, characterized by high bypass ratio, need to provide strategies to reduce the noise emitted by the aircraft [25, 104]. In urban areas, most of the noise comes from ground transportation. The noise from vehicles is generated mainly by the engine noise, the wind noise and the rolling noise, depending at which speed the vehicle travels. Typical spectra for these different sound sources are compared in Figure 1.3. Recently, cities started considering strategies to lower the speeds of the vehicles, bringing the speed limits in the streets from

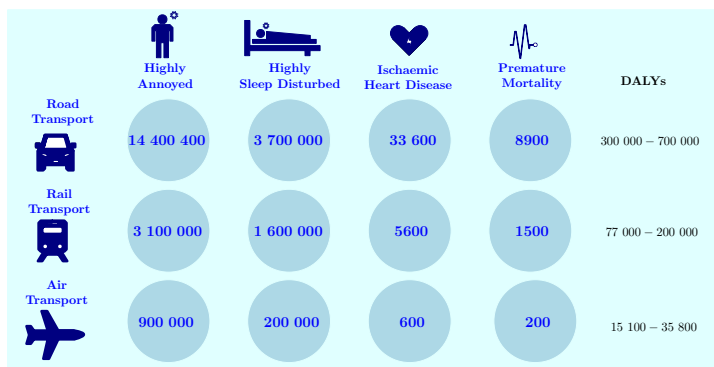


Figure 1.1: Information on the number of people estimated to be highly annoyed and highly sleep disturbed due to noise from road, railway and aircraft. The data report also the information on the estimated number of cases per year of ischaemic heart disease and estimated premature deaths in 2017 in the EU. The values reported in the graphics are employed to estimate the Burden of Disease (BoD) in Disability Adjusted Life Years (DALYs). Source data: [3].

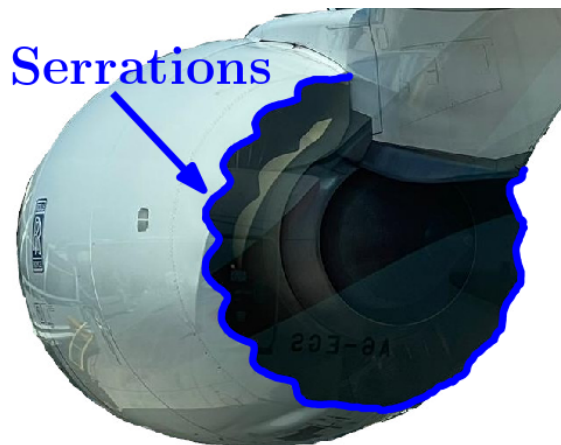


Figure 1.2: Engine with serrations. The effects of serrection is to reduce the noise emitted by the nozzle.

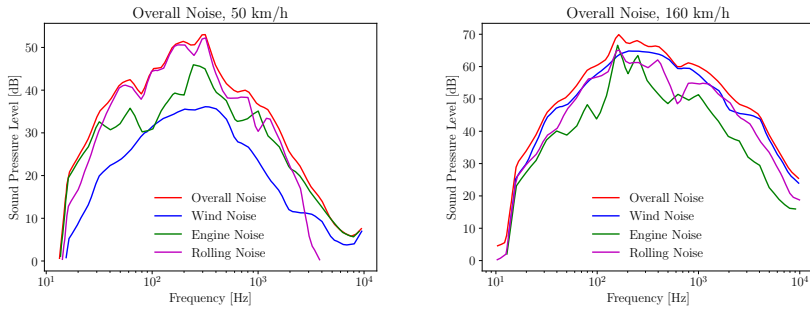


Figure 1.3: Car noise different contributions depending on the vehicle speed. Source: [70].

50 km h^{-1} to 30 km h^{-1} . Although this mainly affects the safety of the pedestrians, it has also a positive impact on the noise generated by the road urban traffic [28]. At higher speeds, the main noise source is due to the aeroacoustic noise, see Figure 1.3. Also, since we are moving towards the electrification of private mobility, wind noise reduction is critical to provide the users with high quality comfort and to reduce noise pollution. Car manufacturers are investigating the possibility of changing the shape of the side-view mirror [37, 152], or changing the shape of the frontal pillar [103] in order to reduce the aeroacoustic noise. Within this framework, it is clear how it is strategical to have a design tool that is able to predict the aeroacoustic noise emitted and it is able to help to provide new noise reduction solutions.

1.2 Computational Aeroacoustics

The aeroacoustic problem is an inherently multiscale problem. In fact, two regions can be typically identified with very different physical behaviours [127]. The *near field* region is where the sound is generated, and it is primarily dominated by the flow problem. Here the relevant length scales are those associated to fluid dynamics. In particular, in the case of turbulent flows, very small spatial and temporal scales have to be accounted for. We might also have large velocity gradients, separations and flow instabilities to further complicate the problem. Conversely, at the *far field* region the flow is typically much simpler, often almost steady and the physics is dominated by the propagation of acoustic waves where the involved length scales are larger. These two problems might interact, having a feedback between the acoustic

pressure fluctuations and the flow field.

In principle, the full aeroacoustic problem can be modelled with a fully compressible Navier-Stokes system. The model would be the most accurate from the physical point of view, taking inherently into account the small scales of the flow problem, the large scales of the acoustic problem and their continuous interplay. With the increase of computational power, simple cases like the laminar flows in [73, 74] are nowadays more affordable, but far from real industrial applications. By combining proper turbulence modelling, in [61] a numerical solution of the flow around a side view mirror the near field noise is obtained. Recently, also Lattice Boltzmann approach gained popularity showing good accuracy in solving the required scales to generate reliable aeroacoustic noise predictions [29, 122, 124]. However, the large amount of computational resources required by direct noise computation makes the full aeroacoustic simulation unpractical when aiming to industrial applications.

By exploiting the different scales of the problem, it is possible to tackle the aeroacoustic computations in a segregated manner employing the aeroacoustic analogies. An aeroacoustic analogy is an acoustic model derived from the Navier-Stokes equations. The first aeroacoustic analogy was introduced by Lighthill in [86, 87], where an exact acoustic wave equation was derived from the mass and momentum balance laws of the compressible Navier Stokes system. The flexibility of the segregated approach allows then to solve the acoustic problem in many ways. In [86, 87], the solution was obtained by employing a far field Green function. In [40], Curle proposed a strategy based on the Kirchhoff integral to solve the acoustic problem. This strategy takes into account the effects of the solid boundary and hence the noise generated by the flow over a rigid body. Following Lighthill's analogy idea, many alternative aeroacoustic analogies have been derived, with the objective of highlighting a particular noise generation mechanism. For instance, Möhring [99] and Powell [116] proposed an aeroacoustic analogy where the sound source term depends on the vorticity of the flow field, strictly linking the vortex motion with the sound generation. A critical contribution was finally introduced by the work of Ffowcs Williams and Hawkings (FWH), [58] and later improved in [27, 42, 82]. While Curle proposed an integral method to compute the noise given the presence of solid boundaries, the FWH extends the result by proposing an integral method that is able to predict the noise of moving bodies. The computational strategy selects a surface that contains

the sound noise sources. On that surface, the flow data is interpolated and the far field pressure fluctuations are obtained by solving integrals over the surface. Often the volume terms present in the formulation are neglected. The FWH and Curle analogy are very practical aeroacoustic methodologies, that allow to obtain a rapid information at the far field and that can be easily interfaced with CFD codes. However, the selection of a surface integral that includes meaningful sound source requires expertise and the solution provided is only at a specific point in the far field space.

Another class of models is based on the decomposition of the physical variables in each physical components. An example of this class of models is the Perturbed Compressible Equation (PCE) [132]. The strategy is to decompose the fluid in incompressible and compressible contributions. In the far-field, the compressible perturbed quantities coincide with the acoustic physical quantities. The final PCE is derived by subtracting the compressible equations from the incompressible ones. Different methods based on the Helmholtz decomposition are considered in [120]. In [69] the Expansion about the Incompressible Flow (EIF) model was proposed, where first the incompressible flow field is solved. Then the acoustic solution is obtained in a second step via a perturbation equations. Other families of models are the Acoustic Perturbed Equations (APE) [53], where hydrodynamic instabilities are filtered out and an equation for the only perturbed pressure is derived. In [102, 121] an alternative derivation of the APE system is obtained by Mach number scaling.

1.3 High Order Numerical Methods for Aeroacoustics

In the context of aeroacoustics, high order numerical methods have been studied since [142] proposed Dispersion-Relation-Preserving (DRP) high order numerical finite difference schemes in order to characterize the properties of possible finite difference discretizations. High order methods provide low dissipation and low dispersion errors, fundamental for properly propagating the acoustic waves. The most relevant breakthroughs in high order methods have been obtained with Spectral Element Methods (SEM). SEM were successfully applied to fluid dynamics [32, 92, 112], and now they are a solid numerical tool, where the theory is mainly covered in [31], while examples of many applications can be found in [33]. Spectral methods are based on local polynomial

approximations very similar to that provided by the p -version of the finite element method, see [20]. They have been largely applied also to wave propagation problems [54, 93] and seismology [139]. The success of the SEM is mainly due to their accuracy [23] and efficiency [2]. The greatest defect of the SEM is the lack of flexibility when dealing with complex geometrical problems where the requirement of conforming grids may need a huge human time and effort in grid generation. The Discontinuous Galerkin (DG) methods were first introduced in [15, 45, 118], and thanks to their flexibility in handling mesh non conformities, different approximation degrees in the discretization and non regular solutions have been applied successfully in a wide range of problems, see [71, 119] for a comprehensive review. To overcome the lack of flexibility of the SEM method and at the same time exploit the accuracy of the SEM, the DGSEM were introduced. The DGSEM numerical method [12, 14, 95] enhance the flexibility of the numerical solver, allowing the user to mesh with small low order elements close to the geometry, while employing high order elements at the far field to best employ the high accuracy of the numerical method. Furthermore, DGSEM are known for being low dissipative and low dispersive high order numerical methods, compare with [4, 5]. DGSEM have already been applied with great success, and with large computational resources, to direct noise computations in [57, 59]. Also, in [106, 126] a hybrid APE is solved via a DGSEM-FV method, where hierarchical Cartesian grids are employed for fast computations and large scalability. In order to achieve high order also in time, Arbitrary high order DERivatives (ADER) have been introduced, see [130]. The ADER time integration scheme combined with the DG paradigm (ADER-DG) allow to obtain high-order accuracy in the space-time domain. ADER-DG have been employed in aeroacoustics to solve the Lineareized Euler Equations, see for instance [121]. Finally, the DG method have been recently generalized to Polyhedral Discontinuous Galerkin (PolyDG) [30]. The PolyDG method discretize in space with the DG philosophy on grids made by arbitrarily shaped polyhedra. Recent applications to wave propagation problems can be found in [9, 10, 13].

1.4 Research Gap and Thesis Novelties

The main objective of the thesis is to explore, given an acoustic forcing term computed from a finite volume CFD solver, high order numerical methods for the Lighthill's wave equation employing the DGSEM

method. In this context, a critical step is to interpolate as accurately as possible the sound source term from the flow problem to the acoustic problem. While simple nearest neighbour interpolation fails to compute the acoustic sources accurately [35], conservative interpolation schemes lack of important analytical framework, although they have been successfully employed, see for instance [80]. In this thesis we propose a novel projection method that can be seen as the extension of the conservative interpolation proposed in [128] and [126], suitable for high order approximations. In fact, we propose a computational strategy to handle intersection between generic polyhedral grids and we combine a quadrature free method to integrate over the intersected polyhedra. The proposed coupling strategy is flexible and acts as a black box, requiring only the sound source term at the cell centre of the fluid cell and hence it is well suited to be plugged onto any finite volume solver. Furthermore, the novel coupling strategy is naturally fitted for high order approximations since the employed quadrature formula integrates exactly arbitrary polynomials and it can be extended by considering high order reconstruction of the sound source term. In this framework, we provide a rigorous theoretical analysis quantifying the effect of the projection error and how it affects the accuracy of the acoustic solver. The developed aeroacoustic solver AeroSPEED [18] extends the high performance library SPEED [95], whose scalability and computational performance have been largely tested. The new aeroacoustic library has to careful handle the I/O of the data in order to preserve the scalability and the computational power of the original library.

1.5 Thesis Outline

In Chapter 2 we introduce the physical models at the foundation of aeroacoustic problems. From the compressible fluid equations we derive the incompressible equations. Then we derive the acoustic wave equation and finally we derive an aeroacoustic model based on the Lighthill's wave equation. In Chapter 2.4.4 we detail the employed numerical methods. We first introduce the SEM method and the DGSEM, then the FV method and we finally detail our novel intergrid projection strategy. The last part of the chapter is dedicated to implementation remarks. In Chapter 3 we provide the novel analysis of the projection method, considering both the case of a piece-wise constant solution coming from the flow grid and the more general case of a re-

constructed high order flow solution. Then we present a novel result on the fully discrete analysis for the acoustic with projected source solution. We provide a priori error estimates that are verified for the projection error and for the fully discrete aeroacoustic problem. In Chapter 4 we assess the efficiency and the accuracy of the acoustic solver, by solving purely acoustic problems. In Chapter 5 we present the application of the developed computational strategy in AeroSPEED to numerous aeroacoustic benchmarks. Finally, Chapter 6 draws the conclusions of the work.

The results in this thesis have been partially submitted for publication, see [17], [18]. The numerical results have been obtained with SPEED [95, 138] and OpenFOAM [111], while for mesh generation we employed CUBIT [24].

Chapter 2

Physical Model

In this chapter, we recall the fundamental physical models governing aeroacoustic problems. The description tries to be at the same time complete and synthetic, giving an overview of the different topics and the fundamentals required to have the proper tools to understand the basic of aeroacoustics. From the mass, momentum and energy balance laws, we derive the system of equations describing compressible flows. Considering low Mach regime, incompressible models are then derived. Moreover, by selecting particular regime conditions, we derive the acoustic wave equation. In the final section, we rewrite again the balance laws for compressible flows and we obtain the Lighthill's wave equation that models the aeroacoustic problem. The employed physical models are well known in the literature and the purpose of this chapter is to give a uniform notation and to have a general outlook on the whole physical setting.

2.1 Compressible Fluid Dynamics

Balance laws are the building blocks for continuum mechanics. They are proposed from physical principles that are assumed to be valid and primitive. The first principle is the conservation of mass. The second principle is the balance of linear momentum, that corresponds to Newton's second law for continua. The third principle is the balance of energy, that follows from the first law of thermodynamics. The last principle is the creation of entropy, which follows from the second law of thermodynamics. From these principles, we are able to derive the governing equations concerning aeroacoustic problems.

2.1.1 Basic Kinematics

Consider a domain $\Omega \subset \mathbb{R}^3$, and denote with $\mathbf{u}(\mathbf{x}, t)$ the Eulerian velocity of the fluid in Ω . The trajectory $\mathbf{x}(t)$ of a fluid particle is obtained as solution to the following Cauchy problem:

$$\begin{cases} \dot{\mathbf{x}}(t) = \mathbf{u}(\mathbf{x}, t), \\ \mathbf{x}(0) = \mathbf{x}_0, \end{cases}$$

where \mathbf{x}_0 is the initial position of the particle at time $t = 0$. We denote with \mathcal{L}_t the Lagrangian map that maps the initial point \mathbf{x}_0 into the point $\mathbf{x}(t)$ at time t . If the velocity \mathbf{u} is regular enough, then the map \mathcal{L}_t is invertible. Consider now a generic scalar field $\chi(\mathbf{x}, t)$. We denote with

$$\frac{D}{Dt}\chi(\mathbf{x}, t) = \frac{\partial}{\partial t}\chi(\mathbf{x}(t), t) = \frac{\partial\chi}{\partial t} + \mathbf{u} \cdot \nabla\chi$$

the material derivative of χ , namely the time derivative of the scalar field χ along the trajectory $\mathbf{x}(t)$. Now, let $V(t)$ be a material volume element of the fluid, namely $V(t) = \mathcal{L}_t(\widehat{V})$ and $\widehat{V} \subset \Omega$.

We recall the following result:

Theorem 2.1.1 (Reynolds' Transport Theorem). *Given an Eulerian velocity field $\mathbf{u}(\mathbf{x}, t)$, the corresponding Lagrangian map \mathcal{L}_t , a material element $V(t) = \mathcal{L}_t(\widehat{V})$ and a differentiable scalar field χ , then:*

$$\frac{D}{Dt} \int_{V(t)} \chi \, d\mathbf{x} = \int_{V(t)} \frac{\partial\chi}{\partial t} \, d\mathbf{x} + \int_{\partial V(t)} \chi \mathbf{u} \cdot \mathbf{n} \, d\sigma = \int_{V(t)} \left(\frac{\partial\chi}{\partial t} + \nabla \cdot (\chi \mathbf{u}) \right) \, d\mathbf{x}$$

where \mathbf{n} is the outward unit normal to the surface $\partial V(t)$.

2.1.2 Mass Balance

We introduce the density field $\rho(\mathbf{x}, t)$, and we define the mass $m(V(t)) = \int_{V(t)} \rho(\mathbf{x}, t) \, d\mathbf{x}$. The principle of mass conservation states that the mass m of any control volume $V(t)$ does not vary in time. We formulate the principle of mass conservation as follows:

$$\frac{D}{Dt} \int_{V(t)} \rho(\mathbf{x}, t) \, d\mathbf{x} = 0.$$

By applying Reynolds' Transport Theorem, we have that:

$$\frac{D}{Dt} \int_{V(t)} \rho(\mathbf{x}, t) \, d\mathbf{x} = \int_{V(t)} \left(\frac{\partial\rho}{\partial t} + \nabla \cdot (\rho \mathbf{u}) \right) \, d\mathbf{x} = 0, \quad (2.1)$$

that is the integral mass balance equation. Since Eq. (2.1) has to be valid for any control volume $V(t)$, we obtain the local mass conservation balance equation:

$$\frac{\partial \rho}{\partial t} + \nabla \cdot (\rho \mathbf{u}) = 0 \quad (2.2)$$

that is also often referred as continuity equation.

2.1.3 Momentum Balance

The next principle follows the second Newton's law, stating that the net forces are equal to the variation of the linear momentum of a system. Hence, we introduce the variation of the linear momentum of an arbitrary volume of fluid $V(t)$ with:

$$\frac{D}{Dt} \int_{V(t)} \rho \mathbf{u} \, d\mathbf{x}.$$

The external forces acting on a volume $V(t)$ can be classified as *volume forces* or *surface forces*. We denote with \mathbf{f}_V the volume force per unit mass such that the total force on $V(t)$ is $\int_V \rho \mathbf{f}_V dV$. We assume the Cauchy principle to be valid, and we apply the Cauchy theorem, see for instance [60]. Then the surface forces acting on the surface of the volume $V(t)$ can be described by $\int_{\partial V(t)} \boldsymbol{\sigma} \cdot \mathbf{n} \, d\sigma$, where $\boldsymbol{\sigma}$ is the Cauchy stress tensor. We obtain the integral balance:

$$\frac{D}{Dt} \int_{V(t)} \rho \mathbf{u} \, d\mathbf{x} = \int_{V(t)} \rho \mathbf{f}_V \, d\mathbf{x} + \int_{\partial V(t)} \boldsymbol{\sigma} \cdot \mathbf{n} \, d\sigma$$

By applying the Reynolds' Transport Theorem and the divergence theorem, we obtain the momentum equation:

$$\frac{\partial}{\partial t} (\rho \mathbf{u}) + \nabla \cdot (\rho \mathbf{u} \otimes \mathbf{u} - \boldsymbol{\sigma}) = \rho \mathbf{f}_V. \quad (2.3)$$

2.1.4 Constitutive Laws for Newtonian Fluids

To complete the definition of the momentum equation 2.66 we need to characterize the Cauchy stress $\boldsymbol{\sigma}$. From the balance of the angular momentum, we obtain that $\boldsymbol{\sigma}$ is symmetric. Next, we ask that at rest

the internal stresses are only due to the fluid pressure. This condition is realized by assuming

$$\boldsymbol{\sigma} = -p\mathbf{I} + \boldsymbol{\tau},$$

where $\boldsymbol{\tau}$ is the viscous stress tensor and \mathbf{I} is the identity matrix. Next, we require that $\boldsymbol{\tau}$ is continuous with respect to $\nabla \mathbf{u}$. Finally, we require the frame invariance property. This means that for any change of coordinates imposed by the orthogonal matrix $Q \in \mathbb{R}^d$, the following holds:

$$Q^T \boldsymbol{\tau}(\nabla \mathbf{u}) Q = \boldsymbol{\tau}(Q^T \nabla \mathbf{u} Q).$$

From all these assumption it is possible to deduce that $\boldsymbol{\tau}$ depends on the strain rate tensor $\mathbf{S}(\mathbf{u}) = \frac{1}{2}(\nabla \mathbf{u} + \nabla \mathbf{u}^T)$. In order to obtain a Newtonian fluid, we require that $\boldsymbol{\tau}$ depends linearly on \mathbf{D} .

$$\boldsymbol{\tau} = \lambda \nabla \cdot \mathbf{u} \mathbf{I} + 2\mu \mathbf{D}(\mathbf{u}),$$

where μ is the dynamic viscosity and λ is the second viscosity coefficient. For incompressible flows, we have that:

$$\boldsymbol{\sigma} = -p\mathbf{I} + \mu \mathbf{S}(\mathbf{u}).$$

2.1.5 Energy Balance

The next balance law comes from thermodynamics. In particular, the first law of thermodynamics states that the rate of change of the total energy of an arbitrary volume of fluid is equal to the sum of the power of the forces acting on the fluid and the heat power supplied to it. We define the total energy per mass unit as the sum of the internal energy and the kinematic energy per mass unit, namely:

$$e = e_i + \frac{1}{2}|\mathbf{u}|^2.$$

The power of the external forces acting on the volume $V(t)$ are given by

$$\int_{V(t)} \rho \mathbf{f}_V \cdot \mathbf{u} \, d\mathbf{x},$$

while the power of the internal forces acting on the surface of the volume $\partial V(t)$ is given by:

$$\int_{\partial V(t)} (\boldsymbol{\sigma} \cdot \mathbf{n}) \cdot \mathbf{u} \, d\sigma.$$

We now denote with s_V and internal heat source per mass unit, and its contribution of heat power supplied to the system is:

$$\int_{V(t)} \rho s_V \, d\mathbf{x}.$$

We finally obtain the integral balance:

$$\begin{aligned} \frac{D}{Dt} \int_{V(t)} \rho e \, d\mathbf{x} &= \int_{V(t)} \rho \mathbf{f}_V \cdot \mathbf{u} \, d\mathbf{x} + \int_{V(t)} \rho s_V \, d\mathbf{x} \\ &\quad + \int_{\partial V(t)} (\boldsymbol{\sigma} \cdot \mathbf{u}) \cdot \mathbf{n} \, d\sigma - \int_{\partial V(t)} \mathbf{q} \cdot \mathbf{n} \, d\sigma \end{aligned}$$

Now, after integrating by parts and employing the Reynolds transport theorem we obtain the final local balance for the energy:

$$\frac{\partial}{\partial t}(\rho e) + \nabla \cdot (\rho e \mathbf{u} - \boldsymbol{\sigma} \cdot \mathbf{u} - \mathbf{q}) = \rho \mathbf{f}_V \cdot \mathbf{u} + \rho s_V. \quad (2.4)$$

2.1.6 Compressible Navier Stokes Equations

From the balance laws introduced in the previous sections, see Equations (2.2), (2.3) and (2.4), we obtain the following system of equations:

$$\begin{aligned} \frac{\partial \rho}{\partial t} + \nabla \cdot (\rho \mathbf{u}) &= 0, \\ \frac{\partial}{\partial t}(\rho \mathbf{u}) + \nabla \cdot (\rho \mathbf{u} \otimes \mathbf{u} - \boldsymbol{\sigma}) &= \rho \mathbf{f}_V, \\ \frac{\partial}{\partial t}(\rho e) + \nabla \cdot (\rho e \mathbf{u} - \boldsymbol{\sigma} \cdot \mathbf{u} - \mathbf{q}) &= \rho \mathbf{f}_V \cdot \mathbf{u} + \rho s_V, \end{aligned}$$

supplemented with suitable boundary and initial conditions. The system of equations is closed after providing a proper state equation.

2.1.7 Entropy

The second principle of thermodynamics states that the entropy function $s(\mathbf{x}, t)$ has to be non decreasing. Hence, following Section 2.3 in [146], we introduce the following inequality:

$$\frac{Ds}{Dt} \geq 0.$$

Often this equation is rewritten in order to explicitly consider both the effects of the dissipation Υ that models the irreversible effects and the heat transfer \mathbf{q} . The above equation becomes:

$$\rho T \frac{Ds}{Dt} = \Upsilon - \nabla \cdot \mathbf{q}.$$

By considering an adiabatic transformation, hence neglecting the effects of the heat transfer \mathbf{q} , and a reversible transformation, where we neglect the dissipative term Υ , we obtain the following equation:

$$\frac{Ds}{Dt} = 0,$$

and hence the entropy of a fluid particle is constant. Such process is said to be isentropic. If we furthermore ask for the flow to be homentropic, we are requiring that:

$$\nabla s = 0.$$

In general a flow can be isentropic or homentropic only if the effects of the viscosity or the heat conduction are negligible. Fluids that can be modelled with neither viscosity nor thermal conductivity are called inviscid.

2.1.8 Adimensional Quantities

In order to describe the different regimes of the flow problems, we introduce the following adimensional numbers. The Reynolds number is defined as

$$Re = \frac{UL}{\nu},$$

where U is the speed of the flow, L is a characteristic dimension of the geometry of the problem and ν is the kinematic viscosity, namely $\nu = \frac{\mu}{\rho}$, where μ is the viscosity. The Reynolds number describes the ratio between the inertial and viscous forces acting on a flow problem. It is usually employed to define the flow regime for flow problems, where low Reynolds number indicates laminar problems and high Reynolds number indicates turbulent problems. The Mach number is defined as

$$Ma = \frac{U}{c},$$

where c is the speed of sound. The Mach number describes the level of compressibility of the flow.

Given a wave signal, we usually identify it by its frequency f , its wavenumber k , its wavelength λ . We now introduce the Strouhal number

$$St = \frac{fL}{U},$$

that describes the oscillatory property of certain types of flows. Next, we define the Helmholtz number as:

$$He = \frac{L}{\lambda} = StMa.$$

The Helmholtz number describes the ratio between the wavelength of the flow sources and the radiated acoustic wave length, and it hence measures of acoustic compactness.

2.2 Incompressible Fluid Dynamics

We consider now flow problems where the density of the fluid doesn't vary along the flow. This condition enforces the incompressibility constraint. After having described the equations for an incompressible flow problem, we focus our description in introducing the main turbulence models employed for the aeroacoustic computations that are shown in Chapter 5. We consider incompressible flow fields in order to simplify the flow problem, since for low Mach flows the effects on the acoustic computations in the hybrid framework is small.

2.2.1 Incompressible Flow Equations

We assume that the density of the fluid is constant, and we denote it with ρ_0 . This approximation is typically considered acceptable for flow where Mach number is $Ma < 0.3$. A fluid with constant density is inherently incompressible. We consider now a viscous Newtonian fluid $\boldsymbol{\sigma} = -p\mathbf{I} + 2\mu\mathbf{S}(\mathbf{u})$ where μ is the dynamic viscosity and $\mathbf{S}(\mathbf{u})$ is the strain rate tensor $\mathbf{S} = \frac{1}{2}(\nabla\mathbf{u}^T + \nabla\mathbf{u})$. The mass balance (2.2) and momentum (2.3) equations become:

$$\frac{\partial \mathbf{u}}{\partial t} + \nabla \cdot (\mathbf{u} \otimes \mathbf{u}) - \nabla \cdot (\nu \nabla \mathbf{u}) + \frac{1}{\rho_0} \nabla p = 0, \quad (2.5)$$

$$\nabla \cdot \mathbf{u} = 0, \quad (2.6)$$

where ν is the kynematic viscosity. The mass equation (2.2) has become in (2.6) the incompressibility constraint. When dealing with

turbulent flows, the smallest scale λ_f that has to be solved is called Kolmogorov length scale. At this scale, the viscosity effects dominate and the turbulent kinetic energy of the flow is dissipated into heat. The largest scales L_f are often referred as integral length scales. This scale describes the correlation length of the velocity. It is possible to show that the ratio between the Kolmogorov length scale and the integral length is $\frac{\lambda_f}{L_f} \approx Re^{-\frac{3}{4}}$, see for instance sec. 6 of [114]. Let us now consider the following example. Imagine that we have to provide a computational grid that is able to solve all the scales for an incompressible flow problem inside a cube $\Omega_f = (-0.5, 0.5)^3$. If we fix the integral length scale to 1 m, the grid has to be able to resolve scales of the order of $\lambda_f = Re^{-\frac{3}{4}}$, meaning that the grid size $\Delta x \approx \lambda_f$. This implies that the number of degrees of freedom for the discretization in space is $Re^{\frac{9}{4}}$. Problems of engineering interest in the field of aeroacoustics such as, for instance, the flow around a car, train aerodynamics or wind over buildings are characterized by Reynolds numbers that may range from 10^4 to 10^8 , meaning that performing a direct numerical simulation that solves equations (2.71) able to resolve all the different scales up to the Kolmogorov scale is unaffordable. In this section we briefly discuss turbulence modelling techniques that try to overcome the problem.

2.2.2 Reynolds Averaged Navier Stokes (RANS)

Instead of solving for the instantaneous velocity and pressure, it could be useful to solve for the averaged velocity or pressure. With this objective, we introduce the Reynolds Averaged Navier Stokes equations. Let us consider the so called *Reynolds decomposition*:

$$\mathbf{u} = \bar{\mathbf{u}} + \mathbf{u}',$$

where the overline denotes the average in time operator defined as:

$$\overline{\phi(\mathbf{x}, t)} = \int_0^t \phi(\mathbf{x}, \tau) d\tau.$$

Now, average in time eq. (2.6) and eq. (2.5):

$$\begin{aligned} \rho_0 \frac{\partial \bar{\mathbf{u}}}{\partial t} + \rho_0 \nabla \cdot (\overline{\mathbf{u} \otimes \mathbf{u}}) &= -\nabla p + \mu \Delta \bar{\mathbf{u}}, \\ \nabla \cdot \bar{\mathbf{u}} &= 0. \end{aligned} \quad (2.7)$$

The non-linear term $\overline{\mathbf{u} \otimes \mathbf{u}}$ in the momentum equation (2.7) can be expanded with the Reynolds decomposition as $\overline{\mathbf{u} \otimes \mathbf{u}} = \overline{\mathbf{u}} \otimes \overline{\mathbf{u}} + \mathbf{u}' \otimes \mathbf{u}'$. Now, we introduce the so called Reynolds stress tensor:

$$\boldsymbol{\tau}_R = -\rho_0 \overline{\mathbf{u}' \otimes \mathbf{u}'},$$

and we finally get:

$$\rho_0 \frac{\partial \overline{\mathbf{u}}}{\partial t} + \rho_0 \nabla \cdot (\overline{\mathbf{u} \otimes \mathbf{u}}) = -\nabla \bar{p} + \nabla \cdot \overline{\boldsymbol{\tau}} + \nabla \cdot \boldsymbol{\tau}^R, \quad (2.8)$$

$$\nabla \cdot \overline{\mathbf{u}} = 0, \quad (2.9)$$

where $\overline{\boldsymbol{\tau}}$ is the *averaged stress tensor* $\overline{\boldsymbol{\tau}} = \mu(\nabla \overline{\mathbf{u}}^T + \nabla \overline{\mathbf{u}})$. In order to provide a closed system of equations, the Reynolds stress tensor $\boldsymbol{\tau}_R$ has to be modelled since we are not resolving \mathbf{u}' . Usually, only the isotropic part of the Reynolds stress tensor is modelled:

$$\boldsymbol{\tau}^A = \boldsymbol{\tau}^R - \frac{1}{3} \text{tr}(\boldsymbol{\tau}^R),$$

and the averaged pressure \bar{p} is redefined as $P = \bar{p} - \frac{1}{3} \text{tr}(\boldsymbol{\tau}^R)$. In fact, the pressure for an incompressible flow is no longer a thermodynamic quantity, but physically only provides a mechanical force that ensures the enforcement of the continuity equation and mathematically is a Lagrangian multiplier for the incompressible constraint.

Eddy Viscosity Models

The mostly employed RANS turbulence model are the so-called eddy viscosity models, where the anisotropic stress tensor is modelled by introducing an artificial turbulent viscosity:

$$\boldsymbol{\tau}^A = 2\nu_T \rho_0 \overline{\mathbf{S}}, \quad (2.10)$$

where $\overline{\mathbf{S}}$ is the averaged shear stress tensor $\overline{\mathbf{S}} = \frac{1}{2}(\nabla \overline{\mathbf{u}}^T + \nabla \overline{\mathbf{u}})$. The underlying idea is that the behaviour of the diffusion for a flow should be similar to the Fick's law from the molecular dynamics, see for instance sec. 4.4 of [114]. The most successful choices to model the turbulent viscosity ν_T have been the two-equation models. By the similarity theory, it is possible to relate the turbulent viscosity ν_T to only two quantities. Then, the main strategy is to provide new evolution equation that model these quantities. One of the most successful turbulence models have been the $k - \epsilon$ model, see [84] and [141]. Its

main limitation is related to its poor performance in simulating the proper behaviour of boundary layers up to separation, see [151]. As an alternative, the $k - \omega$ model was proposed, see for instance [151]. The model is substantially more accurate than the $k - \epsilon$ near the wall layers, but suffers with flows where the separation is induced by the pressure, like for instance the separation occurring in a flow past a bluff body.

$k - \omega$ Shear Stress Transport Turbulence Model

We focus our attention on the $k - \omega$ Shear Stress Transport (SST) model originally proposed in [96] in its version described in [97]. The model is a zonal model that automatically takes advantage of the performance of both the $k - \epsilon$ and of the $k - \omega$ turbulent models in different regions. The $k - \omega$ SST is an eddy viscosity model in which the turbulent viscosity ν_T is modelled as:

$$\nu_T = \frac{a_1 k}{\max(a_1 \omega, \bar{S} F_2)}, \quad (2.11)$$

where a_1 is a constant of the model, k is the turbulent kinetic energy, \bar{S} is the invariant of the shear strain rate $\bar{S} = \sqrt{\mathbf{S} : \mathbf{S}}$, and F_2 is a proper blending function, that will be defined later. This formulation guarantees the selection of an eddy viscosity model based on the shear stress in high pressure gradient regions, since $SF_2 > a_1 \omega$, while the original viscosity coming from the $k - \omega$ is used for the rest of the boundary layer. We need now to provide equations for the turbulent kinetic energy k , and for the turbulent specific dissipation rate ω :

$$\frac{\partial \rho_0 k}{\partial t} + \nabla \cdot (\rho_0 \bar{\mathbf{u}} k) = \widetilde{P}_k - \beta^* \rho_0 k \omega + \nabla \cdot ((\mu + \sigma_k \mu_T) \nabla k) \quad (2.12)$$

$$\begin{aligned} \frac{\partial \rho_0 \omega}{\partial t} + \nabla \cdot (\rho_0 \bar{\mathbf{u}} \omega) &= \alpha \rho_0 \bar{S}^2 - \beta \rho_0 \omega^2 + \nabla \cdot ((\mu + \sigma_\omega \mu_T) \nabla \omega) \\ &\quad + 2(1 - F_1) \rho_0 \sigma_{w_2} \frac{1}{\omega} \nabla k \cdot \nabla \omega \end{aligned} \quad (2.13)$$

Equation (2.12) is the standard transport equation for the turbulent kinetic energy. The term \widetilde{P}_k is defined as:

$$\widetilde{P}_k = \min(P_k, 10\beta^* \rho \omega k),$$

where $P_k = \frac{1}{2} \bar{\boldsymbol{\tau}} : \nabla \bar{\mathbf{S}}$. It is always positive and models the production of kinetic energy, but it has been limited to prevent build-up of

turbulence in strong stagnation regions. The term $-\rho_0 k \omega \beta^*$ is a dissipation term, while the term $\nabla \cdot ((\mu + \sigma_k \mu_T) \nabla k)$ accounts for the diffusion of the turbulent kinetic energy. Equation (2.13) is obtained by first rewriting an ϵ equations in terms of ω , and then by blending the two equations, for more details see [96]. On the right hand side we have the diffusion term $\nabla \cdot ((\mu + \sigma_{\omega_2} \mu_T) \nabla \omega)$, the production term $\alpha \rho_0 \bar{S}^2$, a dissipation term $-\beta \rho_0 \omega^2$, and finally the mixing term $2(1 - F_1) \rho_0 \sigma_{\omega_2} \frac{1}{\omega} \nabla k \cdot \nabla \omega$. The coefficient $(1 - F_1)$ on the mixing term applies a blending that allows to switch to the $k - \epsilon$ model when far away from the surface boundary, while otherwise it is set the $k - \omega$ model. In order to introduce the blending functions F_1, F_2 , we first introduce the turbulent length scale $l_T = \frac{\sqrt{k}}{\beta^* \omega}$. The ratio l_T/y , where y is the distance with the surface, is constant in the logarithmic region, but tends to zero at the edge of the boundary layer. The blending function F_1 is defined as:

$$F_1 = \tanh \left(\left(\min \left(\max \left(\frac{\sqrt{k}}{\beta^* \omega y}, \frac{500 \nu}{y^2 \omega}, \frac{4 \rho_0 \sigma_{\omega_2} k}{CD_{k\omega} y^2} \right) \right)^4 \right) \right),$$

where the maximum ensures that the blending function doesn't go to zero in the viscous sublayer, and the minimum avoids issues when dealing with small freestream values of ω . The cross diffusion $CD_{k\omega}$ is defined as $CD_{k\omega} = \max(2\rho_0 \sigma_{\omega_2} \nabla k \cdot \nabla \omega, 10^{-10})$, and helps to avoid singularities. Now, F_2 is the second blending function entering in (2.11), defined as:

$$F_2 = \tanh \left(\left(\max \left(\frac{2 \sqrt{k}}{\beta^* \omega y}, \frac{500 \nu}{y^2 \omega} \right) \right)^2 \right).$$

The coefficients of the model are: $\beta^* = 0.09$, $\alpha_1 = \frac{5}{9}$, $\beta_1 = \frac{3}{40}$, $\sigma_{k_1} = 0.85$, $\sigma_{\omega_1} = 0.5$, $\alpha_2 = 0.44$, $\beta_2 = 0.0828$, $\sigma_{k_2} = 1$, $\sigma_{\omega_2} = 0.856$. The coefficients $\alpha, \beta, \sigma_\omega, \sigma_k$ are obtained with a blending trough the function F_1 :

$$\varsigma = \varsigma_1 F_1 + \varsigma_2 (1 - F_1), \quad \varsigma \in \{\alpha, \beta, \sigma_\omega, \sigma_k\}.$$

To conclude, the $k - \omega$ SST model solves the mass and momentum equation in (2.9) and (2.8), is an eddy viscosity model, models the turbulent viscosity as in eq. (2.11), and closes the model employing

equations (2.12) and (2.13). Nowadays the $k - \omega$ SST model is largely employed by both industry and academia, being considered one of the most accurate turbulence models. We will employ it in order to initialize our DDES computations.

2.2.3 Large Eddy Simulation (LES)

RANS models have proved to be able to supply predictions on the averaged quantities with adequate accuracy and acceptable computational cost in many applications. However, they ontologically lack of precision when dealing with instantaneous quantities. A more accurate model approach in this respect is Large Eddy Simulation (LES). The main idea in LES is to apply a low-pass filter and then to solve for the flow variables. In this way, the CFD computations solve up to the filter scale, while the effects of the unresolved structures are modelled. In this section we will consider different LES models, discussing some of their properties. First, we introduce the function $G(\mathbf{x}, \mathbf{r})$, that will be a *spatial filter* with width Δ . We denote with $\hat{\phi}$ the filtered variable ϕ , meaning that:

$$\hat{\phi}(\mathbf{x}, t) = \int_{\Omega} G(\mathbf{x}, \mathbf{r}) \phi(\mathbf{x} - \mathbf{r}, t) d\mathbf{r}.$$

The filter $G(\mathbf{x}, \mathbf{r})$ has to satisfy the following property:

$$\int_{\Omega} G(\mathbf{x}, \mathbf{r}) d\mathbf{r} = 1,$$

furthermore we say that the filter $G(\mathbf{x}, \mathbf{r})$ is homogeneous if it is independent from the variable \mathbf{x} and we then denote it with $G(\mathbf{x}, \mathbf{r}) = G(\mathbf{r})$, while it is isotropic if instead of depending to \mathbf{r} depends from its modulus r . Various types of filters have been considered over the years, like the Gaussian filter or the Sharp spectral filter, see [114]. In our case, we consider the box filter:

$$G(r) = \frac{1}{\Delta} \left(\frac{1}{2} \Delta - r \right),$$

which applied to the variable ϕ in three dimension becomes:

$$\hat{\phi}(\mathbf{x}, t) = \int_{z-\Delta_z/2}^{z+\Delta_z/2} \int_{y-\Delta_y/2}^{y+\Delta_y/2} \int_{x-\Delta_x/2}^{x+\Delta_x/2} \phi(\mathbf{x}, t) dx dy dz,$$

where Δ_i , with $i \in \{x, y, z\}$ is the filter dimension in each direction. If we consider a Cartesian uniform grid made by hexaedra, the box

filter is the average of the field over the cell with center \mathbf{x} . If the grid is not uniform, typically we can choose as filter dimension $\Delta = \sqrt[3]{V}$, where V is the volume of the cell, or $\Delta = \max_{i=x,y,z} \Delta_i$. The box filter is homogeneous and the spatial derivatives can commute, but it is not isotropic. Now we define the *residual variable* ϕ' as

$$\phi'(\mathbf{x}, t) = \phi(\mathbf{x}, t) - \widehat{\phi}(\mathbf{x}, t).$$

We will call the quantity $\widehat{\phi}$ as the *resolved quantity*, since we will solve for this quantity, while the *residuals* will be modelled. Note that in general, differently from the time average operator for the RANS equations, $\widehat{\phi}' \neq 0$. This is true in particular for the box filter, since $(\widehat{\phi}) \neq \widehat{\phi}$. We consider now the equations (2.5) and (2.6), and we apply the filter operator, obtaining the filtered Navier Stokes equations:

$$\rho_0 \frac{\partial \widehat{\mathbf{u}}}{\partial t} + \rho_0 \nabla \cdot (\widehat{\mathbf{u}} \otimes \widehat{\mathbf{u}}) = -\nabla \cdot (\widehat{p}\mathbf{I} + \boldsymbol{\tau}_{SGS}) + \mu \Delta \widehat{\mathbf{u}}, \quad (2.14)$$

$$\nabla \cdot \widehat{\mathbf{u}} = 0, \quad (2.15)$$

where $\boldsymbol{\tau}_{SGS}$ is the subgrid scale tensor, defined as

$$\boldsymbol{\tau}_{SGS} = \rho_0 \widehat{\mathbf{u} \otimes \mathbf{u}} - \rho_0 \widehat{\mathbf{u}} \otimes \widehat{\mathbf{u}}.$$

Smagorinsky Model

Let us first consider the following anisotropic sub grid stress tensor:

$$\boldsymbol{\tau}_{SGS}^A = \boldsymbol{\tau}_{SGS} - \frac{1}{3} \text{tr}(\boldsymbol{\tau}_{SGS}). \quad (2.16)$$

As already described in the RANS equations, the isotropic part of the stress tensor is encapsulated on the pressure, namely we define the pressure P as:

$$P = \widehat{p} - \frac{1}{3} \text{tr}(\boldsymbol{\tau}_{SGS}),$$

and we solve for the following momentum equation in:

$$\rho_0 \frac{\partial \widehat{\mathbf{u}}}{\partial t} + \rho_0 \nabla \cdot (\widehat{\mathbf{u}} \otimes \widehat{\mathbf{u}}) = -\nabla \cdot (P\mathbf{I} + \boldsymbol{\tau}_{SGS}^A) + \mu \Delta \widehat{\mathbf{u}}.$$

The Smagorinsky model firstly models the sub grid stress tensor with an eddy-viscosity model:

$$\boldsymbol{\tau}_{SGS}^A = -2\nu_T \rho_0 \overline{\mathbf{S}}, \quad (2.17)$$

where ν_T has to be modelled, while $\bar{\mathbf{S}}$ is the scale resolving strain rate tensor, namely:

$$\hat{\mathbf{S}} = \frac{1}{2} (\nabla \hat{\mathbf{u}} + \nabla \hat{\mathbf{u}}^T),$$

and $|\hat{\mathbf{S}}| = 2(\hat{\mathbf{S}}_{ij}\hat{\mathbf{S}}_{ij})^{\frac{1}{2}}$. Note that, differently than eq. (2.10), the eddy viscosity model has a different sign. Then the turbulent viscosity ν_T is modelled in analogy with the mixing length approach, see for instance Section 10.2.2 of [114], namely:

$$\nu_T = c_S^2 \Delta^2 |\hat{\mathbf{S}}|, \quad (2.18)$$

and c_S is a constant for the model.

The hypotheses for the mixing length model hold true in the inertial subrange and for high Reynolds number. In the viscous wall region, we have that the hypotheses fail, leading to a non zero viscosity near the wall. To correct this behaviour, we employ the *van Driest correction*:

$$\nu_T = \left(C_S \Delta \left(1 - \exp\left(-\frac{y^+}{A}\right) \right) \right)^2 |\bar{\mathbf{S}}|,$$

where A is a constant of the model, typically set to $A = 26$, y^+ is the wall unit distance from the wall. The Smagorinsky LES model is an eddy viscosity model that solves the filtered equations (2.15) and (2.14), it models the subgrid tensor as in eq. (2.16) and employs the mixing length analogy to model the turbulent viscosity, see eq. (2.18). The typical values for the model varies from $C_S = 0.13$ to $C_S = 0.17$, depending on the flow problem, see for instance [114].

One Equation Model

We consider now the following one equation model for the see for instance [83] and [91]. We first introduce the *sub-grid turbulent kinetic energy* k_{SGS} :

$$k_{SGS} = \frac{1}{2} (\widehat{\mathbf{u} \cdot \mathbf{u}} - \hat{\mathbf{u}} \cdot \hat{\mathbf{u}}),$$

that is the trace of the *sub grid stress tensor* $\boldsymbol{\tau}_{SGS}$.

We consider now the same anisotropic stress tensor decomposition in eq. (2.16), but now we replaced the sub-grid turbulent kinetic energy k_{SGS} :

$$\boldsymbol{\tau}_{SGS} = \boldsymbol{\tau}_{SGS}^A + \frac{2}{3} \rho_0 k_{SGS} \text{tr}(\mathbf{I}) \quad (2.19)$$

and again we consider the pressure P such that the momentum equation 2.3 in becomes:

$$\rho_0 \frac{\partial \hat{\mathbf{u}}}{\partial t} + \rho_0 \nabla \cdot (\hat{\mathbf{u}} \otimes \hat{\mathbf{u}}) = -\nabla \cdot (P\mathbf{I} + \boldsymbol{\tau}_{SGS}^A) + \mu \Delta \hat{\mathbf{u}}.$$

Again, the model is an eddy viscosity model, but now we write the turbulent viscosity with respect of the test filter Δ and the turbulent kinetic energy k . By similarity theory we obtain:

$$\nu_T = C_\nu k_{SGS}^{\frac{1}{2}} \Delta, \quad (2.20)$$

Now, in order to close the model we need to provide the turbulent kinetic energy k_{SGS} . The turbulent kinetic energy has to satisfy an evolution equation. In analogy with the k -equation in the $k - \omega$ SST model, we can consider the following equation:

$$\frac{\partial \rho_0 k}{\partial t} + \nabla \cdot (\rho_0 \bar{\mathbf{u}} k) = \boldsymbol{\tau}_{SGS} : \mathbf{S} - C_\epsilon \rho_0 \frac{k^{3/2}}{\Delta} + \nabla \cdot ((\mu + \sigma_k \mu_T) \nabla k), \quad (2.21)$$

see [153] for the derivation of this equation. The one equation LES model solves the filtered equations (2.14) and (2.15), it models the subgrid tensor as in eq. (2.19) and it solves for the turbulent kinetic energy employing equation (2.21). The typical values for the model are $C_\epsilon = 1.048$, $\sigma_k = 1$ and $C_\nu = 0.094$.

Algebraic Smagorinsky Model

Instead of solving a transport equation for the turbulent kinetic energy k_{SGS} , we can compute the k_{SGS} with an algebraic relation [91]. We impose a local equilibrium between the production and the dissipation of the turbulent kinetic energy, meaning $F_\epsilon = F_P$. The dissipation term is modelled as $F_\epsilon = \frac{1}{\Delta} C_\epsilon \rho_0 k^{\frac{3}{2}}$. The production term is modelled as $F_P = \boldsymbol{\tau}_{SGS} : \hat{\mathbf{S}}$. We expand the stress tensor $\boldsymbol{\tau}_{SGS}$ as:

$$\begin{aligned} \boldsymbol{\tau}_{SGS} &= \boldsymbol{\tau}_{SGS}^A + \frac{2}{3} \rho_0 k_{SGS} \text{tr}(\mathbf{I}) \\ &= -2\nu_T \rho_0 \hat{\mathbf{S}} + \rho_0 \frac{2}{3} k_{SGS} \text{tr}(\mathbf{I}) \\ &= -2\rho_0 C_\nu k_{SGS}^{\frac{1}{2}} \Delta \hat{\mathbf{S}} + \frac{2}{3} \rho_0 k_{SGS} \text{tr}(\mathbf{I}) \end{aligned}$$

where we used eq. (2.19), and the eddy viscosity model hypothesis eq. (2.18) and finally we employed (2.20). Thus, we have:

$$\left(-2C_\nu k_{SGS}^{\frac{1}{2}} \Delta \hat{\mathbf{S}} + \frac{2}{3} k_{SGS} \operatorname{tr}(\mathbf{I}) \right) : \mathbf{S} + C_\epsilon \frac{k_{SGS}^{\frac{3}{2}}}{\Delta} = 0.$$

If $k_{SGS} \neq 0$, we obtain a second order algebraic equation in $\sqrt{k_{SGS}}$ and we solve it:

$$k_{SGS} = \left(\frac{-b + \sqrt{b^2 - 4ac}}{2a} \right)^2,$$

where $a = \frac{C_\epsilon}{\Delta}$, $b = \frac{2}{3} \operatorname{tr} \hat{\mathbf{S}}$, $c = -2C_\nu \Delta \hat{\mathbf{S}} : \hat{\mathbf{S}}$.

Hence, k_{SGS} is determined via an algebraic relation obtained by the local balance. The algebraic Smagorinsky LES model solves the filtered equations (2.14) and (2.15), it models the subgrid tensor as in eq. (2.19) and it solves the turbulent kinetic energy k with an algebraic relation, imposing the local energetic balance. The typical values for the model are $C_\nu = 0.094$, $C_\epsilon = 1.048$.

Detached Eddy Simulation (DES)

In many engineering applications, in particular when high Reynolds numbers are considered LES are still computationally prohibitive. When trying to create a computational grid for LES computations, there are two important aspects that increase the number of degrees of freedom of the whole problem. First, in LES the boundary layer needs to be resolved. This means that the first grid point of a mesh for LES has to be placed at $y^+ = 1$. Then, in order to keep a good quality of the grid and to properly resolve the gradients in the boundary layer, an aspect ratio of $1.05 - 1.1$ should be kept. In the zone away from the boundary layer, the mesh elements of the computational grid should be as isotropic as possible, otherwise the filter could resolve different scales in different directions. These constraints easily increase the number of degrees of freedom of the computational grid, becoming critical for many applications. Hence, a new class of models, the so called Detached Eddy Simulation (DES) models has been proposed to further reduce the computational costs but at the same trying to be as accurate as LES. The main idea of DES is to consider only one turbulence model that is able to properly switch between unsteady RANS and LES. The main idea of DES models can be summarized as follows. Let us consider the $k - \omega$ SST equations introduced in eq. (2.12) and

eq. (2.13), and let us consider the reformulation of the $k - \omega$ SST DES presented in [63]. Now, let us rewrite the closure equation as follows:

$$\frac{\partial \rho_0 k}{\partial t} + \nabla \cdot (\rho_0 \bar{\mathbf{u}} k) = \widetilde{P}_k - \rho_0 \frac{k^{3/2}}{l_{DES}} + \nabla \cdot ((\mu + \sigma_k \mu_T) \nabla k) \quad (2.22)$$

$$\begin{aligned} \frac{\partial \rho_0 \omega}{\partial t} + \nabla \cdot (\rho_0 \bar{\mathbf{u}} \omega) &= \alpha \rho_0 \bar{S}^2 - \beta \rho_0 \omega^2 + \nabla \cdot ((\mu + \sigma_\omega \mu_T) \nabla \omega) \\ &\quad + 2(1 - F_1) \rho_0 \sigma_{w_2} \frac{1}{\omega} \nabla k \cdot \nabla \omega \end{aligned} \quad (2.23)$$

where with respect to eq. (2.12) we only changed the dissipative term in the k equation from $\beta^* k \omega$ to $\beta^* k \omega F_{DES}$, namely we included the effect of the DES. Now, the function l_{DES} is defined as:

$$l_{DES} = \max(l_{LES}, l_{RANS}), \quad (2.24)$$

$$l_{LES} = C_{DES} \Delta,$$

$$l_{RANS} = \frac{\sqrt{k}}{C_\mu \omega}$$

where l_{DES} is the DES limiter. Note that, in the RANS regime, eq. (2.22) becomes (2.12), while, in the LES regime, it becomes similar to eq. (2.21) where the only difference is in the kinetic turbulence production term. The action of the DES limiter (2.24) is to switch from a RANS model close to the wall and to a model that depends on a filter scale when far away. When switching, the accuracy of the model is comparable to a LES, because of the effect of the limiter introduced in (2.24). The model acts as a subgrid scale model: indeed, if $F_{DES} > 1$, we recover a k equation similar to the one introduced in eq. (2.21). Furthermore, the DES accuracy in the LES regime has been verified in homogeneous turbulence. For a given dissipation rate the eddy viscosity scales with $\Delta^{4/3}$. Also, the model follows the energy cascade down to a length scale proportional to Δ , see for instance [133]. Also, the model was tested in isotropic turbulence and the $-5/3$ law was verified, which is not achieved for unsteady RANS. To conclude, the DES $k - \omega$ SST model solves the mass and momentum equation in (2.9) and (2.8), is an eddy viscosity model, models the turbulent viscosity as in eq. (2.11), and closes the model employing equations (2.22) and (2.23) combined with the delimiter (2.24). The employed constants of the model are the same as in the RANS model, namely: $\beta^* = 0.09$, $\alpha_1 = \frac{5}{9}$, $\beta_1 = \frac{3}{40}$, $\sigma_{k_1} = 0.85$, $\sigma_{\omega_1} = 0.5$, $\alpha_2 = 0.44$, $\beta_2 = 0.0828$, $\sigma_{k_2} = 1$, $\sigma_{\omega_2} = 0.856$. The coefficients $\alpha, \beta, \sigma_\omega, \sigma_k$ are obtained with a blending through the function F_1 .

Delayed Detached Eddy Simulation (DDES)

It is well known that DES models can generate spurious separation, called *grid induced separation* due to the abrupt switch from the RANS to the LES models, see [97]. To overcome this limitation new more robust models like the Delayed Detached Eddy Simulation (DDES) have been proposed, see for instance [63]. The main idea of DDES is to blend the transition between the RANS region to the LES region. Basically the same equation are solved in order to close the model:

$$\frac{\partial \rho_0 k}{\partial t} + \nabla \cdot (\rho_0 \bar{\mathbf{u}} k) = \widetilde{P}_k - \rho_0 \frac{k^{3/2}}{l_{DDES}} + \nabla \cdot ((\mu + \sigma_k \mu_T) \nabla k) \quad (2.25)$$

$$\begin{aligned} \frac{\partial \rho_0 \omega}{\partial t} + \nabla \cdot (\rho_0 \bar{\mathbf{u}} \omega) &= \alpha \rho_0 \bar{S}^2 - \beta \rho_0 \omega^2 + \nabla \cdot ((\mu + \sigma_\omega \mu_T) \nabla \omega) \\ &\quad + 2(1 - F_1) \rho_0 \sigma_{w_2} \frac{1}{\omega} \nabla k \cdot \nabla \omega, \end{aligned} \quad (2.26)$$

but now the switch between the two turbulence model is handled by the turbulence length l_{DDES} defined as:

$$l_{DDES} = l_{RANS} - f_d \max(0, l_{RANS} - l_{LES}) \quad (2.27)$$

$$l_{RANS} = \frac{\sqrt{k}}{C_\mu \omega}$$

$$l_{LES} = C_{DES} \Delta$$

$$C_{DES} = C_{DES_1} \cdot F_1 + C_{DES_2} \cdot (1 - F_1),$$

where f_d is an empiric blending function, also called *shielding function*, defined as:

$$\begin{aligned} f_d &= 1 - \tanh(C_{d_1} r_d)^{C_{d_2}} \\ r_d &= \frac{\nu_t + \nu}{\kappa^2 y^2 \sqrt{\frac{1}{2}(S^2 + \Omega^2)}}, \end{aligned}$$

where Ω is the magnitude of the vorticity $\Omega = \sqrt{\Omega : \Omega}$, with the vorticity being $\Omega = \nabla \times \mathbf{u}$, y is the wall distance, κ is the Kolmogorov constant, $\kappa = 0.41$. The effect of the shielding function f_d is to delay the separation.

To conclude, the DDES $k - \omega$ SST model solves the mass and momentum equation in (2.9) and (2.8), is an eddy viscosity model, models the turbulent viscosity as in eq. (2.11), and closes the model employing equations (2.25) and (2.26) combined with the DDES delimiter

(2.27). The employed constants are the same as in the DES and in the RANS models previously introduced, and $C_{d_1} = 20$ and $C_{d_2} = 3$.

2.3 Acoustics

Acoustics is the discipline that studies the propagation of waves in media. In this work, we are mostly interested in waves generated by pressure fluctuations that propagate in a fluid. Pressure fluctuations are the effect of the motion of the molecules that alternate compressions and rarefactions generating acoustic waves. The acoustic wave properties depend on the fluid where the propagation occurs. Indeed, the thermal properties and the thermodynamic state of the fluid affect the wave propagation. Also, the relation between the amplitude of the acoustic wave and the mean molecule path can affect the wave properties. For most of the applications, considering an inviscid flow as the medium of propagation of the acoustic wave is satisfactory. In this section, we first derive the time dependent wave equation, we revisit basic analytical approaches to solve the acoustic wave equation problem, and then we describe how to properly model the boundary conditions. In particular, we introduce the impedance boundary conditions in order to model real walls and to solve wave propagation problems in confined geometries. Then, we introduce the absorbing boundary conditions to model free field propagation problems by employing both characteristic impedance and a perfectly matched layer.

2.3.1 Acoustic Wave Equation

Consider the mass balance (2.2) and the momentum balance (2.3) for an inviscid flow, meaning that we assume the fluid to be perfect $\boldsymbol{\sigma} = -p\mathbf{I}$. We obtain the inviscid Euler equations:

$$\frac{\partial \rho}{\partial t} + \nabla \cdot (\rho \mathbf{u}) = 0, \quad (2.28)$$

$$\frac{\partial \rho \mathbf{u}}{\partial t} + \nabla \cdot (\mathbf{u} \otimes \mathbf{u} + p\mathbf{I}) = \mathbf{0}. \quad (2.29)$$

Following [146], assume that the fluid is at rest in his thermodynamic equilibrium, with the undisturbed state described by the reference density ρ_0 and the reference pressure p_0 , with flow velocity $\mathbf{u}_0 = \mathbf{0}$. Recall that these reference values are stationary and homogeneous. The sound waves are the effects of small perturbations in the density and

the pressure. Hence, we decompose the state variables as:

$$\rho = \rho_0 + \rho', \quad p = p_0 + p', \quad \mathbf{u} = \mathbf{0} + \mathbf{u}', \quad (2.30)$$

where $|\rho'| \ll \rho_0$ and $|p'| \ll p_0$, and the fluid velocity fluctuations are considered to be small. By the inviscid assumption, no heat conduction or dissipation are present, and there is no generation of entropy. In particular, the flow is homentropic, meaning that we can describe the thermodynamic state of the problem with one variable, say the density ρ . Hence, we consider the Taylor expansion of the pressure $p(\rho)$ around the reference state ρ_0 and we obtain that:

$$p' = p - p_0 = \left(\frac{\partial p}{\partial \rho} \right)_s (\rho - \rho_0) + \frac{1}{2} \left(\frac{\partial^2 p}{\partial \rho^2} \right)_s (\rho - \rho_0)^2 + \dots$$

Now, we define the speed of sound c_0 as:

$$c_0^2 = \left(\frac{\partial p}{\partial \rho} \right)_s .$$

By neglecting the higher order terms we have the following isentropic state equation:

$$p - p_0 = c_0^2 (\rho - \rho_0). \quad (2.31)$$

We remark that the speed of sound depend on the initial undisturbed state ρ_0 and p_0 , hence $c_0 = c_0(\rho_0, p_0)$. Using the decomposition of the flow velocity, the pressure and the density as introduced in eq. (2.30), the continuity and momentum equations eq. (2.28)-(2.29) become:

$$\begin{aligned} \frac{\partial}{\partial t} (\rho_0 + \rho') + \nabla \cdot ((\rho_0 + \rho') \mathbf{u}') &= 0, \\ \frac{\partial}{\partial t} ((\rho_0 + \rho') \mathbf{u}') + \nabla \cdot (\mathbf{u}' \otimes \mathbf{u}' + (p_0 + p') \mathbf{I}) &= \mathbf{0}. \end{aligned}$$

By neglecting the second order terms and observing that the reference values are constant, we have:

$$\begin{aligned} \frac{\partial \rho'}{\partial t} + \nabla \cdot (\rho_0 \mathbf{u}') &= 0, \\ \rho_0 \frac{\partial \mathbf{u}'}{\partial t} + \nabla p' &= \mathbf{0}. \end{aligned}$$

Finally, by replacing the isentropic state Equation (2.31), we have the

following mass and momentum conservation laws:

$$\frac{1}{\rho_0 c_0^2} \frac{\partial p'}{\partial t} + \nabla \cdot \mathbf{u}' = 0, \quad (2.32)$$

$$\rho_0 \frac{\partial \mathbf{u}'}{\partial t} + \nabla p' = \mathbf{0}. \quad (2.33)$$

By taking the time derivative of the mass equation (2.32) and the divergence of the momentum equation (2.33), we derive the following homogeneous wave equation:

$$\frac{1}{c_0^2} \frac{\partial p'^2}{\partial t^2} - \Delta p' = 0.$$

We remark that due to the homentropic assumption, we can also write the wave equation with respect to the density fluctuations ρ' :

$$\frac{\partial \rho'^2}{\partial t^2} - c_0^2 \Delta \rho' = 0.$$

We have now derived the acoustic wave equation for both density and pressure fluctuations. In the next session we formulate the acoustic wave equation problem with remarks on how it can be solved analytically.

2.3.2 Analytical Methods for the Wave Equation

Let us consider a domain $\Omega_a \subseteq \mathbb{R}^d$, with $d = 1, 2, 3$. Given a sound source $f \in L^2((0, T), \Omega_a)$, an initial condition $g(\mathbf{x}) \in H^1(\Omega_a)$ and $h(\mathbf{x}) \in L^2(\Omega_a)$, we now consider the following acoustic problem. For $t \in (0, T]$, find $p'(\mathbf{x}, t) : \Omega_a \times (0, T] \rightarrow \mathbb{R}$, such that:

$$\begin{aligned} \frac{1}{c_0^2} \frac{\partial^2 p'}{\partial t^2} - \Delta p' &= f, & \text{in } \Omega_a \times (0, T], \\ p'(\mathbf{x}, 0) &= g(\mathbf{x}), & \text{on } \Omega_a, \\ \frac{\partial p'}{\partial t}(\mathbf{x}, 0) &= h(\mathbf{x}), & \text{on } \Omega_a, \end{aligned} \quad (2.34)$$

provided with suitable boundary conditions that are later specified.

One-dimensional Wave Equation

We consider the following one-dimensional problem:

$$\begin{aligned} \frac{1}{c_0^2} \frac{\partial^2 p'}{\partial t^2} - \frac{\partial^2 p'}{\partial x^2} &= 0, \quad x \in \mathbb{R}, \quad t > 0, \\ u(x, 0) = g(x), \quad \frac{\partial}{\partial t} u(x, 0) = h(x), \quad x \in \mathbb{R}. \end{aligned} \tag{2.35}$$

The d'Alembert principle states that eq. (2.35) has a solution to the following form:

$$p'(x, t) = \varphi(x - tc_0) + \psi(x + tc_0),$$

where $\varphi(x - \frac{t}{c})$ is a left travelling wave, while $\psi(x + \frac{t}{c})$ is a right travelling wave.

Fundamental Solution

The fundamental solution method or Green's function method solves analytically a linear partial differential equation, like the wave equation introduced in eq. (2.34).

Consider now the following free field problem, where $\Omega_a = \mathbb{R}^3$ is now an unbounded domain. Given a position $\xi \in \Omega$ and a fixed time instant $\tau \in (0, T)$, for $t \in (0, T]$, find $G(\mathbf{x}, t) : \mathbb{R}^3 \times (0, T] \rightarrow \mathbb{R}$ such that:

$$\begin{aligned} \frac{1}{c^2} \frac{\partial^2 G}{\partial t^2} - \Delta G &= \delta(\mathbf{x} - \xi)\delta(t - \tau), \quad \mathbf{x} \in \mathbb{R}^3, t \in (0, T], \\ G(\mathbf{x}, 0) = 0, \quad \frac{\partial G}{\partial t}(\mathbf{x}, 0) &= 0, \quad \mathbf{x} \in \mathbb{R}^3. \end{aligned} \tag{2.36}$$

The solution to problem (2.36) is called fundamental solution or Green function. To highlight the dependence of the Green function on the source datum, the solution $G(\mathbf{x}, t)$ is often denoted as $G(\mathbf{x}, t; \xi, \tau)$.

Problem (2.36) has the following solution:

$$G(\mathbf{x}, t; \xi, \tau) = \frac{1}{4\pi r} \delta(t - \tau - \frac{r}{c}), \tag{2.37}$$

where $r = |\mathbf{x} - \xi|$ denotes the distance between \mathbf{x} and ξ , see for instance [39]. From the fundamental solution, it is possible to obtain a generic solution to problem (2.34). For simplicity, let us rewrite eq. (2.36) by introducing the formal linear operator L :

$$\begin{aligned} L[G(\mathbf{x}, t)] &= \delta(\mathbf{x} - \xi)\delta(t - \tau), \\ G(\mathbf{x}, 0) = 0, \quad \frac{\partial G}{\partial t}(\mathbf{x}, 0) &= 0, \quad \mathbf{x} \in \mathbb{R}^3. \end{aligned} \tag{2.38}$$

We multiply eq. (2.38) by the source $f(\boldsymbol{\xi}, \tau)$ and we integrate over the domain \mathbb{R}^3 and over the time interval $(0, t^+)$, where $t^+ = \lim_{\epsilon \rightarrow 0} (1 + \epsilon)t$

$$\int_{\mathbb{R}^3} \int_0^{t^+} L[G(\mathbf{x}, t; \boldsymbol{\xi}, \tau)] f(\boldsymbol{\xi}, \tau) d\tau d\boldsymbol{\xi} = \int_{\mathbb{R}^3} \int_0^{t^+} \delta(\mathbf{x} - \boldsymbol{\xi}) \delta(t - \tau) f(\boldsymbol{\xi}, \tau) d\tau d\boldsymbol{\xi}.$$

We highlight that we integrated over t^+ due to causality, since the effects on the solution cannot depend from future times. Now, thanks to the linearity of the differential operator we can bring it outside the integral, since it is independent of the integrated variables. Hence we have that:

$$\begin{aligned} L \left[\int_{\mathbb{R}^3} \int_0^{t^+} G(\mathbf{x}, t; \boldsymbol{\xi}, \tau) f(\boldsymbol{\xi}, \tau) d\tau d\boldsymbol{\xi} \right] \\ = \int_{\mathbb{R}^3} \int_0^{t^+} \delta(\mathbf{x} - \boldsymbol{\xi}) \delta(t - \tau) f(\boldsymbol{\xi}, \tau) d\tau d\boldsymbol{\xi} = f(\mathbf{x}, t). \end{aligned} \quad (2.39)$$

Here we recognise that eq. (2.39) can be written in the following manner:

$$\begin{aligned} L[p'] &= f(\mathbf{x}, t), \quad \mathbf{x} \in \mathbb{R}^3, t \in (0, T], \\ p' &= 0, \quad \frac{\partial p'}{\partial t} = 0, \quad \mathbf{x} \in \mathbb{R}^3 \end{aligned} \quad (2.40)$$

and hence we write that the solution to equation (2.40) is

$$p'(\mathbf{x}, t) = \int_{\mathbb{R}^3} \int_0^{t^+} G(\mathbf{x}, t; \boldsymbol{\xi}, \tau) f(\boldsymbol{\xi}, \tau) d\tau d\boldsymbol{\xi},$$

and by plugging in the Green function in eq. (2.37) we obtain:

$$\begin{aligned} p'(\mathbf{x}, t) &= \int_{\mathbb{R}^3} \int_0^{t^+} \frac{1}{4\pi r} \delta(t - \tau - \frac{r}{c}) f(\boldsymbol{\xi}, t) d\tau d\boldsymbol{\xi} \\ &= \int_{\mathbb{R}^3} \frac{1}{4\pi r} f(\boldsymbol{\xi}, t - \tau - \frac{r}{c}) d\boldsymbol{\xi}. \end{aligned} \quad (2.41)$$

Equation (2.41) gives the solution for a generic free field propagation problem. However, often the boundary conditions that have to be applied on Ω_a involve also solid walls, requiring a tailored Green Function. We will discuss more in details the implications for aeroacoustics in the next sessions.

Monochromatic Monopole Sound Source

From the mass balance and the continuity equation, we consider a net mass source f_m as a small vibrating sphere that generates imbalances in the surrounding air. This can be achieved practically by a vibrating sphere. We assume the radius of the sphere to be very small, considering f_m as a point mass source in \mathbf{x}_0 and modelling $f_m(\mathbf{x}, t)$ as:

$$f_m(\mathbf{x}, t) = Q(t)\delta(\mathbf{x} - \mathbf{x}_0),$$

see for instance section 6.3 of [55]. For simplicity, we consider a monochromatic forcing term, namely we assume that $Q(t) = Q_0 \cos(\omega t)$, where ω is the pulsation and we denote the *volume velocity* as Q_0 [m³/s]. Hence, the mass balance equation (2.32) becomes:

$$\frac{1}{\rho_0 c^2} \frac{\partial p'}{\partial t} + \nabla \cdot \mathbf{u} = Q(t)\delta(\mathbf{x}),$$

where we have a mass flux on the right hand side. We now obtain the following inhomogeneous acoustic wave equation for the case of a monochromatic monopole sound source:

$$\begin{aligned} \frac{1}{c^2} \frac{\partial p'^2}{\partial t^2} - \Delta p' &= \rho_0 \frac{\partial f_m(\mathbf{x}, t)}{\partial t} \\ &= \rho_0 \frac{\partial Q(t)}{\partial t} \delta(\mathbf{x} - \mathbf{x}_0) \\ &= -\rho_0 Q_0 \omega \sin(\omega t) \delta(\mathbf{x} - \mathbf{x}_0). \end{aligned} \quad (2.42)$$

By denoting with $\mathbf{r} = \mathbf{x} - \mathbf{x}_0$ and $r = |\mathbf{r}|$, we apply eq. (2.41) to eq. (2.42) and we obtain the following analytical solution:

$$p'(\mathbf{x}, t) = -\frac{\rho_0 Q_0 \omega}{4\pi r} \sin(\omega t - kr). \quad (2.43)$$

Usually, for instance in [107], it is more convenient to express the solution in (2.43) with the *phasor* notation. Then we have that:

$$\begin{aligned} p'(\mathbf{x}, t) &= -\frac{\rho_0 \omega Q_0}{4\pi r} \sin(\omega t - kr) \\ &= \frac{\rho_0 Q_0}{4\pi r} \frac{\partial}{\partial t} (\cos(\omega t - kr)) \\ &= \frac{j\omega \rho_0 Q_0}{4\pi r} \exp(j(\omega t - kr)). \end{aligned}$$

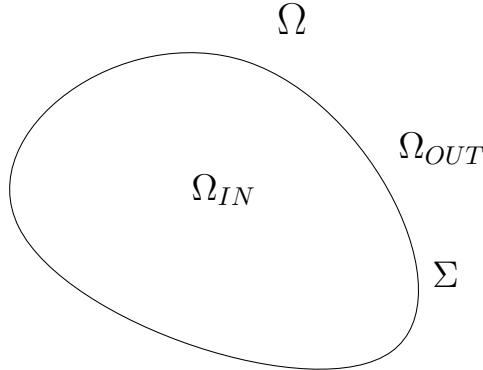


Figure 2.1: Ω is divided by the surface Σ in two regions Ω_{IN} , Ω_{OUT} .

Kirchhoff Integral

We proceed now with the derivation of the Kirchhoff integral formula, that extends the previous result on the free field Green's function to take into account the presence of a solid boundary for wave propagation problems. Let us consider the unbounded domain Ω , and the surface Σ . The surface Σ identifies two regions, Ω_{IN} and Ω_{OUT} , such that $\Omega = \Omega_{IN} \cup \Omega_{OUT}$, and where $\partial\Omega_{IN} = \Sigma$, see Figure 2.1. We want to solve the following unbounded problem:

$$\begin{aligned} L[p'] &= f(\mathbf{x}, t), \quad \text{in } \Omega_{OUT} \times (0, T], \\ \frac{\partial p'}{\partial \mathbf{n}} &= 0, \quad \text{on } \Sigma, \end{aligned} \tag{2.44}$$

with initial conditions $p'(\mathbf{x}, 0) = \frac{\partial p'}{\partial t}(\mathbf{x}, 0) = 0$, with $\mathbf{x} \in \Omega_{OUT}$. We next extend the definition of the solution also in the domain Ω_{IN} with the aim of employing the Green function of eq. (2.37). We hence consider now the following bounded smooth function $a(\mathbf{x})$:

$$\begin{cases} a(\mathbf{x}) < 0 & \mathbf{x} \in \Omega_{IN}, \\ a(\mathbf{x}) = 0 & \mathbf{x} \text{ on } \Sigma, \\ a(\mathbf{x}) > 0 & \mathbf{x} \in \Omega_{OUT}, \end{cases}$$

and we require that the function $a(\mathbf{x})$ is such that $|\nabla a| = 1$ on the surface Σ . We first observe that the unit normal vector \mathbf{n} to Σ is given by $\mathbf{n} = \nabla a$. The function $a(\mathbf{x})$ describes the presence of the body in the space Ω . Now, following [56] we define the pressure extension in

the whole domain Ω as follows:

$$\varpi(\mathbf{x}, t) = H(a)p(\mathbf{x}, t),$$

where H is the Heaviside function:

$$\begin{cases} H(x) = 0 & x \leq 0, \\ H(x) = 1 & x > 0. \end{cases}$$

This allows us to take into account the presence of a rigid body enclosed in the surface Σ and at the same time to work with the whole domain Ω being the new pressure ϖ defined on all the domain. Problem (2.44) can be reformulated in the whole domain Ω for the extended pressure ϖ as follows:

$$L[\varpi] = L[H(a)p(\mathbf{x}, t)].$$

Recalling that $\nabla H(a) = \frac{dH}{da}\nabla a = \delta(a)\nabla a$, where $\delta(\cdot)$ is the Dirac delta, and we obtain:

$$L[H(a)p(\mathbf{x}, t)] = H(a)\frac{1}{c^2}\frac{\partial^2 p}{\partial t^2} - H(a)\Delta p - \nabla \cdot (p\delta(a)\nabla a) - \delta(a)\nabla p \cdot \nabla a.$$

We observe that $H(a)\frac{1}{c^2}\frac{\partial^2 p}{\partial t^2} - H(a)\Delta p = H(a)f(\mathbf{x}, t)$, from equation (2.44). Therefore, we obtain the following problem:

$$\begin{aligned} L(\varpi) &= H(a)f(\mathbf{x}, t) - \nabla \cdot (p\delta(a)\nabla a) - \delta(a)\nabla p \cdot \nabla a, \quad \text{in } \Omega \times (0, T], \\ \varpi &= 0, \quad \frac{\partial \varpi}{\partial t} = 0, \quad \text{in } \Omega \times \{0\}. \end{aligned}$$

The problem is defined on the whole Ω , and it is a free propagation problem. Hence, we can employ the fundamental solution G defined in problem (2.36), to obtain:

$$\begin{aligned} \varpi(\mathbf{x}, t) &= \int_{-\infty}^{+\infty} \int_{\Omega} H(a)f(\mathbf{y}, \tau)G(\mathbf{x}, t|\mathbf{y}, \tau)d\mathbf{y}d\tau - \\ &\quad \int_{-\infty}^{+\infty} \int_{\Omega} \left(\nabla \cdot (p\delta(a)\nabla a) + \delta(a)\nabla p \cdot \nabla a \right) G(\mathbf{x}, t|\mathbf{y}, \tau)d\mathbf{y}d\tau. \end{aligned} \quad (2.45)$$

On the first term in the second integral at the right hand side of eq. (2.45), we apply the following identity of the divergence operator:

$$\nabla \cdot (p\delta(a)\nabla a)G = \nabla \cdot (p\delta(a)\nabla aG) - p\delta(a)\nabla a \cdot \nabla G.$$

We now need to compute the integral:

$$\int_{\Omega} \nabla \cdot (p\delta(a)\nabla a G) + \delta(a)(p\nabla G \cdot \nabla a - G\nabla p \cdot \nabla a) d\mathbf{y},$$

where we collected the $\delta(a)$ on the last two terms. We observe that

$$\int_{\Omega} \nabla \cdot (p\delta(a)\nabla a G) d\mathbf{y} = 0.$$

Next, we employ the identity:

$$\int_{\Omega} g(\mathbf{y})\delta(a) d\mathbf{y} = \int_{\Sigma} g(\mathbf{y}) d\sigma,$$

and we write the following:

$$\int_{\Omega} \delta(a)(p\nabla G \cdot \nabla a - G\nabla p \cdot \nabla a) d\mathbf{y} = \int_{\Sigma} p\nabla G \cdot \mathbf{n} - G\nabla p \cdot \mathbf{n} d\sigma,$$

where, since we are on the surface Σ , we replaced $\nabla a = \mathbf{n}$. Finally, given an observer located at $\mathbf{x} \in \Omega_{OUT}$ at the time t , a body described by the surface $\Sigma \subset \Omega$, we can finally write the *Kirchhoff integral* formula:

$$\begin{aligned} p(\mathbf{x}, t) &= \int_{-\infty}^{+\infty} \int_{\Omega} f(\mathbf{y}, \tau) G(\mathbf{x}, t | \mathbf{y}, \tau) d\mathbf{y} d\tau \\ &\quad + \int_{-\infty}^{+\infty} \int_{\Sigma} \left(p(\mathbf{y}, \tau) \frac{\partial G(\mathbf{x}, t | \mathbf{y}, \tau)}{\partial \mathbf{n}} - G(\mathbf{x}, t | \mathbf{y}, \tau) \frac{\partial p(\mathbf{y}, \tau)}{\partial \mathbf{n}} \right) d\sigma d\tau. \end{aligned} \quad (2.46)$$

In the next sections we analyse the boundary conditions that can be imposed to eq. (2.34) discussing more in details impedance boundary conditions, hard or soft sound boundaries and absorbing boundary conditions.

2.3.3 Boundary Conditions

We introduce suitable boundary conditions for problem problem (2.34), where now Ω_a is a bounded domain. First, we introduce the concept of impedance boundary conditions, in order to model real walls for confined acoustic problems. Next, we introduce absorbing boundary conditions like in [48] and finally we discuss the Perfectly Matched Layer (PML).

Impedance Conditions

In order to model real wall boundaries, we define the acoustic impedance Z as follows:

$$Z = \frac{p'(\mathbf{x}, t)}{\mathbf{u}(\mathbf{x}, t) \cdot \mathbf{n}}, \quad (2.47)$$

where \mathbf{n} is the outward unit normal to the boundary. The effect of the impedance Z is to partially reflect the incident wave. We now consider the momentum equation and project it on the boundary unit normal \mathbf{n} :

$$\frac{\partial \mathbf{u} \cdot \mathbf{n}}{\partial t} + \frac{1}{\rho_0} \nabla p' \cdot \mathbf{n} = 0. \quad (2.48)$$

By substituting the definition of impedance in eq. (2.47) we obtain the following *impedance boundary condition*:

$$\frac{1}{\rho_0} \nabla p'(\mathbf{x}, t) \cdot \mathbf{n} = -\frac{1}{Z} \frac{\partial p'}{\partial t}.$$

The proposed impedance boundary condition is a Robin condition. In fact, for $Z \rightarrow +\infty$ we obtain the following Neumann boundary condition, also known as *sound hard wall condition*, namely:

$$\frac{1}{\rho_0} \nabla p'(\mathbf{x}, t) \cdot \mathbf{n} = 0$$

that enforces the particle velocities at the boundary to be zero.

By choosing $Z = 0$ we obtain the following Dirichlet condition, also called *sound soft wall boundary condition*:

$$\frac{\partial p'(\mathbf{x}, t)}{\partial t} = p'(\mathbf{x}, t) = 0,$$

compare also with the definition of impedance in eq. (2.47).

We now consider a one-dimensional transmission problem. Our objective is to discuss what is the analytical solution for this problem and to understand for which value of the impedance we have full transmission. Let us then consider the domain $\Omega_a = \Omega_\ell \cup \Omega_r$, where $\Omega_\ell = (-1, 0)$ and $\Omega_r = (0, +\infty)$. We denote with Γ_d the Dirichlet boundary at $x = -1$, while with Γ_i the interface at $x = 0$. We consider now the following transmission problem. For $t \in (0, T]$, find $p(x, t) : \Omega_a \times (0, T] \rightarrow \mathbb{R}$,

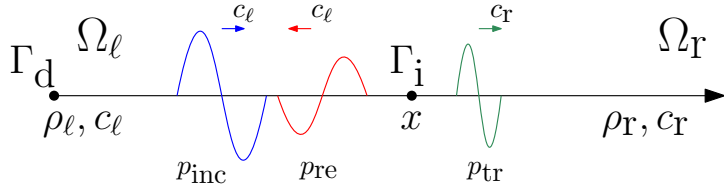


Figure 2.2: Transmission acoustic problem. The blue wave p'_{inc} is the incident wave, the red wave p'_{re} is the reflected wave and the green wave p'_{tr} is the transmitted wave.

such that

$$\begin{aligned} \frac{1}{c_a(x)^2} \frac{\partial^2 p'}{\partial t^2} - \frac{\partial^2 p'}{\partial x^2} &= 0, && \text{in } \Omega_a \times (0, T], \\ p'(x, t) &= g(t), && \text{on } \Gamma_d \times (0, T], \\ p'(x, 0) &= 0, && \text{in } \Omega_a, \\ \frac{\partial p'}{\partial t}(x, 0) &= 0, && \text{in } \Omega_a, \end{aligned}$$

where

$$\rho_a(x) = \begin{cases} \rho_\ell, & x \in \Omega_\ell, \\ \rho_r, & x \in \Omega_r, \end{cases}, \quad c_a(x) = \begin{cases} c_\ell, & x \in \Omega_\ell, \\ c_r, & x \in \Omega_r, \end{cases},$$

where $\rho_\ell, \rho_r \in \mathbb{R}$ are the densities of the material and $c_\ell, c_r \in \mathbb{R}$ are the speed of the waves respectively in Ω_a and Ω_r . At the interface of the two domain the solution is continuous. By denoting with p_ℓ the solution $p(x, t)$ for $x \in \Omega_\ell$ and by p_r the solution for $x \in \Omega_r$, we impose that $p_\ell(x, t) = p_r(x, t)$, x on Γ_i . Also, we require the conservation of the normal velocity at the interface Γ_i , hence employing eq. (2.48), we obtain:

$$\frac{1}{\rho_\ell} \frac{\partial p'_\ell}{\partial x} - \frac{1}{\rho_r} \frac{\partial p'_r}{\partial x} = 0. \quad (2.49)$$

At the interface Γ_i we have both an incident right travelling wave, a reflected left travelling wave and a right travelling transmitted wave that we denote respectively with $p'_{\text{inc}}(t - \frac{x}{c_\ell})$, $p'_{\text{re}}(t + \frac{x}{c_\ell})$ and $p'_{\text{tr}}(t - \frac{x}{c_r})$.

Hence, the continuity equation reads:

$$p'_{\text{inc}}(t - \frac{x}{c_\ell}) + p'_{\text{re}}(t + \frac{x}{c_\ell}) = p'_{\text{tr}}(t - \frac{x}{c_r}).$$

Now, we enforce the continuity at $x = 0$,

$$p'_{\text{inc}}(t) + p'_{\text{re}}(t) = p'_{\text{tr}}(t).$$

We define the reflection coefficient ϕ_{re} as :

$$p'_{\text{re}} = -\phi_{\text{re}} p'_{\text{inc}}, \quad p'_{\text{tr}} = (1 - \phi_{\text{re}}) p_{\text{inc}}. \quad (2.50)$$

We are interested in finding the value of the reflection coefficient ϕ_{re} . From the momentum balance from (2.49) at the interface we obtain the following:

$$\frac{1}{\rho_\ell} \frac{\partial}{\partial x} \left(p'_{\text{inc}}(t - \frac{x}{c_\ell}) + p'_{\text{re}}(t + \frac{x}{c_\ell}) \right) = \frac{1}{\rho_r} \frac{\partial}{\partial x} \left(p'_{\text{tr}}(t - \frac{x}{c_r}) \right).$$

By computing the spatial derivatives, by plugging in the Definition (2.50) and then evaluating at the interface Γ_i , we have that:

$$\begin{aligned} \frac{1}{\rho_\ell c_\ell} \frac{\partial}{\partial x} \left(-p'_{\text{inc}}(t - \frac{x}{c_\ell}) + p'_{\text{re}}(t + \frac{x}{c_\ell}) \right) &= -\frac{1}{\rho_r c_r} \frac{\partial}{\partial x} \left(p'_{\text{tr}}(t - \frac{x}{c_r}) \right), \\ \frac{1}{\rho_\ell c_\ell} (-p'_{\text{inc}}(t) + p'_{\text{re}}(t)) &= -\frac{1}{\rho_r c_r} \frac{\partial}{\partial x} (p'_{\text{tr}}(t)), \\ -\frac{1}{\rho_\ell c_\ell} (p'_{\text{inc}}(t) + \phi_{\text{re}} p'_{\text{inc}}(t)) &= -\frac{1}{\rho_r c_r} \frac{\partial}{\partial x} ((1 - \phi_{\text{re}}) p'_{\text{inc}}(t)), \end{aligned}$$

and with $p'_{\text{inc}}(t) \neq 0$, we obtain:

$$\frac{1}{\rho_\ell c_\ell} (1 + \phi_{\text{re}}) = \frac{1}{\rho_r c_r} (1 - \phi_{\text{re}}).$$

The reflection coefficient ϕ_{re} is:

$$\phi_{\text{re}} = \frac{\rho_r c_r - \rho_\ell c_\ell}{\rho_\ell c_\ell + \rho_r c_r}.$$

Hence we have that the reflected wave at the interface Γ_i is:

$$p'_{\text{re}}(t) = \frac{\rho_r c_r - \rho_\ell c_\ell}{\rho_\ell c_\ell + \rho_r c_r} p'_{\text{inc}}(t), \quad (2.51)$$

while the transmitted wave is:

$$p'_{\text{tr}}(t) = \frac{2\rho_r c_r}{\rho_\ell c_\ell + \rho_r c_r} p'_{\text{inc}}(t). \quad (2.52)$$

Now, we indicate with $Z_i = \rho_i c_i$ the characteristic resistance of a material. Observe that we can rewrite eq. (2.51) and eq. (2.52) as:

$$p'_{\text{re}}(t) = \frac{Z_2 - Z_\ell}{Z_\ell + Z_r}, \quad p'_{\text{tr}}(t) = \frac{2Z_r}{Z_\ell + Z_r},$$

and observe that for $Z_\ell = Z_r$ we have fully transmission. So, by choosing $Z = \rho c$ the obtained boundary condition is an absorbing boundary condition, namely:

$$\nabla p'(\mathbf{x}, t) \cdot \mathbf{n} = -\frac{1}{c_0} \frac{\partial p'}{\partial t}. \quad (2.53)$$

The absorbing boundary condition in hence obtained via *impedance matching* and the proposed boundary condition in eq. (2.53) are analogous to the first order absorbing conditions described in [48]. Those kind of absorbing conditions work well in \mathbb{R}^3 for normal incident waves, but usually fail when trying to fully propagate waves outside boundaries with corners, introducing spurious reflection. Being able to properly model absorbing boundary conditions it is crucial in practice when dealing with free field propagation problems. Instead of using an unbounded domain, in order to perform numerical simulations of the problem, we must consider a bounded domain.

Finally, we state the acoustic problem with impedance boundary conditions. Let us consider a domain $\Omega_a \subset \mathbb{R}^d$, with $d = 2, 3$. Given a sound source $f \in L^2((0, T), L^2(\Omega_a))$, an initial condition $g(\mathbf{x}) \in H^1(\Omega_a)$ and $h(\mathbf{x}) \in L^2(\Omega_a)$, we now consider the following acoustic problem. For $t \in (0, T]$, find $p'(\mathbf{x}, t) : \Omega_a \times (0, T] \rightarrow \mathbb{R}$, such that:

$$\begin{aligned} \frac{1}{c_0^2} \frac{\partial^2 p'}{\partial t^2} - \Delta p' &= f, & \text{in } \Omega_a \times (0, T], \\ p'(\mathbf{x}, 0) &= g(\mathbf{x}), & \text{on } \Omega_a, \\ \frac{\partial p'}{\partial t}(\mathbf{x}, 0) &= h(\mathbf{x}), & \text{on } \Omega_a, \\ \nabla p'(\mathbf{x}, t) \cdot \mathbf{n} &= -\frac{1}{Z} \frac{\partial p'}{\partial t}, & \text{on } \partial\Omega_a \times (0, T]. \end{aligned} \quad (2.54)$$

where we denoted with Γ_b the boundary $\partial\Omega_a$.

Perfectly Matched Layer

As discussed previously, the boundary condition described in eq. (2.53) is effective only with a normal incident wave. In order to overcome these limitation, the perfectly matched layer (PML) technique is considered. The main idea is to envelop the computational domain with an additional layer such that the incoming wave equation is damped inside the PML region. Here we follow the strategy presented in [65]

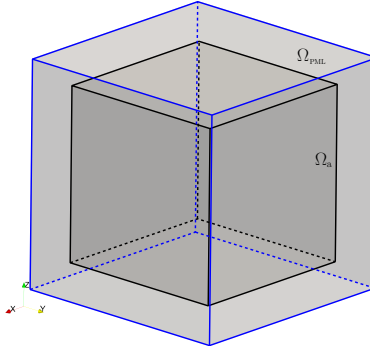


Figure 2.3: Example of a domain where we employ the PML conditions.

and [77]. We consider the harmonic wave equation:

$$\left(\frac{j\omega}{c}\right)^2 \hat{p} - \Delta \hat{p} = 0, \quad (2.55)$$

where \hat{p} are the Fourier transform of p' , ω is the angular frequency and j is the imaginary unit. Now, we introduce the complex change of variables

$$\begin{aligned} \tilde{x}(x) &= x + \frac{1}{j\omega} \int_0^x \sigma_x(x) dx, \\ \tilde{y}(y) &= y + \frac{1}{j\omega} \int_0^y \sigma_y(y) dy, \\ \tilde{z}(z) &= z + \frac{1}{j\omega} \int_0^z \sigma_z(z) dz, \end{aligned}$$

where $\sigma_x, \sigma_y, \sigma_z$ are suitable scalar damping functions. As stated in [144], this change of variables can be interpreted as an analytical continuation of the solution in the complex space. We define now ξ_i as follows:

$$\xi_i = \frac{\partial \tilde{x}_i}{\partial x_i} = 1 + \frac{\sigma_i}{j\omega}, \quad i = x, y, z. \quad (2.56)$$

The damping functions $\sigma_x, \sigma_y, \sigma_z$ are positive in Ω_{PML} , while they vanishes in Ω_a . The effect of the change of variables is to damp the incoming wave, avoiding thus spurious reflections. Observing that $\frac{\partial}{\partial \tilde{x}} = \frac{1}{\xi} \frac{\partial}{\partial x}$, we substitute eq. (2.56) into eq. (2.55) and we obtain

the following modified Helmholtz equation:

$$\xi_x \xi_y \xi_z \left(\frac{j\omega}{c} \right)^2 \hat{p} - \xi_y \xi_z \frac{\partial}{\partial x} \left(\frac{1}{\xi_x} \frac{\partial \hat{p}}{\partial x} \right) - \xi_x \xi_z \frac{\partial}{\partial y} \left(\frac{1}{\xi_y} \frac{\partial \hat{p}}{\partial y} \right) - \xi_x \xi_y \frac{\partial}{\partial z} \left(\frac{1}{\xi_z} \frac{\partial \hat{p}}{\partial z} \right) = 0. \quad (2.57)$$

We exploit the fact that $\frac{\partial \xi_i}{\partial x_j} = \delta_{ij}$, being δ_{ij} the Kronecker delta, and we rewrite eq. (2.57) as follows:

$$\xi_x \xi_y \xi_z \left(\frac{j\omega}{c} \right)^2 \hat{p} - \frac{\partial}{\partial x} \left(\frac{\xi_y \xi_z}{\xi_x} \frac{\partial \hat{p}}{\partial x} \right) - \frac{\partial}{\partial y} \left(\frac{\xi_x \xi_z}{\xi_y} \frac{\partial \hat{p}}{\partial y} \right) - \frac{\partial}{\partial z} \left(\frac{\xi_x \xi_y}{\xi_z} \frac{\partial \hat{p}}{\partial z} \right) = 0. \quad (2.58)$$

Furthermore, we reorder eq. (2.58):

$$I - \frac{\partial}{\partial x} II_x - \frac{\partial}{\partial y} II_y - \frac{\partial}{\partial z} II_z = 0, \quad (2.59)$$

where

$$I = \xi_x \xi_y \xi_z \left(\frac{j\omega}{c} \right)^2 \hat{p}, \quad (2.60)$$

and

$$II_x = \frac{\xi_y \xi_z}{\xi_x} \frac{\partial \hat{p}}{\partial x}, \quad II_y = \frac{\xi_x \xi_z}{\xi_y} \frac{\partial \hat{p}}{\partial y}, \quad II_z = \frac{\xi_x \xi_y}{\xi_z} \frac{\partial \hat{p}}{\partial z}.$$

We now want to expand all the terms in eq. (2.59). By introducing proper auxiliary variables we want to obtain a formulation for the PML problem. In particular, by employing the definitions eq. (2.56) we expand the term I in eq. (2.60) and we obtain:

$$I = \frac{1}{c^2} \left((j\omega)^2 + j\omega(\sigma_x + \sigma_y + \sigma_z) + (\sigma_x \sigma_y + \sigma_x \sigma_z + \sigma_x \sigma_y) + \left(\frac{\sigma_x \sigma_y \sigma_z}{jw} \right) \right) \hat{p}. \quad (2.61)$$

We introduce the following harmonic auxiliary variables:

$$\hat{v} = \frac{\hat{p}}{j\omega}, \quad (2.62)$$

$$\begin{cases} \hat{u}_x = \frac{1}{\sigma_x + j\omega} \left(\sigma_y \sigma_z \frac{\partial v}{\partial x} - (\sigma_x - \sigma_y - \sigma_z) \frac{\partial \hat{p}}{\partial x} \right), \\ \hat{u}_y = \frac{1}{\sigma_y + j\omega} \left(\sigma_x \sigma_z \frac{\partial v}{\partial y} - (\sigma_y - \sigma_x - \sigma_z) \frac{\partial \hat{p}}{\partial y} \right), \\ \hat{u}_z = \frac{1}{\sigma_z + j\omega} \left(\sigma_x \sigma_y \frac{\partial v}{\partial z} - (\sigma_z - \sigma_x - \sigma_y) \frac{\partial \hat{p}}{\partial z} \right). \end{cases} \quad (2.63)$$

Next, we consider the term Π_x in (2.60) and reorder it as follows:

$$\Pi_x = \frac{(\sigma_y + j\omega)(\sigma_z + j\omega)}{j\omega(\sigma_x + j\omega)} \frac{\partial \hat{p}}{\partial x} = \frac{(j\omega)^2 + j\omega(\sigma_y + \sigma_z) + \sigma_y\sigma_z}{j\omega(\sigma_x + j\omega)} \frac{\partial \hat{p}}{\partial x}.$$

Now we add and subtract the term $\frac{\sigma_x}{\sigma_x + j\omega} \frac{\partial \hat{p}}{\partial x}$ and use eq. (2.62):

$$\begin{aligned} & \frac{1}{\sigma_x + j\omega} \left(\sigma_y\sigma_z \frac{\partial \hat{v}}{\partial x} - (\sigma_x - \sigma_y - \sigma_z) \frac{\partial \hat{p}}{\partial x} + j\omega \frac{\partial \hat{p}}{\partial x} \right) + \frac{\sigma_x}{\sigma_x + j\omega} \frac{\partial \hat{p}}{\partial x} = \\ & \frac{1}{\sigma_x + j\omega} \left(\sigma_y\sigma_z \frac{\partial \hat{v}}{\partial x} - (\sigma_x - \sigma_y - \sigma_z) \frac{\partial \hat{p}}{\partial x} \right) + \frac{\partial \hat{p}}{\partial x}. \end{aligned}$$

The same reasoning applies to the terms Π_y and Π_z . Substituting in eq. (2.63), eq. (2.61) and the terms Π_x, Π_y, Π_z , into eq. (2.57) we have:

$$\begin{aligned} & \frac{(jw)^2}{c^2} \hat{p} + \frac{j\omega}{c^2} (\sigma_x + \sigma_y + \sigma_z) \hat{p} + \frac{1}{c^2} (\sigma_y\sigma_z + \sigma_x\sigma_y + \sigma_x\sigma_y) \hat{p} \\ & + \frac{1}{c^2} (\sigma_x\sigma_y\sigma_z) \hat{v} - \Delta \hat{p} - \nabla \cdot \hat{\mathbf{u}} = 0 \end{aligned} \quad (2.64)$$

By applying the inverse Fourier transform to eq. (2.62), eq. (2.63) and eq. (2.64), we obtain the following time dependent problem:

$$\begin{aligned} & \frac{1}{c^2} \frac{\partial^2 p}{\partial t^2} + \alpha \frac{\partial p}{\partial t} + \beta p + \gamma v - \Delta p - \nabla \cdot \mathbf{u} = f, \\ & \frac{\partial \mathbf{u}}{\partial t} + \mathbf{A}\mathbf{u} + \mathbf{B}\nabla p - \mathbf{C}\nabla v = 0, \quad \Omega \times (t_0, T] \\ & \frac{\partial v}{\partial t} - p = 0, \end{aligned}$$

coupled with the following initial and boundary conditions:

$$p(t, \mathbf{x}) = 0, \quad \mathbf{u}(t, \mathbf{x}) = 0, \quad v(t, \mathbf{x}) = 0 \quad t \in (t_0, T], \mathbf{x} \in \partial\Omega$$

$$\frac{\partial p(t_0, \mathbf{x})}{\partial t} = \dot{p}_0, \quad p(t_0, \mathbf{x}) = p_0, \quad \mathbf{u}(t_0, \mathbf{x}) = \mathbf{u}_0, \quad v(t_0, \mathbf{x}) = v_0 \quad \forall \mathbf{x} \in \Omega,$$

here we choose the initial conditions $p_0, \mathbf{u}_0, v_0, \dot{p}_0$ equal to zero and where f is the forcing term. The forcing term is defined only on Ω_a , while it is zero in Ω_{PML} . The matrices \mathbf{A}, \mathbf{B} and \mathbf{C} are given by:

$$\begin{aligned} A &= \begin{bmatrix} \sigma_x & 0 & 0 \\ 0 & \sigma_y & 0 \\ 0 & 0 & \sigma_z \end{bmatrix}, \quad B = \begin{bmatrix} \sigma_x - \sigma_y - \sigma_z & 0 & 0 \\ 0 & \sigma_y - \sigma_x - \sigma_z & 0 \\ 0 & 0 & \sigma_z - \sigma_x - \sigma_y \end{bmatrix}, \\ C &= \begin{bmatrix} \sigma_y \sigma_z & 0 & 0 \\ 0 & \sigma_x \sigma_z & 0 \\ 0 & 0 & \sigma_x \sigma_y \end{bmatrix}. \end{aligned}$$

Consider now a domain $\Omega = \Omega_a \cup \Omega_{\text{PML}}$ with $\Omega \subset \mathbb{R}$, and where $\Omega_a = [-d; d]$, while $\Omega_{\text{PML}} = (-L - d) \cup (d + L)$. The parameter L is the thickness of the PML layer. We introduce now the damping functions σ .

Constant Damping. The *constant damping* σ^{const} is defined as

$$\sigma(x) = \begin{cases} 0 & \text{if } 0 \leq |x| < d, \\ -\frac{c}{2L} \ln(R) & |x| > d, \end{cases}$$

where R is a constant parameter and c is the speed of sound. Usually the parameter R is taken equal to $R = 0.001$. Smaller values of R might lead to instabilities when solving the problem numerically, while higher values of R might not provide enough damping.

Inverse Damping. The *inverse damping* σ^{inv} is defined as

$$\sigma^{\text{inv}}(x) = \begin{cases} 0 & \text{if } 0 \leq |x| < d, \\ \frac{c}{d + L - |x|} & |x| > d, \end{cases}$$

where c is the speed of sound. The length of the layer thickness of the PML is crucial to properly damp the incoming waves, as shown numerically in [77].

2.4 Aeroacoustic Model

In this section, starting from the equations from the mass and momentum balance introduced in eq. (2.2) and eq. (2.3), we deduce the Lighthill's wave equation. Then, we apply the analytical strategies introduced in the acoustic section in order to deduce the so called semi-analytical models. Semi-analytical models rely on the possibility to apply a suitable Green function in order to solve the aeroacoustic problem.

2.4.1 Motivations

We presented in Section 2.1.6 the fully coupled compressible Navier-Stokes system. The model solves for the density of the fluid and is able to capture the behaviour of acoustics. However, let us consider the following problem. Imagine a flow impinging an object of characteristic length $L = 0.1$ m at the center of a room $4\text{ m} \times 4\text{ m} \times 4\text{ m}$. We are interested in solving at least up to 5000 Hz, meaning that if we place at least 8 points per wave length we need at least 10^8 degrees of freedom only for the acoustic problem. Next, we need also to solve the flow scales, at least reasonably close to the object. As already discussed, the grid size for the flow problem requires at least $Re^{9/4}$ degrees of freedom, and hence the higher the Reynolds number, the higher the computational cost. Turbulence modelling might reduce the computational cost, but still if we are employing a LES model we need to resolve the boundary layer, meaning that the computational grid close to the wall has to have $y^+ \approx 1$. Furthermore, larger domains require larger times for statistics to convergence, and hence to have fully develop solutions, furtherly increasing the computational time. In the next sections, we discuss the segregated aeroacoustic approach. The main advantage of the segregated approach is that it solves the flow problem and the acoustic problem in a segregated manner. The flow problem can be then treated as a stand alone problem, allowing for employing ad hoc strategies, like smaller computational domains, different numerical methods and models. More conveniently, the acoustic problem becomes linear decreasing the computational cost. Also, again, ad hoc numerical methods can be applied to further leverage the properties of the linear wave propagation problem.

2.4.2 Lighthill's Wave Equation

Now, we obtain the Lighthill's wave equation, exact reformulation of the mass and momentum equation that allow us to describe the wave propagation from the full compressible aeroacoustic model. Recall the mass and momentum equation introduced in Section 2.1:

$$\frac{\partial \rho}{\partial t} + \nabla \cdot (\rho \mathbf{u}) = 0, \quad (2.65)$$

$$\frac{\partial \rho \mathbf{u}}{\partial t} + \nabla \cdot (\rho \mathbf{u} \otimes \mathbf{u}) = -\nabla p + \nabla \cdot \boldsymbol{\sigma}. \quad (2.66)$$

We derive the Lighthill's wave equation, see [87], by taking the time derivative of (2.65) and subtracting the divergence of the momentum equation (2.66). Then, we obtain:

$$\frac{\partial^2 \rho}{\partial t^2} = \nabla \cdot \nabla \cdot (\rho \mathbf{u} \otimes \mathbf{u} + p \mathbf{I} - \boldsymbol{\sigma}).$$

Summing and subtracting in the above equation the term $c_0^2 \Delta \rho$, we obtain the following wave equation:

$$\frac{\partial^2 \rho}{\partial t^2} - c_0^2 \Delta \rho = \nabla \cdot \nabla \cdot \mathbf{T}, \quad (2.67)$$

where the right-hand side has been reformulated by introducing the so-called Lighthill's tensor

$$\mathbf{T} = \rho \mathbf{u} \otimes \mathbf{u} + (p - c_0^2 \rho) \mathbf{I} - \boldsymbol{\sigma}, \quad (2.68)$$

being \mathbf{I} the identity tensor.

We now consider an object with boundary Γ_b , the momentum equation in (2.66) and multiply it by the normal \mathbf{n} :

$$\left(\frac{\partial \rho \mathbf{u}}{\partial t} + \nabla \cdot (\rho \mathbf{u} \otimes \mathbf{u}) \right) \cdot \mathbf{n} = (-\nabla p + \nabla \cdot \boldsymbol{\sigma}) \cdot \mathbf{n}.$$

We impose that the normal velocity $\mathbf{u} \cdot \mathbf{n} = 0$ and plug in the definition of the Lighthill tensor:

$$\nabla \cdot \mathbf{T} \cdot \mathbf{n} = -c_0^2 \nabla \rho \cdot \mathbf{n}. \quad (2.69)$$

In the case of rigid body, we have that $\nabla p \cdot \mathbf{n} = 0$, but then also $c_0^2 \nabla \rho \cdot \mathbf{n} = 0$, forcing $\nabla \cdot \mathbf{T} \cdot \mathbf{n} = 0$. The model (2.67)-(2.68) can be further simplified depending on the problem of interest. For a sufficiently high Reynolds number, it is possible to neglect the viscous source term in the Lighthill's tensor. Assuming a low Mach number and no reactive effects, the fluid can be considered isentropic, leading to $p = c_0^2 \rho$. Under these assumptions, the Lighthill's tensor in (2.68) reduces to $\mathbf{T} = \rho_0 \mathbf{u} \otimes \mathbf{u}$, where ρ_0 is the constant flow density. This leads to the following non-homogeneous wave equation:

$$\frac{\partial^2 \rho}{\partial t^2} - c_0^2 \Delta \rho = \nabla \cdot \nabla \cdot (\rho_0 \mathbf{u} \otimes \mathbf{u}), \quad (2.70)$$

which describes the evolution of the density in a quiescent material where the speed of propagation is given by c_0 and the sound source is given by the approximation of the Lighthill's stress tensor. Equation (2.70) is then supplemented with suitable initial and boundary conditions, as detailed in the following.

2.4.3 The Hybrid Aeroacoustic Model

With the aim of studying aeroacoustic problems related to the noise generated by external flows around bodies, we consider the following setup. We assume acoustic compactness, which means that the size of the flow source structures that generate the acoustic field are small compared to the acoustic generated wavelength. This hypothesis is inherently fulfilled for low Mach number applications. Next, we consider a connected domain Ω_f , having sufficiently regular boundary $\partial\Omega_f$, embedded in a connected domain Ω_a , with sufficiently regular boundary $\partial\Omega_a$, see Figure 2.4.

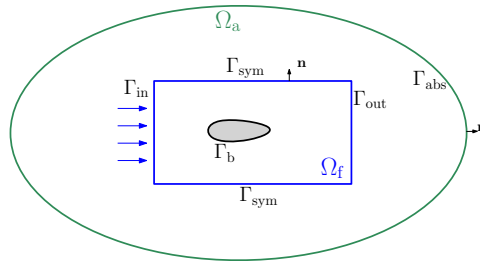


Figure 2.4: Computational domain for the aeroacoustic problem and sketch of the hybrid numerical strategy. First, the fluid problem is solved on Ω_f . Then the acoustic source term is computed from the flow velocity. Finally, an inhomogeneous acoustic wave equation is solved on Ω_a .

The hybrid algorithm requires to solve the following sequence of problems:

a. *Flow Problem.* For the flow problem we consider the incompressible Navier-Stokes equations, that read as for $t \in (0, T]$, find $\mathbf{u}(\mathbf{x}, t) : \Omega_f \times (0, T] \rightarrow \mathbb{R}^3$ and $p(\mathbf{x}, t) : \Omega_f \times (0, T] \rightarrow \mathbb{R}$ such that

$$\begin{aligned} \frac{\partial \mathbf{u}}{\partial t} + \nabla \cdot (\mathbf{u} \otimes \mathbf{u}) - \nu \Delta \mathbf{u} + \frac{1}{\rho_0} \nabla p &= 0, & \text{in } \Omega_f \times (0, T], \\ \nabla \cdot \mathbf{u} &= 0, & \text{in } \Omega_f \times (0, T], \\ \mathbf{u}(\mathbf{x}, 0) &= \mathbf{0}, & \text{in } \Omega_f, \\ \mathbf{u} &= \mathbf{0}, & \text{on } \Gamma_b \times (0, T], \\ \mathbf{u} &= \mathbf{g}, & \text{on } \Gamma_{in} \times (0, T], \\ \nu \nabla \mathbf{u} \cdot \mathbf{n} - p \mathbf{n} &= \mathbf{0}, & \text{on } \Gamma_{out} \times (0, T], \\ \mathbf{u} \cdot \mathbf{n} &= \mathbf{0}, & \text{on } \Gamma_{sym} \times (0, T], \\ \nabla(\mathbf{u} - (\mathbf{u} \cdot \mathbf{n})\mathbf{n}) \cdot \mathbf{n} &= \mathbf{0}, & \text{on } \Gamma_{sym} \times (0, T], \end{aligned} \tag{2.71}$$

where \mathbf{n} is the outward unit normal vector to $\partial\Omega_f$, ν is the kinematic viscosity, ρ_0 is the flow density assumed to be constant and \mathbf{g} is the inlet Dirichlet datum. Here, we suppose the fluid boundary can be decomposed in the pairwise disjoint portions $\Gamma_{in}, \Gamma_{out}, \Gamma_b, \Gamma_{sym}$, such that $\partial\Omega_f = \Gamma_{in} \cup \Gamma_{out} \cup \Gamma_b \cup \Gamma_{sym}$.

b. Acoustic Source. From the fluid velocity \mathbf{u} we define the Lighthill's tensor as

$$\mathbf{T} = \begin{cases} \rho_0 \mathbf{u} \otimes \mathbf{u} & \text{if } \mathbf{x} \in \Omega_f, \\ \mathbf{0} & \text{if } \mathbf{x} \in \Omega_a \setminus \Omega_f. \end{cases} \quad (2.72)$$

The Lighthill's tensor has support only on the fluid domain $\Omega_f \subseteq \Omega_a$, and it depends on the solution \mathbf{u} to problem (2.71), being the coupling term between the flow problem (2.71) and the acoustic problem (2.73).

c. Acoustic Problem. We consider in Ω_a the following non-homogeneous acoustic problem based on the Lighthill's wave equation: for $t \in (0, T]$, find $\rho(\mathbf{x}, t) : \Omega_a \times (0, T] \rightarrow \mathbb{R}$ such that

$$\begin{aligned} \frac{\partial^2 \rho}{\partial t^2} - c_0^2 \Delta \rho &= \nabla \cdot \nabla \cdot \mathbf{T}, & \text{in } \Omega_a \times (0, T], \\ c_0^2 \frac{\partial \rho}{\partial \mathbf{n}} &= 0, & \text{on } \Gamma_b \times (0, T], \\ \frac{1}{\rho_0} \frac{\partial \rho}{\partial \mathbf{n}} &= -\frac{1}{\rho_0 c_0} \frac{\partial \rho}{\partial t}(\mathbf{x}, t), & \text{on } \Gamma_{abs} \times (0, T], \\ \rho(\mathbf{x}, 0) &= 0, & \mathbf{x} \in \Omega_a, \\ \frac{\partial \rho}{\partial t}(\mathbf{x}, 0) &= 0, & \mathbf{x} \in \Omega_a, \end{aligned} \quad (2.73)$$

where c_0 is the speed of propagation of the wave and ρ_0 is the fluid density. The boundary $\partial\Omega_a$ has been split as $\partial\Omega_a = \Gamma_{abs} \cup \Gamma_b$. On the external boundary Γ_{abs} , cf. Figure 2.4, we apply non-reflective boundary conditions, see [48], while on Γ_b we set a sound hard boundary condition, modelling a rigid wall. Initial conditions are set to zero. We are aware that the validity of this hybrid strategy and the underlying one-way coupling assumption is strongly problem-specific, depending on the geometry of the problem and the flow features. However, this approach is widely used in the context of aeroacoustics simulations, see for instance [79, 77, 157, 53].

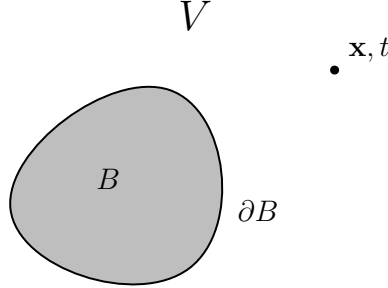


Figure 2.5: Domain for the Curle's analogy. The pressure fluctuations generated by the flow in V on the body B are evaluated in \mathbf{x} at time t .

2.4.4 Semi Analytical Models

Classical strategies to compute the far field pressure fluctuations employ semi-analytical models that, based on a flow solution obtained numerically, solve analytically problem (2.73). The first model was proposed by Lighthill, in which he directly solve problem (2.73) by employing the free field Green function in eq. (2.37), neglecting the presence of any obstacle. Next, we derive the Curle's solution, that includes the presence of solid boundaries. Curle's strategy to solve Lighthill's acoustic wave equation employs the Kirchhoff formula introduced in eq. (2.46) to problem (2.73), where we are assuming that Ω_a is unbounded as done in [40]. We will employ the Curle aeroacoustic solution for problem (2.73) in the numerical results presented in Chapter 5 for comparison. Given an observer located at \mathbf{x} at the time t , a volume V and a body $B \subset V$ see Figure 2.5, we have that:

$$\begin{aligned} p(\mathbf{x}, t) = & \int_{-\infty}^{+\infty} \int_V \nabla \cdot \nabla \cdot \mathbf{T}(\mathbf{y}, \tau) G(\mathbf{x}, t | \mathbf{y}, \tau) d\mathbf{y} d\tau \\ & + \int_{-\infty}^{+\infty} \int_{\partial B} \left(p(\mathbf{y}, \tau) \frac{\partial G(\mathbf{x}, t | \mathbf{y}, \tau)}{\partial \mathbf{n}} - G(\mathbf{x}, t | \mathbf{y}, \tau) \frac{\partial p(\mathbf{y}, \tau)}{\partial \mathbf{n}} \right) d\sigma d\tau, \end{aligned} \quad (2.74)$$

where G is a suitable Green function, V is the control volume, \mathbf{n} is the outward unit normal to the boundary ∂B . We denote with $\mathbf{r} = \mathbf{x} - \mathbf{y}$, being r its modulus. We choose as Green function $G(\mathbf{x}, t | \mathbf{y}, \tau) =$

$\frac{1}{4\pi r} \delta(\tau - t + \frac{r}{c_0})$ in eq. (2.74) to obtain:

$$\begin{aligned} p(\mathbf{x}, t) = & \frac{1}{4\pi} \int_V \frac{1}{r} \left[\nabla \cdot \nabla \cdot \mathbf{T} \right]_{\text{ret}} d\mathbf{y} \\ & + \int_{\partial B} \frac{1}{4\pi r} \left[\left(\frac{1}{c_0} \frac{\partial p}{\partial t} + \frac{p}{r} \right) \frac{\mathbf{r}}{r} \cdot \mathbf{n} - \frac{\partial p}{\partial \mathbf{n}} \right]_{\text{ret}} d\sigma, \end{aligned}$$

where $[\cdot]_{\text{ret}}$ means that the function has to be evaluated at the retarded time $t - \frac{r}{c_0}$. Now, we perform the following simplifications (see [50] for details), deviating from the original Curle's solution. First, the volume term containing the Lighthill tensor \mathbf{T} is neglected. Then the retarded times are neglected. This assumption is reasonable if the considered sound sources are compact, that means if the characteristic length of the emitting object D is much smaller than the characteristic length λ of the acoustic wave, namely if $D \ll \lambda$. Furthermore, since the object is considered acoustically rigid, i.e. $\frac{\partial p}{\partial \mathbf{n}} \Big|_{\partial B} = 0$, we have that:

$$p(\mathbf{x}, t) = \int_{\partial B} \frac{1}{4\pi r} \left(\left(\frac{1}{c_0} \frac{\partial p}{\partial t} + \frac{p}{r} \right) \frac{\mathbf{r}}{r} \cdot \mathbf{n} \right) d\sigma.$$

By neglecting the viscous forces and considering $\mathbf{F} = \int_{\partial B} p \mathbf{n} d\sigma$, we have that:

$$p(\mathbf{x}, t) = \frac{1}{4\pi} \frac{\mathbf{r}}{r^2} \cdot \left(\frac{\mathbf{F}}{r} + \frac{1}{c_0} \frac{\partial \mathbf{F}}{\partial t} \right).$$

Finally, while Lighthill's solution only considers the sound source volume and the Curle solution includes also the presence of the body, further improvements can be in the semi-analytical models have been proposed. For instance, the Ffoc's-William and Howking (FWH) model extends Curle's solution by considering moving surface, see for [58, 42] for additional details.

Chapter 3

Numerical Approximation

We detail the employed numerical methods to solve the hybrid aeroacoustic problem. We first introduce the Spectral Element Method (SEM). The SEM allows for high accuracy, but it lacks the flexibility of dealing with non conforming grids. To this hand, we introduce the Discontinuous Galerkin Spectral Element Method (DGSEM) and we employ it to discretize the Lighthill's wave equation. Next, we introduce the discretization of the flow problem employing a cell centered Finite Volume (FV) method. In order to couple the two problems, we introduce the intergrid projection method and the intergrid intersection algorithms. We conclude the section with some implementation remarks.

3.1 Notations

Given a Lipschitz domain $\Omega \subset \mathbb{R}^3$, the Lebesgue space of integrable functions over Ω reads as:

$$L^2(\Omega) = \{v : \Omega \rightarrow \mathbb{R} \mid v \text{ is Lebesgue measurable}, \int_{\Omega} |v|^2 < +\infty\},$$

endowed with the following inner product and norm:

$$(u, v)_{\Omega} = \int_{\Omega} uv, \quad \|u\|_{L^2(\Omega)}^2 = \int_{\Omega} |u|^2 \quad \forall u, v \in L^2(\Omega).$$

We introduce the usual Sobolev spaces, see for instance [1]. Given a sufficiently regular function u , we denote with

$$D^{\alpha} u = \partial_x^{\alpha_1} \partial_y^{\alpha_2} \partial_z^{\alpha_3} u \quad \forall \alpha = (\alpha_1, \alpha_2, \alpha_3) \in \mathbb{N}^3,$$

the $\boldsymbol{\alpha}$ derivative of u . By denoting with C_0^∞ the space of functions with compact support

$$C_0^\infty = \{u \in C^\infty(\Omega) \mid \text{supp}(u) \text{ is compact subset of } \Omega\},$$

we introduce the notion of $\boldsymbol{\alpha}$ weak derivative. Given $u \in L^2(\Omega)$, we say that $v \in L^2(\Omega)$ is the $\boldsymbol{\alpha}$ weak derivative of u if:

$$\int_{\Omega} u D^{\boldsymbol{\alpha}} \phi = (-1)^{|\boldsymbol{\alpha}|} \int_{\Omega} v \phi \quad \forall \phi \in C_0^\infty(\Omega),$$

where here $|\cdot|$ denotes the ℓ^1 norm:

$$|\boldsymbol{\alpha}| = \alpha_1 + \alpha_2 + \alpha_3 \quad \forall \boldsymbol{\alpha} = (\alpha_1, \alpha_2, \alpha_3) \in \mathbb{N}^3.$$

Given a positive integer $k > 0$, we define the Sobolev space of order k over Ω as follows:

$$H^k(\Omega) = \{v \in L^2(\Omega) \mid \|v\|_{H^k(\Omega)} < +\infty\},$$

where the respective inner product and norm read:

$$(u, v)_{H^k(\Omega)} = \sum_{\boldsymbol{\alpha} \in \mathbb{N}^3, |\boldsymbol{\alpha}| \leq k} (D^{\boldsymbol{\alpha}} u, D^{\boldsymbol{\alpha}} v)_{\Omega} \quad \forall u, v \in H^k(\Omega)$$

$$\|u\|_{H^k(\Omega)}^2 = \sum_{\boldsymbol{\alpha} \in \mathbb{N}^3, |\boldsymbol{\alpha}| \leq k} \|D^{\boldsymbol{\alpha}} u\|_{\Omega}^2 \quad \forall u \in H^k(\Omega).$$

To handle time dependent problems, we introduce Bochner spaces for a generic Sobolev space

$$L^2(0, T; H^k(\Omega)) = \{u : (0, T) \rightarrow H^k(\Omega)$$

$$\text{s.t. } u \text{ is measurable, } \int_0^T \|u(t)\|_{H^k(\Omega)}^2 dt < +\infty\}.$$

In a similar manner, we can introduce the space of continuous functions over a generic Sobolev space:

$$C^m(0, T; H^k(\Omega)) = \{v : (0, T) \rightarrow H^k(\Omega) \text{ s.t. } u \text{ is measurable,}$$

$$\max_{0 \leq \ell \leq m} (\sup_{0 \leq t \leq T} \|v^{(\ell)}\|_{H^k(\Omega)}) < +\infty\},$$

endowed with the norm

$$\|v\|_{C^m(0, T; H^k(\Omega))} = \max_{0 \leq \ell \leq m} (\sup_{0 \leq t \leq T} \|v^{(\ell)}\|_{H^k(\Omega)}), \quad (3.1)$$

where $v^{(\ell)}$ is the time derivative of order ℓ $v^{(\ell)} = \frac{\partial^\ell}{\partial t^\ell} v$. For more details see [52, 123].

3.2 Discretization of the Acoustic Problem

In this section, we first introduce the Spectral Element Method (SEM), and we then employ it to discretize first the acoustic wave equation introduced in eq. (2.54) and then the Lighthill's wave equation introduced in eq. (2.73). Next, we introduce the Discontinuous Galerkin Spectral Element Method (DGSEM) and we employ it to discretize the Lighthill's wave equation.

3.2.1 SEM Discretization of the Acoustic Wave Equation

Consider a conforming decomposition \mathcal{T}_a of the domain Ω_a made by hexahedral elements K_a . We denote by \hat{K} the reference element $[-1, 1]^3$, and we suppose that for any mesh element $K_a \in \mathcal{T}_a$ there exists a suitable trilinear invertible map $\boldsymbol{\theta}_{K_a} : \hat{K} \rightarrow K_a$ such that:

$$K_a = \boldsymbol{\theta}_{K_a}(\hat{K}) \quad (3.2)$$

with positive Jacobian \mathbf{J}_{K_a} . We define the characteristic mesh dimension as $h_a = \max_{K_a \in \mathcal{T}_a} h_{K_a}$, being h_{K_a} the diameter of the element K_a . Next, we introduce the finite-dimensional space:

$$V_a = \left\{ v \in C^0(\bar{\Omega}_a) \cap H^1(\Omega_a) : v|_{K_a} \circ \boldsymbol{\theta}_{K_a}^{-1} \in \mathbb{Q}_r(\hat{K}) \ \forall K_a \in \mathcal{T}_a \right\}, \quad (3.3)$$

where $\mathbb{Q}_r(\hat{K})$ is the space of polynomials of total degree smaller than or equal to r , with $r \geq 1$ in each coordinate direction, and where we denote by N_a the dimension of V_a . Now, for any $u, w \in V_a$, we introduce the following bilinear form by means of the tensor product Gauss-Legendre-Lobatto (GLL) quadrature rule:

$$(u, w)_{K_a}^{\text{NI}} = \sum_{i,j,k=0}^r u(\boldsymbol{\theta}_{K_a}(\xi_{i,j,k}^{\text{GLL}})) w(\boldsymbol{\theta}_{K_a}(\xi_{i,j,k}^{\text{GLL}})) \omega_{i,j,k}^{\text{GLL}} |\det(\mathbf{J})| \approx (u, w)_{K_a},$$

where ξ^{GLL} are the GLL quadrature nodes, and ω^{GLL} their corresponding weights, defined in $[-1, 1]^3$ (cf. [117]) and NI stands for numerical integration. The GLL integrates exactly polynomials up to degree

$2r - 1$, where $r + 1$ is the number of quadrature nodes. We define

$$(u, w)_{\mathcal{T}_a}^{\text{NI}} = \sum_{K_a \in \mathcal{T}_a} (u, w)_{K_a}^{\text{NI}} \quad \forall u, w \in V_a, \quad (3.4)$$

that induces the following discrete norm:

$$\|u\|_h^2 = (u, u)_{\mathcal{T}_a}^{\text{NI}} = \sum_{K_a \in \mathcal{T}_a} (u, u)_{K_a}^{\text{NI}}. \quad (3.5)$$

We next introduce the discrete bilinear form $a_h(u, v)$, namely:

$$a_h(u, v) = c^2 (\nabla u, \nabla v)_{\mathcal{T}_a}^{\text{NI}} \quad \forall u, v \in V_a. \quad (3.6)$$

Let $\{\phi_{a,i}\}_{i=1}^{N_a}$ be the Lagrangian basis functions of the space V_a , defined on the GLL nodes in such a way that the quadrature nodes are the same as the degrees of freedom. We introduce hence the mass $M \in \mathbb{R}^{N_a \times N_a}$ and the stiffness matrices $K \in \mathbb{R}^{N_a \times N_a}$:

$$M_{i,j} = (\phi_{a,i}, \phi_{a,j})_{\mathcal{T}_a}^{\text{NI}} \quad \forall \phi_{a,i}, \phi_{a,j} \in V_a, \quad (3.7)$$

$$K_{i,j} = a_h(\phi_{a,i}, \phi_{a,j}) \quad \forall \phi_{a,i}, \phi_{a,j} \in V_a. \quad (3.8)$$

Note that, since we are employing the GLL in the quadrature formula, the mass matrix M is diagonal, see for instance [46]. Next, we apply the Spectral Element discretization to first the acoustic problem (2.54) and then to the aeroacoustic problem introduced in eq. (2.73). We now consider the variational formulation of the acoustic problem (2.54), requiring that $Z \rightarrow \infty$ in order to have a Neumann boundary condition on Γ_b . We have that, for $t \in (0; T]$, find $\rho(\mathbf{x}, t) \in H^1(\Omega_a)$ such that $\forall w \in H^1(\Omega_a)$:

$$\left(\frac{\partial^2 \rho}{\partial t^2}, w \right)_{\Omega_a} + c_0^2 (\nabla \rho, \nabla w)_{\Omega_a} + c_0^2 \int_{\Gamma_b} \nabla \rho \cdot \mathbf{n} w \, d\sigma = (f, w)_{\Omega_a},$$

with initial conditions $\rho(\mathbf{x}, 0) = \frac{\partial \rho(\mathbf{x}, 0)}{\partial t} = 0$ in $\Omega_a \times \{0\}$, being $(\cdot, \cdot)_{\Omega_a}$ the L^2 product over the domain Ω_a . The semi-discrete SEM formulation of problem (2.84) with numerical integration (SEM-NI) reads: for any time $t \in (0; T]$ find $\rho_h \in V_a$ such that:

$$\left(\frac{\partial^2 \rho_h}{\partial t^2}, w_h \right)_{\mathcal{T}_a}^{\text{NI}} + a_h(\rho_h, w_h) = (f, w_h)_{\mathcal{T}_a}^{\text{NI}} \quad \forall w_h \in V_a,$$

with null initial conditions on both $\rho_h, \dot{\rho}_h \in V_a$. Consider $\rho_h(\mathbf{x}, t) = \sum_{j=1}^{N_a} \boldsymbol{\rho}_j(t) \phi_{a,j}(\mathbf{x})$, with $\{\phi_{a,j}\}_{j=1}^{N_a}$ the Lagrangian basis for V_a , we have:

$$\left(\frac{\partial^2}{\partial t^2} \sum_{j=1}^{N_a} \boldsymbol{\rho}_j \phi_{a,j}, \phi_{a,i} \right)_{T_a}^{\text{NI}} + a_h \left(\sum_{j=1}^{N_a} \boldsymbol{\rho}_j \phi_{a,j}, \phi_{a,i} \right) = (f, \phi_{a,i})_{T_a}^{\text{NI}} \quad \forall \phi_{a,i} \in V_a.$$

We obtain then the following semi-discrete algebraic formulation:

$$M \ddot{\boldsymbol{\rho}}(t) + K \boldsymbol{\rho}(t) = \mathbf{b}(t),$$

where M, K have been defined in equations (2.81)-(2.82), respectively, and

$$\mathbf{b}_i(t) = (f(t), \phi_{a,i})_{T_a}^{\text{NI}} \quad \forall \phi_{a,i} \in V_a.$$

3.2.2 Fully Discretization of the Acoustic Wave Equation

We can rewrite the semidiscrete formulation in the following manner:

$$\ddot{\boldsymbol{\rho}} = \Phi(\boldsymbol{\rho}, t), \tag{3.9}$$

where $\Phi(\boldsymbol{\rho}, t) = M^{-1}(\mathbf{b} - K\boldsymbol{\rho})$. Given the time interval $[0, T]$ and a fixed Δt we divide $[0, T]$ in N intervals such that $t_n = n\Delta t$, with $n = 0, \dots, N$. We discretize problem (2.83) with the so called Newmark scheme, see for instance [93]:

$$\begin{aligned} \boldsymbol{\rho}^{n+1} &= \boldsymbol{\rho}^n + \Delta t \dot{\boldsymbol{\rho}}^n + \Delta t^2 [\beta \Phi^{n+1} + (\frac{1}{2} - \beta) \Phi^n], & n \geq 0, \\ \dot{\boldsymbol{\rho}}^{n+1} &= \dot{\boldsymbol{\rho}}^n + \Delta t [\gamma \Phi^{n+1} + (1 - \gamma) \Phi^n], & n \geq 0, \end{aligned}$$

where we denote with $\boldsymbol{\rho}^n$ the approximation $\boldsymbol{\rho}(t_n)$ and with $\Phi^n \approx \Phi(\boldsymbol{\rho}^n, t_n)$, and where the parameters γ and β are such that $0 \leq \beta \leq \frac{1}{2}$ and $0 \leq \gamma \leq 1$. By selecting $\beta = 0$ and $\gamma = \frac{1}{2}$, we obtain the explicit second order Leap Frog scheme:

$$\frac{\boldsymbol{\rho}^{n+1} - 2\boldsymbol{\rho}^n + \boldsymbol{\rho}^{n-1}}{\Delta t^2} = M^{-1}(\mathbf{b}^n - K\boldsymbol{\rho}^n).$$

Note that in SEM the mass matrix is diagonal meaning that its inverse can be computed easily. However, the Leap Frog method is conditionally stable. A second order unconditionally stable method can be obtained by selecting $\beta = \frac{1}{4}$ and $\gamma = \frac{1}{2}$.

3.2.3 SEM Discretization of Lighthill's Wave Equation

We start by considering the variational formulation of the Lighthill's wave equation in (2.73): for $t \in (0; T]$, find $\rho(\mathbf{x}, t) \in H^1(\Omega_a)$ such that $\forall w \in H^1(\Omega_a)$:

$$\begin{aligned} \left(\frac{\partial^2 \rho}{\partial t^2}, w \right)_{\Omega_a} + c_0^2 (\nabla \rho, \nabla w)_{\Omega_a} + c_0 \int_{\Gamma_{\text{abs}}} \frac{\partial \rho}{\partial t} w \, ds \\ = -(\nabla \cdot \mathbf{T}, \nabla w)_{\Omega_a}, \quad (3.10) \end{aligned}$$

with initial conditions $\rho(\mathbf{x}, 0) = \frac{\partial \rho(\mathbf{x}, 0)}{\partial t} = 0$ in $\Omega_a \times \{0\}$, being $(\cdot, \cdot)_{\Omega_a}$ the L^2 product over the domain Ω_a . The source term comes from the integration by parts of $(\nabla \cdot \nabla \cdot \mathbf{T}, w)_{\Omega_a}$:

$$\int_{\Omega_a} \nabla \cdot \nabla \cdot \mathbf{T} w = \int_{\partial \Omega_a} \nabla \cdot \mathbf{T} \cdot \mathbf{n} w - \int_{\Omega_a} \nabla \cdot \mathbf{T} \cdot \nabla w,$$

where $\int_{\Gamma_{\text{abs}}} (\nabla \cdot \mathbf{T}) \cdot \mathbf{n} w = 0$ since \mathbf{T} is zero on the domain $\Omega_a \setminus \Omega_f$ and where $\int_{\Gamma_b} (\nabla \cdot \mathbf{T}) \cdot \mathbf{n} w = 0$ for eq. (2.69), as it is done for instance in [80].

The semi-discrete Spectral Element Formulation of problem (2.84) with numerical integration (SEM-NI) reads: for any time $t \in (0; T]$ find $\rho_h \in V_a$ such that:

$$\begin{aligned} \left(\frac{\partial^2 \rho_h}{\partial t^2}, w_h \right)_{T_a}^{\text{NI}} + a_h(\rho_h, w_h) + c_0 \int_{\Gamma_{\text{abs}}} \frac{\partial \rho_h}{\partial t} w_h \, ds \\ = -(\nabla \cdot \mathbf{T}, \nabla w_h)_{T_a}^{\text{NI}} \quad \forall w_h \in V_a, \quad (3.11) \end{aligned}$$

with null initial conditions $\rho_h, \dot{\rho}_h \in V_a$. We recall that the term $\nabla \cdot \mathbf{T}$ is an external source that in our case is obtained from a numerical solution to problem (2.71). The semi-discrete algebraic formulation of eq. (2.85) reads:

$$M \ddot{\rho}(t) + M_{\Gamma\Gamma} \dot{\rho}(t) + K \rho(t) = g(t),$$

where the mass M and the stiffness K have been defined in equations (2.81), (2.82), while the boundary mass matrix is defined as:

$$M_{\Gamma\Gamma} = \int_{\Gamma_{\text{abs}}} \phi_{a,j} \phi_{a,i} \quad \forall \phi_{a,i}, \phi_{a,j} \in V_a,$$

and where the right hand side term \mathbf{g} is given by:

$$\mathbf{g}_i = - \int_{\Omega_a} (\nabla \cdot \mathbf{T}) \cdot \nabla \phi_{a,i} \quad \forall \phi_{a,i} \in V_a.$$

Again, we discretize the whole problem with the Newmark method introduced in Section 2.6.1.

In Section 2.8, we will detail how to compute the projection of the field $\nabla \cdot \mathbf{T}$, i.e., how to approximate a field defined on the fluid mesh \mathcal{T}_f with a field defined on the acoustic grid \mathcal{T}_a .

3.2.4 DGSEM Discretization of Lighthills's Wave Equation

One of the main limitation of the Spectral Element Method is the constraint of grid conformity: no hanging nodes are allowed. Let us consider, for instance, a wave propagation problem around a curved object. If we do not know the analytical shape of the object, or if we are just employing a trilinear map, then refining in the polynomial degree might be not very convenient since the numerical discretization would miss features of the geometry, see for instance Figure 2.6 in which clearly the high order approximation introduces a geometrical error when approximating to the rounded geometry. The optimal strategy would be to have a low order refinement in the element dimension h close to the object, and a greater spacing with higher order elements far from the object. This enables the method to best approximate the geometry and to best solve the wave propagation problem, placing the degrees of freedom in the optimal positions. To overcome the conformity constraint imposed by the SEM discretization, we enhance the Spectral Element Method with Discontinuous Galerkin and we introduce the Discontinuous Galerkin Spectral Element Method (DGSEM). The main idea of the following DGSEM method is to have three levels. The first (macro) level can be geometrically non-conforming. The second level (meso) must be geometrically conforming. The third level (micro) is associated with the degrees of freedom, see Figure 2.7. At the meso and micro level the SEM method introduced in Section 2.6.1 is employed. At the macro level the DG method allows to treat the non conformities, both geometrically and for the polynomial approximation degree. So, let us consider the domain $\Omega_a \in \mathbb{R}^3$. We denote with \mathcal{T}_a the macro partition $\mathcal{T}_a = \{\Omega_{a,\ell}\}_{\ell=1}^{N_L}$, such that $\overline{\Omega}_a = \cup_{\ell=1}^{N_L} \Omega_{a,\ell}$, with $\Omega_{a,\ell} \cap \Omega_{a,\ell'} = \emptyset$ for $\ell \neq \ell'$. On each macro element $\Omega_{a,\ell}$ we define a conforming (meso) decomposition $\mathcal{T}_{a,\ell} = \{K_{\ell}^j\}_{j=1}^{N_{L,\ell}}$, where $N_{L,\ell}$

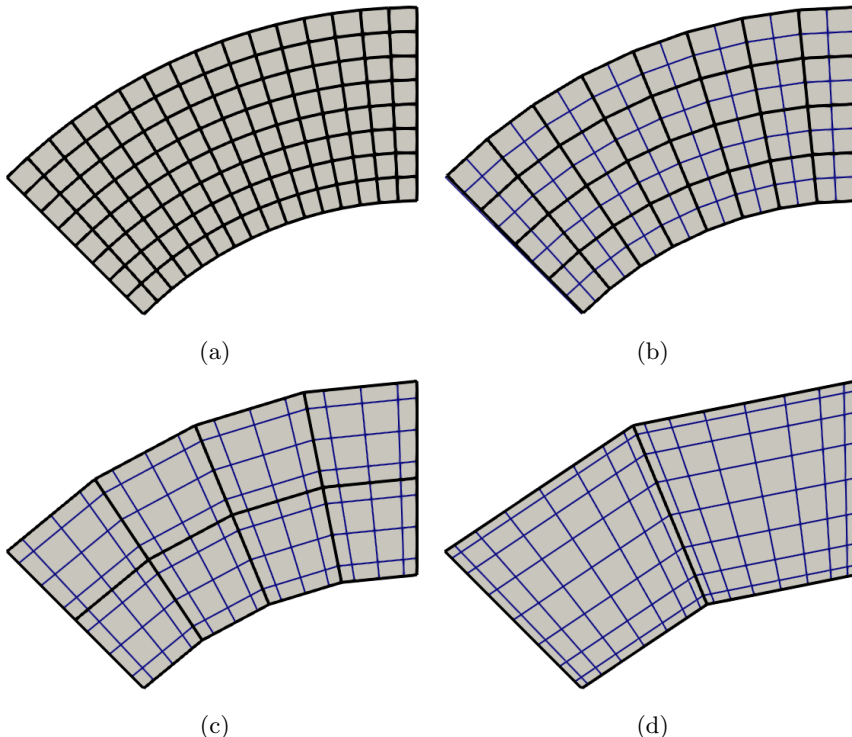


Figure 3.1: (a) Discretization employing $r = 1$ elements. (b) Discretization employing $r = 2$ elements. (c) Discretization employing $r = 4$ elements. (d) Discretization employing $r = 8$ elements. In black, edges of the mesh elements. In blue, edges connecting the degrees of freedom. The number of degrees of freedom of the discretized geometry are the same, but the low order approximation is able to better capture the rounded geometrical feature of the object.

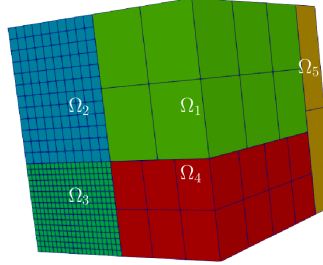


Figure 3.2: Example of a DG decomposition.

is the number of elements of the meso decomposition. We consider each element K_ℓ^j as the image of a suitable trilinear map $\theta_{K_\ell^j}$, as the one introduced in eq. (2.76). An example of the described geometrical decomposition can be found in Fig. 2.7.

Given two adjacent region $\Omega_a^+, \Omega_a^- \in \mathcal{T}_a$, we define the interior face F^I as the non empty intersection between $\bar{K}_+ \cap \bar{K}_-$ where $K_+ \in \mathcal{T}_{a,+}$ and $K_- \in \mathcal{T}_{a,-}$, respectively. All the interior faces are collected in the set \mathcal{F}_a^I . Analogously we define the set of the boundary faces $F^B = \bar{K}_\ell \cap \partial \bar{K}$, for some $K_\ell \in \mathcal{T}_{a,\ell}$ and we collect all the boundary faces in \mathcal{F}_a^B . We assumed that the mesh respects the decomposition of the boundary, meaning that on the face $F \in \mathcal{F}_a^B$ we either impose a Dirichlet or a Neumann type boundary condition. Finally, we denote with $\mathcal{F}_a = \mathcal{F}_a^B \cup \mathcal{F}_a^I$.

Given two adjacent elements $K_\pm \in \mathcal{T}_a^\pm$, sharing a face $F \in \mathcal{F}_a^I$, let \mathbf{n}^\pm be the outward unit normal vector to F , positive with respect to K_\pm . Let u, \mathbf{v} two regular enough scalar-valued and vector-valued functions, we denote with u^\pm and \mathbf{v}^\pm their traces on the face $F \in \mathcal{F}_a^I$. If the $F \in \mathcal{F}_a^I$ we set:

$$\begin{aligned}\{u\} &= \frac{1}{2}(u^+ + u^-) & [u] &= u^+ \mathbf{n}^+ + u^- \mathbf{n}^- \\ \{\mathbf{v}\} &= \frac{1}{2}(\mathbf{v}^+ + \mathbf{v}^-) & [\mathbf{v}] &= \mathbf{v}^+ \cdot \mathbf{n}^+ + \mathbf{v}^- \cdot \mathbf{n}^-, \end{aligned}$$

while if \mathcal{F}_a^B we set:

$$\begin{aligned}\{u\} &= u & [u] &= u \mathbf{n} \\ \{\mathbf{v}\} &= \mathbf{v} & [\mathbf{v}] &= \mathbf{v} \cdot \mathbf{n}. \end{aligned}$$

On the meso decomposition, we denote by $V_{a,\ell}(\Omega_{a,\ell})$ the Spectral Ele-

ment Space defined as before in eq. (2.77):

$$V_{a,\ell}(\Omega_{a,\ell}) = \left\{ v \in C^0(\bar{\Omega}_{a,\ell}) \cap H^1(\Omega_{a,\ell}) : v|_{K_\ell} \circ \boldsymbol{\theta}_{K_\ell}^{-1} \in \mathbb{Q}_r(\hat{K}) \quad \forall K_\ell \in \mathcal{T}_{a,\ell} \right\}.$$

On the macro decomposition, we denote with V_a^{DG} the Discontinuous Galerkin space:

$$V_a^{\text{DG}}(\Omega_a) = \left\{ v \in L^2(\Omega_a) : v|_{\Omega_{a,\ell}} \in V_{a,\ell}(\Omega_{a,\ell}) \quad \forall \Omega_{a,\ell} \in \mathcal{T}_a \right\}.$$

Given $s \geq 0$, we define now the broken Sobolev space $H^s(\mathcal{T}_a)$:

$$H^s(\mathcal{T}_a) = \left\{ v \in L^2(\Omega_a) : v|_{\Omega_{a,\ell}} \in H^s(\Omega_{a,\ell}) \quad \forall \Omega_{a,\ell} \in \mathcal{T}_a \right\},$$

and we denote with $(\cdot, \cdot)_{\mathcal{T}_a}$ its continuous inner product:

$$(u, v)_{\mathcal{T}_a}^{\text{NI}} = \sum_{\Omega_{a,\ell} \in \mathcal{T}_a} (u, v)_{\Omega_{a,\ell}}^{\text{NI}}. \quad (3.12)$$

We recall that since we will employ on the meso decomposition a Spectral Element Method, the product (2.86) becomes:

$$(u, v)_{\mathcal{T}_a}^{\text{NI}} = \sum_{\Omega_{a,\ell} \in \mathcal{T}_a} (u, v)_{\Omega_{a,\ell}}^{\text{NI}} = \sum_{\Omega_{a,\ell} \in \mathcal{T}_a} \sum_{K_\ell^i \in \mathcal{T}_{a,\ell}} (u, v)_{K_\ell^i}^{\text{NI}}.$$

The main idea is to build a discrete solution that is globally discontinuous on Ω_a but continuous inside each macro region $\Omega_{a,\ell}$. The semi-discrete DGSEM approximation of problem (2.73) reads: $\forall t \in (0, T]$, find $\rho_h \in V_a^{\text{DG}}$ such that:

$$(\ddot{\rho}_h, v_h)_{\mathcal{T}_a} + \mathcal{A}_h(\rho_h, v_h) + \mathcal{B}(\rho_h, v_h) = -(\nabla \cdot \mathbf{T}, \nabla v_h)_{\mathcal{T}_a}^{\text{NI}} \quad \forall v_h \in V_a^{\text{DG}},$$

where

$$\mathcal{A}_h(w, v) = \sum_{\Omega_{a,\ell} \in \mathcal{T}_a} \sum_{K_\ell^i \in \mathcal{T}_{a,\ell}} c_0^2(\nabla w, \nabla v)_{K_\ell^i}^{\text{NI}} \quad \forall w, v \in V_a^{\text{DG}},$$

and where

$$\begin{aligned} \mathcal{B}(w, v) = & - \sum_{F \in \mathcal{F}_a} \int_F \{\!\{ \nabla_h w \}\!\} \cdot [\![v]\!] ds \\ & - \sum_{F \in \mathcal{F}_a} \int_F \{\!\{ \nabla_h v \}\!\} \cdot [\![w]\!] ds + \sum_{F \in \mathcal{F}_a} \int_F \sigma [\![w]\!] \cdot [\![v]\!] \quad \forall w, v \in V_a^{\text{DG}}. \end{aligned}$$

The penalty function σ is defined as

$$\sigma = \gamma_\sigma \frac{r^2}{h_a},$$

where γ_σ is large enough to ensure stability, see [16].

Remark 3.2.1 When $N_L = 1$, i.e. when the macro decomposition is made only by one element, the set of all the interface face $\mathcal{F} = \emptyset$. Hence, the DG-SEM method corresponds to the SEM method introduced in Section 2.6.1. While if the number of partitions is exactly the number of elements, the method corresponds to the DG method.

3.2.5 Robust DGSEM

One of the issue of the DG method introduced in the previous section is that in presence of high heterogeneous discretization parameters the stability parameter can be very large, leading to ill-conditioned systems. We report the robust interior penalty method, see [43]. Let us first introduce the following weighted averages:

$$\{u\}_\theta = \theta u^+ + (1 - \theta)u^-, \quad \{\mathbf{v}\}_\theta = \theta \mathbf{v}^+ + (1 - \theta)\mathbf{v}^-,$$

and modify the bilinear for $\mathcal{B}(u, v)$ as follow:

$$\begin{aligned} \mathcal{B}(u, v) = & - \sum_{F \in \mathcal{F}} \int_F \{\nabla_h w\}_\theta \cdot [\![v]\!] ds \\ & - \sum_{F \in \mathcal{F}} \int_F \{\nabla_h v\}_\theta \cdot [\![u]\!] ds + \sum_{F \in \mathcal{F}} \int_F \sigma_\theta [\![u]\!] \cdot [\![v]\!]. \end{aligned}$$

We define the penalty function in the following manner

$$\sigma_\theta \approx \frac{1}{(\xi^+ + \xi^-)^2},$$

where

$$\xi^\pm = \frac{1}{2\sqrt{6}C_{inv,\pm}},$$

where $C_{inv,\pm} \approx \sqrt{r_\pm^2/h_{a,\pm}}$. Finally, we take as weight the following:

$$\theta = \frac{\xi^+}{\xi^+ + \xi^-}.$$

The introduced DG method is robust with large heterogeneous discretization parameter, and overall bounds the condition number of the stiffness matrix coming from the discretization.

3.3 Discretization of the Flow Problem

In this section, we first introduce the Finite Volume (FV) discretization of the flow problem and we next recall the basics for the Pressure Implicit with Splitting of Operators (PISO) algorithm [75].

3.3.1 Time Discretization of the Flow Problem

First, we discretize the incompressible flow equations (2.71) in time. We divide the temporal interval $(0, T]$ into N subintervals, such that $T = N\Delta t$, setting $t^n = n\Delta t$, with $n = 0, \dots, N$.

We consider a backward differentiation formula of second order, namely $\frac{\partial \mathbf{u}}{\partial t} \approx \frac{3\mathbf{u}^{n+1} - 4\mathbf{u}^n + \mathbf{u}^{n-1}}{2\Delta t}$ and we discretize the whole problem in a semi-implicit way:

$$\begin{aligned} \frac{3\mathbf{u}^{n+1} - 4\mathbf{u}^n + \mathbf{u}^{n-1}}{2\Delta t} + \nabla \cdot ((2\mathbf{u}^n - \mathbf{u}^{n-1}) \otimes \mathbf{u}^{n+1}) \\ - \nu \Delta \mathbf{u}^{n+1} + \nabla p^{n+1} = \mathbf{0}, \\ \nabla \cdot \mathbf{u}^{n+1} = 0. \end{aligned} \quad (3.13)$$

Notice that the flux term is treated explicitly in time.

3.3.2 Finite Volume Discretization of the Flow Problem

We discretize the problem in space employing the FV method. Let us first consider a polyhedral tessellation \mathcal{T}_f of the domain Ω_f . Given two neighbouring cells K_+ and K_- , we denote with F their common face, see Fig. 2.8. Let us denote with \mathbf{x}_+ and \mathbf{x}_- the barycentres of the polyhedrons K_+ , K_- , respectively with \mathbf{x}_F the barycentre of the face F , and with \mathbf{n} the unit normal to the face F , outward with respect to the element K_+ . Now, let \mathbf{h} be the vector connecting the cell barycentres $\mathbf{h} = \mathbf{x}_+ - \mathbf{x}_-$, and let $h = |\mathbf{h}|$ be its modulus. We denote with τ the cosine of the angle between the vectors \mathbf{h} and \mathbf{n} , namely:

$$\tau = \frac{\mathbf{h} \cdot \mathbf{n}}{h},$$

that measures the non-orthogonality between two cells. Now, let \mathbf{x}_\cap be the intersection point between the face F and the vector \mathbf{h} . We introduce the interpolation weights w :

$$w = \frac{h_+}{h_+ + h_-},$$

where $h_+ = |\mathbf{x}_\cap - \mathbf{x}_+|$ and $h_- = |\mathbf{x}_\cap - \mathbf{x}_-|$. Then, we introduce the space of piecewise constant functions

$$V_f = \{v_f \in L^2(\Omega_f) : v_f|_K \in \mathbb{P}^0(K) \ \forall K \in \mathcal{T}_f\},$$

with $N_f = \dim(V_f)$ and we denote with $\mathbf{V}_f = [V_f]^3$ the vector valued discrete space. In order to obtain a finite volume discretization of problem (2.87), we integrate the momentum equation over the polyhedron $K \in \mathcal{T}_f$, obtaining:

$$\begin{aligned} & \int_K \frac{3\mathbf{u}^{n+1} - 4\mathbf{u}^n + \mathbf{u}^{n-1}}{2\Delta t} d\mathbf{x} + \int_K \nabla \cdot ((2\mathbf{u}^n - \mathbf{u}^{n-1}) \otimes \mathbf{u}^{n+1}) d\mathbf{x} \\ & \quad - \int_K \nu \Delta \mathbf{u}^{n+1} d\mathbf{x} + \int_K \nabla p^{n+1} d\mathbf{x} = 0, \\ & \int_K \nabla \cdot \mathbf{u}^{n+1} d\mathbf{x} = 0. \end{aligned} \quad (3.14)$$

Next, we proceed by discussing the discretization of each term, introducing $\mathbf{u}_h^n \in \mathbf{V}_f$ and $p_h^n \in V_f$. The spatial approximation of the first integral in (2.88) is straightforward, namely,

$$\begin{aligned} \int_K \frac{3\mathbf{u}^{n+1} - 4\mathbf{u}^n + \mathbf{u}^{n-1}}{2\Delta t} d\mathbf{x} & \approx \int_K \frac{3\mathbf{u}_h^{n+1} - 4\mathbf{u}_h^n + \mathbf{u}_h^{n-1}}{2\Delta t} d\mathbf{x} \\ & = |K| \frac{3\mathbf{u}_h^{n+1} - 4\mathbf{u}_h^n + \mathbf{u}_h^{n-1}}{2\Delta t}, \end{aligned}$$

where $|K|$ is the volume of the element K and where a mid-point quadrature rule is employed. Next, thanks to the Gauss theorem, the viscous term in (2.88) can be approximated as follows

$$\int_K \nabla \cdot (\nu \nabla \mathbf{u}^{n+1}) d\mathbf{x} = \int_{\partial K} (\nu \nabla \mathbf{u}^{n+1}) \mathbf{n} d\sigma \approx \sum_{F \in \partial K} \nu \nabla \mathbf{u}_F^{n+1} \mathbf{n} |F| \quad (3.15)$$

where $\nabla \mathbf{u}_F^{n+1} = \nabla \mathbf{u}^{n+1}(\mathbf{x}_F)$, being \mathbf{x}_F the face cell barycentre. Note that in the last step, we use a mid-point quadrature rule on the face F . Now, if the face cell F is shared by two elements K_+ and K_- , we reconstruct a linear function $\nabla \mathbf{u}_F^{n+1} \mathbf{n}$.

First, recall the following Gauss gradient reconstruction. Given an element K , the Gauss gradient of a scalar function ϕ computed at the

cell centre is approximated by:

$$\nabla\phi \approx \frac{1}{|K|} \sum_{F \in \partial K} \phi_F \mathbf{n}_F |F|, \quad (3.16)$$

where \mathbf{n}_F is the outward normal face to F , and the value of ϕ is computed with a linear interpolation:

$$\phi_F = w\phi_+ + (1-w)\phi_-,$$

where ϕ_\pm is the scalar field ϕ_\pm evaluated at the barycenter of the cells K_\pm .

The gradient $\nabla \mathbf{u}_F^{n+1} \mathbf{n}$ coming from the discretization of the diffusion term in eq. (2.89) is reconstructed linearly:

$$\nabla \mathbf{u}_F^{n+1} \mathbf{n} \approx \frac{\mathbf{u}_+^{n+1} - \mathbf{u}_-^{n+1}}{\tau h} + (w \nabla \mathbf{u}_+^n + (1-w) \nabla \mathbf{u}_-^n) \left(\mathbf{n} - \frac{\mathbf{h}}{h\tau} \right). \quad (3.17)$$

Note that the gradients $\nabla \mathbf{u}_\pm^n$ are treated explicitly and computed with a Gauss formula at the cell centres of the elements K_\pm , see eq. (2.90). In eq. (2.91) we have employed a non orthogonal correction, see Section 3.3.1.3 in [76]. Note that in the case of structured orthogonal grids, the formula simply reduces to $\nabla \mathbf{u}_F^{n+1} \mathbf{n} \approx \frac{\mathbf{u}_+^{n+1} - \mathbf{u}_-^{n+1}}{h}$.

Concerning the convective term in (2.88), integrating by parts, we get:

$$\begin{aligned} \int_K \nabla \cdot ((2\mathbf{u}^n - \mathbf{u}^{n-1}) \otimes \mathbf{u}^{n+1}) d\mathbf{x} \\ = \int_{\partial K} \mathbf{u}^{n+1} ((2\mathbf{u}^n - \mathbf{u}^{n-1}) \cdot \mathbf{n}) d\sigma \\ \approx \sum_{F \in \partial K} \mathbf{u}_F^{n+1} ((2\mathbf{u}_F^n - \mathbf{u}_F^{n-1}) \cdot \mathbf{n}) |F|, \end{aligned} \quad (3.18)$$

where we applied a mid-point quadrature rule on the face F . Since we are treating the convective term in a semi-implicit way, the flux $(2\mathbf{u}_F^n - \mathbf{u}_F^{n-1}) \cdot \mathbf{n}$ is known. We denote it with b , and we discretize the convective term in eq. (2.92) with a linear upwind scheme:

$$\sum_{F \in \partial K} \mathbf{u}_F^{n+1} b |F| = \sum_{F \in \partial K} (\mathbf{u}_{\text{up}}^{n+1} + \nabla \mathbf{u}_{\text{up}}^n (\mathbf{x}_F - \mathbf{x}_{\text{up}})) b |F|, \quad (3.19)$$

where the index up is

$$\text{up} = \begin{cases} + & \text{if } b \geq 0, \\ - & \text{if } b < 0, \end{cases}$$

and $\nabla \mathbf{u}_{\text{up}}^n$ is computed with a Gauss formula and it is treated explicitly. For the algebraic formulation it is convenient to rewrite eq. (2.93) as:

$$\sum_{F \in \partial K} (\mathbf{u}_{\text{up}}^{n+1} + \nabla \mathbf{u}_{\text{up}}^{n+1}(\mathbf{x}_F - \mathbf{x}_{\text{up}})) b|F| = \sum_{F \in \partial K} b|F| \left(a \mathbf{u}_+ + (1-a) \mathbf{u}_- + \nabla \mathbf{u}_{\text{up}}^n(\mathbf{x}_F - \mathbf{x}_{\text{up}}) \right),$$

where

$$a = \begin{cases} 1 & \text{if } b \geq 0, \\ 0 & \text{if } b < 0. \end{cases}$$

Finally, the pressure gradient term in eq. (2.88) is discretized similarly, by observing that $\nabla p = \nabla \cdot (p\mathbf{I})$ and by applying the Gauss theorem, see eq. (2.90). This means that:

$$\int_K \nabla p^{n+1} d\mathbf{x} \approx \sum_{F \in \partial K} p_F^{n+1} \mathbf{n}_F |F| = \sum_{F \in \partial K} (w p_+^{n+1} + (1-w) p_-^{n+1}) \mathbf{n}_F |F|.$$

Finally, we remark that we compute at any time t^n the aeroacoustic sound source term as a post-process of the fluid solution \mathbf{u}_h^n , i.e., $\nabla \cdot \mathbf{T} \approx \nabla \cdot (\rho_0 \mathbf{u}_h^n \otimes \mathbf{u}_h^n)$, see (2.84) and also (2.92).

Now, we construct the algebraic discretization of problem (2.71). Let

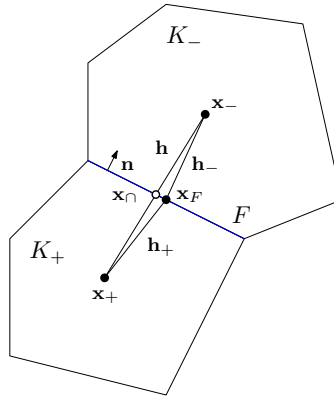


Figure 3.3: Sketch of the geometrical notation for the finite volume discretization. The polyhedral cells K_+ and K_- have barycentre \mathbf{x}_+ , \mathbf{x}_- , that is connected trough the segment \mathbf{h} . The segment \mathbf{h} intersects the face F , shared by both elements K_- and K_+ in \mathbf{x}_\cap . We denote with \mathbf{x}_F the face F barycentre, and with \mathbf{h}_- and \mathbf{h}_+ the segments that connect the barycenters \mathbf{x}_- , \mathbf{x}_+ to the face barycentre \mathbf{x}_F .

us consider the element $K_i \in \mathcal{T}_f$ and its faces F_{ij} , where $i = 1, \dots, N_f$

denotes the current element, while $j = 1, \dots, N_f$ denotes the global index of the neighbouring element being F_{ij} the shared face. We first introduce the matrix $A = \mathbb{R}^{3N_f \times 3N_f}$, block matrix made as:

$$A = \begin{bmatrix} A^x & 0 & 0 \\ 0 & A^y & 0 \\ 0 & 0 & A^z \end{bmatrix},$$

where each block can be built for $k = x, y, z$ as:

$$\begin{aligned} A_{ii}^k &= |K_i| \frac{3}{2\Delta t} + \sum_{F \in \partial K_i} |F| \frac{\nu}{\tau h} + \sum_{F \in \partial K_i} ab|F| \quad \forall i = 1, \dots, N_f, \\ A_{ij}^k &= -\frac{\nu}{\tau h} |F_{ij}| + (1-a)b|F_{ij}| \quad \forall i, j = 1, \dots, N_f, \text{ with } i \neq j. \end{aligned}$$

Moreover we introduce the matrix $B = \mathbb{R}^{N_f \times 3N_f}$, where

$$B = [B^x \ B^y \ B^z],$$

and each block B^k with $k = x, y, z$ is defined as:

$$\begin{aligned} B_{ii}^k &= \sum_{F \in \partial K_i} w \mathbf{n}_F^k |F| \quad \forall i = 1, \dots, N_f, \\ B_{ij}^k &= (1-w) \mathbf{n}_{F_{ij}}^k |F_{ij}| \quad \forall i, j = 1, \dots, N_f, \text{ with } i \neq j \end{aligned}$$

while the term \mathbf{f}^n collects all the explicit terms:

$$\begin{aligned} \mathbf{f}_i^n &= \frac{2}{\Delta t} \mathbf{u}_i^n - \frac{1}{2\Delta t} \mathbf{u}_i^{n-1} + \sum_{F_{ij} \in K_i} (w \nabla \mathbf{u}_i^n + (1-w) \nabla \mathbf{u}_j^n) \left(\mathbf{n} - \frac{\mathbf{h}}{h\tau} \right) \\ &\quad - \sum_{F \in K_i} \nabla \mathbf{u}_{\text{up}}^n (\mathbf{x}_F - \mathbf{x}_{\text{up}}) b |F| \quad \forall i = 1, \dots, N_f. \end{aligned}$$

We finally write the fully coupled algebraic problem for the Navier-Stokes equations:

$$\begin{bmatrix} A & B^T \\ B & 0 \end{bmatrix} \begin{bmatrix} \mathbf{u}_h^{n+1} \\ \mathbf{p}_h^{n+1} \end{bmatrix} = \begin{bmatrix} \mathbf{f}^n \\ \mathbf{0} \end{bmatrix},$$

where, with an abuse of notation, we are denoting with the same symbol the cell values of the vector $\mathbf{u}_h^{n+1} \in \mathbb{R}^{3N_f}$ and the finite volume solution $\mathbf{p}_h^{n+1} \in \mathbb{R}^{N_f}$. In the next section, we introduce a splitting strategy to solve the coupled system.

3.3.3 Velocity Pressure Coupling for the Flow Problem

For the numerical solution to the time-dependent incompressible Navier-Stokes equations (2.71), that is, in turn, used for evaluating the source term of the acoustic problem (2.72), the OpenFOAM solver `pisoFoam` is adopted. The solver is based on the so-called Pressure Implicit with Splitting of Operators (PISO) algorithm [75], a popular segregated pressure-based method widely adopted in the CFD community for the solution to unsteady incompressible flows.

Algorithm 1 PISO Algorithm

Consider the decomposition $A = D - H$, being D the diagonal matrix of A and $-H$ its off-diagonal terms. Given $\mathbf{p}_h^n \in V_f$, $\mathbf{u}_h^n \in \mathbf{V}_f$, for $t_n = n\Delta t$ with $n = 0, \dots, N-1$ we have:

$$\text{velocity predictor:} \quad A\mathbf{u}_{h,0}^{n+1} = -B^T \mathbf{p}_h^n + \mathbf{f}^n, \quad (3.20)$$

Next, subiterate for $k = 0, \dots, N_{PISO}$, where $N_{PISO} > 0$:

$$\text{velocity update:} \quad D\tilde{\mathbf{u}} = H\mathbf{u}_{h,k}^{n+1} + \mathbf{f}^n, \quad (3.21)$$

$$\text{pressure predictor:} \quad BD^{-1}B^T \mathbf{p}_{h,k+1}^{n+1} = B\tilde{\mathbf{u}}, \quad (3.22)$$

$$\text{velocity corrector:} \quad \mathbf{u}_{h,k+1}^{n+1} = \tilde{\mathbf{u}} - D^{-1}B^T \mathbf{p}_{h,k+1}^{n+1}, \quad (3.23)$$

where finally $\mathbf{p}_h^{n+1} = \mathbf{p}_{h,N_{PISO}}^{n+1}$ and $\mathbf{u}_h^{n+1} = \mathbf{u}_{h,N_{PISO}}^{n+1}$.

To achieve the decomposition between pressure and velocity, first the PISO Algorithm 1 computes a prediction of the velocity in eq. (2.94). Equation (2.94) corresponds to the momentum equation, where the pressure gradient is treated explicitly. Next, we subiterate as follows. First, we update the velocity employing an algebraic splitting in eq. (2.95). Next, we solve a Poisson equation, see eq. (2.96), where the source term is the gradient of the updated velocity. Finally, we correct the velocity employing the new pressure in Equation (2.97) in order to impose the divergence-free constraint on the corrected velocity. The method subiterates until the maximum number of PISO iterations is computed, which usually is set to $N_{PISO} = 2$.

3.4 Intergrid Projection Method

To solve the hybrid aeroacoustic problem (2.73), we need to map the acoustic sound source solution defined on the flow space to the acoustic space. In order to minimize the L^2 error, we introduce a novel intergrid

projection method. Let $q_f \in V_f$ be a function defined on the fluid grid \mathcal{T}_f such that $q_f = \sum_{i=1}^{N_f} \hat{q}_{f,i} \phi_{f,i}$, where $\{\phi_{f,i}\}_i^{N_f}$ is the set of N_f basis functions associated to V_f , and $\hat{q}_{f,i}$ are the corresponding expansion coefficients. We define the L^2 -projection of the field q_f into V_a as

$$q_a = \operatorname{argmin}_{q \in V_a} \|q_f - q\|_{L^2(\mathcal{T}_a)},$$

where q_f has been extended by zero also on Ω_a . Problem (2.8) is equivalent to the following: find $q_a \in V_a$ s.t.

$$(q_a, \phi_{a,i})_{\mathcal{T}_a} = (q_f, \phi_{a,i})_{\mathcal{T}_a} \quad \forall \phi_{a,i} \in V_a,$$

where $q_a \in V_a$ is a function defined on the acoustic grid \mathcal{T}_a such that $q_a = \sum_{i=1}^{N_a} \hat{q}_{a,i} \phi_{a,i}$, where $\{\phi_{a,i}\}_i^{N_a}$ is the set of N_a basis functions, and $\hat{q}_{a,i}$ are the corresponding expansion coefficients.

Projection of Piecewise Constants Functions

Motivated by the solution method used in Section 2.7.2 we address the case where q_f is a piecewise constant function over \mathcal{T}_f . Then, problem (2.8) can be recast as follows:

$$\sum_{K_a \in \mathcal{T}_a} (q_a, \phi_{a,i})_{K_a} = \sum_{K_a \in \mathcal{T}_a} \left(\sum_{\ell=1}^{N_f} \hat{q}_{f,\ell} \phi_{f,\ell}, \phi_{a,i} \right)_{K_a} = \sum_{K_a \in \mathcal{T}_a} \sum_{\ell=1}^{N_f} \hat{q}_{f,\ell} (1, \phi_{a,i})_{K_a \cap K_{f,\ell}}, \quad (3.24)$$

where we have used that $K_{f,\ell} = \operatorname{supp}(\phi_{f,\ell})$. The discrete algebraic counterpart of (2.98) becomes

$$M^{aa} \hat{\mathbf{q}}_a = M^{af} \hat{\mathbf{q}}_f, \quad (3.25)$$

where $M^{aa} \in \mathbb{R}^{N_a \times N_a}$ is the full acoustic mass matrix, i.e.,

$$M_{i,j}^{aa} = \sum_{K_a \in \mathcal{T}_a} (\phi_{a,j}, \phi_{a,i})_{K_a}, \quad i, j = 1, \dots, N_a,$$

where we are employing enough quadrature points to integrate it exactly, and hence $M^{aa} \neq M$, that is the mass equation employed in the SEM method introduced in equation (2.81). The $M^{af} \in \mathbb{R}^{N_a \times N_f}$ is the coupling mass defined as

$$M_{i,\ell}^{af} = \sum_{K_a \in \mathcal{T}_a} \sum_{\ell=1}^{N_f} \hat{q}_{f,\ell} (1, \phi_{a,i})_{K_a \cap K_{f,\ell}}^{\text{QF}},$$

where $(\cdot, \cdot)^{\text{QF}}$ refers to a suitable quadrature formula over the polyhedral elements $K_a \cap K_{f,\ell}$, see sec. 2.10.1. The vector $\hat{\mathbf{q}}_a$ in (2.99) collects all the expansion coefficients of the acoustic field q_a , while $\hat{\mathbf{q}}_f$ collects all the expansion coefficients of the fluid field q_f .

Projection of Piecewise Linear Functions

Finite volume methods assume that the field is linear across the cells, but in order to explicitly obtain the linear formulation, we have to introduce a linear reconstruction. Consider the space of the linearly reconstructed functions V_f^{lin} :

$$V_f^{\text{lin}} = \{v_f^{\text{lin}} \in L^2(\Omega_f) : v_f^{\text{lin}}|_{K_f} = v_f + \nabla_h v_f \cdot (\mathbf{x} - \mathbf{x}_0), \forall v_f \in V_f\},$$

where $\nabla_h v_f$ is a discrete reconstruction of the gradient and \mathbf{x}_0 is the barycentre of the element K_f . Hence, problem (2.8) can be rewritten in the following manners: find $q_a \in V_a$ such that:

$$(q_a, \phi_{a,i})_{\mathcal{T}_a} = (q_f^{\text{lin}}, \phi_{a,i})_{\mathcal{T}_a} \quad \forall \phi_{a,i} \in V_a,$$

The projection problem with the linear reconstruction (2.8) can be recast as follows:

$$\begin{aligned} \sum_{K_a \in \mathcal{T}_a} (q_a, \phi_{a,i})_{K_a} &= \sum_{K_a \in \mathcal{T}_a} \left(\sum_{\ell=1}^{N_f} \hat{q}_{f,\ell} \phi_{f,\ell}, \phi_{a,i} \right)_{K_a} = \\ &\sum_{K_a \in \mathcal{T}_a} \sum_{\ell=1}^{N_f} \hat{q}_{f,\ell} (1, \phi_{a,i})_{K_a \cap K_{f,\ell}} + ((\nabla_h q_f) \cdot (\mathbf{x} - \mathbf{x}_0), \phi_{a,i})_{K_a \cap K_{f,\ell}}. \end{aligned}$$

The algebraic problem for the projection of the reconstructed linear datum becomes:

$$M^{aa} \mathbf{q}_a = M^{af} \mathbf{q}_f + G^x \mathbf{g}_f^x + G^y \mathbf{g}_f^y + G^z \mathbf{g}_f^z,$$

where for $i = 1, \dots, N_a$, $\ell = 1, \dots, N_f$ we define the matrices G^x, G^y, G^z

as:

$$G_{i,\ell}^x = \sum_{K_a \in \mathcal{T}_a} \sum_{\ell=1}^{N_f} \int_{K_a \cap K_{f,\ell}} (x - x_0) \phi_{a,i} \, dx, \quad (3.26)$$

$$G_{i,\ell}^y = \sum_{K_a \in \mathcal{T}_a} \sum_{\ell=1}^{N_f} \int_{K_a \cap K_{f,\ell}} (y - y_0) \phi_{a,i} \, dy, \quad (3.27)$$

$$G_{i,\ell}^z = \sum_{K_a \in \mathcal{T}_a} \sum_{\ell=1}^{N_f} \int_{K_a \cap K_{f,\ell}} (z - z_0) \phi_{a,i} \, dz, \quad (3.28)$$

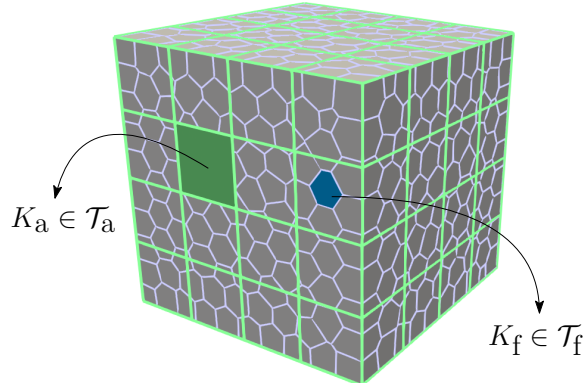
and where the discrete gradient is $\mathbf{g}_{f,\ell}^x = (\nabla_h q_{f,\ell})^x$, $\mathbf{g}_{f,\ell}^y = (\nabla_h q_{f,\ell})^y$, $\mathbf{g}_{f,\ell}^z = (\nabla_h q_{f,\ell})^z$. As for the matrix M^{af} , in order to evaluate the integrals (2.100), (2.101), (2.102) we employ the quadrature formula described in Section 2.10.1.

3.5 Intergrid Geometrical Coupling

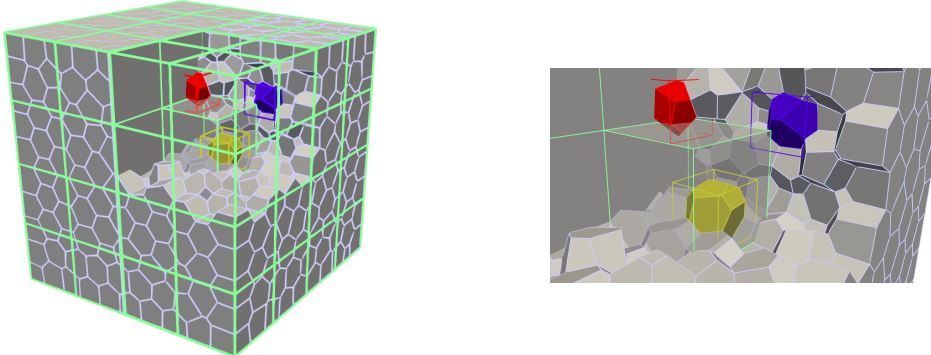
One of the most important challenges in computing the intergrid projection method is to compute explicitly the geometrical term $K_a \cap K_f$. Since we want to apply the hybrid aeroacoustic methodology introduced in Section 2.4.3 to problems where the computational grid is fixed, computing explicitly the intersections is affordable, and it is done only once and offline with respect to the time evolution of the problem. However, the computational cost of the algorithm is still relevant. We then discuss the employed acceleration algorithms that make the computational strategy viable and affordable.

3.5.1 Grid Intersection Algorithm

The benefits of computing explicitly the intersection elements when projecting have been already explored in the context of low-order finite elements for aeroacoustics on tetrahedral meshes, see for instance [128]. The new grid obtained after the intersection is nested both with respect to the fluid grid and with respect to the acoustic grid. Here, we propose a geometrical algorithm for computing the intersections between generic polyhedral grids. In particular, we consider a polyhedral tessellation \mathcal{T}_f for the fluid domain Ω_f , while a hexahedral tessellation \mathcal{T}_a for the acoustic domain Ω_a , see for instance Figure 2.9a. This choice is inherited from the numerical scheme that we apply to the aeroacoustic problem (see Section 2.7.2- 2.6.3), even if the proposed algorithm

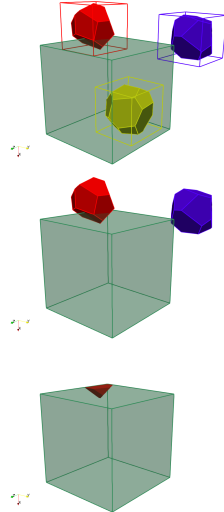


(a) Example of acoustic \mathcal{T}_a and fluid \mathcal{T}_f tessellations made of hexahedral and polyhedral elements, respectively, for the domain $\Omega = \Omega_a = \Omega_f$.



(b) *Bounding Box search.* Left, overview on the whole domain. Right, zoom on a selected acoustic element K_a . At this stage, all the bounding box of the fluid elements intersecting $\mathcal{B}(K_a)$ are selected and collected in the set \mathcal{K}_a . We show some of the selected fluid elements (yellow ●, red ● and blue ●) and their respective bounding box.

Figure 3.4: Schematic representation of Algorithm 2. (●) Acoustic element K_a . (●) Example of a fluid element $K_f \in \mathcal{I}_a$. (●) Example of a fluid element $K_f \in \mathcal{K}_a$ but not intersecting with the selected element K_a . (●) Example of a fluid element $K_f \in \mathcal{C}_a$.



(a) *Bounding Box selection.* At this stage, we check if the bounding box of a fluid element is contained inside K_a . For example, the yellow (●) fluid element is contained in K_a , and hence it is added to \mathcal{C} .

(b) *Separating Axis Theorem selection.* At this stage, we check if the fluid elements in $\mathcal{K}_a \setminus \mathcal{C}_a$ are intersecting with K_a . We see that the red element (●) is intersecting, and hence it is pushed in \mathcal{I} . The blue element (●) is not intersecting, so it is discarded.

(c) *Intersection computation.* The intersection is explicitly computed only for the red element (●). A new object is obtained, which is then stored and used for the projection computation.

Figure 3.5: Schematic representation of Algorithm 2. (●) Acoustic element K_a . (●) Example of a fluid element $K_f \in \mathcal{I}_a$. (●) Example of a fluid element $K_f \in \mathcal{K}_a$ but not intersecting with the selected element K_a . (●) Example of a fluid element $K_f \in \mathcal{C}_a$.

is valid for generic polyhedral grids. Depending on the characteristic wave-length of the problem and the numerical schemes considered, we assume that the number of fluid elements is larger than the number of acoustic ones and that the elements are all convex polyhedra. Considering polyhedra elements allows us to use the Separating Axis Theorem (SAT) for detecting if two elements have non-empty intersection. The main idea of the SAT is that, if two elements have empty intersection, then there exists a plane that separates them. Only a few directions depending on the normals to the faces of the elements and the edge elements have to be checked. A detailed description of the SAT algorithm can be found in [47, Chapter 8]. Before presenting the algorithm for computing the intersections between two generic elements $K_a \in \mathcal{T}_a$ and $K_f \in \mathcal{T}_f$ we introduce some definitions and notations.

Definition 3.5.1 (Cartesian Bounding Box) Given a polyhedral element $K \subset \mathbb{R}^3$, we denote with $\mathbf{v}_i = (x_i, y_i, z_i)$ with $i = 1, \dots, n_v$ the n_v vertices of K . We indicate with $\mathcal{B}(K)$ his Cartesian bounding box:

$$\mathcal{B}(K) = [x_{\min}, x_{\max}] \times [y_{\min}, y_{\max}] \times [z_{\min}, z_{\max}],$$

where $x_{\min} = \min_{i=1, \dots, n_v} x_i$, $x_{\max} = \max_{i=1, \dots, n_v} x_i$, $y_{\min} = \min_{i=1, \dots, n_v} y_i$, $y_{\max} = \max_{i=1, \dots, n_v} y_i$, $z_{\min} = \min_{i=1, \dots, n_v} z_i$, $z_{\max} = \max_{i=1, \dots, n_v} z_i$.

For any element $K_a \in \mathcal{T}_a$, we define:

- the set \mathcal{K}_a collecting all the fluid elements K_f whose bounding box $\mathcal{B}(K_f)$ intersects the bounding box $\mathcal{B}(K_a)$, i.e., $\mathcal{B}(K_f) \cap \mathcal{B}(K_a) \neq \emptyset$;
- the set \mathcal{C}_a collecting all the fluid elements K_f whose bounding box $\mathcal{B}(K_f)$ is strictly contained inside K_a , i.e. $\mathcal{B}(K_f) \subset K_a$;
- the set \mathcal{I}_a collects all the remaining fluid elements intersecting with K_a . The fluid elements K_f do intersect with K_a , but their bounding box is not fully contained inside K_a and hence the intersection has to be computed explicitly.

We remark that the cardinality of \mathcal{K}_a is strictly greater than the cardinality of $\mathcal{C}_a \cup \mathcal{I}_a$. Furthermore, note that not all the elements intersecting with K_a are in \mathcal{I}_a , since part of them is contained in \mathcal{C}_a . Algorithm 2 computes the intersections between \mathcal{T}_a and \mathcal{T}_f proceeding as follows: for any element $K_a \in \mathcal{T}_a$,

1. *Bounding Box search*: search over the intersecting bounding boxes of the fluid elements $\mathcal{B}(K_f)$ and the bounding box $\mathcal{B}(K_a)$ of the acoustic element K_a . If the intersection is not empty, the element K_f is added to the set \mathcal{K}_a , see Figure 2.9b.
2. *Bounding Box selection*: map the vertices of $\mathcal{B}(K_f)$ via a Newton-Raphson algorithm by employing the trilinear map θ_{K_a} . If all the vertices are inside the reference element \hat{K}_A , then K_f is added to \mathcal{C}_a , see Figure 2.10a.
3. *Separating Axis Theorem selection*: apply the SAT collision detection algorithm in order to understand if the intersections have to be computed. In fact, there might be fluid elements in \mathcal{K}_a that are not effectively intersecting K_a , see for instance Figure 2.10b. The intersecting elements are added to \mathcal{I}_a .
4. *Intersection computation*: compute explicitly the intersection between the fluid elements in \mathcal{I}_a and the acoustic element K_a , cf. Figure 2.10c.

We remark that Step 2 of the algorithm is justified by the assumption that fluid elements are much smaller than the acoustic ones. The final intersection (Step 4) is computed by employing the Computational Geometry Algorithms Library (CGAL) [145], and it is based on the Nef implementation [66] that allows performing Boolean operations

between solids. Algorithm 2 summarizes the proposed intersection strategy.

Algorithm 2 Algorithm to compute the intersection $\mathcal{T}_a \cap \mathcal{T}_f$ between the grids \mathcal{T}_a and \mathcal{T}_f .

```
[ $\mathcal{T}_a \cap \mathcal{T}_f$ ] = compute_intersection( $\mathcal{T}_a, \mathcal{T}_f$ )
1: for  $K_a \in \mathcal{T}_a$  do
2:   Compute  $\mathcal{B}(K_a)$ .
3:   for  $K_f \in \mathcal{T}_f$  do
4:     Compute  $\mathcal{B}(K_f)$ .
5:     if  $\mathcal{B}(K_a) \cap \mathcal{B}(K_f)$  then
6:       Add  $K_f$  in  $\mathcal{K}_a$ .
7:       if  $\mathcal{B}(K_f) \subset K_a$  then
8:          $K_f \cap K_a = K_f$  and  $K_f \in \mathcal{C}_a$ .
9:         Add  $K_f$  to  $\mathcal{T}_a \cap \mathcal{T}_f$ .
10:        break
11:      end if
12:      if  $K_a \cap K_f$  then
13:        Add  $K_f$  in  $\mathcal{I}_a$ .
14:      else
15:        Elements are not intersecting.
16:      end if
17:    end if
18:   end for
19:   for ( $K_f \in \mathcal{I}_a$ ) do
20:     Compute intersection ( $K_a \cap K_f$ ) with CGAL.
21:     Add  $K_f \cap K_a$  to  $\mathcal{T}_a \cap \mathcal{T}_f$ .
22:   end for
23: end for
```

3.5.2 Accuracy of the Intergrid Intersection Algorithm

In this section, we investigate some computational aspects of the algorithm presented in Section 2.9.1. First, we test the intersection algorithm in terms of accuracy and scalability. Then, we use Algorithm 2 together with the quadrature-free method in Section 2.10.1 to compute integrals of polynomials over the computed intersected domain Ω .

To check the accuracy of the proposed intersection algorithm we consider the following mesh configurations. In the first test, we set $\Omega = \Omega_f = \Omega_a = (-2, 2) \times (-2, 2) \times (-0.05, 0.05)$ and define the acoustic grid \mathcal{T}_a^1 (resp. fluid grid \mathcal{T}_f^1) by extruding in the vertical direction distorted quadrilaterals (resp. polygons), cf. Figure 2.11. The acoustic grid has 64 elements and the original Cartesian mesh size was $h_a = 0.5$, while

mesh	$E_{rel}(1)$	$E_{rel}(x^2y^2)$	$E_{rel}(x^4y^4)$
\mathcal{T}_a^1	5.551×10^{-16}	6.661×10^{-16}	8.882×10^{-16}
\mathcal{T}_f^1	5.551×10^{-16}	4.441×10^{-16}	4.441×10^{-16}
$\mathcal{T}_a^1 \cap \mathcal{T}_f^1$	5.551×10^{-16}	1.11×10^{-16}	2.22×10^{-16}

Table 3.1: Computed $E_{rel}(f)$, for different meshes: acoustic grid \mathcal{T}_a^1 , fluid grid \mathcal{T}_f^1 and their intersection $\mathcal{T}_a^1 \cap \mathcal{T}_f^1$. Here, $\Omega = (-2, 2) \times (-2, 2) \times (-0.05, 0.05)$.

mesh	$E_{rel}(1)$	$E_{rel}(x^2y^2z^2)$	$E_{rel}(x^4y^4z^4)$
\mathcal{T}_a^2	0	0	4.441×10^{-16}
\mathcal{T}_f^2	4.441×10^{-16}	2.22×10^{-16}	1.11×10^{-15}
$\mathcal{T}_a^2 \cap \mathcal{T}_f^2$	0	0	0

Table 3.2: Computed error $E_{rel}(f)$ for different meshes: acoustic grid \mathcal{T}_a^2 , fluid grid \mathcal{T}_f^2 and their intersection $\mathcal{T}_a^2 \cap \mathcal{T}_f^2$. Here, $\Omega = (-0.5, 0.5)^3$.

the fluid grid has 109 elements and $h_f = 0.5$. In the second test, we consider $\Omega = \Omega_f = \Omega_a = (-0.5, 0.5)^3$ and use a Cartesian grid \mathcal{T}_a^2 with 64 elements and $h_a = 0.25$ in Ω_a , while a Voronoi polyhedral grid \mathcal{T}_f^2 with 1000 elements and $h_f = 0.1$ in Ω_f , see Figure 2.12. The computed intersections are shown in Figures 2.11 and 2.12. To have a quality check of the performed algorithm we color the resulting grid $\mathcal{T}_a^1 \cap \mathcal{T}_f^1$ in the following way. All the intersections between elements in \mathcal{T}_f^1 and a single element in \mathcal{T}_a^1 have the same color. It is possible to notice that even small elements are intersected properly by the proposed intersection algorithm, cf. Figures 2.11 and 2.12. To show the accuracy of the proposed intersection algorithm, we consider the following verification test that computes the integral of polynomial functions over the intersection grid $\mathcal{T}_a \cap \mathcal{T}_f$. In Tables 2.1 and 2.2 we report the relative errors

$$E_{rel}(f) = \frac{\left| \left(\int_{\Omega} f d\mathbf{x} - \int_{\mathcal{T}} f d\mathbf{x} \right) \right|}{\left| \left(\int_{\Omega} f d\mathbf{x} \right) \right|},$$

computed by employing the quadrature free method [11], described in Section 2.10.1, by varying the mesh size of the domain Ω . Here, f is a generic monomial function. Since the quadrature-free algorithm is exact for homogeneous functions, from these results it is possible to conclude that the intersection algorithm does not introduce any additional error.

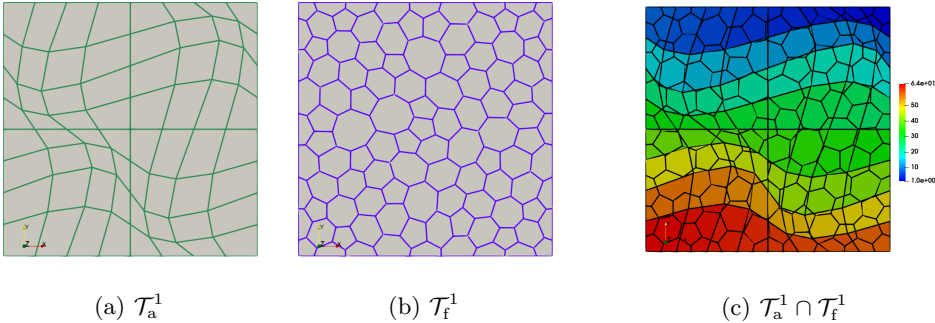


Figure 3.6: (a) Distorted acoustic grid \mathcal{T}_a^1 . (b) Generic polyhedral fluid grid \mathcal{T}_f^1 . (c) Two-dimensional view of the computed intersections between \mathcal{T}_a^1 and \mathcal{T}_f^1 . The considered computational grids are first generated in two dimensions and then extruded in the third dimension, with only one element in the vertical direction. All the intersections between elements in \mathcal{T}_f^1 and a single element in \mathcal{T}_a^1 have the same colour.

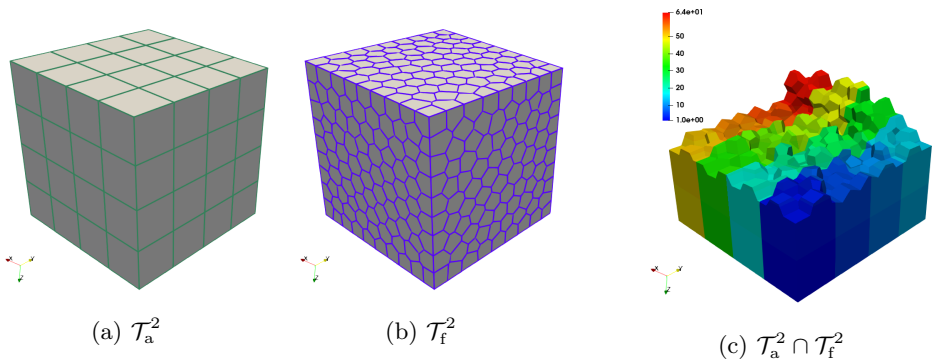


Figure 3.7: (a) Cartesian acoustic grid \mathcal{T}_a^2 . (b) Voronoi fluid grid \mathcal{T}_f^2 . (c) Intersection between \mathcal{T}_a^2 and \mathcal{T}_f^2 . The fluid grid is made of polyhedral elements, while the acoustic grid is made of hexahedral elements. All the intersections between elements in \mathcal{T}_f^2 and a single element in \mathcal{T}_a^2 have the same color.

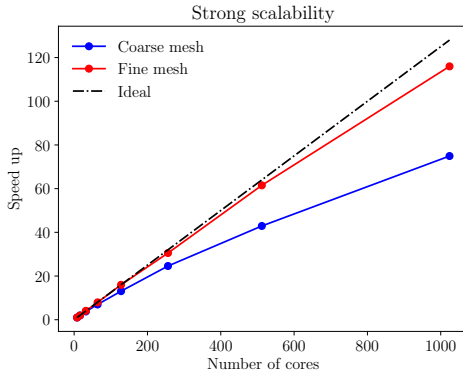


Figure 3.8: Scalability test. The speed-up is computed with respect to the test performed on 8 cores. The coarse mesh has 884736 intersections, while the fine mesh has 7077888 intersections.

3.5.3 Scalability of the Intergrid Intersection Algorithm

To assess the scalability of the algorithm we consider $\Omega = \Omega_f = \Omega_a = (-0.5, 0.5)^3$. We tessellate the domain Ω_a (resp. Ω_f) with a grid made by 32^3 (resp. 65^3) elements. The total number of computed intersections is 884736, with $\sum_{K_a \in \mathcal{T}_a} \text{card}(\mathcal{C}_a) = 39304$ and $\sum_{K_a \in \mathcal{T}_a} \text{card}(\mathcal{I}_a) = 845432$, see Section 2.9.1, that is where most of the computational time is spent by the algorithm concerns the evaluation of actual intersections, i.e., lines 17-19 of Algorithm 2.

We perform a strong scalability test on the G100 cluster located at Cineca, by keeping the same computational grids while varying the number of available cores. From Figure 2.13 it is possible to notice that the algorithm scales well up to 128 cores. Then, since the partitioning of the acoustic mesh is independent of the underlying fluid grid, the number of intersecting elements for larger decompositions might vary largely between the processors, leading to unbalance in the intersection computations. To verify this, we design a larger test where an acoustic Cartesian grid with 64^3 elements and a fluid grid with 65^3 elements are considered. The total number of computed intersections is $\sum_{K_a \in \mathcal{T}_a} \text{card}(\mathcal{I}_a) = 7077888$. On this latter test, where more elements are employed, the balance of the intersection is good and the scalability is almost ideal.

3.6 Implementation Remarks

Hybrid methods like the one introduced in Section 2.4.3 solve first the flow problem, then compute a post-process on the flow solution and then solve an acoustic problem. The acoustic sound source is computed from the flow problem and then it is stored. Next, it needs to be read by the acoustic solver. The reading phase might be a strong bottleneck of the computational method, if not handled carefully. In this section we discuss some of the strategies we employed to optimize the overall computational cost. First, we consider a new weighting for the acoustic decomposition. This is crucial when assembling large problems with heterogeneous degrees of freedom. Then, we discuss our original strategy to read large amount of data, with the idea of providing a scalable strategy.

3.6.1 A Quadrature-Free Method for Integral Evaluation

We now explain how to compute numerically the integrals defined on the right-hand side of (2.98). In the aeroacoustic solver this technique is used for computing the right-hand side of (2.85). We remark that if in V_a we consider only linear polynomials in each space direction, i.e., $r = 1$, and if the maps $\boldsymbol{\theta}_{K_a}$ are linear for any $K_a \in \mathcal{T}_a$, then it is convenient to use a mid-point quadrature method. In this case, (2.99) becomes

$$\sum_{K_a \in \mathcal{T}_a} (q_a, \phi_{a,i})_{K_a} = \sum_{K_a \in \mathcal{T}_a} \sum_{\ell=1}^{N_f} \widehat{q}_{f,\ell}(1, \phi_{a,i})_{K_a \cap K_{f,\ell}} = \\ \sum_{K_a \in \mathcal{T}_a} \sum_{\ell=1}^{N_f} \widehat{q}_{f,\ell} \phi_{a,i}(\mathbf{x}_b) |K_a \cap K_{f,\ell}|, \quad (3.29)$$

where \mathbf{x}_b is the barycentre of the intersection element $K_a \cap K_{f,\ell}$, and $|K_a \cap K_{f,\ell}|$ is the volume of the intersection. The cut-volume cell-based interpolation that was proposed in [128] can be interpreted exactly as this mid point quadrature projection method. In fact in the latter work, the projection is evaluated by computing the intersections between a tetrahedral acoustic grid and a tetrahedral fluid grid and then using a mid-point quadrature rule on the intersected elements. However, when considering higher-order polynomials, i.e., $r > 1$ in V_a , or generic trilinear maps, leads to inexact quadrature integration that deteriorates the quality of the projection. For this reason, we look for

a quadrature formula that is able to integrate high-order polynomials on generic polyhedral elements (intersection of fluid and acoustic elements). When integrating polynomials over a polyhedral domain, one of the most popular choices is to sub-tessellate the polyhedral domain and then apply therein a standard quadrature formula over the tetrahedral mesh. This is in general computationally expensive. For that reason we employ the integration method described in [36], that has already been successfully applied in the context of discontinuous Galerkin methods, see for instance [11]. The employed quadrature formula is able to integrate exactly homogeneous functions over general polyhedra K . We report here for completeness the main feature of the quadrature method, and refer to [11] for further details. Let the polyhedron $K \subset \mathbb{R}^3$ be a closed polytope, whose boundary ∂K is defined by m faces $F_i \in \mathbb{R}^2$, with $i = 1, \dots, m$. To each face F_i we associate a normal vector \mathbf{n}_i . Also, each face F_i lies on a hyperplane \mathcal{H}_i , and hence to each face F_i we associate a scalar b_i such that $\forall \mathbf{x} \in \mathcal{H}_i$ we have that $\mathbf{n}_i \cdot \mathbf{x} = b_i$. Moreover, we split the polyhedron boundary as the union of m faces, i.e., $\partial K = \bigcup_i^m F_i$, and the boundary of each face F_i as the union of m_i edges, i.e., $\partial F_i = \bigcup_j^{m_i} F_{ij}$. Finally, the m_{ij} vertices of each edge F_{ij} are denoted by $\partial F_{ij} = \bigcup_k^{m_{ij}} F_{ijk}$. Let g to be homogeneous of degree $q > 0$, namely,

$$qg(\mathbf{x}) = \nabla g(\mathbf{x}) \cdot \mathbf{x} \quad \forall \mathbf{x} \in \mathcal{K}, \quad (3.30)$$

and recall the generalized Stokes' theorem, see [143]:

$$\int_K (\nabla \cdot \mathbf{V}(\mathbf{x}))g(\mathbf{x})d\mathbf{x} + \int_K \nabla g(\mathbf{x}) \cdot \mathbf{V}(\mathbf{x})d\mathbf{x} = \int_{\partial K} \mathbf{V}(\mathbf{x}) \cdot \mathbf{n}g(\mathbf{x})d\sigma,$$

where $\mathbf{V} : K \rightarrow \mathbb{R}^3$ is a generic vector field. By selecting $\mathbf{V}(\mathbf{x}) = \mathbf{x}$, and by applying (2.104) we have

$$\int_K g(\mathbf{x})d\mathbf{x} = \frac{1}{3+q} \int_{\partial K} \mathbf{x} \cdot \mathbf{n}g(\mathbf{x})d\sigma = \frac{1}{3+q} \sum_{i=1}^m b_i \int_{F_i} g(\mathbf{x})d\sigma. \quad (3.31)$$

Next, by applying recursively integration by parts on (2.105), we obtain the following quadrature formula for computing the integral of a

homogeneous function over a polyhedron K :

$$\begin{aligned} \int_K g(\mathbf{x}) d\mathbf{x} &= \frac{1}{q+3} \sum_{i=1}^m \frac{b_i}{2+q} \left(\sum_{j=1}^{m_i} d_{ij} \int_{F_{ij}} g(\mathbf{x}) d\nu + \int_{F_i} \mathbf{x}_{0,i} \cdot \nabla g(\mathbf{x}) d\sigma \right), \\ \int_{F_{ij}} g(\mathbf{x}) d\nu &= \frac{1}{1+q} \left(\sum_{k=1}^{m_{ij}} d_{ijk} \int_{F_{ijk}} g(\mathbf{x}) d\xi + \int_{F_{ij}} \mathbf{x}_{0,ij} \cdot \nabla g(\mathbf{x}) d\nu \right), \end{aligned} \quad (3.32)$$

where d_{ij} is the Euclidean distance between the arbitrary point $\mathbf{x}_{0,i}$ and the edge F_{ij} and d_{ijk} is the Euclidean distance between the arbitrary point $\mathbf{x}_{0,ij} \in F_{ij}$ and the vertex F_{ijk} . We now apply the quadrature free rule described by Equation (2.106) to (2.98). Each polynomial can be seen as sum of monomials, that are homogeneous function in the sense of eq. (2.104). Moreover, since we are employing spectral element methods, we usually integrate over a family of monomials. To speed up the whole algorithm, the integrated monomials over K are stored and reused upon need. For further details on the implementation, we refer to Algorithm 2 in [11].

3.6.2 Source Time Storage

The acoustic source coming from the flow solver is stored by employing the OpenFOAM's function object `ensightWrite`. This function object stores the data employing the `Ensight` file format, see [49]. The data is stored element wise and the grid information saved is only the fluid element connectivity and its coordinates. A good feature of this OpenFOAM's function object is that it allows to consider a limited region when saving the data. This is very useful, since often we do not need the whole flow domain Ω_f , or sometimes we might want to isolate some noise generation mechanisms. A relevant downside, however, is that we do not store the connectivity of the computational grid of the flow. This means that if we want to employ a higher order reconstruction of the flow data we need to recompute the connectivity, that might be very costly.

3.6.3 Parallel Decomposition

In this section, we briefly discuss the decomposition strategy adopted on the acoustic space. The acoustic mesh is first read and then decomposed employing Metis [81]. Based on the connectivity of the mesh, Metis constructs the associated graph. Then, it decomposes

the computational grid in n processors with the objective of minimizing the communication. With the outlook of employing the DGSEM discretization strategy and hence spaces with different polynomial degree or mesh size, we further assign a weight $w = r^3$ on each element of the graph that depends on the polynomial degree r . This allows Metis to give a more balanced decomposition with respect to the degrees of freedom, speeding up the assembly phase, see Figure 2.14. Next, the linear Algebra backhand used in AeroSPEED is PETSc [21]. PETSc is a suite of data structures and routines that provides tools for the implementation of large-scale application codes on parallel computers. During the assembly phase, we rely on the Metis decomposition in order to call the wrappers to build the algebraic blocks for PETSc. Next, at the algebraic level each core employs the PETSc decomposition, see Figure 2.15. It is convenient to have Metis as a first partitioner in order to have an initial parallelization of the code. Then, it is convenient to employ PETSc to exploit its internal routines that are able to handle sparse matrices and complex solvers.

3.6.4 Source Time File Reading

The final implementation remark is related to the I/O, which is a critical aspect in the hybrid aeroacoustic strategy. We need to read the noise sound source coming from the flow problem in an efficient way. We assume that the flow solution is stored as described for instance in Section 2.10.2 and that literally the acoustic solver can be run in a second moment, after the entire flow run has been performed. One of the possible strategies to efficiently read the flow datum is to enforce a decomposition on the flow solution and to read the decomposed data. However, this strategy requires the further post process of the stored flow datum, increasing the computational time. Furthermore, it requires to define a map between the flow decomposition and the acoustic decomposition. This map can be known and employed after the intersection method, however the whole strategy still remains cumbersome.

As an alternative, we propose the following strategy, see Figure 2.16. Suppose that we have to read N time steps, and we have n cores. Also, assume that the source term has been stored at the time t_1, t_2, \dots, t_N and denote it with $b(t_1), b(t_2), \dots, b(t_N)$. At the first time step t_1 , each core c_i , with $i = 1, \dots, n$, reads the acoustic source datum $b(t)$ coming from the flow solution, in the following manner. We make core i read

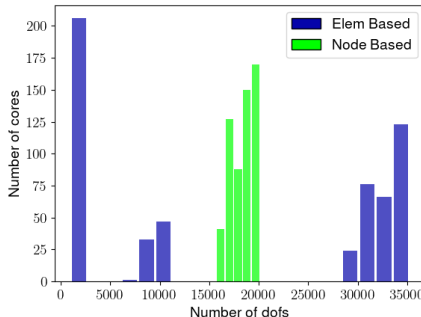


Figure 3.9: Decomposition of a computational grid employing DGSEM. The domain Ω_1 has $r = 1$ and 225000 elements, Ω_2 has $r = 2$ and 90000 elements, and the remaining Ω_3 has $r = 3$ and 300000 elements. We decompose the whole domain employing 512 cores. We notice that introducing the weighting improves the decomposition.

the time step $b(t_i)$ with $i = 1, \dots, n$. This allows the solver to perform the costly read operation only once every n time steps, increasing the overall performance. At the acoustic time step t_j , with j such that $j \neq kn$, with $k \in \mathbb{N}_0$ the core j communicates each chunk of the flow solution to the respective cores for the online computations. The cost of communications are limited since we need only to communicate contiguous chunks of the source data. We believe that the greatest drawback of this method is the memory limitations, since storing n flow data can be very expensive. However, we found out that we were able to read at least 24 million of vector valued data, which is more than enough for our current applications.

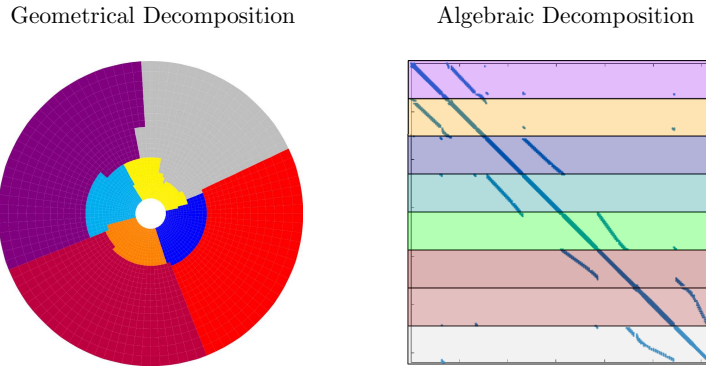


Figure 3.10: Geometrical decomposition and algebraic decomposition employing 8 cores. During the assembly phase the PETSc wrapper is called assembling the matrices with the new algebraic decomposition.

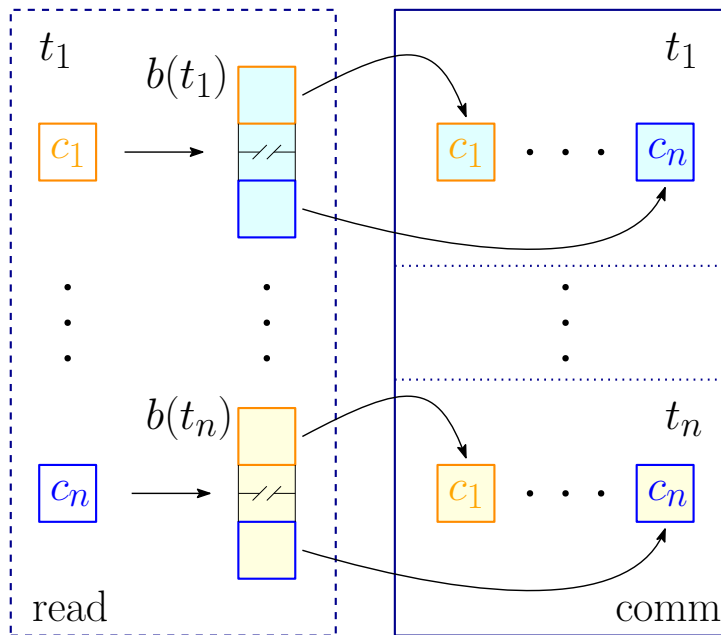


Figure 3.11: The scheme represents the reading strategy of the vectors b for the times t_1, \dots, t_n with n cores c_1, \dots, c_n . At time t_1 , each core c_i reads the source $b(t_i)$. Hence, the source $b(t_i)$ is known only by the core c_i . At the time t_j the core c_j communicates each piece of the vector $b(t_j)$ to all the respective core, using the decomposition required by the algebraic solver.

Chapter 4

Theoretical Analysis

In this chapter, we present the theoretical analysis of the Spectral Element Method for the segregated problem. First, we analyse the SEM fully discrete acoustic wave equation. Next, we propose an a priori estimate for the error of the intergrid projection method presented in Section 2.8. The obtained estimate is then verified through numerical tests. Afterwards, we consider an acoustic wave equation problem where the right hand-side term is obtained by post-processing of the solution to the flow problem and projecting it onto the acoustic finite dimensional space. We propose an a priori estimates and we verify the obtained theoretical result. The obtained result allows to understand the effect of the intergrid projection method on the numerical error of the discretization of the Lighthill's wave equation.

4.1 Preliminaries

Given a domain Ω and its discretization \mathcal{T}_h , we denote with $\|\cdot\|_{\mathcal{T}_h}$ the broken norm associated to the space $H^s(\mathcal{T}_h)$, namely:

$$\|v\|_{H^s(\mathcal{T}_h)}^2 = \sum_{K \in \mathcal{T}_h} \|v\|_K^2. \quad (4.1)$$

Next, we introduce the following definition.

Definition 4.1.1 *The space of continuous functions $C^m(0, T; H^s(\Omega))$ is the space of all functions $v(\mathbf{x}, t) \in H^s(\Omega)$ such that $v^{(\ell)}$ is continuous for every $0 \leq l \leq m$ and such that the norm:*

$$\|v\|_{C^m(0, T; H^s(\Omega))} = \max_{0 \leq \ell \leq m} (\sup_{0 \leq t \leq T} \|v^{(\ell)}\|_{H^s(\Omega)}),$$

is bounded.

The next lemma and its corollary show the equivalence between the discrete norm introduced in equation (2.79) and the continuous L^2 norm and the broken norm $\|\cdot\|_{\mathcal{T}_h}$.

Lemma 4.1.2 ([34], Lemma 3.2) *Let V_a be the space introduced in eq. (2.77). The L^2 norm $\|\cdot\|_{L^2(\Omega)}$ and the discrete norm $\|\cdot\|_h$ introduced in equation (2.79) are equivalent in V_a , i.e. there exists a constant $C > 0$ such that:*

$$\|v_h\|_{L^2(\Omega)} \leq \|v_h\|_h \leq C \|v_h\|_{L^2(\Omega)} \quad \forall v_h \in V_a.$$

Corollary 4.1.3 *The norm (3.1) and the norm (2.79) are equivalent:*

$$\|v_h\|_{\mathcal{T}_h} \leq \|v_h\|_h \lesssim \|v_h\|_{\mathcal{T}_h} \quad \forall v_h \in V_a.$$

We now introduce the Lagrangian interpolant on the Gauss-Legendre-Lobatto (GLL) nodes.

Definition 4.1.4 (*Local interpolation operator*) *For a positive integer r , the GLL interpolation operator $I_{h,r}^{\text{GLL},K} : C(K) \rightarrow \mathbb{Q}^r(K)$ is defined in such a way that, for $v \in C(K)$:*

$$I_{h,r}^{\text{GLL},K} v(\boldsymbol{\theta}_K(\boldsymbol{\xi}_{i,j,k})) = v(\boldsymbol{\theta}_K(\boldsymbol{\xi}_{i,j,k})) \quad \forall i, j, k = 0, \dots, r,$$

where $\boldsymbol{\xi}_{i,j,k}$ are the GLL points and $\boldsymbol{\theta}_K$ is the trilinear map from the reference element \hat{K} to the element K .

The global operator $I_{h,r}^{\text{GLL}}$ is obtained by considering:

$$I_{h,r}^{\text{GLL}} v|_K = I_{h,r}^{\text{GLL},K} v(\boldsymbol{\theta}_K(\boldsymbol{\xi}_{i,j,k})) \quad \forall K \in \mathcal{T}_h.$$

In the next lemma we present an a priori error estimate for the Lagrangian interpolant on the GLL nodes.

Lemma 4.1.5 (*Interpolation error on GLL nodes*). *Given $f \in H^s(\Omega)$ for some $s \geq 1$, consider the Lagrangian interpolant $I_{h,r}^{\text{GLL}} f$ at the Gauss-Legendre-Lobatto nodes, where r denotes the polynomial degree of the interpolant function and h_a is the mesh size of \mathcal{T}_h . Assuming h_a to be quasi uniform, we the following bounds:*

$$\|f - I_{h,r}^{\text{GLL}} f\|_{L^2(K)} \lesssim \frac{h_a^{\min(r+1,s)}}{r^s} \|f\|_{H^s(K)},$$

$$\|f - I_{h,r}^{\text{GLL}} f\|_{L^2(\Omega)} \lesssim \frac{h_a^{\min(r+1,s)}}{r^s} \|f\|_{H^s(\Omega)},$$

where the hidden constants depends on the regularity s .

The proof of Lemma 3.1.5 can be found in [22, Theorem (4.2)]. Next, we recall a Lemma on the a priori quadrature error of the GLL quadrature formula.

Lemma 4.1.6 (*Quadrature error for GLL quadrature formula*). *Let $s \geq 2$ and $r \geq 2$. If $v \in H^2(\Omega)$ we have that:*

$$(v, v_h) - (v, v_h)^{\text{NI}} \lesssim \frac{h_a^{\min(r,s)}}{r^s} \|v\|_{H^s(\mathcal{T}_h)} \|v_h\|_{L^2(\Omega)} \quad \forall v_h \in V_a. \quad (4.2)$$

The proof can be found in [6], see Lemma 4.3. Now, we write the hp -inverse trace inequality for polynomials.

Lemma 4.1.7 (*hp-inverse inequality*) *Assume now that $K = \theta_K(\widehat{K})$ is a hexahedral element s.t. $K \subset \mathbb{R}^3$, where θ_K is a trilinear map. Then we have that:*

$$\|\nabla v\|_{L^2(K)} \lesssim \frac{r^2}{h_K} \|v\|_{L^2(K)} \quad \forall v \circ \theta_K^{-1} \in Q_r(\widehat{K}),$$

where h_K is $\text{diam}(K)$.

The proof can be obtained via standard tensor product argument combining the mono-dimensional result in [129, Theorem 3.9.1].

As an immediate consequence of that, we can prove the following corollary:

Corollary 4.1.8 ([110], Lemma 3.6) *Assume \mathcal{T}_h to be quasi-uniform. Then, given the bilinear form $a_h(\cdot, \cdot)$ introduced in (2.80), we have that:*

$$a_h(v_h, v_h) \leq C_a \frac{h_a^2}{r^4} \|v_h\|_h^2 \quad \forall v_h \in V_a,$$

where C_a is a positive constant.

Next, we introduce the following discrete elliptic operator that is employed in the fully discrete analysis.

Definition 4.1.9 (*Discrete elliptic projection operator*) *We define the elliptic projection operator $\Pi_h^{\mathcal{E}} : V \rightarrow V_a$ solution to the following problem:*

$$a_h(\Pi_h^{\mathcal{E}}(v), v_h) = a(v, v_h) \quad \forall v_h \in V_a.$$

In the upcoming Lemma, we give the a priori estimate for the elliptic projection operator previously defined.

Lemma 4.1.10 (*Approximation error for the discrete elliptic projection operator*) Given $v \in H^s(\mathcal{T}_h) \cap H^1(\Omega)$ with $s \geq 2$ and that $r \geq 2$. Then the following bounds hold:

$$\|v - \Pi_h^\mathcal{E} v\|_{H^1(\Omega)} \lesssim \frac{h_a^{\min(r,s)-1}}{r^{s-1}} \|v\|_{H^s(\mathcal{T}_h)},$$

$$\|v - \Pi_h^\mathcal{E} v\|_{L^2(\Omega)} \lesssim \frac{h_a^{\min(r,s)}}{r^s} \|v\|_{H^s(\mathcal{T}_h)}.$$

The proof can be found in Lemma 4.5 and Corollary 4.6 of [6].

Lemma 4.1.11 (*h -optimal approximation error for the discrete elliptic projection operator*) Given $v \in H^s(\mathcal{T}_h) \cap H^1(\Omega)$ with $s \geq 3$ and that there exists a constant C_r that depends on the polynomial degree r , such that:

$$\|v - \Pi_h^\mathcal{E} v\|_{H^1(\Omega)} \lesssim C_r h_a^{\min(r,s-1)} \|v\|_{H^s(\mathcal{T}_h)}.$$

Proof. We sketch the proof, that follows the lines of [6]. First, we employ a triangular inequality:

$$\|v - \Pi_h^\mathcal{E} v\|_{H^1(\Omega)} \leq \|v - v_h\|_{H^1(\Omega)} + \|\Pi_h^\mathcal{E} v - v_h\|_{H^1(\Omega)}.$$

Next, we denote with $w_h = \Pi_h^\mathcal{E} v - v_h$. From the coercivity of the bilinear form a_h we have that:

$$\begin{aligned} \|\Pi_h^\mathcal{E} v - v_h\|_{H^1(\Omega)}^2 &\lesssim a_h(\Pi_h^\mathcal{E} v - v_h, w_h) \\ &= a(v, w_h) - a_h(v_h, w_h) \\ &= a(v, w_h) - a(v_h, w_h) + a(v_h, w_h) - a_h(v_h, w_h) \\ &= a(v - v_h, w_h) + a(v_h, w_h) - a_h(v_h, w_h) \\ &\lesssim \|v - v_h\|_{H^1(\Omega)} \|w_h\|_{H^1(\Omega)} + [a(v_h, w_h) - a_h(v_h, w_h)], \end{aligned}$$

that yields to

$$\|\Pi_h^\mathcal{E} v - v_h\|_{H^1(\Omega)} \lesssim \|v - v_h\|_{H^1(\Omega)} + \sup_{z_h \in V_a} \frac{a(v_h, z_h) - a_h(v_h, z_h)}{\|z_h\|_{H^1(\Omega)}}.$$

Now, we can obtain the inequality in Lemma 3.1.10 by choosing $v_h = I_{h,r-1}^{\text{GLL}} v$, but the result is suboptimal with respect to h_a . We consider

that, since $z_h \in V_a$:

$$\begin{aligned} a(v_h, z_h) - a_h(v_h, z_h) &= (\nabla v_h, \nabla z_h) - (\nabla v_h, \nabla z_h)^{\text{NI}} \\ &\lesssim \frac{h_a^{\min(r,s)}}{r^s} \|\nabla v_h\|_{H^{q+1}(\mathcal{T}_h)} \|\nabla z_h\|_{L^2(\Omega)} \\ &\lesssim \frac{h_a^{\min(r,s)}}{r^s} \|v_h\|_{H^s(\mathcal{T}_h)} \|z_h\|_{H^1(\Omega)}. \end{aligned}$$

where we applied the quadrature error estimate in Lemma 3.1.6. Now, by taking $v_h = I_{h,r}^{\text{GLL}}v$, we obtain:

$$a(I_{h,r}^{\text{GLL}}v, z_h) - a_h(I_{h,r}^{\text{GLL}}v, z_h) \lesssim \frac{h_a^{\min(r,s)}}{r^s} \|I_{h,r}^{\text{GLL}}v\|_{H^s(\mathcal{T}_h)} \|z_h\|_{H^1(\Omega)}.$$

Now, from Section 4.4 of [26] we have that:

$$\|I_{h,r}^{\text{GLL}}v\|_{H^s(\mathcal{T}_h)} \lesssim C_r \|v\|_{H^s(\mathcal{T}_h)} \quad \forall v \in H^s(\mathcal{T}_h) \cap H^1(\Omega).$$

Finally, we have that:

$$\|v - \Pi_h^\mathcal{E}v\|_{H^1(\Omega)} \leq C_r (\|v - I_{h,r}^{\text{GLL}}v\|_{H^1(\Omega)} + h_a^{\min(r,q-1)} \|v\|_{H^q(\mathcal{T}_h)}).$$

Employing the interpolation estimate in Lemma 3.1.5 we obtain the thesis:

$$\|v - \Pi_h^\mathcal{E}v\|_{H^1(\Omega)} \lesssim C_r h_a^{\min(r,s-1)} \|v\|_{H^s(\mathcal{T}_h)}.$$

Finally, we conclude this section by recalling an useful result on Poincaré–Friedrich inequality:

Lemma 4.1.12 *Given $v \in H^1(K)$, where K is an open bounded convex domain in \mathbb{R}^d and $v \in L_0^2(K) = \left\{ u \in L^2(K) : \int_K u = 0 \, d\mathbf{x} \right\}$ then we have that:*

$$\|v\|_{L^2(K)} \lesssim \frac{\text{diam}(K)^{1+d/2}}{|K|^{1/2}} \|\nabla v\|_{L^2(K)}.$$

We refer the reader to [156, Corollary 3.4] and to [8, Remark 5.8] for further details on the proof.

4.2 A Priori Error Estimate

We recall the main theorems on the a priori error bounds for the wave equation approximated with the Spectral Element Method. The results

are taken from [6], where the authors employed the results of [64], [110] and [155]. Extensive research have been dedicated to provide the optimal error bound, as indicated in [6]. Only recently, optimal error bounds have been obtained in the h -version, while the theory in hp is still incomplete. We start by writing the acoustic problem that we employ for the analysis, see Section 2.6.1. For brevity, we denote the inner product defined in eq. (2.78) as $(\cdot, \cdot)^{\text{NI}} = (\cdot, \cdot)_{\mathcal{T}_a}^{\text{NI}}$. Given $\Delta t > 0$, we divide the time domain $[0, T]$ into N uniform intervals of size Δt . We want to find $\rho_h \in V_a$, for $n = 1, \dots, N$ such that $\forall w_h \in V_a$:

$$\begin{aligned} \left(\frac{\rho_h^{n+1} - 2\rho_h^n + \rho_h^{n-1}}{\Delta t^2}, w_h \right)^{\text{NI}} + a_h(\rho_h^n, v_h) &= (f, w_h)^{\text{NI}}, \\ (\rho_h^0, w_h)^{\text{NI}} &= (\rho_0, w_h)^{\text{NI}}, \\ (g_h^0, w_h)^{\text{NI}} &= (\rho_1, w_h)^{\text{NI}}, \\ \frac{2}{\Delta t} (\rho_h^1 - \rho_h^0 - \Delta t g_h^0, v_h)^{\text{NI}} + a_h(\rho_h^0, v_h) &= (f, w_h)^{\text{NI}}, \end{aligned} \quad (4.3a)$$

where we employed the Leap-Frog scheme for the time discretization.

Theorem 4.2.1 (*hp version*) *Let us assume that the following stability condition holds:*

$$\Delta t < \frac{2h_a}{r^2} \frac{1}{\sqrt{C_a}},$$

where C_a is the continuity constant in Corollary 3.1.8. Given ρ_h^n solution to the problem (3.3), $\rho \in (0, T; H^\ell(\Omega) \cap H^1(\Omega))$ solution to the problem 2.6.1 and $f \in (0, T; H^s(\Omega) \cap H^1(\Omega))$, where if Ω is regular enough we can set $\ell = s + 2$, we have that the following hp -error estimate holds:

$$\begin{aligned} \max_{0 \leq n \leq N-1} \|\rho(t_n) - \rho_h^n\|_{H^1(\Omega)} &\lesssim \left[\frac{h_a^{\min(r, \ell)-1}}{r^{\ell-1}} \|\rho\|_{C^0(0, T; H^\ell(\Omega))} \right. \\ &\quad + \frac{h_a^{\min(r, s)}}{r^s} \|f\|_{C^0(0, T; H^s(\Omega))} \\ &\quad + \frac{h_a^{\min(r, \ell)}}{r^{\ell-1}} \|\rho\|_{C^2(0, T; H^\ell(\mathcal{T}_h))} \\ &\quad \left. + \Delta t^2 \|\rho\|_{C^4(0, T; L^2(\Omega))} \right]. \end{aligned}$$

The proof can be found in [6, Theorem 5.5].

Theorem 4.2.2 (*h* version) Under the same hypothesis of Theorem 3.2.1, we have that the following *h*-error estimate holds:

$$\begin{aligned} \max_{0 \leq n \leq N-1} \|\rho(t_n) - \rho_h^n\|_{H^1(\Omega)} &\leq C_r \left[h_a^{\min(r,\ell-1)} \|\rho\|_{C^0(0,T;H^\ell(\Omega))} \right. \\ &\quad + h_a^{\min(r,s)} \|f\|_{C^0(0,T;H^s(\Omega))} \\ &\quad + h_a^{\min(r,\ell)} \|\rho\|_{C^0(0,T;H^\ell(\Omega))} \\ &\quad \left. + \Delta t^2 \|\rho\|_{C^4(0,T;L^2(\Omega))} \right], \end{aligned}$$

where C_r is a constant that depends on the polynomial degree r introduced in Lemma 3.1.11.

The proof can be found in [6, Theorem 5.6].

4.3 Approximation Properties of the Intergrid Projection Operator

In this section, we show the approximation properties of the intergrid projection operator introduced in Section 2.8. We first consider the case of piecewise constant flow source. This choice mimics the fact that the FV solution can be seen as a function defined onto a space of piecewise constant functions. Next, we address the case where the flow solution has been element-wise reconstructed with a high order polynomial function.

4.3.1 Piecewise Constant Flow Source Term

In the next section, for the sake of presentation, we consider the following setup: let $\Omega = \Omega_f = \Omega_a$ be a polygonal domain and let \mathcal{T}_f and \mathcal{T}_a be two nested grids of Ω as shown in Figure 3.1, namely for all elements $K_a \in \mathcal{T}_a$ we assume that there exists a set of index \mathcal{L}_{K_a} such that $K_a = \bigcup_{\ell \in \mathcal{L}_{K_a}} K_{f,\ell}$. Since we are explicitly computing the intersections

for the intergrid projection method, requiring that the grids are nested naturally follows after the application intersection algorithm. We now introduce the following projection operators: $\Pi_{0,h_f} : L^2(\Omega) \rightarrow V_f$ and $\Pi_{r,h_a} : L^2(\Omega) \rightarrow V_a$, and we define the following functions:

$$f_f = \Pi_{0,h_f} f,$$

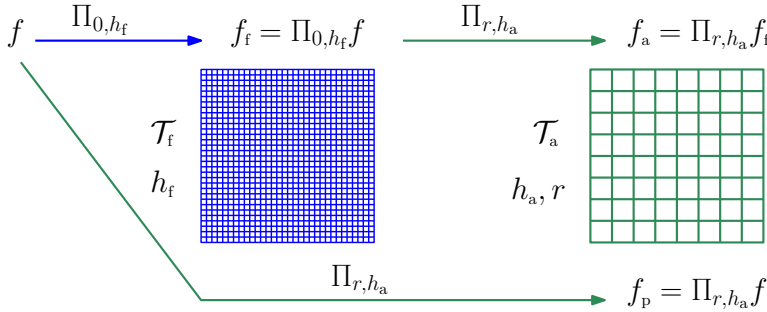


Figure 4.1: Schematic representation of the computational grids and the corresponding projection operators. For a given function $f \in L^2(\Omega)$, f_f is the projection $\Pi_{0,h_f}f$, f_a is the projection $\Pi_{r,h_a}f_f$ and f_p is the projection $\Pi_{r,h_a}f_f$. The computational grids \mathcal{T}_a and \mathcal{T}_f are assumed to be nested.

that is the L^2 projection of $f \in L^2(\Omega)$ onto the space V_f ,

$$f_p = \Pi_{r,h_a}f,$$

that is the L^2 projection of $f \in L^2(\Omega)$ onto the space V_a ,

$$f_a = \Pi_{r,h_a}f_f, \quad (4.4)$$

that is the L^2 projection of $f_f \in V_f$ onto the space V_a , see Figure 3.1.

Now, we can state the following result.

Theorem 4.3.1 (Approximation Theorem). *Let \mathcal{T}_a and \mathcal{T}_f be two grids of the same computational domain $\Omega_f = \Omega_a = \Omega$ such that \mathcal{T}_f is nested to \mathcal{T}_a , namely, for every element K_f there exists K_a such that $K_f \subset K_a$. Given $f \in H^s(\Omega)$ with $s \geq 1$, let $f_f = \Pi_{0,h_f}f$ be the projection of f onto the space V_f and let $f_a = \Pi_{r,h_a}f_f$, namely the projection of f_f onto the space V_a . Then, it holds:*

$$\|f - f_a\|_{L^2(\Omega)} \lesssim \frac{h_a^{\min(r+1,s)}}{r^s} \|f\|_{H^s(\Omega)} + \frac{h_f^2}{h_a} r^2 \|f\|_{H^s(\Omega)}. \quad (4.5)$$

Proof. Let $f_p = \Pi_{r,h_a}f$, cf. Figure 3.1. By triangular inequality we have that

$$\|f - f_a\|_{L^2(\Omega)} \leq \|f - f_p\|_{L^2(\Omega)} + \|f_p - f_a\|_{L^2(\Omega)}.$$

The first term on the right hand side can be estimated by employing Lemma 3.1.5, i.e.:

$$\begin{aligned} \|f - f_p\|_{L^2(\Omega)} &= \min_{\varphi \in V_a} \|f - \varphi\|_{L^2(\Omega)} \lesssim \|f - I_a^{\text{GLL}}f\|_{L^2(\Omega)} \\ &\lesssim \frac{h_a^{\min(r+1,s)}}{r^s} \|f\|_{H^s(\Omega)}. \end{aligned} \quad (4.6)$$

Next, we observe that by definition of the L^2 -projection we get

$$(f_a, \phi)_{L^2(\Omega)} = (f_f, \phi)_{L^2(\Omega)} \quad \forall \phi \in V_a, \quad (4.7)$$

$$(f_p, \phi)_{L^2(\Omega)} = (f, \phi)_{L^2(\Omega)} \quad \forall \phi \in V_a. \quad (4.8)$$

Then, by subtracting (3.7) to (3.8), we obtain

$$(f_p - f_a, \phi)_{L^2(\Omega)} = (f - f_f, \phi)_{L^2(\Omega)} \quad \forall \phi \in V_a. \quad (4.9)$$

Furthermore, since $f_p - f_a \in V_a$, we can write

$$\begin{aligned} \|f_p - f_a\|_{L^2(\Omega)}^2 &= \int_{\Omega} (f - f_f)(f_p - f_a) \, d\mathbf{x} \\ &= \sum_{K_f \in \mathcal{T}_f} \int_{K_f} (f - f_f)(f_p - f_a) \, d\mathbf{x}, \end{aligned}$$

and notice that

$$(f - f_f, \varphi)_{L^2(K_f)} = 0 \quad \forall \varphi \in \mathbb{P}^0(K_f),$$

where $\mathbb{P}^0(K_f)$ is the space of the constant functions over K_f . By taking $\varphi = \Pi_{0,h_f}(f_p - f_a)$ in the above equation yields to

$$\begin{aligned} \sum_{K_f \in \mathcal{T}_f} \int_{K_f} (f - f_f)(f_p - f_a) \, d\mathbf{x} \\ &= \sum_{K_f \in \mathcal{T}_f} \int_{K_f} (f - f_f)(f_p - f_a - \Pi_{0,h_f}(f_p - f_a)) \, d\mathbf{x} \\ &\lesssim \sum_{K_f \in \mathcal{T}_f} \|f - f_f\|_{L^2(K_f)} \|f_p - f_a - \Pi_{0,h_f}(f_p - f_a)\|_{L^2(K_f)} \\ &\lesssim h_f^2 \sum_{K_f \in \mathcal{T}_f} \|\nabla f\|_{L^2(K_f)} \|\nabla(f_p - f_a)\|_{L^2(K_f)}, \end{aligned}$$

where in the last step we employ Lemma 3.1.12. By linearity of the integral, noticing that by hypothesis $K_f \subset K_a$ and using that

$\|\nabla f\|_{L^2(K_f)} \leq \|\nabla f\|_{L^2(K_a)}$ we obtain

$$\begin{aligned} & \sum_{K_f \in \mathcal{T}_f} h_f^2 \|\nabla f\|_{L^2(K_f)} \|\nabla(f_p - f_a)\|_{L^2(K_f)} \\ & \lesssim \sum_{K_a \in \mathcal{T}_a} h_f^2 \|\nabla f\|_{L^2(K_a)} \|\nabla(f_p - f_a)\|_{L^2(K_a)} \\ & \lesssim \sum_{K_a \in \mathcal{T}_a} r^2 \frac{h_f^2}{h_a} \|\nabla f\|_{L^2(K_a)} \|f_p - f_a\|_{L^2(K_a)} \\ & \lesssim r^2 \frac{h_f^2}{h_a} \|\nabla f\|_{L^2(\Omega)} \|f_p - f_a\|_{L^2(\Omega)}, \end{aligned}$$

where in the last step we used the inverse inequality of Lemma 3.1.7. Finally, we get

$$\|f_p - f_a\|_{L^2(\Omega)}^2 \lesssim r^2 \frac{h_f^2}{h_a} \|\nabla f\|_{L^2(\Omega)} \|f_p - f_a\|_{L^2(\Omega)},$$

or equivalently

$$\|f_p - f_a\|_{L^2(\Omega)} \lesssim r^2 \frac{h_f^2}{h_a} \|\nabla f\|_{L^2(\Omega)}, \quad (4.10)$$

and, since $\|\nabla f\|_{L^2(\Omega)} \lesssim \|f\|_{H^s(\Omega)}$, that concludes the proof.

4.3.2 High Order Reconstruction of the Flow Source Term

We extend the previous result for the case in which the flow source is reconstructed with a high order piecewise polynomial. To mimic a high order finite volume reconstruct formula we employ a high order local projection. We denote with V_f the following space:

$$V_f = \left\{ v \in L^2(\Omega) : v|_{K_f} \circ \boldsymbol{\theta}_{K_f}^{-1} \in \mathbb{Q}^q \ \forall K_f \in \mathcal{T}_f \right\}.$$

Next, we first consider the local projection operator $\Pi_{q,h_f}^{K_f} : K_f \rightarrow V_f$:

$$(\Pi_{q,h_f}^{K_f} f, v_f)_{K_f} = (f, v_f)_{K_f} \quad \forall v_f \in V_f,$$

and we define the function f_f as:

$$f_f|_{K_f} = \sum_{K_f \in \mathcal{T}_f} \Pi_{q,h_f}^{K_f} f = \Pi_{q,h_f} f. \quad (4.11)$$

The function f_f is a generic piecewise polynomial of order q that mimics a high order reconstruction based on a finite volume solution.

Theorem 4.3.2 (*Approximation theorem for high order reconstruction*). Let \mathcal{T}_a and \mathcal{T}_f be two grids of the same computational domain $\Omega_f = \Omega_a = \Omega$ made by hexahedral elements, such that \mathcal{T}_f is nested to \mathcal{T}_a , namely, for every element K_f there exists K_a such that $K_f \subset K_a$. Given $f \in H^s(\Omega)$ with $s \geq 1$, let $f_f = \Pi_{q,h_f} f$ be defined as in eq. (3.11) and let $f_a = \Pi_{r,h_a} f_f$, namely the projection of f_f onto the space V_a . For a sufficiently regular function f , such that $s > q + 1$, and if we take $r > q + 1$, we write:

$$\|f_p - f_a\|_{L^2(\Omega)} \lesssim \frac{h_f^{2(q+1)}}{h_a^{q+1}} \frac{r^{2(q+1)}}{q^{s+r}} \|f\|_{H^s(\Omega)} \|f_p - f_a\|_{L^2(\Omega)}.$$

Proof. The idea is similar to the previous proof. By denoting with $f_p = \Pi_{r,h_a} f$ we apply the triangular inequality and obtain

$$\|f - f_a\|_{L^2(\Omega)} \leq \|f - f_p\|_{L^2(\Omega)} + \|f_p - f_a\|_{L^2(\Omega)}.$$

The first term on the right hand side can be estimated by employing eq. (3.6), i.e.:

$$\|f - f_p\|_{L^2(\Omega)} \lesssim \frac{h_a^{\min(r+1,s)}}{r^s} \|f\|_{H^s(\Omega)}.$$

Notice that a similar results in particular holds for $\Pi_{q,h_f}^{K_f} f$:

$$\|f - \Pi_{q,h_f}^{K_f} f\|_{L^2(K_f)} \lesssim \frac{h_f^{\min(q+1,s)}}{r^s} \|f\|_{H^s(K_f)}. \quad (4.12)$$

Next, by considering the identity in eq. (3.9) and by taking as test function $\phi = f_p - f_a$, we write:

$$\begin{aligned} \|f_p - f_a\|_{L^2(\Omega)}^2 &= \int_{\Omega} (f - f_f)(f_p - f_a) \, d\mathbf{x} \\ &= \sum_{K_f \in \mathcal{T}_f} \int_{K_f} (f - f_f)(f_p - f_a) \, d\mathbf{x}, \end{aligned}$$

and notice that

$$(f - f_f, \varphi)_{L^2(K_f)} = 0 \quad \forall \varphi \circ \boldsymbol{\theta}_{K_f}^{-1} \in \mathbb{Q}^q(K_f),$$

where $\mathbb{Q}^q(K_f)$ is the space of polynomials of total degree of order less than or equal to q . By subtracting $\varphi = \Pi_{q,h_f}^{K_f}(f_p - f_a)$ in the above

equation yields to

$$\begin{aligned}
& \sum_{K_f \in \mathcal{T}_f} \int_{K_f} (f - f_f)(f_p - f_a) \, d\mathbf{x} \\
&= \sum_{K_f \in \mathcal{T}_f} \int_{K_f} (f - f_f)(f_p - f_a - \Pi_{q,h_f}^{K_f}(f_p - f_a)) \, d\mathbf{x} \\
&\lesssim \sum_{K_f \in \mathcal{T}_f} \|f - f_f\|_{L^2(K_f)} \|f_p - f_a - \Pi_{q,h_f}^{K_f}(f_p - f_a)\|_{L^2(K_f)} \\
&\lesssim \sum_{K_f \in \mathcal{T}_f} \frac{h_f^{\min(q+1,s)}}{q^s} \|f\|_{H^s(K_f)} \frac{h_f^{\min(q+1,r)}}{q^r} \|f_p - f_a\|_{H^r(K_f)} \\
&\lesssim \sum_{K_f \in \mathcal{T}_f} \frac{h_f^{\min(q+1,s)+\min(q+1,r)}}{q^{s+r}} \|f\|_{H^s(K_f)} \|f_p - f_a\|_{H^r(K_f)},
\end{aligned}$$

where we employed eq. (3.12). By linearity of the integral, noticing that by hypothesis $K_f \subset K_a$ and using that $\|f\|_{H^s(K_f)} \leq \|f\|_{H^s(K_a)}$ we obtain

$$\begin{aligned}
& \sum_{K_f \in \mathcal{T}_f} \frac{h_f^{\min(q+1,s)+\min(q+1,r)}}{q^{s+r}} \|f\|_{H^s(K_f)} \|f_p - f_a\|_{H^r(K_f)} \\
&\lesssim \sum_{K_a \in \mathcal{T}_a} \frac{h_f^{\min(q+1,s)+\min(q+1,r)}}{q^{s+r}} \|f\|_{H^s(K_a)} \|f_p - f_a\|_{H^r(K_a)} \\
&\lesssim \sum_{K_a \in \mathcal{T}_a} \frac{h_f^{\min(q+1,s)+\min(q+1,r)}}{q^{s+r}} \frac{r^{2(q+1)}}{h_a^{q+1}} \|f\|_{H^s(K_a)} \|f_p - f_a\|_{L^2(K_a)} \\
&\lesssim \frac{h_f^{\min(q+1,s)+\min(q+1,r)}}{q^{s+r}} \frac{r^{2(q+1)}}{h_a^{q+1}} \|f\|_{H^s(\Omega)} \|f_p - f_a\|_{L^2(\Omega)},
\end{aligned}$$

where in the last step we used the inverse inequality of Lemma 3.1.7 $q + 1$ times. Finally, we get

$$\|f_p - f_a\|_{L^2(\Omega)}^2 \lesssim \frac{h_f^{\min(q+1,s)+\min(q+1,r)}}{q^{s+r}} \frac{r^{2(q+1)}}{h_a^{q+1}} \|f\|_{H^s(\Omega)} \|f_p - f_a\|_{L^2(\Omega)}.$$

Assuming that the datum f is regular, such that $s > q + 1$, and we assume that the discretization degree of the acoustic space is $r > q + 1$. We then obtain:

$$\|f_p - f_a\|_{L^2(\Omega)} \lesssim \frac{h_f^{2(q+1)}}{h_a^{q+1}} \frac{r^{2(q+1)}}{q^{s+r}} \|f\|_{H^s(\Omega)} \|f_p - f_a\|_{L^2(\Omega)}.$$

4.4 Numerical Results: Verification of the a Priori Projection Error

In this section, we verify the a priori error estimate in Theorem 3.3.1 for the intergrid projection method by considering the case of a constant flow source term, see Section 2.8. This test is particularly relevant since all the numerical results presented in Chapter 5 are obtained by supposing that the flow solution is a piecewise constant function. Next, we consider the case where the flow source is reconstructed by a piecewise linear polynomial, compare with Section 2.8. Finally, we present the numerical results that validate Theorem 3.3.2 where the reconstructed flow source term is obtained via a high order local projection.

4.4.1 Piecewise Constant Flow Source Term

We first consider the case where we assume that the source solution is piecewise constant on the domain. We consider a cubic domain $\Omega = \Omega_a = \Omega_f = (-0.5, 0.5)^3$ and two Cartesian nested tessellation \mathcal{T}_a and \mathcal{T}_f , being the acoustic mesh size h_a a multiple of fluid one h_f . Next, we consider $f = \cos(2\pi x) \cos(2\pi y) \cos(\pi z)$ and compute $E_a = \|f - f_a\|_{L^2(\Omega)}$, where f_a is the projection defined as in Figure 3.1 and computed as described in eq. (2.98) employing the quadrature method discussed in Sec. 2.10.1. In Figure 3.2 we report the projection error E_a , by varying h_f for fixed values of h_a and the polynomial degree r . According to the Theorem 3.3.1 the error E_a saturates as we refine h_f . Indeed, by triangle inequality, we observe that

$$E_a \leq \|f - f_p\|_{L^2(\Omega)} + \|f_p - f_a\|_{L^2(\Omega)}, \quad (4.13)$$

where $\|f - f_p\|_{L^2(\Omega)}$ is the acoustic projection error, while $\|f_p - f_a\|_{L^2(\Omega)}$ is the projected flow error. The acoustic projection error $\|f - f_p\|_{L^2(\Omega)}$ is the leading term of the error independent of h_f . This is confirmed by the plots reported in Figure 3.3 where we show computed error $\|f_p - f_a\|_{L^2(\Omega)}$ as a function of h_f . The latter is proportional to h_f^2 as predicted by eq. (3.10). On the other hand, the error $\|f - f_p\|_{L^2(\Omega)}$ remains constant, cf. eq. (3.6). Moreover, we notice that increasing the polynomial degree r , keeping fixed h_a , reduces the saturation value reached by the error $\|f - f_a\|_{L^2(\Omega)}$. Finally, in Figure 3.4a, we plot the error $\|f - f_p\|_{L^2(\Omega)}$ versus the mesh size h_a while in Figure 3.4b the

same quantity is shown as a function of r . The expected convergence rate given by the estimate in eq. (3.6) is confirmed by the numerical results.

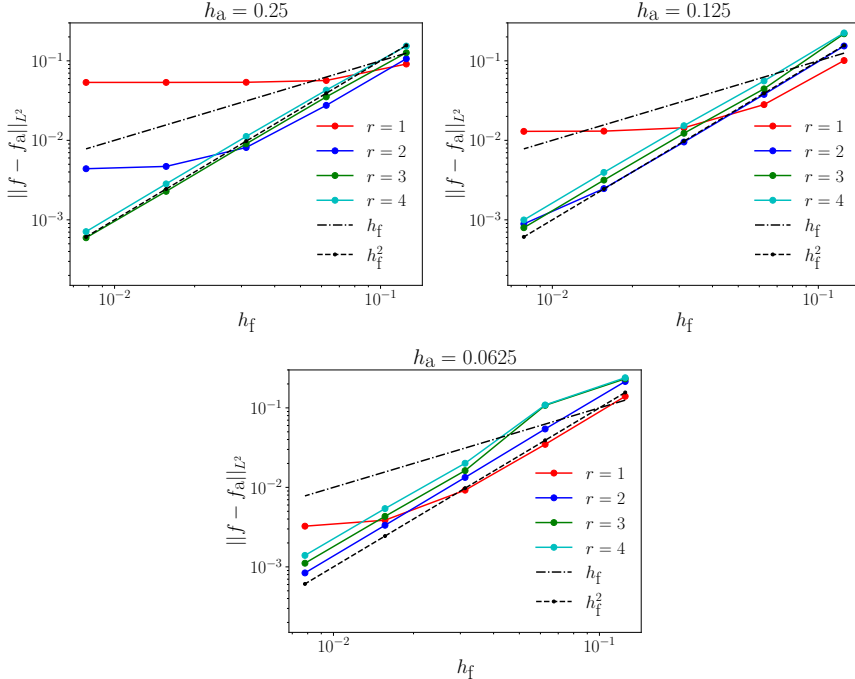


Figure 4.2: Computed errors $\|f - f_a\|_{L^2(\Omega)}$ versus h_f , for different polynomial degrees $r = 1, 2, 3, 4$ and different choices of $h_a = 0.25, 0.125, 0.0625$.

We provide the following rule of thumb to decide how to relate the acoustic and fluid grid in terms of mesh sizes h_a , h_f , and polynomial degree r . Lower projection errors would be generally obtained if both grids have a similar number of degrees of freedom. As seen from estimate in eq. (3.5), the approximation error E_a is lower employing for the acoustic problem a low order polynomial degree and a spatial resolution comparable to the fluid grid, namely $h_f \approx h_a$. However, this choice deteriorates the convergence error estimates provided by the Strang Lemma for the SEM-NI method, see e.g., [117, Lemma 10.1]. The numerical tests presented above show that the dependence on the polynomial degree is not so severe as stated in eq. (3.5), encouraging the use of high-order basis functions.

We now consider the mid-point projection defined in eq. (2.103). As already discussed, the difference between the projection f_a defined in

4.4. Numerical Results: Verification of the a Priori Projection Error 101

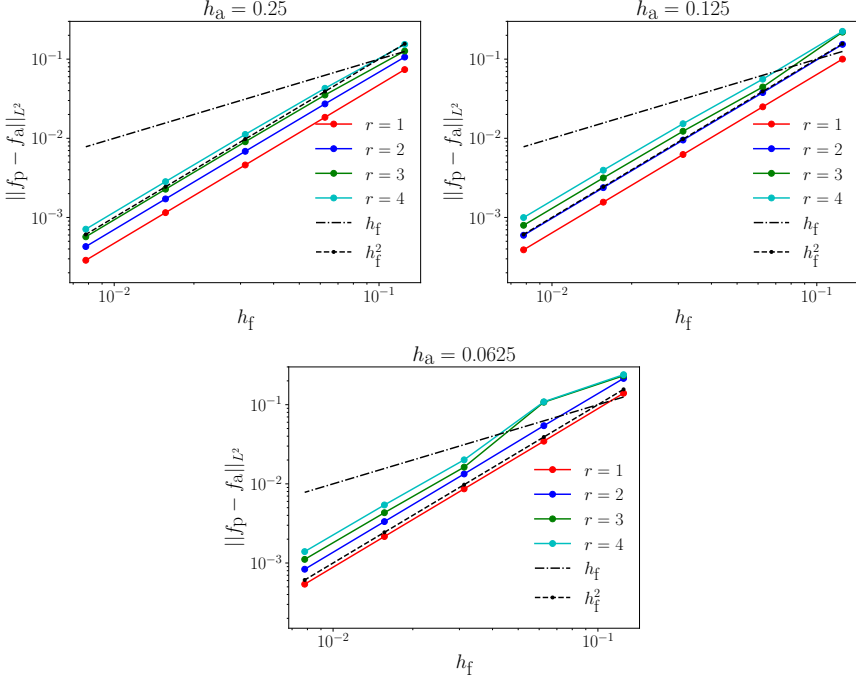


Figure 4.3: Computed errors $\|f_p - f_a\|_{L^2(\Omega)}$ versus h_f , for different polynomial degrees $r = 1, 2, 3, 4$ and different choices of $h_a = 0.25, 0.125, 0.0625$.

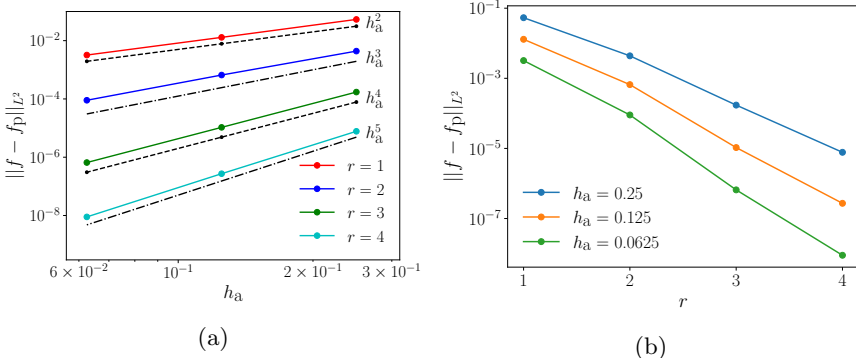


Figure 4.4: Computed errors $\|f - f_p\|_{L^2(\Omega)}$ versus h_a (a) and r (b), for different choices of $r = 1, 2, 3, 4$ and $h_a = 0.25, 0.125, 0.0625$.

eq. (2.98) and eq. (2.103) is the employed quadrature rule. We first observe that if the underlying map θ_{K_a} is linear for all $K_a \in \mathcal{T}_a$, for $r = 1$ the two methods coincide. However, as we increase the polynomial degree or if we employ a trilinear map, the quadrature error

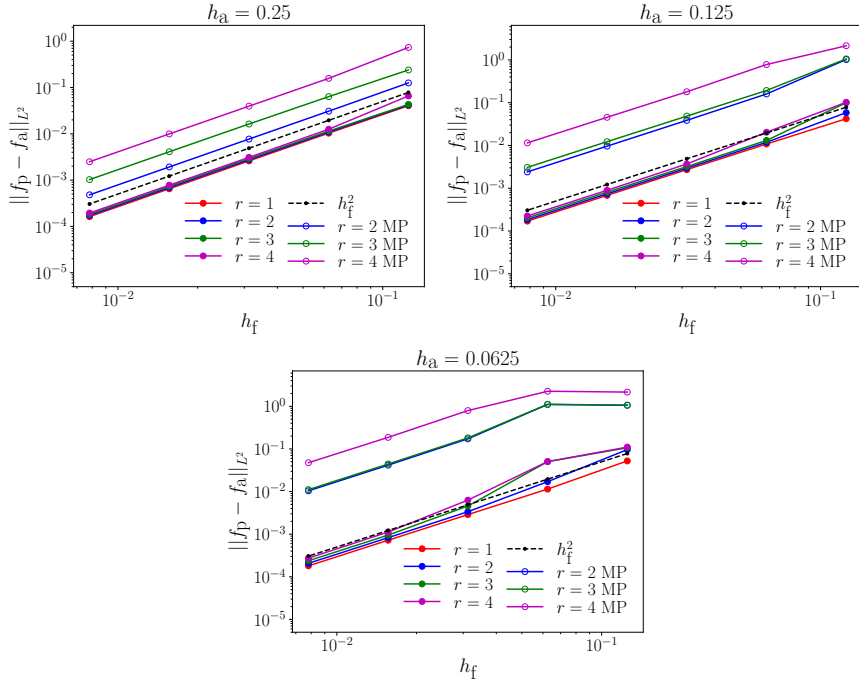


Figure 4.5: Computed errors $\|f_p - f_a\|_{L^2(\Omega)}$ versus h_f , for different polynomial degrees $r = 1, 2, 3, 4$ and different choices of $h_a = 0.25, 0.125, 0.0625$ comparing our proposed projection method and mid point projection method, [128].

increases showing that the projection computed with an exact quadrature formula is clearly more accurate, see Fig. 3.5. Indeed, if we want to employ high order polynomials on the acoustic grid, as already discussed before, it is crucial to minimize the projection error to exploit the accuracy provided by the spectral solver. From the numerical tests, it can be seen that the use of the midpoint projection method still provides accurate results since the convergence rate is h_f^2 . However, the number of fluid elements required to have an accurate projection that does not spoil the discretization error of the acoustic solver increases considerably. The latter makes the computational cost for the computation of the fluid solution, which is the real bottleneck of the workflow, very high.

4.4.2 Piecewise Linear Flow Source Term

We now consider the case in which we reconstruct the flow solution by employing the piecewise linear reconstruction described in Section 2.8.

We consider again a cubic domain $\Omega = \Omega_a = \Omega_f = (-0.5, 0.5)^3$ and two Cartesian nested tessellation \mathcal{T}_a and \mathcal{T}_f , being the acoustic mesh size h_a a multiple of fluid one h_f . Next, we take $f = \cos(2\pi x) \cos(2\pi y) \cos(\pi z)$ and we compute the error $E_a = \|f - f_a\|_{L^2(\Omega)}$, where f_a is the projection defined in (3.4). The behaviour of the error is qualitatively similar to the error as in the constant case. In particular, we again identify two contributions:

$$E_a \leq \|f - f_p\|_{L^2(\Omega)} + \|f_p - f_a\|_{L^2(\Omega)},$$

that are the acoustic projection error and the projected flow error. The first term depends only on h_a and r , while the second term depends on h_f , h_a and r . We compute the error E_a for fixed h_a and r varying h_f and we observe a similar behaviour as in the constant case. After a certain threshold, the error E_a is dominated mainly by the acoustic projection error $\|f - f_p\|_{L^2(\Omega)}$, compare with Figure 3.6. We next consider the projected flow error $\|f_p - f_a\|_{L^2(\Omega)}$ and we keep fixed h_a and r varying h_f . In Figure 3.7 we obtain the expected h_f^4 convergence.

4.4.3 On High Order Reconstruction of the Flow Source Terms

We now consider the case in which we reconstruct the flow solution by employing high order reconstruction. For this case only, we consider the following monodimensional domain $\Omega = \Omega_a = \Omega_f = (0, 1)$ and two Cartesian nested tessellation \mathcal{T}_a and \mathcal{T}_f , being the acoustic mesh size h_a a multiple of fluid one h_f . Next, we take $f = x \sin(5\pi x)$. Since the error E_a has been already investigated, we focus only on the contribution given by the projected flow error, namely $\|f_a - f_p\|_{L^2(\Omega)}$. In the first case, see Figure 3.8, we consider a linear projection with $q = 1$. We keep r and h_a fixed while varying h_f and we obtain the expected results, namely the error $\|f_a - f_p\|_{L^2(\Omega)}$ scales like h_f^4 . Next, in Figure 3.9, we consider a quadratic reconstruction and we compute the projected flow error $\|f_a - f_p\|_{L^2(\Omega)}$. We keep r and h_a fixed while varying h_f and we show that the error behaves like h_f^6 , as expected from Theorem 3.3.2.

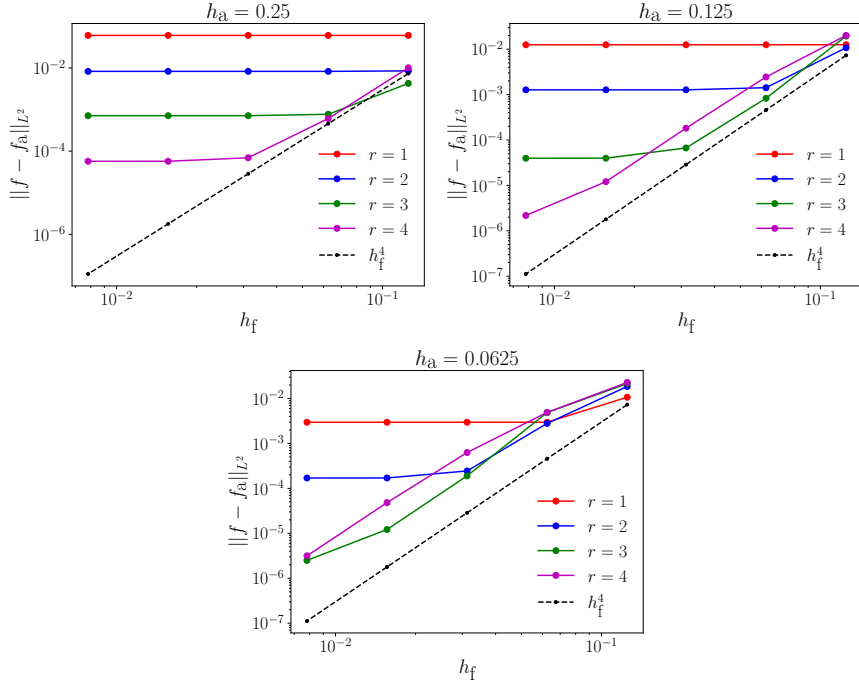


Figure 4.6: Computed errors $\|f - f_a\|_{L^2(\Omega)}$ versus h_f , for different polynomial degrees $r = 1, 2, 3, 4$ and different choices of $h_a = 0.25, 0.125, 0.0625$.

4.5 A Priori Error Estimate with Projected Right Hand Side

In Section 3.2 we presented the main results for the error bounds for the acoustic wave equation. In the following, we modify the presented results in order to be able to consider a projected source f_a , where f_a was defined in eq. (3.4). Given Δt , we divide the time domain $[0, T]$ in N uniform intervals of size Δt . We denote $\rho_h(t_n) = \rho_h^n$, and we want to find $\rho_h(t_n) = \rho_h^n \in V_a$, for $n = 0, \dots, N$ such that $\forall w_h \in V_a$:

$$\begin{aligned}
 & \left(\frac{\rho_h^{n+1} - 2\rho_h^n + \rho_h^{n-1}}{\Delta t^2}, w_h \right)^{\text{NI}} + a_h(\rho_h^n, w_h) = (f_a, w_h)^{\text{NI}}, \\
 & (\rho_h^0, w_h)^{\text{NI}} = (\rho_0, w_h)^{\text{NI}}, \\
 & (g_h^0, w_h)^{\text{NI}} = (\rho_1, w_h)^{\text{NI}}, \quad (4.14a)
 \end{aligned}$$

$$\frac{2}{\Delta t} (\rho_h^1 - \rho_h^0 - \Delta t g_h^0, w_h)^{\text{NI}} + a_h(\rho_h^0, w_h) = (f_a(t_0), w_h)^{\text{NI}}, \quad (4.14b)$$

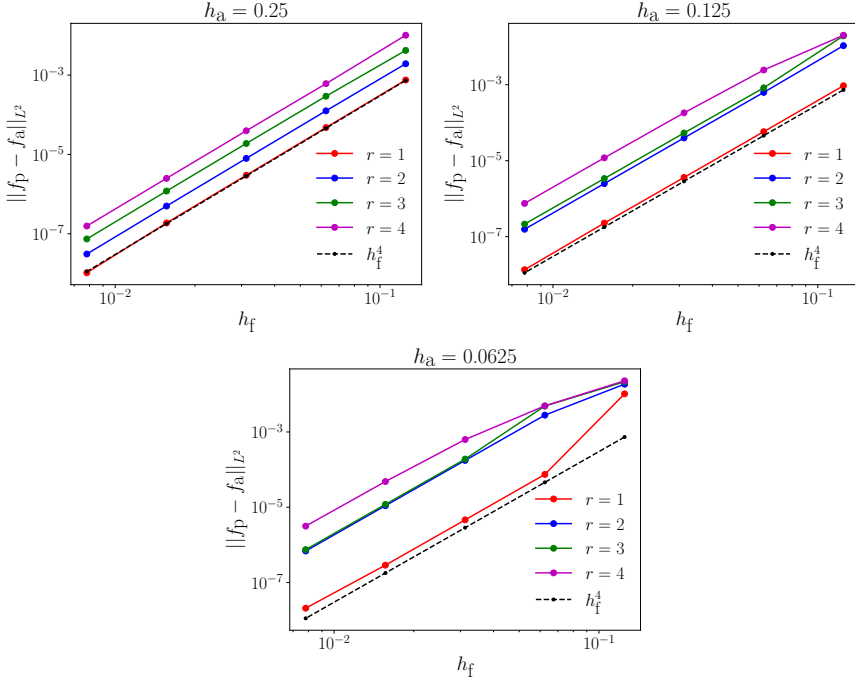


Figure 4.7: Computed errors $\|f_p - f_a\|_{L^2(\Omega)}$ versus h_f , for different polynomial degrees $r = 1, 2, 3, 4$ and different choices of $h_a = 0.25, 0.125, 0.0625$.

where we have discretized in time employing the Leap-Frog method. In the forthcoming analysis, we consider ρ_h^n solution to the problem (3.14), $\rho \in (0, T; H^\ell(\Omega) \cap H^1(\Omega))$ solution to the problem (2.84) and $f \in (0, T; H^s(\Omega) \cap H^1(\Omega))$ its source, where if Ω is regular enough we can set $\ell = s + 2$.

4.5.1 Preliminary Results

We introduce the following notation that is employed during the analysis. Given a function $v_h \in V_a$, let ρ be the solution to the continuous problem (2.84), and let ρ_h^n be the numerical solution to problem (3.14) at the time t_n . We also define the auxiliary variables:

$$\begin{aligned}\phi^n &= \Pi_h^\mathcal{E} \rho(t_n) - \rho_h^n \quad n = 0, \dots, N, \\ z^n &= \delta^2 \Pi_h^\mathcal{E} \rho(t_n) - \ddot{\rho}(t_n) \quad n = 1, \dots, N, \\ q^n &= (f(t_n) - \ddot{\rho}(t_n), v_h^n) - (f_a(t_n) - \ddot{\rho}(t_n), v_h^n)^{\text{NI}} \quad n = 1, \dots, N, \\ z^0 &= q^0,\end{aligned}\tag{4.15a}$$

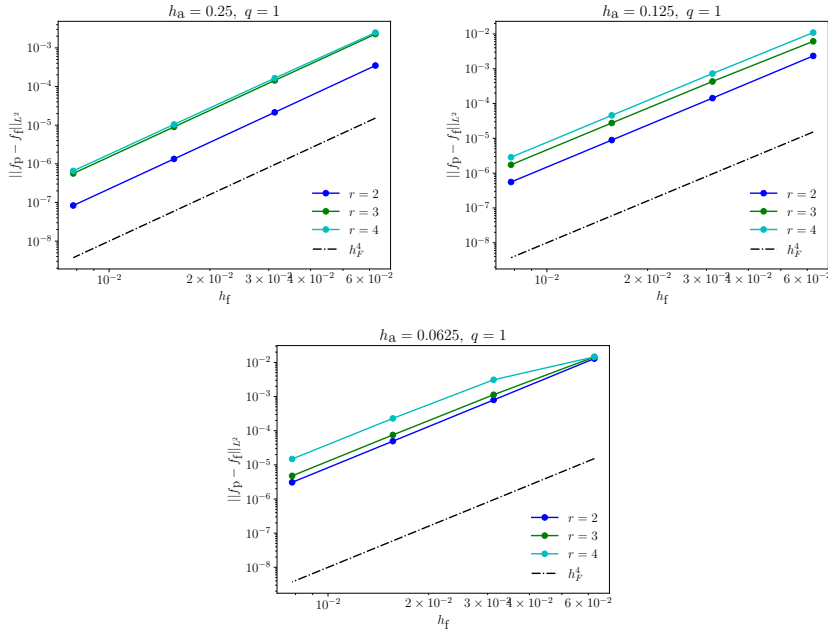


Figure 4.8: Computed errors $\|f_p - f_a\|_{L^2(\Omega)}$ versus h_f , for different polynomial degrees $r = 2, 3, 4$ and different choices of $h_a = 0.25, 0.125, 0.0625$, with a linear flow reconstruction.

where we denoted with δ^2 the second order finite difference operator such that:

$$\delta^2 \rho = \frac{\rho^{n+1} - 2\rho^n + \rho^{n-1}}{\Delta t^2}.$$

We analyse problem (3.14) by following the same strategy in [6] for the acoustic problem in Section 3.2.

Lemma 4.5.1 *Let ϕ, z, q be the variables defined in eq. (3.15). Given $m = 0, \dots, N - 1$, we have:*

$$\begin{aligned} C^* \|\phi^{m+1} - \phi^m\|_h^2 &\leq \|\phi^1 - \phi^0\|_h^2 + \Delta t^2 a_h(\phi^0, \phi^1) \\ &\quad + \Delta t^2 \sum_{n=0}^m \left[(z^n, \phi^{n+1} - \phi^{n-1})^{NI} + q^n (\phi^{n+1} - \phi^{n-1}) \right], \end{aligned}$$

under the stability condition

$$\Delta t < \frac{2h_a}{r^2 \sqrt{C_a}}, \quad (4.16)$$

where C_a is the positive constant in Corollary (3.1.8).

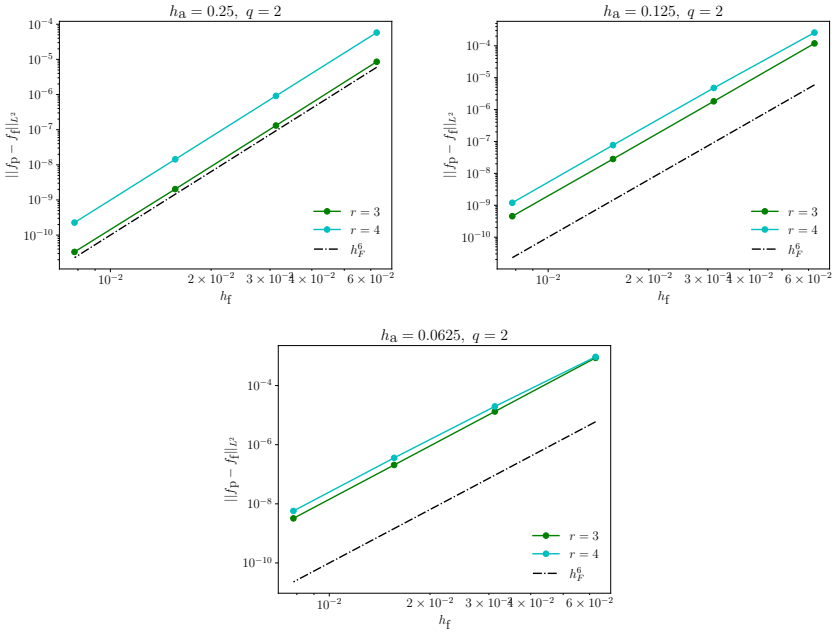


Figure 4.9: Computed errors $\|f_p - f_a\|_{L^2(\Omega)}$ versus h_f , for different polynomial degrees $r = 3, 4$ and different choices of $h_a = 0.25, 0.125, 0.0625$, with a quadratic reconstruction.

Proof. Consider the following identities:

$$(\ddot{\rho}(t_n), v_h^n) + a(\rho_h^n, v_h^n) = (f(t_n), v_h^n) \quad \forall v_h^n \in V_a, (4.17)$$

$$(\delta^2 \rho(t_n), v_h^n)^{NI} + a_h(\rho_h^n, v_h^n) = (f_a(t_n), v_h^n)^{NI} \quad \forall v_h^n \in V_a, (4.18)$$

namely, the continuous wave equation defined in (2.84) and the discrete wave equation in eq. (3.3a). Next, subtract eq. (3.17) and eq. (3.18) to obtain:

$$\begin{aligned} (\ddot{\rho}(t_n), v_h^n) + a(\rho_h^n, v_h^n) - (\delta^2 \rho(t_n), v_h^n)^{NI} - a_h(\rho_h^n, v_h^n) = \\ (f(t_n), v_h^n) - (f_a(t_n), v_h^n)^{NI}. \end{aligned} \quad (4.19)$$

We add to both sides of eq. (3.19) the terms $(\delta^2 \Pi_h^\mathcal{E} \rho(t_n), v_h^n)^{\text{NI}}$ and $(\ddot{\rho}(t_n), v_h^n)^{\text{NI}}$, obtaining:

$$\begin{aligned} & (\delta^2 \Pi_h^\mathcal{E} \rho(t_n), v_h^n)^{\text{NI}} + (\ddot{\rho}(t_n), v_h^n) + a(\rho_h^n, v_h^n) \\ & \quad - (\delta^2 \rho(t_n), v_h^n)^{\text{NI}} - a_h(\rho_h^n, v_h^n) + (\ddot{\rho}(t_n), v_h^n)^{\text{NI}} = \\ & (\delta^2 \Pi_h^\mathcal{E} \rho(t_n), v_h^n)^{\text{NI}} + (f(t_n), v_h^n) \\ & \quad - (f_a(t_n), v_h^n)^{\text{NI}} + (\ddot{\rho}(t_n), v_h^n)^{\text{NI}}. \end{aligned} \quad (4.20)$$

By using the Definition 3.1.9 of the discrete elliptic projection operator we can rewrite eq. (3.20) as:

$$\begin{aligned} & (\delta^2 \Pi_h^\mathcal{E} \rho(t_n), v_h^n)^{\text{NI}} + (\ddot{\rho}(t_n), v_h^n) + a_h(\Pi_h^\mathcal{E} \rho(t_n), v_h^n) \\ & \quad - (\delta^2 \rho(t_n), v_h^n)^{\text{NI}} - a_h(\rho_h^n, v_h^n) + (\ddot{\rho}(t_n), v_h^n)^{\text{NI}} = \\ & (\delta^2 \Pi_h^\mathcal{E} \rho(t_n), v_h^n)^{\text{NI}} + (f(t_n), v_h^n) \\ & \quad - (f_a(t_n), v_h^n)^{\text{NI}} + (\ddot{\rho}(t_n), v_h^n)^{\text{NI}}. \end{aligned} \quad (4.21)$$

Now, we reorder eq. (3.21) to get:

$$\begin{aligned} & (\delta^2 \Pi_h^\mathcal{E} \rho(t_n), v_h^n)^{\text{NI}} - (\delta^2 \rho(t_n), v_h^n)^{\text{NI}} \\ & \quad + a_h(\Pi_h^\mathcal{E} \rho(t_n), v_h^n) - a_h(\rho_h^n, v_h^n) \\ & = (\delta^2 \Pi_h^\mathcal{E} \rho(t_n), v_h^n)^{\text{NI}} - (\ddot{\rho}(t_n), v_h^n)^{\text{NI}} + (f(t_n), v_h^n) \\ & \quad - (\ddot{\rho}(t_n), v_h^n) - (f_a(t_n), v_h^n)^{\text{NI}} + (\ddot{\rho}(t_n), v_h^n)^{\text{NI}}. \end{aligned}$$

We next use the definitions in eq. (3.15) to obtain:

$$(\delta^2 \phi^n, v_h^n)^{\text{NI}} + a_h(\phi^n, v_h^n) = (z^n, v_h^n)^{\text{NI}} + q^n(v_h^n). \quad (4.22)$$

Consider now as a test function $v_h^n = \phi^{n+1} - \phi^{n-1}$ and sum from $n = 1$ to m , with $m = 1, \dots, N - 1$, to achieve:

$$\begin{aligned} & \sum_{n=1}^m (\delta^2 \phi^n, \phi^{n+1} - \phi^{n-1})^{\text{NI}} + \sum_{n=1}^m a_h(\phi^n, \phi^{n+1} - \phi^{n-1}) \\ & = \sum_{n=1}^m \left[(z^n, \phi^{n+1} - \phi^{n-1})^{\text{NI}} + q^n(\phi^{n+1} - \phi^{n-1}) \right]. \end{aligned} \quad (4.23)$$

Using the definition of the operator $\delta^2(\cdot)$ we can rewrite the term $\sum_{n=1}^m (\delta^2 \phi^n, \phi^{n+1} - \phi^{n-1})^{\text{NI}}$ as:

$$\begin{aligned}
 \Delta t^2 \sum_{n=1}^m & (\delta^2 \phi^n, \phi^{n+1} - \phi^{n-1})^{\text{NI}} = \\
 & = \sum_{n=1}^m (\phi^{n+1}, \phi^{n+1} - \phi^{n-1})^{\text{NI}} - 2(\phi^n, \phi^{n+1} - \phi^{n-1})^{\text{NI}} \\
 & \quad + (\phi^{n-1}, \phi^{n+1} - \phi^{n-1})^{\text{NI}} \\
 & = \sum_{n=1}^m (\phi^{n+1}, \phi^{n+1})^{\text{NI}} - 2(\phi^n, \phi^{n+1} - \phi^{n-1})^{\text{NI}} \\
 & \quad - (\phi^{n-1}, \phi^{n-1})^{\text{NI}} \\
 & = \sum_{n=2}^{m+1} (\phi^n, \phi^n)^{\text{NI}} - 2 \sum_{n=1}^m (\phi^n, \phi^{n+1} - \phi^{n-1})^{\text{NI}} \\
 & \quad - \sum_{n=0}^{m-1} (\phi^n, \phi^n)^{\text{NI}} \\
 & = (\phi^{m+1}, \phi^{m+1})^{\text{NI}} + (\phi^m, \phi^m)^{\text{NI}} - 2(\phi^m, \phi^{m+1})^{\text{NI}} \\
 & \quad + 2(\phi^1, \phi^0)^{\text{NI}} - (\phi^0, \phi^0)^{\text{NI}} - (\phi^1, \phi^1)^{\text{NI}} \\
 & = \|\phi^{m+1} - \phi^m\|_h^2 - \|\phi^1 - \phi^0\|_h^2.
 \end{aligned} \tag{4.24}$$

With the same computations we can show that

$$\sum_{n=1}^m a_h(\phi^n, \phi^{n+1} - \phi^{n-1}) = a_h(\phi^m, \phi^{m+1}) - a_h(\phi^0, \phi^1). \tag{4.25}$$

By substituting (3.24) and (3.25) in eq. (3.23), we get

$$\begin{aligned}
 \frac{1}{\Delta t^2} \|\phi^{m+1} - \phi^m\|_h^2 + a_h(\phi^m, \phi^{m+1}) \\
 & = \frac{1}{\Delta t^2} \|\phi^1 - \phi^0\|_h^2 + a_h(\phi^0, \phi^1) \\
 & \quad + \sum_{n=1}^m (z^n, \phi^{n+1} - \phi^{n-1})^{\text{NI}} + q^n(\phi^{n+1} - \phi^{n-1}).
 \end{aligned} \tag{4.26}$$

Given that $q^0 = z^0 = 0$ we can easily extend the sum to zero. We next have that:

$$\begin{aligned} a_h(\phi^m, \phi^{m+1}) &= a_h\left(\frac{\phi^m + \phi^{m+1}}{2}, \frac{\phi^m + \phi^{m+1}}{2}\right) \\ &\quad - a_h\left(\frac{\phi^m - \phi^{m+1}}{2}, \frac{\phi^m - \phi^{m+1}}{2}\right) \\ &\geq -\frac{1}{4}a_h(\phi^m - \phi^{m+1}, \phi^m - \phi^{m+1}), \end{aligned} \quad (4.27)$$

where the last inequality holds due to the coercivity of the bilinear form a_h . By applying Lemma 3.1.8 to eq. (3.27), we conclude that:

$$a_h(\phi^m, \phi^{m+1}) \geq -\frac{1}{4}C_a \frac{r^4}{h_a^2} \|\phi^m - \phi^{m+1}\|_h^2. \quad (4.28)$$

We substitute eq. (3.28) in eq. (3.26) and we get

$$\begin{aligned} \left(\frac{1}{\Delta t^2} - \frac{1}{4}C_a \frac{r^4}{h_a^2}\right) \|\phi^{m+1} - \phi^m\|_h^2 &\leq \frac{1}{\Delta t^2} \|\phi^1 - \phi^0\|_h^2 + a_h(\phi^0, \phi^1) \\ &\quad + \sum_{n=0}^m \left[(z^n, \phi^{n+1} - \phi^{n-1})^{\text{NI}} + q^n(\phi^{n+1} - \phi^{n-1}) \right]. \end{aligned}$$

If we multiply both sides of the equation by Δt^2 and define the positive constant $C^* = (1 - C_a \frac{\Delta t^2 r^4}{4 h_a^2})$, we obtain that:

$$\begin{aligned} C^* \|\phi^{m+1} - \phi^m\|_h^2 &\leq \|\phi^1 - \phi^0\|_h^2 + \Delta t^2 a_h(\phi^0, \phi^1) \\ &\quad + \Delta t^2 \sum_{n=0}^m \left[(z^n, \phi^{n+1} - \phi^{n-1})^{\text{NI}} + q^n(\phi^{n+1} - \phi^{n-1}) \right], \end{aligned}$$

and that concludes the proof. \square

Lemma 4.5.2 *The functions ϕ^0 and ϕ^1 defined in (3.15a) verify the following bound:*

$$\begin{aligned} \|\phi^1 - \phi^0\|_h^2 + \Delta t^2 a_h(\phi^0, \phi^1) &\lesssim \left[\Delta t \frac{h_a^{\min(r,\ell)}}{r^\ell} \|\dot{\rho}\|_{C^0(0,T;H^\ell(\mathcal{T}_h))} \right. \\ &\quad + \Delta t^2 \|f(t_0) - f_a(t_0)\|_{H^s(\mathcal{T}_h)} \\ &\quad + \Delta t^3 \|\rho^{(3)}\|_{C^0(0,T;L^2(\Omega))} \\ &\quad \left. + \Delta t \frac{h_a^{\min(r,\ell)-1}}{r^{\ell-1}} \|\rho_0\|_{H^\ell(\mathcal{T}_h)} \right]^2. \end{aligned}$$

Proof. We start with the following identity:

$$\begin{aligned} (\phi^1 - \phi^0, v_h)^{\text{NI}} &= (\Pi_h^\mathcal{E} \rho(t_1) - \rho_h^1, v_h)^{\text{NI}} - (\Pi_h^\mathcal{E} \rho(t_0) - \rho_h^0, v_h)^{\text{NI}} \\ &= (\Pi_h^\mathcal{E} \rho(t_1) - \rho(t_1), v_h)^{\text{NI}} - (\Pi_h^\mathcal{E} \rho(t_0) - \rho_0, v_h)^{\text{NI}} \\ &\quad + (\rho(t_1) - \rho_h^1, v_h)^{\text{NI}} - (\rho_0 - \rho_h^0, v_h)^{\text{NI}}, \end{aligned}$$

where we added and subtracted on the right hand side the terms $(\rho(t_1), v_h)^{\text{NI}}$ and $(\rho_0, v_h)^{\text{NI}}$. By applying the fundamental theorem of calculus we obtain:

$$\begin{aligned} (\phi^1 - \phi^0, v_h)^{\text{NI}} &= \int_{t_0}^{t_1} (\Pi_h^\mathcal{E} \dot{\rho}(s) - \dot{\rho}(s), v_h)^{\text{NI}} ds \\ &\quad + (\rho(t_1) - \rho_0, v_h)^{\text{NI}} - (\rho_h^1 - \rho_h^0, v_h)^{\text{NI}}. \end{aligned} \tag{4.29}$$

We next bound each of the three terms on the right hand side of eq. (3.29). We denote $\xi(s) = \Pi_h^\mathcal{E} \dot{\rho}(s) - \dot{\rho}(s)$, and we consider the integral in (3.29):

$$\begin{aligned} \int_{t_0}^{t_1} (\Pi_h^\mathcal{E} \dot{\rho}(s) - \dot{\rho}(s), v_h)^{\text{NI}} ds &= \int_{t_0}^{t_1} (\xi(s), v_h)^{\text{NI}} ds, \\ &= \int_{t_0}^{t_1} \left[(\xi(s), v_h)^{\text{NI}} - (\xi(s), v_h) \right] ds \\ &\quad + \int_{t_0}^{t_1} (\xi(s), v_h) ds, \end{aligned} \tag{4.30}$$

where on the last equality we sum and subtracted $\int_{t_0}^{t_1} (\xi(s), v_h) ds$.

Now, we need to estimate the quadrature error for $(\xi(s), v_h)^{\text{NI}} - (\xi(s), v_h)$. To this end, let us introduce the local L^2 projection operator. Given an element $K \in \mathcal{T}_h$, we denote with $\Pi_{h_a, r}^K : L^2(K) \rightarrow V_a(K)$ the local L^2 projection operator such that:

$$(\Pi_{r, h_a}^K v, v_h)_K = (v, v_h)_K \quad \forall v_h \in V_a. \tag{4.31}$$

Recall that, if the map θ_K is linear, then the following identity holds:

$$(\Pi_{r-1, h_a}^K v, v_h)_K^{\text{NI}} = (\Pi_{r-1, h_a}^K v, v_h)_K. \tag{4.32}$$

Let us consider a generic mesh element $K \in \mathcal{T}_h$. In particular, we have

the following:

$$\begin{aligned}
(\xi, v_h)_K^{\text{NI}} - (\xi, v_h)_K &= (I_{h,r}^{\text{GLL}, K} \xi, v_h)_K^{\text{NI}} - (\Pi_{r-1, h_a}^K \xi, v_h)_K^{\text{NI}} \\
&\quad + (\Pi_{r-1, h_a}^K \xi, v_h)_K^{\text{NI}} - (\xi, v_h)_K \\
&= (I_{h,r}^{\text{GLL}, K} \xi, v_h)_K^{\text{NI}} - (\Pi_{r-1, h_a}^K \xi, v_h)_K^{\text{NI}} \\
&\quad + (\Pi_{r-1, h_a}^K \xi, v_h)_K - (\xi, v_h)_K,
\end{aligned} \tag{4.33}$$

where we added and subtracted $(\Pi_{r-1, h_a}^K \xi, v_h)_K^{\text{NI}}$, we used the identity in eq. (3.32) and the identity $(\xi, v_h)_K^{\text{NI}} = (I_{h,r}^{\text{GLL}, K} \xi, v_h)_K^{\text{NI}}$. Next, we bound the right hand side of (3.33) to get:

$$\begin{aligned}
(\xi, v_h)_K^{\text{NI}} - (\xi, v_h)_K &\leq \|I_{h,r}^{\text{GLL}, K} \xi - \Pi_{r-1, h_a}^K \xi\|_h \|v_h\|_{L^2(K)} \\
&\quad + \|\xi - \Pi_{r-1, h_a}^K \xi\|_{L^2(K)} \|v_h\|_{L^2(K)},
\end{aligned}$$

where we employed the Cauchy-Schwarz inequality. Note that

$$\begin{aligned}
&\|I_{h,r}^{\text{GLL}, K} \xi - \Pi_{r-1, h_a}^K \xi\|_h \|v_h\|_{L^2(K)} \\
&\lesssim \|I_{h,r}^{\text{GLL}, K} \xi - \Pi_{r-1, h_a}^K \xi\|_{L^2(K)} \|v_h\|_{L^2(K)},
\end{aligned} \tag{4.34}$$

due to Lemma 3.1.2. Also, we can bound $\|I_{h,r}^{\text{GLL}, K} \xi - \Pi_{r-1, h_a}^K \xi\|_{L^2(K)}$ as follows:

$$\begin{aligned}
&\|I_{h,r}^{\text{GLL}, K} \xi - \Pi_{r-1, h_a}^K \xi\|_{L^2(K)} \\
&= \|I_{h,r}^{\text{GLL}, K} \xi - \xi + \xi - \Pi_{r-1, h_a}^K \xi\|_{L^2(K)} \\
&\lesssim \|I_{h,r}^{\text{GLL}, K} \xi - \xi\|_{L^2(K)} + \|\xi - \Pi_{r-1, h_a}^K \xi\|_{L^2(K)}.
\end{aligned} \tag{4.35}$$

Combining eq. (3.34) and eq. (3.35), we obtain the local inequality:

$$\begin{aligned}
&(\xi, v_h)_K^{\text{NI}} - (\xi, v_h)_K \\
&\lesssim \left(\|I_{h,r}^{\text{GLL}, K} \xi - \xi\|_{L^2(K)} + \|\xi - \Pi_{r-1, h_a}^K \xi\|_{L^2(K)} \right) \|v_h\|_{L^2(K)},
\end{aligned}$$

and summing over the K to get:

$$\begin{aligned}
&(\xi, v_h)^{\text{NI}} - (\xi, v_h) \\
&\lesssim \left(\|I_{h,r}^{\text{GLL}} \xi - \xi\|_{L^2(\Omega)} + \|\xi - \Pi_{r-1, h_a}^K \xi\|_{L^2(\mathcal{T}_h)} \right) \|v_h\|_{L^2(\Omega)}.
\end{aligned}$$

Now, we focus our attention on the term $\|\xi - \Pi_{r-1, h_a}^K \xi\|_{L^2(K)}$. We observe that by definition of the local L^2 projection in eq. (3.31) we

have that $(\xi - \Pi_{r-1,h_a}^K \xi, \Pi_{r-1,h_a}^K \xi) = 0$, and hence we write:

$$\begin{aligned}\|\xi - \Pi_{r-1,h_a}^K \xi\|_{L^2(K)}^2 &= (\xi - \Pi_{r-1,h_a}^K \xi, \xi)_{L^2(K)} \\ &\leq \|\xi - \Pi_{r-1,h_a}^K \xi\|_{L^2(K)} \|\xi\|_{L^2(K)},\end{aligned}$$

that shows that $\|\xi - \Pi_{r-1,h_a}^K \xi\|_{L^2(K)} \leq \|\xi\|_{L^2(K)}$.

We now plug in the definition of $\xi(s)$, observing that $I_{h,r}^{\text{GLL}} \xi - \xi = \dot{\rho} - I_{h,r}^{\text{GLL}} \dot{\rho}$ since $I_{h,r}^{\text{GLL}}(\Pi_h^\varepsilon \xi) = \Pi_h^\varepsilon \xi$, and we obtain:

$$\begin{aligned}(\xi, v_h)^{\text{NI}} - (\xi, v_h) &\lesssim \left(\|I_{h,r}^{\text{GLL}} \xi - \xi\|_{L^2(\Omega)} + \|\xi - \Pi_{r-1,h_a}^K \xi\|_{L^2(\mathcal{T}_h)} \right) \|v_h\|_{L^2(\Omega)} \\ &\lesssim \left(\|I_{h,r}^{\text{GLL}} \xi - \xi\|_{L^2(\Omega)} + \|\xi\|_{L^2(\mathcal{T}_h)} \right) \|v_h\|_{L^2(\Omega)} \\ &= \left(\|\dot{\rho} - I_{h,r}^{\text{GLL}} \dot{\rho}\|_{L^2(\Omega)} + \|\Pi_h^\varepsilon \dot{\rho} - \dot{\rho}\|_{L^2(\mathcal{T}_h)} \right) \|v_h\|_{L^2(\Omega)}.\end{aligned}$$

Now, employing eq. (3.2) and Lemma 3.1.10, we obtain that:

$$\begin{aligned}(\xi, v_h)^{\text{NI}} - (\xi, v_h) &\lesssim \left(\|\dot{\rho} - I_{h,r}^{\text{GLL}} \dot{\rho}\|_{L^2(\Omega)} + \|\Pi_h^\varepsilon \dot{\rho} - \dot{\rho}\|_{L^2(\mathcal{T}_h)} \right) \|v_h\|_{L^2(\Omega)} \\ &\lesssim \frac{h_a^{\min(r,\ell)}}{r^\ell} \|\dot{\rho}\|_{H^\ell(\mathcal{T}_h)} \|v_h\|_{L^2(\Omega)}\end{aligned}$$

Finally we observe that:

$$\int_{t_0}^{t_1} (\xi, v_h)^{\text{NI}} - (\xi, v_h) \lesssim \Delta t \frac{h_a^{\min(r,\ell)}}{r^\ell} \|\dot{\rho}\|_{C(0,T;H^\ell(\mathcal{T}_h))} \|v_h\|_{C^0(0,T;L^2(\Omega))} \quad (4.36)$$

and that:

$$\int_{t_0}^{t_1} (\xi, v_h) \lesssim \Delta t \frac{h_a^{\min(r,\ell)}}{r^\ell} \|\dot{\rho}\|_{C(0,T;H^\ell(\mathcal{T}_h))} \|v_h\|_{C^0(0,T;L^2(\Omega))}, \quad (4.37)$$

where we employed the approximation estimate on the elliptic projector in Lemma 3.1.10. We go back to eq. (3.30), and combining eq.(3.36) and eq.(3.37) we finally write that

$$\begin{aligned}\int_{t_0}^{t_1} (\Pi_h^\varepsilon \dot{\rho}(s) - \dot{\rho}(s), v_h)^{\text{NI}} ds \\ &= \int_{t_0}^{t_1} (\xi(s), v_h)^{\text{NI}} - (\xi(s), v_h) ds + \int_{t_0}^{t_1} (\xi(s), v_h) ds \\ &\lesssim \Delta t \frac{h_a^{\min(r,\ell)}}{r^\ell} \|\dot{\rho}\|_{C(0,T;H^\ell(\mathcal{T}_h))} \|v_h\|_{C^0(0,T;L^2(\Omega))}.\end{aligned} \quad (4.38)$$

We now need to bound $(\rho(t_1) - \rho_0, v_h)^{\text{NI}} - (\rho_h^1 - \rho_h^0, v_h)^{\text{NI}}$ in (3.29). Consider equation (3.14b):

$$\frac{2}{\Delta t^2}(\rho_h^1 - \rho_h^0 - \Delta t g_h^0, v_h)^{\text{NI}} + a_h(\rho_h^0, v_h) = (f_a(t_0), v_h)^{\text{NI}}.$$

We sum and subtract $a(\rho_0, v_h)$, $(f(t_0), v_h)$ and $(f(t_0), v_h)^{\text{NI}}$, and then we write the following:

$$\begin{aligned} \frac{2}{\Delta t^2}(\rho_h^1 - \rho_h^0, v_h)^{\text{NI}} + a_h(\rho_h^0, v_h) &= \left(\frac{2}{\Delta t} g_h^0, v_h \right)^{\text{NI}} \\ &\quad + [(f_a(t_0), v_h)^{\text{NI}} - (f(t_0), v_h)^{\text{NI}}] \\ &\quad + [(f(t_0), v_h)^{\text{NI}} - (f(t_0), v_h)] \\ &\quad + [(f(t_0), v_h) - a(\rho_0, v_h)] + a(\rho_0, v_h). \end{aligned}$$

By observing that $(\ddot{\rho}_0, v_h) = (f(t_0), v_h) - a(u_0, v_h)$ and multiplying the equation with the term $\frac{2}{\Delta t^2}$, we obtain:

$$\begin{aligned} (\rho_h^1 - \rho_h^0, v_h)^{\text{NI}} &= \Delta t (g_h^0, v_h)^{\text{NI}} \\ &\quad + \frac{\Delta t^2}{2} [(f_a(t_0), v_h)^{\text{NI}} - (f(t_0), v_h)^{\text{NI}}] \\ &\quad + \frac{\Delta t^2}{2} [(f(t_0), v_h)^{\text{NI}} - (f(t_0), v_h)] \\ &\quad + \frac{\Delta t^2}{2} (\ddot{\rho}_0, v_h) + \frac{\Delta t^2}{2} [a(\rho_0, v_h) - a_h(\rho_h^0, v_h)]. \end{aligned} \tag{4.39}$$

From the Definition of the elliptic operator $\Pi_h^{\mathcal{E}}(\cdot)$ in eq. (3.1.9) and considering the definition of ϕ^0 (3.15a), we obtain:

$$\begin{aligned} (\rho_h^1 - \rho_h^0, v_h)^{\text{NI}} &= \Delta t (g_h^0, v_h)^{\text{NI}} \\ &\quad + \frac{\Delta t^2}{2} [(f_a(t_0), v_h)^{\text{NI}} - (f(t_0), v_h)^{\text{NI}}] \\ &\quad + \frac{\Delta t^2}{2} [(f(t_0), v_h)^{\text{NI}} - (f(t_0), v_h)] \\ &\quad + \frac{\Delta t^2}{2} (\ddot{\rho}_0, v_h) - \frac{\Delta t^2}{2} a(\phi_0, v_h). \end{aligned} \tag{4.40}$$

Now, consider the Taylor expansion

$$\rho(t_1) = \rho(t_0) + \Delta t \dot{\rho}(t_0) + \frac{\Delta t^2}{2} \ddot{\rho}(t_0) + R_3, \tag{4.41}$$

where R_3 is the remainder:

$$R_3 = \frac{1}{2} \int_{t_0}^{t_1} (\Delta t - s)^2 \rho^{(3)}(s) ds.$$

Since $\dot{\rho}(t_0) = \rho_1$ is given as initial datum, from equation (3.41) we obtain:

$$\frac{\Delta t^2}{2} \ddot{\rho}(t_0) = \rho(t_1) - \rho(t_0) - \Delta t \rho_1 - R_3,$$

and plug it into eq. (3.40).

$$\begin{aligned} (\rho_h^1 - \rho_h^0, v_h)^{\text{NI}} + &= \Delta t (g_h^0, v_h)^{\text{NI}} + \frac{\Delta t^2}{2} [(f_a(t_0), v_h)^{\text{NI}} - (f(t_0), v_h)^{\text{NI}}] \\ &+ \frac{\Delta t^2}{2} [(f(t_0), v_h)^{\text{NI}} - (f(t_0), v_h)] \\ &+ (\rho(t_1) - \rho(t_0) - \Delta t \rho_1 - R_3, v_h) - \frac{\Delta t^2}{2} a(\phi_0, v_h). \end{aligned}$$

We sum and subtract $(\rho(t_1) - \rho^0, v_h)^{\text{NI}}$, and we obtain the following:

$$\begin{aligned} &(\rho(t_1) - \rho^0, v_h)^{\text{NI}} - (\rho_h^1 - \rho_h^0, v_h)^{\text{NI}} \\ &= (\rho(t_1) - \rho^0, v_h)^{\text{NI}} - (\rho(t_1) - \rho(t_0), v_h) \\ &+ \Delta t (\rho_1, v_h) - \Delta t (g_h^0, v_h)^{\text{NI}} \\ &+ \frac{\Delta t^2}{2} [(f(t_0), v_h)^{\text{NI}} - (f_a(t_0), v_h)^{\text{NI}}] \\ &+ \frac{\Delta t^2}{2} [(f(t_0), v_h) - (f(t_0), v_h)^{\text{NI}}] \\ &+ (R_3, v_h) - \frac{\Delta t^2}{2} a(\phi_0, v_h) \\ &= \sum_{i=1}^5 T_i. \end{aligned} \tag{4.42}$$

Next, we bound each term of eq. (4.42). We observe that:

$$\begin{aligned} T_1 &= (\rho(t_1) - \rho(t_0), v_h) - (\rho(t_1) - \rho^0, v_h)^{\text{NI}} \\ &= \int_{t_0}^{t_1} (\dot{\rho}(s), v_h) - (\dot{\rho}(s), v_h)^{\text{NI}} ds \\ &\lesssim \Delta t \max_{t_0 \leq t \leq t_1} ((\dot{\rho}(t), v_h) - (\dot{\rho}(t), v_h)^{\text{NI}}) \\ &\lesssim \Delta t \frac{h_a^{\min(r,\ell)}}{r^\ell} \|\dot{\rho}\|_{C^0(0,T;H^\ell(\Omega))} \|v_h\|_{L^2(\Omega)}. \end{aligned} \tag{4.43}$$

Then, from eq. (3.2) and from the initial condition eq. (3.14a), it follows immediately:

$$T_2 = \Delta t(\rho_1, v_h) - \Delta t(g_h^0, v_h)^{\text{NI}} \lesssim \Delta t \frac{h_a^{\min(r,\ell)}}{r^\ell} \|\rho_1\|_{H^\ell(\mathcal{T}_h)} \|v_h\|_{L^2(\Omega)}.$$

For the term $(f(t_0), v_h) - (f(t_0), v_h)^{\text{NI}}$, we apply again eq. (3.2) and we obtain:

$$\begin{aligned} T_3 &= \frac{\Delta t^2}{2} [(f(t_0), v_h) - (f(t_0), v_h)^{\text{NI}}] \\ &\lesssim \Delta t^2 \frac{h_a^{\min(r,s)}}{r^s} \|f(t_0)\|_{H^s(\mathcal{T}_h)} \|v_h\|_{L^2(\mathcal{T}_h)}. \end{aligned}$$

For the remainder of the Taylor expansion, the strategy is again the same:

$$\begin{aligned} T_4 &= (R_3, v_h) = \left(\frac{1}{2} \int_{t_0}^{t_1} (\Delta t - s)^2 \rho^{(3)} ds, v_h \right) \\ &\lesssim \Delta t^3 \max_{t_0 \leq t \leq t_1} ((\rho^{(3)}, v_h)) \\ &\lesssim \Delta t^3 \|\rho^{(3)}\|_{C^0(0,T;L^2(\Omega))} \|v_h\|_{L^2(\Omega)}, \end{aligned}$$

where in the last inequality we employed Cauchy-Schwarz. Now, we need to estimate the error introduced by the aeroacoustic term, namely $(f_a(t_0), v_h)^{\text{NI}} - (f(t_0), v_h)^{\text{NI}}$. We have that:

$$\begin{aligned} T_5 &= \frac{\Delta t^2}{2} (f_a(t_0), v_h)^{\text{NI}} - (f(t_0), v_h)^{\text{NI}} \\ &\lesssim \Delta t^2 \|f_a(t_0) - f(t_0)\|_h \|v_h\|_h \\ &\lesssim \Delta t^2 \|f_a(t_0) - f(t_0)\|_{L^2(\Omega)} \|v_h\|_{L^2(\Omega)} \end{aligned} \quad (4.44)$$

where we first employed Cauchy-Schwarz inequality on the discrete product $(\cdot, \cdot)_h$. Then, we employed Lemma 3.1.2. Combining the inequalities (3.43)- (3.44) we plug them into eq. (3.42) to obtain:

$$\begin{aligned} &(\rho(t_1) - \rho(t_0), v_h) - (\rho_h^1 - \rho_h^0, v_h)^{\text{NI}} \lesssim \\ &\left[\Delta t \frac{h_a^{\min(r,\ell)}}{r^\ell} \|\dot{\rho}\|_{C^0(0,T;H^\ell(\mathcal{T}_h))} + \Delta t^2 \|f_a(t_0) - f(t_0)\|_{L^2(\Omega)} \right. \\ &\left. + \Delta t^3 \|\rho^{(3)}\|_{C^0(0,T;L^2(\Omega))} \right] \|v_h\|_{L^2(\Omega)} - \frac{\Delta t^2}{2} a_h(\phi^0, v_h), \end{aligned} \quad (4.45)$$

where we also observed that since $\rho_1 = \dot{\rho}(0)$ the norm $\|\rho_1\|_{H^\ell(\mathcal{T}_h)}$ is bounded by $\|\dot{\rho}\|_{C^0(0,T;H^\ell(\mathcal{T}_h))}$, from the Definition 2.75. Next, we consider the original equation (3.29). Take as a test function $v_h = \phi^1 - \phi^0$,

employ the estimates eq. (3.38) and eq. (3.45), and obtain:

$$\begin{aligned} \|\phi^1 - \phi^0\|_h^2 &\lesssim \left[\Delta t \frac{h_a^{\min(r,\ell)}}{r^\ell} \|\dot{\rho}\|_{C^0(0,T;H^\ell(\mathcal{T}_h))} + \Delta t^2 \|f_a(t_0) - f(t_0)\|_{L^2(\Omega)} \right. \\ &\quad \left. + \Delta t^3 \|\rho^{(3)}\|_{C^0(0,T;L^2(\Omega))} \right] \|\phi^1 - \phi^0\|_0 - \frac{\Delta t^2}{2} a_h(\phi^0, \phi^1 - \phi^0). \end{aligned}$$

Then, we employ the equivalence of the discrete and continuous norm described in Lemma 3.1.2 to $\|\phi^1 - \phi^0\|_0 \lesssim \|\phi^1 - \phi^0\|_h$ and we split the bilinear form:

$$\begin{aligned} \|\phi^1 - \phi^0\|_h^2 + \frac{\Delta t^2}{2} a_h(\phi^0, \phi^1) &\lesssim \left[\Delta t \frac{h_a^{\min(r,\ell)}}{r^\ell} \|\dot{\rho}\|_{C^0(0,T;H^\ell(\mathcal{T}_h))} \right. \\ &\quad + \Delta t^2 \|f_a(t_0) - f(t_0)\|_{L^2(\Omega)} \\ &\quad \left. + \Delta t^3 \|\rho^{(3)}\|_{C^0(0,T;L^2(\Omega))} \right] \|\phi^1 - \phi^0\|_h \\ &\quad + \frac{\Delta t^2}{2} a_h(\phi^0, \phi^0). \end{aligned}$$

Now, recalling that $2ab \leq a^2 + b^2$, we obtain:

$$\begin{aligned} \|\phi^1 - \phi^0\|_h^2 + \frac{\Delta t^2}{2} a_h(\phi^0, \phi^1) &\lesssim \frac{1}{2} \left[\Delta t \frac{h_a^{\min(r,\ell)}}{r^\ell} \|\dot{\rho}\|_{C^0(0,T;H^\ell(\mathcal{T}_h))} \right. \\ &\quad + \Delta t^2 \|f_a(t_0) - f(t_0)\|_{L^2(\Omega)} \\ &\quad \left. + \Delta t^3 \|\rho^{(3)}\|_{C^0(0,T;L^2(\Omega))} \right]^2 \\ &\quad + \frac{1}{2} \|\phi^1 - \phi^0\|_h^2 + \frac{\Delta t^2}{2} a_h(\phi^0, \phi^0). \end{aligned}$$

To bound the last term on the right-hand side, we first need to show that:

$$\begin{aligned} \|\phi^0\|_{H^1(\Omega)} &= \|\Pi_h^\mathcal{E} \rho(t_0) - \rho_h^0\|_{H^1(\Omega)} \\ &\lesssim \|\Pi_h^\mathcal{E} \rho(t_0) - \rho_0 + \rho_0 - \rho_h^0\|_{H^1(\Omega)} \\ &\lesssim \|\Pi_h^\mathcal{E} \rho(t_0) - \rho_0\|_{H^1(\Omega)} + \|\rho_0 - I_{h,r}^{\text{GLL}} \rho_0\|_{H^1(\Omega)} \quad (4.46) \\ &\lesssim \frac{h_a^{\min(r,\ell)-1}}{r^{\ell-1}} \|\rho_0\|_{H^\ell(\mathcal{T}_h)}, \end{aligned}$$

where we first applied the definition of ϕ^0 , we added and subtracted ρ_0 , we then observed that $\rho_h^0 = I_{h,r}^{\text{GLL}} \rho_0$, we employed the triangular

inequality and finally the Lemma 3.1.10 and Lemma 3.1.5. Now, from the continuity of the bilinear discrete form we obtain:

$$a_h(\phi^0, \phi^0) \lesssim \|\phi^0\|_{H^1(\Omega)}^2 \lesssim \frac{h^{2\min(r,\ell)-2}}{r^{2\ell-2}} \|\rho_0\|_{H^\ell(\mathcal{T}_h)}^2.$$

Finally, we obtain:

$$\begin{aligned} \|\phi^1 - \phi^0\|_h^2 + \Delta t^2 a_h(\phi^0, \phi^1) &\lesssim \left[\Delta t \frac{h_a^{\min(r,\ell)}}{r^\ell} \|\dot{\rho}\|_{C^0(0,T;H^\ell(\mathcal{T}_h))} \right. \\ &\quad + \Delta t^2 \|f_a(t_0) - f(t_0)\|_{L^2(\Omega)} \\ &\quad + \Delta t^3 \|\rho^{(3)}\|_{C^0(0,T;L^2(\Omega))} \\ &\quad \left. + \Delta t \frac{h_a^{\min(r,\ell)-1}}{r^{\ell-1}} \|\rho_0\|_{H^\ell(\mathcal{T}_h)} \right]^2, \end{aligned}$$

and that concludes the proof. \square

Lemma 4.5.3 *For any sequence of functions $v_h^n \in V_h$, $n = 0, \dots, N-1$, and for any $m = 0, \dots, N-1$ we have*

$$\begin{aligned} \sum_{n=0}^m \left[(z^n, v_h^n)_h + q^n(v_h^n) \right] &\lesssim N \left[\frac{h_a^{\min(r,s)}}{r^s} \|f\|_{C(0,T;H^s(\mathcal{T}_h))} \right. \\ &\quad + \|f - f_a\|_{C(0,T;L^2(\mathcal{T}_h))} \\ &\quad + \frac{h_a^{\min(r,\ell)}}{r^{\ell-1}} \|\ddot{\rho}\|_{C^0(0,T;H^\ell(\mathcal{T}_h))} \\ &\quad \left. + \Delta t^2 \|\rho^{(4)}\|_{C^0(0,T;L^2(\Omega))} \right] \max_{1 \leq n \leq m} \|v_h^n\|_h. \end{aligned}$$

Proof. We set $q^0 = z^0 = 0$. Let us consider then the term $\sum_{n=1}^m q^n(v_h^n)$.

We have that:

$$\begin{aligned} \sum_{n=1}^m q^n(v_h^n) &= \sum_{n=1}^m (f(t_n) - \ddot{\rho}(t_n), v_h^n) - (f_a(t_n) - \ddot{\rho}(t_n), v_h^n)^{\text{NI}} \\ &= \sum_{n=1}^m (f(t_n), v_h^n) - (\ddot{\rho}(t_n), v_h^n) + (f(t_n), v_h^n)^{\text{NI}} \\ &\quad - (f(t_n), v_h^n)^{\text{NI}} - (f_a(t_n), v_h^n)^{\text{NI}} + (\ddot{\rho}(t_n), v_h^n)^{\text{NI}} \end{aligned}$$

where we added and subtracted $(f(t_n), v_h^n)^{\text{NI}}$. Then, we reordered the terms:

$$\begin{aligned} \sum_{n=1}^m q^n(v_h^n) &= \sum_{n=1}^m (f(t_n), v_h^n) - (f(t_n), v_h^n)^{\text{NI}} + (\ddot{\rho}(t_n), v_h^n)^{\text{NI}} - (\ddot{\rho}(t_n), v_h^n) \\ &\quad + (f(t_n), v_h^n)^{\text{NI}} - (f_a(t_n), v_h^n)^{\text{NI}} \\ &\lesssim \sum_{n=1}^m |(f(t_n), v_h^n) - (f(t_n), v_h^n)^{\text{NI}}| + |(\ddot{\rho}(t_n), v_h^n)^{\text{NI}} - (\ddot{\rho}(t_n), v_h^n)| \\ &\quad + |(f(t_n), v_h^n)^{\text{NI}} - (f_a(t_n), v_h^n)^{\text{NI}}| \end{aligned}$$

Concerning the first term on the right hand side, we use Cauchy Schwarz, then employ the Lemma 3.1.2 and then use the approximation Theorem 3.3.1 to obtain:

$$\begin{aligned} |(f(t_n), v_h^n)^{\text{NI}} - (f_a(t_n), v_h^n)^{\text{NI}}| &\lesssim \|f(t_n) - f_a(t_n)\|_h \|v_h^n\|_h \\ &\lesssim \|f(t_n) - f_a(t_n)\|_{L^2(\mathcal{T}_h)} \|v_h^n\|_h \end{aligned}$$

Next, to estimate the remaining terms we use the eq. (3.2) obtaining:

$$\begin{aligned} \sum_{n=1}^m q^n(v_h^n) &\lesssim \sum_{n=1}^m \left[\frac{h_a^{\min(r,s)}}{r^s} \|f(t_n)\|_{H^s(\mathcal{T}_h)} \|v_h^n\|_{L^2(\Omega)} \right. \\ &\quad + \frac{h_a^{\min(r,\ell)}}{r^\ell} \|\ddot{\rho}(t_n)\|_{H^\ell(\mathcal{T}_h)} \|v_h^n\|_{L^2(\Omega)} \\ &\quad \left. + \|f(t_n) - f_a(t_n)\|_{L^2(\mathcal{T}_h)} \|v_h^n\|_h \right] \end{aligned}$$

Now, we remove the time dependence by taking the maximum and using the definition of the norm (2.75):

$$\begin{aligned} \sum_{n=1}^m q^n(v_h^n) &\lesssim N \left[\frac{h_a^{\min(r,\ell)}}{r^\ell} \max_{1 \leq n \leq m} \|\ddot{\rho}(t_n)\|_{H^\ell(\mathcal{T}_h)} \right. \\ &\quad + \max_{1 \leq n \leq m} \|f(t_n) - f_a(t_n)\|_{L^2(\mathcal{T}_h)} \\ &\quad \left. + \frac{h_a^{\min(r,s)}}{r^s} \max_{1 \leq n \leq m} \|f(t_n)\|_{H^s(\mathcal{T}_h)} \right] \max_{1 \leq n \leq m} \|v_h^n\|_h \quad (4.47) \\ &\lesssim N \left[\frac{h_a^{\min(r,\ell)}}{r^\ell} \|\ddot{\rho}\|_{C(0,T;H^\ell(\mathcal{T}_h))} \right. \\ &\quad + \|f - f_a\|_{C(0,T;L^2(\mathcal{T}_h))} \\ &\quad \left. + \frac{h_a^{\min(r,s)}}{r^s} \|f\|_{C(0,T;H^s(\mathcal{T}_h))} \right] \max_{1 \leq n \leq m} \|v_h^n\|_h. \end{aligned}$$

Now, we need to bound $\sum_{n=1}^m (z^n, v_h)_h$. First, we use the Lemma 4.3 in [110], and get:

$$\begin{aligned}\|z^n\|_h &\lesssim \frac{h_a^{\min(r+1,l)}}{r^{\ell-1}} \|\ddot{\rho}\|_{H^\ell(\mathcal{T}_h)} \\ &\quad + \frac{1}{\Delta t} \int_{t_{n-1}}^{t_{n+1}} \|\Pi_h^\varepsilon \ddot{\rho}(s) - \ddot{\rho}(s)\|_{L^2(\Omega)} ds \\ &\quad + \frac{\Delta t}{6} \int_{t_{n-1}}^{t_{n+1}} \|\rho^{(4)}(s)\|_{L^2(\Omega)} ds.\end{aligned}$$

By applying Lemma 3.1.10, we have that:

$$\|z^n(s)\|_h \lesssim \frac{h_a^{\min(r,\ell)}}{r^{\ell-1}} \|\ddot{\rho}(s)\|_{C^0(0,T;H^\ell(\mathcal{T}_h))} + \Delta t^2 \|\rho^{(4)}(s)\|_{C^0(0,T;L^2(\Omega))}. \quad (4.48)$$

Hence now we have that:

$$\begin{aligned}\sum_{n=1}^m (z^n, v_h)_h &\lesssim \sum_{n=1}^m \|z^n\|_h \|v_h\|_h \\ &\lesssim N \left(\frac{h_a^{\min(r,\ell)}}{r^{\ell-1}} \|\ddot{\rho}\|_{C^0(0,T;H^\ell(\mathcal{T}_h))} + \Delta t^2 \|\rho^{(4)}\|_{C^0(0,T;L^2(\Omega))} \right) \max_{1 \leq l \leq m} \|v_h^n\|_h,\end{aligned} \quad (4.49)$$

where the first inequality follows from Cauchy-Schwarz inequality, and in the last inequality we applied eq. (3.48) and used (2.75). We obtain the final result by combining (3.49) and (3.47):

$$\begin{aligned}\sum_{n=0}^m (z^n, v_h^n)_h + q^n(v_h^n) &\lesssim N \left[\frac{h_a^{\min(r,s)}}{r^s} \|f\|_{C(0,T;H^s(\mathcal{T}_h))} + \|f - f_a\|_{C(0,T;L^2(\mathcal{T}_h))} \right. \\ &\quad \left. + \frac{h_a^{\min(r,\ell)}}{r^{\ell-1}} \|\ddot{\rho}\|_{C^0(0,T;H^\ell(\mathcal{T}_h))} \right. \\ &\quad \left. + \Delta t^2 \|\rho^{(4)}\|_{C^0(0,T;L^2(\Omega))} \right] \max_{1 \leq n \leq m} \|v_h^n\|_h.\end{aligned}$$

That concludes the proof. \square

Lemma 4.5.4 *Assuming the stability condition in equation (3.16) holds,*

then $\phi^{n+1} - \phi^n$, for $n = 0, \dots, N_T$ satisfies:

$$\begin{aligned} \max_{0 \leq n \leq N-1} \|\phi^{n+1} - \phi^n\|_h &\lesssim \Delta t \left[\frac{h_a^{\min(r,\ell)}}{r^\ell} \|\dot{\rho}\|_{C^0(0,T;H^\ell(\mathcal{T}_h))} \right. \\ &\quad + \Delta t^2 \|\rho^{(3)}\|_{C^0(0,T;L^2(\Omega))} + \frac{h_a^{\min(r,\ell)-1}}{r^{\ell-1}} \|\rho_0\|_{H^\ell(\mathcal{T}_h)} \\ &\quad + \frac{h_a^{\min(r,s)}}{r^s} \|f\|_{C(0,T;H^s(\mathcal{T}_h))} + \|f - f_a\|_{C(0,T;L^2(\mathcal{T}_h))} \\ &\quad \left. + \frac{h_a^{\min(r,\ell)}}{r^{\ell-1}} \|\ddot{\rho}\|_{C^0(0,T;H^\ell(\mathcal{T}_h))} + \Delta t^2 \|\rho^{(4)}\|_{C^0(0,T;L^2(\Omega))} \right]. \end{aligned}$$

Proof. Recall the estimate from Lemma 3.5.1:

$$\begin{aligned} C^* \|\phi^{m+1} - \phi^m\|_h^2 &\leq \|\phi^1 - \phi^0\|_h^2 + \Delta t^2 a_h(\phi^0, \phi^1) \\ &\quad + \Delta t^2 \sum_{n=0}^m (z^n, \phi^{n+1} - \phi^{n-1})^{\text{NI}} + q^n(\phi^{n+1} - \phi^{n-1}). \end{aligned}$$

We employ Lemma 3.5.2 and Lemma 3.5.3 to bound the terms on the right hand side, and then we take the maximum of both sides:

$$\begin{aligned} \max_{0 \leq n \leq N-1} \|\phi^{n+1} - \phi^n\|_h^2 &\lesssim \left[\Delta t \frac{h_a^{\min(r,\ell)}}{r^\ell} \|\dot{\rho}\|_{C^0(0,T;H^\ell(\mathcal{T}_h))} \right. \\ &\quad + \Delta t^2 \|f(t_0) - f_a(t_0)\|_{L^2(\mathcal{T}_h)} \\ &\quad + \Delta t^3 \|\rho^{(3)}\|_{C^0(0,T;L^2(\Omega))} \\ &\quad \left. + \Delta t \frac{h_a^{\min(r,\ell)-1}}{r^{\ell-1}} \|\rho_0\|_{H^\ell(\mathcal{T}_h)} \right]^2 \\ &\quad + T \Delta t \left[\frac{h_a^{\min(r,s)}}{r^s} \|f\|_{C(0,T;H^s(\mathcal{T}_h))} \right. \\ &\quad + \|f - f_a\|_{C(0,T;L^2(\mathcal{T}_h))} \\ &\quad + \frac{h_a^{\min(r,\ell)}}{r^{\ell-1}} \|\ddot{\rho}\|_{C^0(0,T;H^\ell(\mathcal{T}_h))} \\ &\quad \left. + \Delta t^2 \|\rho^{(4)}\|_{C^0(0,T;L^2(\Omega))} \right] \max_{1 \leq n \leq N-1} \|\phi^{n+1} - \phi^{n-1}\|_h. \end{aligned}$$

Next, we use the classical inequality $2ab \leq \varepsilon a^2 + \frac{b^2}{\varepsilon}$, with $\varepsilon = 2$, and obtain:

$$\begin{aligned}
\max_{0 \leq n \leq N-1} \|\phi^{n+1} - \phi^n\|_h^2 &\lesssim \left[\Delta t \frac{h_a^{\min(r,\ell)}}{r^\ell} \|\dot{\rho}\|_{C^0(0,T;H^\ell(\mathcal{T}_h))} \right. \\
&\quad + \Delta t^2 \|f(t_0) - f_a(t_0)\|_{L^2(\mathcal{T}_h)} \\
&\quad + \Delta t^3 \|\rho^{(3)}\|_{C^0(0,T;L^2(\Omega))} \\
&\quad \left. + \Delta t \frac{h_a^{\min(r,\ell)-1}}{r^{\ell-1}} \|\rho_0\|_{H^\ell(\mathcal{T}_h)} \right]^2 \\
&\quad + T \Delta t \left[\frac{h_a^{\min(r,s)}}{r^s} \|f\|_{C(0,T;H^s(\mathcal{T}_h))} \right. \\
&\quad + \|f - f_a\|_{C(0,T;L^2(\mathcal{T}_h))} \\
&\quad \left. + \frac{h_a^{\min(r,\ell)}}{r^{\ell-1}} \|\ddot{\rho}\|_{C^0(0,T;H^\ell(\mathcal{T}_h))} \right. \\
&\quad \left. + \Delta t^2 \|\rho^{(4)}\|_{C^0(0,T;L^2(\Omega))} \right]^2 \\
&\quad + \frac{1}{4} \max_{1 \leq n \leq N-1} \|\phi^{n+1} - \phi^{n-1}\|_h^2.
\end{aligned}$$

Recall now the following bound:

$$\begin{aligned}
\max_{1 \leq n \leq N-1} \|\phi^{n+1} - \phi^{n-1}\|_h &\leq \max_{1 \leq n \leq N-1} \|\phi^{n+1} - \phi^n\|_h + \max_{1 \leq n \leq N-1} \|\phi^n - \phi^{n-1}\|_h \\
&\leq \max_{1 \leq n \leq N-1} \|\phi^{n+1} - \phi^n\|_h + \max_{0 \leq n \leq N-2} \|\phi^{n+1} - \phi^n\|_h \\
&\leq \max_{0 \leq n \leq N-1} 2 \|\phi^{n+1} - \phi^n\|_h.
\end{aligned} \tag{4.50}$$

By collecting all the terms and observing that $\Delta t^2 \|f(t_0)\|_{H^s(\mathcal{T}_h)} \lesssim \Delta t T \|f\|_{C(0,T;H^s(\mathcal{T}_h))}$, we finally obtain:

$$\begin{aligned}
\max_{0 \leq n \leq N-1} \|\phi^{n+1} - \phi^n\|_h &\lesssim \Delta t \left[\frac{h_a^{\min(r,\ell)}}{r^\ell} \|\dot{\rho}\|_{C^0(0,T;H^\ell(\mathcal{T}_h))} \right. \\
&\quad + \Delta t^2 \|\rho^{(3)}\|_{C^0(0,T;L^2(\Omega))} + \frac{h_a^{\min(r,\ell)-1}}{r^{\ell-1}} \|\rho_0\|_{H^\ell(\mathcal{T}_h)} \\
&\quad + \frac{h_a^{\min(r,s)}}{r^s} \|f\|_{C(0,T;H^s(\mathcal{T}_h))} + \|f - f_a\|_{C(0,T;L^2(\mathcal{T}_h))} \\
&\quad \left. + \frac{h_a^{\min(r,\ell)}}{r^{\ell-1}} \|\ddot{\rho}\|_{C^0(0,T;H^\ell(\mathcal{T}_h))} + \Delta t^2 \|\rho^{(4)}\|_{C^0(0,T;L^2(\Omega))} \right],
\end{aligned}$$

where the hidden constant depends on the time T . \square

4.5.2 Main Results of the Acoustic Problem with Projected Source Term

Now, we apply the results showed in the previous section to obtain a fully discrete estimate for the acoustic problem with projection.

Theorem 4.5.5 (*hp version*) *Let us assume that the following stability condition holds:*

$$\Delta t < \frac{2h_a}{r^2} \frac{1}{\sqrt{C_a}},$$

where C_a is the continuity constant in Corollary 3.1.8. Given ρ_h^n solution to the problem (3.14), $\rho \in (0, T; H^\ell(\Omega) \cap H^1(\Omega))$ solution to the problem (2.84) and $f \in (0, T; H^s(\Omega) \cap H^1(\Omega))$, where if Ω is regular enough we can set $\ell = s + 2$, we have that the following hp-error estimate holds:

$$\begin{aligned} \max_{0 \leq n \leq N-1} \|\rho(t_n) - \rho_h^n\|_{H^1(\Omega)} &\lesssim \left[\frac{h_a^{\min(r,s)}}{r^s} \|f\|_{C(0,T;H^s(\mathcal{T}_h))} \right. \\ &\quad + \|f - f_a\|_{C(0,T;L^2(\mathcal{T}_h))} \\ &\quad + \frac{h_a^{\min(r,\ell)-1}}{r^{\ell-1}} \|\rho\|_{C(0,T;H^\ell(\mathcal{T}_h))} \\ &\quad + \frac{h_a^{\min(r,\ell)}}{r^{\ell-1}} \|\rho\|_{C^2(0,T;H^\ell(\mathcal{T}_h))} \\ &\quad \left. + \Delta t^2 \|\rho\|_{C^4(0,T;L^2(\Omega))} \right]. \end{aligned}$$

Proof. We want to estimate the error $\max_{0 \leq n \leq N} \|e^n\|_{H^1(\Omega)}$. First, we consider the following triangular inequality:

$$\begin{aligned} \max_{0 \leq n \leq N-1} \|\rho(t_n) - \rho_h^n\|_{H^1(\Omega)} &= \max_{0 \leq n \leq N} \|\rho(t_n) - \Pi_h^\mathcal{E} \rho(t_n) + \Pi_h^\mathcal{E} \rho(t_n) - \rho_h^n\|_{H^1(\Omega)} \quad (4.51) \\ &\leq \max_{0 \leq n \leq N} \|\rho(t_n) - \Pi_h^\mathcal{E} \rho(t_n)\|_{H^1(\Omega)} + \max_{0 \leq n \leq N} \|\phi^n\|_{H^1(\Omega)}. \end{aligned}$$

The first term $\max_{0 \leq n \leq N} \|\rho(t_n) - \Pi_h^\mathcal{E} \rho(t_n)\|_{H^1(\Omega)}$ is directly bounded by Lemma 3.1.10:

$$\max_{0 \leq n \leq N} \|\rho(t_n) - \Pi_h^\mathcal{E} \rho(t_n)\|_{H^1(\Omega)} \lesssim \frac{h_a^{\min(r,\ell)-1}}{r^{\ell-1}} \|\rho\|_{C(0,T;H^\ell(\mathcal{T}_h))}, \quad (4.52)$$

For the second term $\max_{0 \leq n \leq N} \|\phi^n\|_{H^1(\Omega)}$, we begin by considering the identity deduced in Lemma 3.5.1, hence eq. (3.22):

$$(\delta^2 \phi^n, v_h^n)^{\text{NI}} + a_h(\phi^n, v_h^n) = (z^n, v_h^n)^{\text{NI}} + q^n(v_h^n).$$

Next, we sum from $n = 1$ to m , where $m \leq N - 1$, obtaining:

$$\sum_{n=1}^m (\delta^2 \phi^n, v_h^n)^{\text{NI}} + \sum_{n=1}^m a_h(\phi^n, v_h^n) = \sum_{n=1}^m (z^n, v_h^n)^{\text{NI}} + q^n(v_h^n). \quad (4.53)$$

We choose now $v_h^n = \phi^{n+1} - \phi^{n-1}$ for $1 \leq n \leq m - 1$ and $v_h^m = \phi^m - \phi^{m-1}$. We rewrite $\sum_{n=1}^m (\delta^2 \phi^n, v_h^n)^{\text{NI}}$ as:

$$\begin{aligned} & \Delta t^2 \left(\sum_{n=1}^{m-1} (\delta^2 \phi^n, \phi^{n+1} - \phi^{n-1})^{\text{NI}} + (\delta^2 \phi^m, \phi^m - \phi^{m-1})^{\text{NI}} \right) \\ &= 2(\phi^1, \phi^0)_h - (\phi^0, \phi^0)_h - (\phi^1, \phi^1)_h \\ & \quad + (\phi^{m-1}, \phi^{m-1})_h + (\phi^m, \phi^m)_h - 2(\phi^{m-1}, \phi^m)_h \quad (4.54) \\ & \quad + (\phi^{m+1}, \phi^m)_h - 2(\phi^m, \phi^m)_h \phi^{m-1}, \phi^m)_h \\ & \quad - \phi^{m+1}, \phi^{m-1})_h + 2\phi^m, \phi^{m-1})_h - \phi^{m-1}, \phi^{m-1})_h \\ &= (\phi^{m+1} - \phi^m, \phi^m - \phi^{m-1})^{\text{NI}} - \|\phi^1 - \phi^0\|_h^2. \end{aligned}$$

Next we simplify $\sum_{n=1}^m a_h(\phi^n, v_h^n)$:

$$\begin{aligned} & \sum_{n=1}^{m-1} a_h(\phi^n, \phi^{n+1} - \phi^{n-1}) + a_h(\phi^m, \phi^m - \phi^{m-1}) \\ &= \sum_{n=1}^{m-1} a_h(\phi^n, \phi^{n+1}) - a_h(\phi^n, \phi^{n-1}) + a_h(\phi^m, \phi^m - \phi^{m-1}) \\ &= \sum_{n=1}^{m-1} a_h(\phi^n, \phi^{n+1}) - a_h(\phi^{n-1}, \phi^n) + a_h(\phi^m, \phi^m - \phi^{m-1}) \quad (4.55) \\ &= \sum_{n=1}^{m-1} a_h(\phi^n, \phi^{n+1}) - \sum_{n=0}^{m-2} a_h(\phi^{n-1}, \phi^n) + a_h(\phi^m, \phi^m - \phi^{m-1}) \\ &= a_h(\phi^{m-1}, \phi^m) - a_h(\phi^0, \phi^1) + a_h(\phi^m, \phi^m - \phi^{m-1}) \\ &= a_h(\phi^m, \phi^m) - a_h(\phi^0, \phi^1) \end{aligned}$$

Now, we plug equations (3.54) and (3.55), into equation (3.53) and we obtain:

$$\begin{aligned}
 a_h(\phi^m, \phi^m) &= \frac{1}{\Delta t^2} (\phi^m - \phi^{m+1}, \phi^m - \phi^{m-1})^{\text{NI}} \\
 &\quad + \frac{1}{\Delta t^2} \|\phi^1 - \phi^0\|_h^2 + a_h(\phi^0, \phi^1) \\
 &\quad + \sum_{n=1}^{m-1} \left[(z^n, \phi^{n+1} - \phi^{n-1})^{\text{NI}} + q^n(\phi^{n+1} - \phi^{n-1}) \right] \\
 &\quad + (z^n, \phi^m - \phi^{m-1})^{\text{NI}} + q^m(\phi^m - \phi^{m-1})
 \end{aligned}$$

We observe that:

$$(\phi^m - \phi^{m+1}, \phi^m - \phi^{m-1})_h \leq \max_{0 \leq n \leq m} \|\phi^{n+1} - \phi^n\|_h^2, \quad (4.56)$$

that follows immediately from the Cauchy-Schwarz inequality. We next employ the coercivity of the bilinear form $\|\phi^m\|_{H^1(\Omega)} \lesssim a_h(\phi^m, \phi^m)$ and eq. (3.56), obtaining:

$$\begin{aligned}
 \|\phi\|_{H^1(\Omega)}^2 &\lesssim a_h(\phi^m, \phi^m) = \frac{1}{\Delta t^2} (\phi^m - \phi^{m+1}, \phi^m - \phi^{m-1})^{\text{NI}} \\
 &\quad + \frac{1}{\Delta t^2} \|\phi^1 - \phi^0\|_h^2 + a_h(\phi^0, \phi^1) \\
 &\quad + \sum_{n=1}^{m-1} \left[(z^n, \phi^{n+1} - \phi^{n-1})^{\text{NI}} + q^n(\phi^{n+1} - \phi^{n-1}) \right] \\
 &\quad + (z^n, \phi^m - \phi^{m-1})^{\text{NI}} + q^m(\phi^m - \phi^{m-1}) \\
 &\leq \frac{1}{\Delta t^2} \max_{0 \leq n \leq m} \|\phi^{n+1} - \phi^n\|_h \\
 &\quad + \frac{1}{\Delta t^2} \|\phi^1 - \phi^0\|_h^2 + a_h(\phi^0, \phi^1) \\
 &\quad + \sum_{n=1}^{m-1} \left[(z^n, \phi^{n+1} - \phi^{n-1})^{\text{NI}} + q^n(\phi^{n+1} - \phi^{n-1}) \right] \\
 &\quad + (z^n, \phi^m - \phi^{m-1})^{\text{NI}} + q^m(\phi^m - \phi^{m-1}) \\
 &= T_1 + T_2 + T_3,
 \end{aligned}$$

Next, we use Lemma 3.5.2 to bound T_1 and Lemma 3.5.3 to bound T_2 and T_3 obtaining:

$$\begin{aligned} \|\phi\|_{H^1(\Omega)}^2 &\lesssim \frac{1}{\Delta t^2} \max_{0 \leq n \leq m} \|\phi^{n+1} - \phi^n\|_h \\ &+ \left[\Delta t \frac{h_a^{\min(r,\ell)}}{r^\ell} \|\dot{\rho}\|_{C^0(0,T;H^\ell(\mathcal{T}_h))} + \Delta t^2 \|f(t_0) - f_a(t_0)\|_{H^s(\mathcal{T}_h)} \right. \\ &+ \Delta t^3 \|\rho^{(3)}\|_{C^0(0,T;L^2(\Omega))} + \Delta t \frac{h_a^{\min(r,\ell)-1}}{r^{\ell-1}} \|\rho_0\|_{H^\ell(\mathcal{T}_h)} \Big]^2 \\ &+ N \left[\frac{h_a^{\min(r,s)}}{r^s} \|f\|_{C(0,T;H^s(\mathcal{T}_h))} + \|f - f_a\|_{C(0,T;L^2(\mathcal{T}_h))} \right. \\ &+ \frac{h_a^{\min(r,\ell)}}{r^{\ell-1}} \|\ddot{\rho}\|_{C^0(0,T;H^\ell(\mathcal{T}_h))} + \Delta t^2 \|\rho^{(4)}\|_{C^0(0,T;L^2(\Omega))} \Big] \\ &\cdot \max_{1 \leq n \leq m} \left(\|\phi^{n+1} - \phi^{n-1}\|_h + \|\phi^m - \phi^{m-1}\|_h \right). \end{aligned}$$

Next, we employ Young's inequality $2ab \leq \varepsilon a^2 + \frac{b^2}{\varepsilon}$ with $\varepsilon = \Delta t^2$, to obtain:

$$\begin{aligned} \|\phi\|_{H^1(\Omega)}^2 &\lesssim \frac{1}{\Delta t^2} \max_{0 \leq n \leq m} \|\phi^{n+1} - \phi^n\|_h^2 + \\ &\left[\Delta t \frac{h_a^{\min(r,\ell)}}{r^\ell} \|\dot{\rho}\|_{C^0(0,T;H^\ell(\mathcal{T}_h))} + \Delta t^2 \|f(t_0) - f_a(t_0)\|_{H^s(\mathcal{T}_h)} \right. \\ &+ \Delta t^3 \|\rho^{(3)}\|_{C^0(0,T;L^2(\Omega))} + \Delta t \frac{h_a^{\min(r,\ell)-1}}{r^{\ell-1}} \|\rho_0\|_{H^\ell(\mathcal{T}_h)} \Big]^2 \\ &+ T^2 \left[\frac{h_a^{\min(r,s)}}{r^s} \|f\|_{C(0,T;H^s(\mathcal{T}_h))} + \|f - f_a\|_{C(0,T;L^2(\mathcal{T}_h))} \right. \\ &+ \frac{h_a^{\min(r,\ell)}}{r^{\ell-1}} \|\ddot{\rho}\|_{C^0(0,T;H^\ell(\mathcal{T}_h))} + \Delta t^2 \|\rho^{(4)}\|_{C^0(0,T;L^2(\Omega))} \Big]^2 \\ &+ \frac{1}{2\Delta t^2} \max_{1 \leq n \leq m} \left(\|\phi^{n+1} - \phi^{n-1}\|_h + \|\phi^m - \phi^{m-1}\|_h \right)^2. \end{aligned}$$

Next, we recall that $\max_{1 \leq n \leq N-1} \|\phi^{n+1} - \phi^{n-1}\|_h \leq \max_{0 \leq n \leq N-1} 2\|\phi^{n+1} - \phi^n\|_h$, see eq. (3.50) and we observe that:

$$\begin{aligned} & \frac{1}{\Delta t^2} \max_{0 \leq n \leq m} \|\phi^{n+1} - \phi^n\|_h^2 \\ & + \frac{1}{2\Delta t^2} \max_{1 \leq n \leq m} (\|\phi^{n+1} - \phi^{n-1}\|_h + \|\phi^m - \phi^{m-1}\|_h)^2 \\ & \lesssim \frac{1}{\Delta t^2} \max_{0 \leq n \leq N-1} \|\phi^{n+1} - \phi^n\|_h^2. \end{aligned}$$

Hence we can apply Lemma 3.5.4, and we finally obtain:

$$\begin{aligned} & \|\phi\|_{H^1(\Omega)}^2 \\ & \lesssim \left[\Delta t \frac{h_a^{\min(r,\ell)}}{r^\ell} \|\dot{\rho}\|_{C^0(0,T;H^\ell(\mathcal{T}_h))} + \Delta t^2 \|f(t_0) - f_a(t_0)\|_{H^s(\mathcal{T}_h)} \right. \\ & \quad \left. + \Delta t^3 \|\rho^{(3)}\|_{C^0(0,T;L^2(\Omega))} + \Delta t \frac{h_a^{\min(r,\ell)-1}}{r^{\ell-1}} \|\rho_0\|_{H^\ell(\mathcal{T}_h)} \right]^2 \\ & + T^2 \left[\frac{h_a^{\min(r,s)}}{r^s} \|f\|_{C(0,T;H^s(\mathcal{T}_h))} + \|f - f_a\|_{C(0,T;L^2(\mathcal{T}_h))} \right. \\ & \quad \left. + \frac{h_a^{\min(r,\ell)}}{r^{\ell-1}} \|\ddot{\rho}\|_{C^0(0,T;H^\ell(\mathcal{T}_h))} + \Delta t^2 \|\rho^{(4)}\|_{C^0(0,T;L^2(\Omega))} \right]^2 \quad (4.57) \\ & + \left[\frac{h_a^{\min(r,\ell)}}{r^\ell} \|\dot{\rho}\|_{C^0(0,T;H^\ell(\mathcal{T}_h))} \right. \\ & \quad \left. + \Delta t^2 \|\rho^{(3)}\|_{C^0(0,T;L^2(\Omega))} + \frac{h_a^{\min(r,\ell)-1}}{r^{\ell-1}} \|\rho_0\|_{H^\ell(\mathcal{T}_h)} \right. \\ & \quad \left. + \frac{h_a^{\min(r,s)}}{r^s} \|f\|_{C(0,T;H^s(\mathcal{T}_h))} + \|f - f_a\|_{C(0,T;L^2(\mathcal{T}_h))} \right. \\ & \quad \left. + \frac{h_a^{\min(r,\ell)}}{r^{\ell-1}} \|\ddot{\rho}\|_{C^0(0,T;H^\ell(\mathcal{T}_h))} + \Delta t^2 \|\rho^{(4)}\|_{C^0(0,T;L^2(\Omega))} \right]^2. \end{aligned}$$

We next combine all the terms, recalling that $\Delta t < T$:

$$\begin{aligned} \max_{1 \leq n \leq N-1} \|\phi^n\|_{H^1(\Omega)} &\lesssim \left[\frac{h_a^{\min(r,\ell)}}{r^\ell} \|\dot{\rho}\|_{C^0(0,T;H^\ell(\mathcal{T}_h))} \right. \\ &\quad + \frac{h_a^{\min(r,s)}}{r^s} \|f\|_{C(0,T;H^s(\mathcal{T}_h))} + \|f - f_a\|_{C(0,T;L^2(\mathcal{T}_h))} \\ &\quad + \Delta t^3 \|\rho^{(2)}\|_{C^0(0,T;L^2(\Omega))} + \frac{h_a^{\min(r,\ell)-1}}{r^{\ell-1}} \|\rho_0\|_{H^\ell(\mathcal{T}_h)} \\ &\quad \left. + \frac{h_a^{\min(r,\ell)}}{r^{\ell-1}} \|\ddot{\rho}\|_{C^0(0,T;H^\ell(\mathcal{T}_h))} + \Delta t^2 \|\rho^{(4)}\|_{C^0(0,T;L^2(\Omega))} \right], \end{aligned}$$

where the hidden constant depends on T . Finally, to extend the bound to ϕ^0 , we recall eq. (3.46):

$$\|\phi^0\|_{H^1(\Omega)} \lesssim \frac{h_a^{\min(r,\ell)-1}}{r^{\ell-1}} \|\rho_0\|_{H^\ell(\mathcal{T}_h)} \quad (4.58)$$

Finally, by combining equations (3.52), (3.57), (3.58) into eq.(3.51), we obtain:

$$\begin{aligned} \max_{0 \leq n \leq N-1} \|\rho(t_n) - \rho_h^n\|_{H^1(\Omega)} &\lesssim \left[\frac{h_a^{\min(r,\ell)}}{r^\ell} \|\dot{\rho}\|_{C^0(0,T;H^\ell(\mathcal{T}_h))} \right. \\ &\quad + \frac{h_a^{\min(r,s)}}{r^s} \|f\|_{C(0,T;H^s(\mathcal{T}_h))} + \|f - f_a\|_{C(0,T;L^2(\mathcal{T}_h))} \\ &\quad + \Delta t^3 \|\rho^{(2)}\|_{C^0(0,T;L^2(\Omega))} + \frac{h_a^{\min(r,\ell)-1}}{r^{\ell-1}} \|\rho\|_{C(0,T;H^\ell(\mathcal{T}_h))} \\ &\quad \left. + \frac{h_a^{\min(r,\ell)}}{r^{\ell-1}} \|\ddot{\rho}\|_{C^0(0,T;H^\ell(\mathcal{T}_h))} + \Delta t^2 \|\rho^{(4)}\|_{C^0(0,T;L^2(\Omega))} \right], \end{aligned}$$

that can be further simplified with the norm definition, by observing that:

$$\Delta t^2 \|\rho^{(2)}\|_{C^0(0,T;L^2(\Omega))} + \Delta t^2 \|\rho^{(4)}\|_{C^0(0,T;L^2(\Omega))} \leq \Delta t^2 \|\rho\|_{C^4(0,T;L^2(\Omega))},$$

and

$$\begin{aligned} \frac{h_a^{\min(r,\ell)}}{r^{\ell-1}} \|\ddot{\rho}\|_{C^0(0,T;H^\ell(\mathcal{T}_h))} + \frac{h_a^{\min(r,\ell)}}{r^\ell} \|\dot{\rho}\|_{C^0(0,T;H^\ell(\mathcal{T}_h))} \\ \lesssim \frac{h_a^{\min(r,\ell)}}{r^{\ell-1}} \|\rho\|_{C^2(0,T;H^\ell(\mathcal{T}_h))}. \end{aligned}$$

Finally, we can conclude that:

$$\begin{aligned} \max_{0 \leq n \leq N-1} \|\rho(t_n) - \rho_h^n\|_{H^1(\Omega)} &\lesssim \left[\frac{h_a^{\min(r,s)}}{r^s} \|f\|_{C(0,T;H^s(\mathcal{T}_h))} \right. \\ &\quad + \|f - f_a\|_{C(0,T;L^2(\mathcal{T}_h))} \\ &\quad + \frac{h_a^{\min(r,\ell)-1}}{r^{\ell-1}} \|\rho\|_{C(0,T;H^\ell(\mathcal{T}_h))} \\ &\quad + \frac{h_a^{\min(r,\ell)}}{r^{\ell-1}} \|\rho\|_{C^2(0,T;H^\ell(\mathcal{T}_h))} \\ &\quad \left. + \Delta t^2 \|\rho\|_{C^4(0,T;L^2(\Omega))} \right]. \end{aligned}$$

Next, in the spirit of [6] we propose also the optimal h -version of the previous theorem.

Theorem 4.5.6 (*h -version*) *Under the same hypothesis of Theorem 3.5.5, it is possible to obtain the following result:*

$$\begin{aligned} \max_{0 \leq n \leq N-1} \|\rho(t_n) - \rho_h^n\|_{H^1(\Omega)} &\lesssim C_r \left[\left(h_a^{\min(r,s)} \|f\|_{C(0,T;H^s(\mathcal{T}_h))} \right. \right. \\ &\quad + \|f - f_a\|_{C(0,T;L^2(\mathcal{T}_h))} \\ &\quad + h_a^{\min(r,\ell)} \|\rho\|_{C(0,T;H^\ell(\mathcal{T}_h))} \\ &\quad + h_a^{\min(r,\ell)} \|\rho\|_{C^2(0,T;H^\ell(\mathcal{T}_h))} \\ &\quad \left. \left. + \Delta t^2 \|\rho\|_{C^4(0,T;L^2(\Omega))} \right) \right]. \end{aligned}$$

Finally, we apply the results in Theorem 3.3.2.

Corollary 4.5.7 *Let \mathcal{T}_a and \mathcal{T}_f be two grids of the same computational domain $\Omega_f = \Omega_a = \Omega$ such that \mathcal{T}_f is nested to \mathcal{T}_a , namely, for every element K_f there exists K_a such that $K_f \subset K_a$, where we denote with $h_a = \text{diam } K_a$, with $h_f = \text{diam } K_f$. Given $f \in H^s(\Omega)$ with $s \geq 1$, let $f_f|_{K_f} = \Pi_{q,h_f} f$ be the projection of f onto K_f and let $f_a = \Pi_{r,h_a} f_f$, namely the projection of f_f onto the space V_a , being r the polynomial degree of the space V_a . Let us assume that the following stability condition holds:*

$$\Delta t < \frac{2h_a}{r^2} \frac{1}{\sqrt{C_a}},$$

where C_a is the continuity constant in Corollary 3.1.8. Given ρ_h^n solution to the problem (3.14), $\rho \in (0, T; H^\ell(\Omega) \cap H^1(\Omega))$ solution to

the problem (2.84) and $f \in (0, T; H^s(\Omega) \cap H^1(\Omega))$, where if Ω is regular enough we can set $\ell = s + 2$, we have that the following hp -error estimate holds:

$$\begin{aligned} & \max_{0 \leq n \leq N-1} \|\rho(t_n) - \rho_h^n\|_{H^1(\Omega)} \\ & \lesssim C_r \left[\left(\frac{h_a^{\min(r,s)}}{r^s} + r^{2(q+1)} \frac{h_f^{2(q+1)}}{h_a^{q+1}} \right) \|f\|_{C(0,T;H^s(\mathcal{T}_h))} \right. \\ & \quad + \frac{h_a^{\min(r,\ell)-1}}{r^{\ell-1}} \|\rho\|_{C(0,T;H^\ell(\mathcal{T}_h))} \\ & \quad + \frac{h_a^{\min(r,\ell)}}{r^{\ell-1}} \|\rho\|_{C^2(0,T;H^\ell(\mathcal{T}_h))} \\ & \quad \left. + \Delta t^2 \|\rho\|_{C^4(0,T;L^2(\Omega))} \right]. \end{aligned}$$

Proof. Apply the approximation Theorem 3.3.2 combined with Theorem 3.5.5. We conclude with the following remark:

Remark 4.5.8 Under the same hypothesis of Corollary 3.5.7, by choosing $q = 0$, namely piecewise constant functions, the hp estimate becomes:

$$\begin{aligned} & \max_{0 \leq n \leq N-1} \|\rho(t_n) - \rho_h^n\|_{H^1(\Omega)} \\ & \lesssim C_r \left[\left(\frac{h_a^{\min(r,s)}}{r^s} + r^2 \frac{h_f^2}{h_a} \right) \|f\|_{C(0,T;H^s(\mathcal{T}_h))} \right. \\ & \quad + \frac{h_a^{\min(r,\ell)-1}}{r^{\ell-1}} \|\rho\|_{C(0,T;H^\ell(\mathcal{T}_h))} \\ & \quad + \frac{h_a^{\min(r,\ell)}}{r^{\ell-1}} \|\rho\|_{C^2(0,T;H^\ell(\mathcal{T}_h))} \\ & \quad \left. + \Delta t^2 \|\rho\|_{C^4(0,T;L^2(\Omega))} \right]. \end{aligned}$$

4.6 Numerical Results: Verification of the a Priori Error Estimate with Projected Right Hand Side

In Corollary 3.5.8 we provided an a priori bound that describes the fully discrete error on the acoustic problem in the segregated strategy. Now, we verify the a priori estimate with numerical tests. Consider

the following problem:

$$\begin{aligned} \frac{\partial^2 \rho}{\partial t^2} - c^2 \Delta \rho &= f, & \mathbf{x} \in \Omega, \quad t \in (0, T], \\ \rho(\mathbf{x}, t) &= d(\mathbf{x}, t), & \mathbf{x} \in \partial\Omega, \quad t \in (0, T], \\ \rho(\mathbf{x}, 0) &= g(\mathbf{x}), & \mathbf{x} \in \Omega, \\ \frac{\partial \rho(\mathbf{x}, t)}{\partial t} \Big|_{t=0} &= h(\mathbf{x}), & \mathbf{x} \in \Omega, \end{aligned}$$

where f is the source term, c is the speed of the wave, $d(\mathbf{x}, t)$ is the Dirichlet datum, $g(\mathbf{x})$ and $h(\mathbf{x})$ are the initial conditions. We construct the following manufactured solution by choosing

$$f(x, y, z, t) = \left(9c^2 - \frac{1}{4}\right) \pi^2 \cos(2\pi x) \cos(2\pi y) \cos(\pi z) \sin\left(\frac{\pi}{2}t\right),$$

and we choose $\Omega = (-0.5, 0.5)^3$ m³ and $T = 1$ s. The boundary conditions and the initial conditions of the problem are choosing to enforce as exact solution:

$$\rho(x, y, z, t) = \cos(2\pi x) \cos(2\pi y) \cos(\pi z) \sin\left(\frac{\pi}{2}t\right),$$

where for simplicity we choose $c = 1$ m s⁻¹. The fluid and acoustic grids are Cartesian grids. For the fluid we employed $h_f = \frac{1}{8}, \dots, \frac{1}{256}$ and for the acoustic grid we employed $h_a = \frac{1}{4}, \dots, \frac{1}{32}$. The time step is fixed at $\Delta t = 1 \times 10^{-4}$ s.

Since we are employing a Cartesian grid, assume that the generic element $K_f \in \mathcal{T}_f$ is $K_f = (x_{\min}, x_{\max}) \times (y_{\min}, y_{\max}) \times (z_{\min}, z_{\max})$, we have that the flow solution on the fluid element K_f is given by:

$$\begin{aligned} f_f|_{K_f} &= \frac{1}{|K_f|} \int_{K_f} f(\mathbf{y}, t) d\mathbf{y} \\ &= \frac{1}{4\pi^3 |K_f|} \left(9c^2 - \frac{1}{4}\right) (\sin(2\pi x_{\max}) - \sin(2\pi x_{\min})) \\ &\quad (\sin(2\pi y_{\max}) - \sin(2\pi y_{\min})) (\sin(\pi z_{\max}) - \sin(\pi z_{\min})) \sin\left(\frac{\pi}{2}t\right), \end{aligned}$$

We compute the numerical solution to problem 3.6 by taking $f_a = \Pi_{h_a, r} f_f$. We remark that the approximation error obtained in can be

written as follows:

$$\begin{aligned} \|\rho(t^n) - \rho_h^n\|_{C^0(0,T;H^1(\Omega))} &\leq \|f - f_a\|_{C^0(0,T;H^1(\Omega))} + \frac{h^{r-1}}{r^s} \|\rho\|_{C^0(0,T;H^1(\Omega))} \\ &= E_f + E_\rho, \end{aligned} \quad (4.59)$$

where we denoted with $E_f = \|f - f_a\|_{C^0(0,T;H^1(\Omega))}$ the error on the source, and with $E_\rho = \frac{h^{r-1}}{r^s} \|\rho\|_{C^0(0,T;H^1(\Omega))}$ the error related with the solution. Although the hp estimate is suboptimal in h_a , we expect optimality, see for instance [6]. From equation (3.59), we note that the error is dominated by the source error E_f or by the solution error E_ρ . We first discuss the error on the source term, comparing with Fig. 3.10. The source term has been obtain through a projection, and the error behaves as shown in Theorem 3.3.1. In particular, if we keep h_a and r fixed, the error behaves like h_f^2 , up until it reaches the threshold given by the projected acoustic error $\|f - f_p\|_{L^2(\Omega)}$, as already discussed in the previous sections, see eq. (3.13). Now, we consider the error $\|\rho(t^n) - \rho_h^n\|_{C^0(0,T;H^1(\Omega))}$, by varying h_f and keeping h_a and r fixed, see Figure 3.11. In Fig. 3.11a we see that the error saturates rapidly for $r = 1, 2$. This is likely due to the fact that the error $\|f - f_a\|_{C^0(0,T;H^1(\Omega))}$ is no longer improving. As we decrease h_a , we notice that we still have the error bounded even for h_a very small, see Fig. 3.11d. By comparing with Fig. 3.10d we notice that however the projection error $\|f - f_a\|_{C^0(0,T;H^1(\Omega))}$ decreases. We note that in the last case the error is hence bounded by the error on the solution E_ρ rather than on the error from the projected source E_f . This means that even if we could decrease the projection error (say, by employing a high order reconstruction on the flow solution), the overall error wouldn't improve. As we refine r , the error decreases, since we are decreasing the error on the solution E_ρ , up until it is completely dominated again by E_f and we obtain the convergence error of the projection. Next, we consider the error $\|\rho(t^n) - \rho_h^n\|_{C^0(0,T;H^1(\Omega))}$ by varying h_a and while keeping h_f and r fixed. In this case it is not easy to determine if the error is following the source error or the solution error, but is easy to see that if the fluid mesh is too much coarse, we can't improve the obtained error. When the error saturates, the flow grid is too coarse, and hence the source error E_f is dominating. Finally, by considering Fig. 3.12f we notice that if is h_f is small enough, we recover the optimal

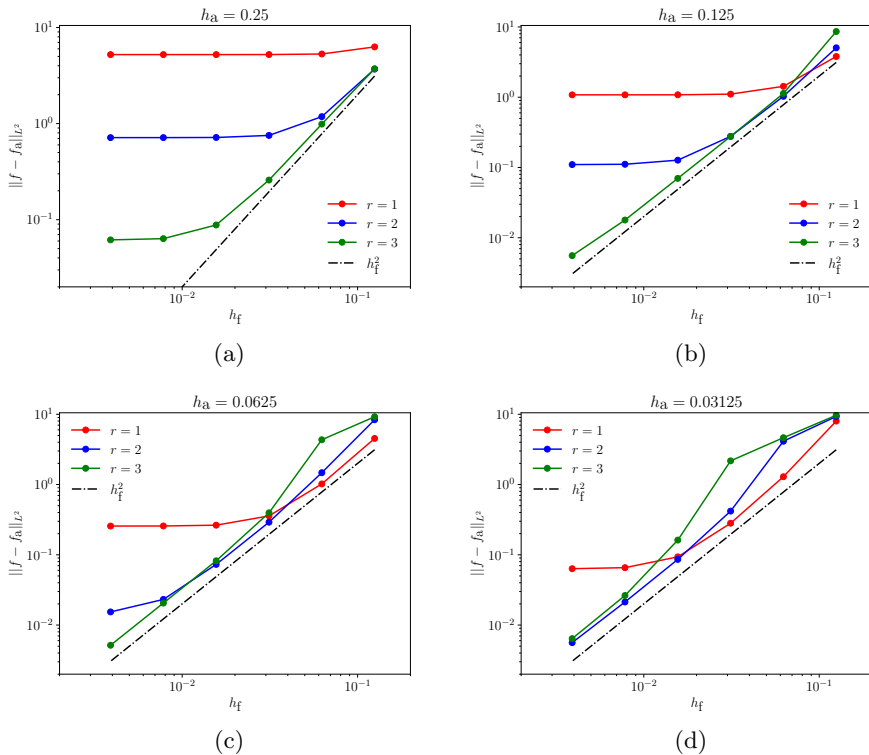


Figure 4.10: Computed errors $\|f - f_a\|_{L^2}$ versus h_f , for different polynomial degrees $r = 1, 2, 3$ and different choices of $h_a = 0.25, 0.125, 0.0625, 0.03125$.

estimates.

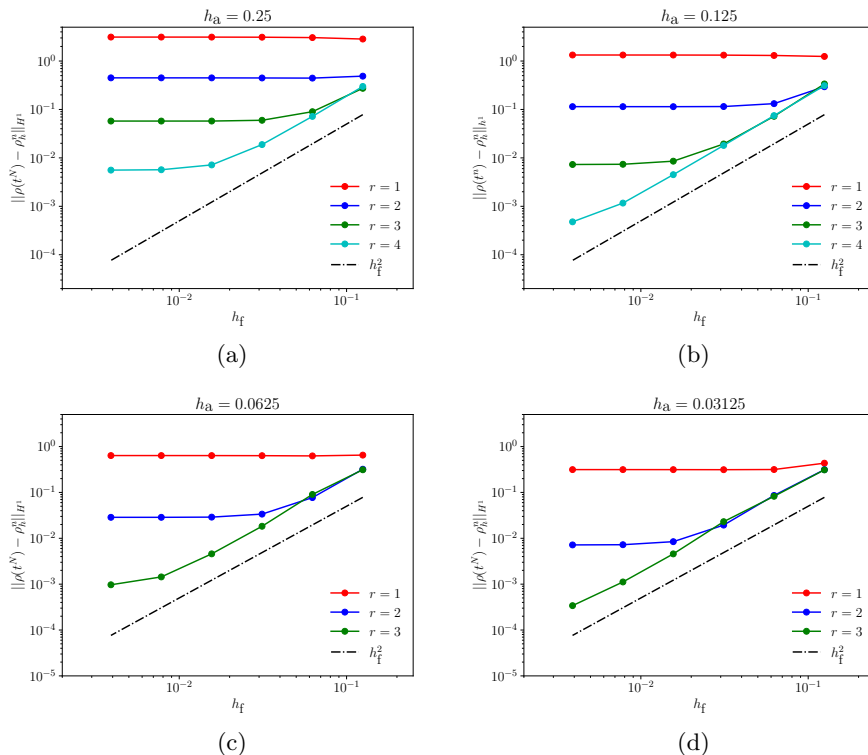


Figure 4.11: Computed errors $\|\rho(t^N) - \rho_h^n\|_{H^1}$ versus h_f , for different polynomial degrees $r = 1, 2, 3, 4$ and different choices of $h_a = 0.25, 0.125, 0.0625, 0.03125$.

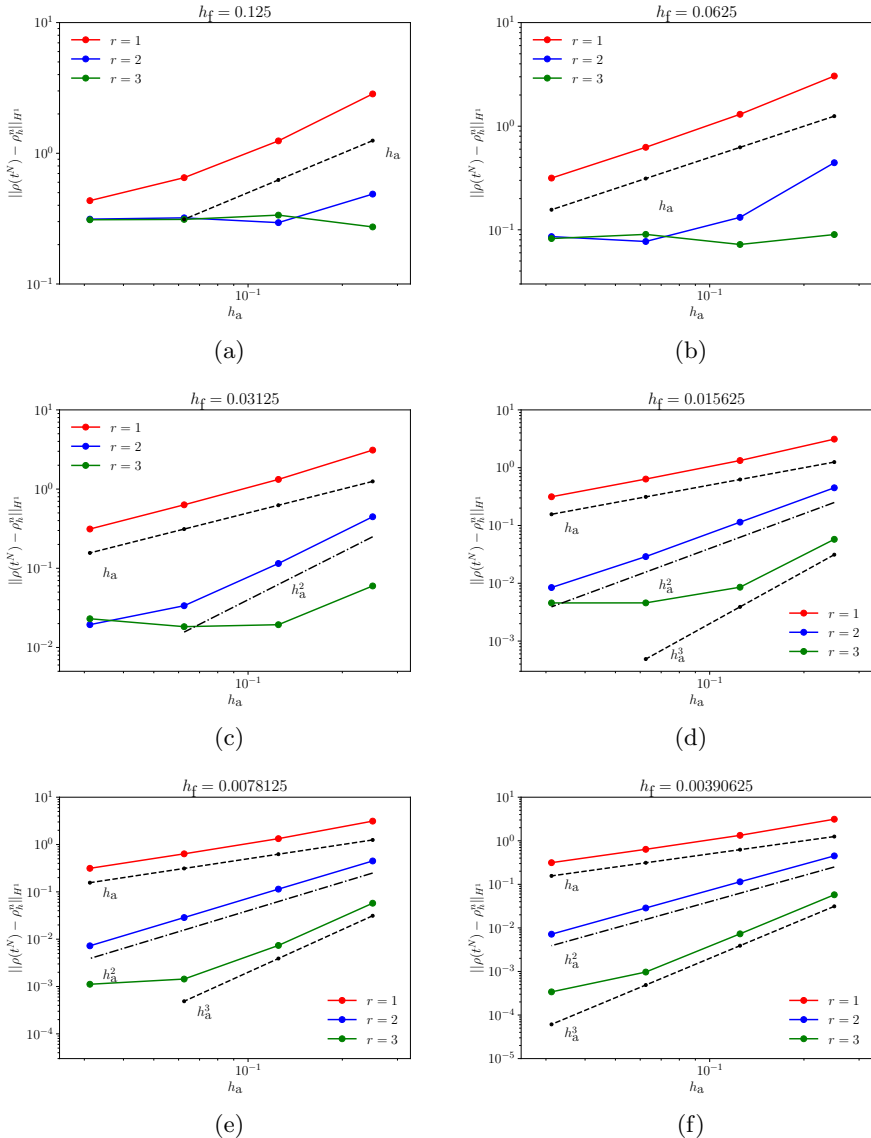


Figure 4.12: Computed errors $\|\rho(t^N) - \rho_h^n\|_{H^1}$ versus h_a , for different polynomial degrees $r = 1, 2, 3$ and different choices of $h_f = 0.125, 0.0625, 0.03125, 0.015625, 0.0078125, 0.00390625$.

Chapter 5

Numerical Results on Acoustics Problems

We dedicate this chapter to present the numerical results obtained with the acoustic solver AeroSPEED. First, we consider a manufactured solution and we verify the theoretical estimates presented in Theorem 3.2.1. At the same time, we compare our solver AeroSPEED with COMSOL Multiphysics® [101], a commercial Lagrangian based finite element solver. Next, we test the implementation of the impedance boundary conditions introduced in Section 2.3.3, that is used to model the wave transmission through different media. Then we test our implementation of the Perfectly Matched Layer (PML), for the planar wave problem and a free field radiating monopole. Next, we apply the PML boundary conditions to model the walls of an anechoic chamber, comparing the obtained solution with an analytical solution and an experimental solution. Finally, we consider a realistic domain geometry, simulating the acoustics in a car cockpit, the so called Noise Box. In this case, we further compare our numerical results with the results obtained with COMSOL Multiphysics®.

5.1 Manufactured Solution

We first consider a simple model problem where we compare the performance of AeroSPEED with the commercial software COMSOL Multiphysics®, in terms of accuracy and computational efficiency. COMSOL Multiphysics® is a multi-physics solver based on the Lagrangian Finite Element Method (FEM), see [101]. We solve an inhomogeneous

wave equation on the cube $\Omega_a = (0, L)^3$, where $L = 1$ m with Dirichlet boundary conditions on the whole boundary $\partial\Omega_a$, with $c_0 = 1 \text{ m s}^{-1}$:

$$\begin{aligned} \frac{1}{c_0^2} \frac{\partial p'^2}{\partial t^2} - \Delta p' &= f(\mathbf{x}, t), & \text{in } \Omega_a \times (0, T], \\ p'(\mathbf{x}, t) &= p'_{\text{ex}}(\mathbf{x}, t), & \text{on } \partial\Omega_a \times (0, T], \\ p'(\mathbf{x}, 0) &= p'_{\text{ex}}(\mathbf{x}, 0), & \text{in } \Omega_a, \\ \frac{\partial p'}{\partial t}(\mathbf{x}, 0) &= \frac{\partial p'_{\text{ex}}}{\partial t}(\mathbf{x}, 0), & \text{in } \Omega_a, \end{aligned} \quad (5.1)$$

where p'_{ex} is the given manufactured solution

$$p'_{\text{ex}}(x, y, z, t) = \sin(\pi t) \sin(4\pi(x-1)(y-1)(z-1)) \sin(4\pi xyz),$$

and $f(\mathbf{x}, t)$ is the corresponding source obtained by plugging into eq. (4.1) the solution p'_{ex} . We employ a very small time step $\Delta t = 10^{-6}$ s and we use a Newmark scheme with parameters $\gamma = 0.5$ and $\beta = 0.25$. The scheme is implicit and second order in time. We solve the test case both in AeroSPEED and in COMSOL, for different refinement levels of the acoustic grid and different polynomial degrees of the underlying polynomial approximation. We then compute the error $E_2 = \|p'_{\text{ex}} - p'_h\|_{L^2(\Omega)}$ at the final time $T = 0.5$ s. We report in Fig. 4.1 the computed errors versus the number of degrees of freedom (left) and the CPU time (right) obtained with the AeroSPEED and COMSOL solvers varying the polynomial approximation degree $r = 1, 2, 3, 4$ for a sequence of meshes with comparable granularity. The expected convergence rates are obtained for both the underlying SEM and FEM approximations. For a comparable number of degrees of freedom, the SEM approximation is more accurate and less expensive. The results reported in Fig. 4.1 (right) clearly indicate that AeroSPEED is able to achieve the same error in a much shorter computational time. Moreover, as the underlying polynomial approximation degree increases, AeroSPEED becomes more and more efficient compared to COMSOL.

5.2 One-dimensional Bar: Impedance Boundary Conditions

We consider the simple case of a travelling one-dimensional planar wave. We solve this problem in order to validate the impedance boundary conditions as described in Section 2.3.3. We first introduce a trans-

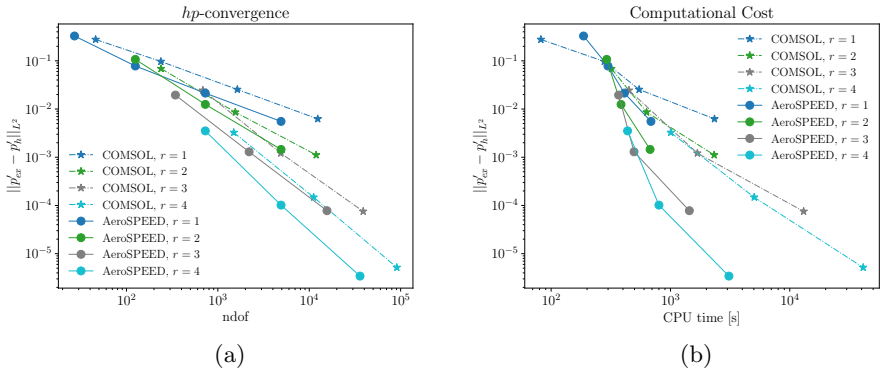


Figure 5.1: Comparison between the SEM solver AeroSPEED and the Lagrangian FEM solver COMSOL. (a) Computed errors vs number of degrees of freedom (ndof). (b) Computed error versus CPU time. The computational tests were performed on 4 cores Intel(R) Xeon(R) Gold 6226 CPU at 2.70GHz.

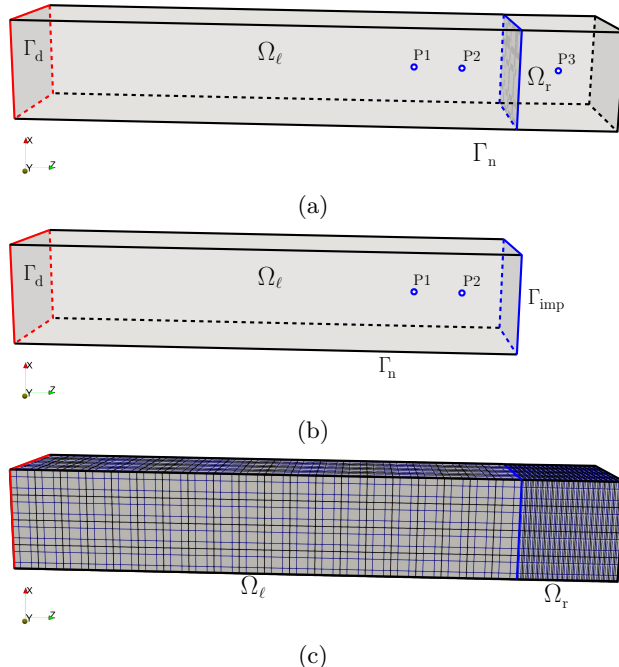


Figure 5.2: (a) Computational domain for the transmission problem. (b) Computational domain for the problem with impedance conditions. (c) Example of the computational grid. The grid elements have black edges, while in blue we represented the edges connecting the internal nodes of the spectral grid.

mission problem and then its reduced equivalent problem that models the presence of the adjacent domain with an impedance boundary condition. Let us consider the domain $\Omega_a = \Omega_\ell \cup \Omega_r$, where $\Omega_\ell = (-L, L)^2 \times (-L_\ell, 0)$ and $\Omega_r = (-L, L)^2 \times (0, L_r)$, see Figure 4.2a with $L = 0.1$ m, $L_\ell = 1$ m and $L_r = 0.2$ m. We denote with Γ_d the Dirichlet boundary at $z = -1$ and with Γ_n the Neumann boundary $\partial\Omega_a \setminus \Gamma_d$. We consider now the following transmission problem. For $t \in (0, T]$, with $T = 7.5 \times 10^{-3}$ s, find $p'(\mathbf{x}, t) : \Omega_a \times (0, T] \rightarrow \mathbb{R}$, such that

$$\begin{aligned} \frac{1}{c_a(\mathbf{x})^2} \frac{\partial^2 p'}{\partial t^2} - \Delta p' &= 0, & \text{in } \Omega_a \times (0, T], \\ p'(\mathbf{x}, t) &= g(t), & \text{on } \Gamma_d \times (0, T], \\ \nabla p'(\mathbf{x}, t) \cdot \mathbf{n} &= 0, & \text{on } \Gamma_n \times (0, T], \\ p'(\mathbf{x}, 0) &= 0, & \text{in } \Omega_a, \\ \frac{\partial p'}{\partial t}(\mathbf{x}, 0) &= 0, & \text{in } \Omega_a, \end{aligned} \quad (5.2)$$

where

$$c_a(\mathbf{x}) = \begin{cases} c_\ell, & \mathbf{x} \in \Omega_\ell, \\ c_r, & \mathbf{x} \in \Omega_r, \end{cases}$$

where $c_\ell = 343 \text{ m s}^{-1}$ and $c_r = 68.6 \text{ m s}^{-1}$ are the speed of the waves respectively in Ω_a and Ω_r , see Figure 4.2. The Dirichlet input datum on Γ_d is:

$$g(t) = -2 \frac{\pi^2}{c_\ell^2} f_0 (t f_0 - 1) \exp(-\pi^2 (t f_0 - 1)^2).$$

At the same time, we solve the reduced problem with the impedance condition. For $t \in (0, T]$, find $p'(\mathbf{x}, t) : \Omega_\ell \times (0, T] \rightarrow \mathbb{R}$, such that

$$\begin{aligned} \frac{1}{c_a(\mathbf{x})^2} \frac{\partial^2 p'}{\partial t^2} - \Delta p' &= 0, & \text{in } \Omega_\ell \times (0, T], \\ p'(\mathbf{x}, t) &= g(t), & \text{on } \Gamma_d \times (0, T], \\ \nabla p'(\mathbf{x}, t) \cdot \mathbf{n} &= 0, & \text{on } \Gamma_n \times (0, T], \\ \frac{1}{\rho_0} \nabla p'(\mathbf{x}, t) \cdot \mathbf{n} &= -\frac{1}{Z_r} \frac{\partial p'}{\partial t}, & \text{on } \Gamma_{\text{imp}} \times (0, T], \\ p'(\mathbf{x}, 0) &= 0, & \text{in } \Omega_\ell, \\ \frac{\partial p'}{\partial t}(\mathbf{x}, 0) &= 0, & \text{in } \Omega_\ell, \end{aligned}$$

where the impedance is set to $Z_r = \rho_0 c_r$, see Figure 4.2. Although the problem is three dimensional, the solution is constant along the plane xy , and hence we describe the exact solution to problem (4.2) only with respect to the variable r , where r is the distance between the wall Γ_d and the position \mathbf{x} . We define with $k_\ell = f_0/c_\ell$ and $k_r = f_0/c_r$ the wave numbers in Ω_ℓ and Ω_r , respectively. For $t \in (0, T]$, given $\tau' = \frac{2L_\ell - r}{c_0}$, we have the following analytical solution:

$$p'_\ell(r, t) = \begin{cases} g(f_0 t - k_\ell r), & \text{for } t \leq \tau' \\ g(f_0 t - k_\ell r) - \phi_{re} g(f_0 t - k_\ell(2L_\ell - r)) & \text{for } t > \tau' \end{cases}, \quad \mathbf{x} \in \Omega_\ell,$$

and by denoting $\tau = \frac{L_\ell}{c_0}$, we have that:

$$p'_r(r, t) = \begin{cases} 0 & \text{for } t \leq \tau \\ (1 - \phi_{re})g(f_0 t - k_\ell L_\ell - k_r(r - L_\ell)) & \text{for } t > \tau \end{cases}, \quad \mathbf{x} \in \Omega_r,$$

where after the time τ' there is a reflected wave that interferes with the incident wave inside the domain Ω_ℓ , and after the time τ there is a transmitted wave in the domain Ω_r . The reflection coefficient ϕ_{re} was defined in equation (2.50):

$$\phi_{re} = \frac{Z_r - Z_\ell}{Z_r + Z_\ell},$$

where in this case $Z_\ell = \rho_0 c_\ell$ and $Z_r = \rho_0 c_r$. For the transmission problem we recorded the computed numerical solution at $P1 = (0, 0, -0.2L_\ell)$, $P2 = (0, 0, -0.1L_\ell)$, $P3 = (0, 0, 0.5L_r)$, see Figure 4.2. For the impedance problem the numerical solution is computed only at $P1$ and $P2$. Next, in Figure 4.3 we notice a perfect match between the numerical solutions and the analytical solution. In $P1$ and $P2$, we are in Ω_ℓ and since $Z_\ell > Z_r$ we notice *a phase change* in the reflective wave. In $P3$ we are inside the domain Ω_r , and since $Z_\ell > Z_r$ we notice *a compression* of the amplitude of the acoustic wave.

5.3 One-dimensional Bar: Absorbing Conditions

We consider the simple case of a travelling one-dimensional planar wave at a speed c_0 in a semi-infinite domain $\Omega = (-L, L)^2 \times (-L_\ell, +\infty)$, with $L = 0.1$ m and $L_\ell = 1$ m, where $c_0 = 343$ m s⁻¹. We employ this case in order to validate the absorbing boundary conditions as described in

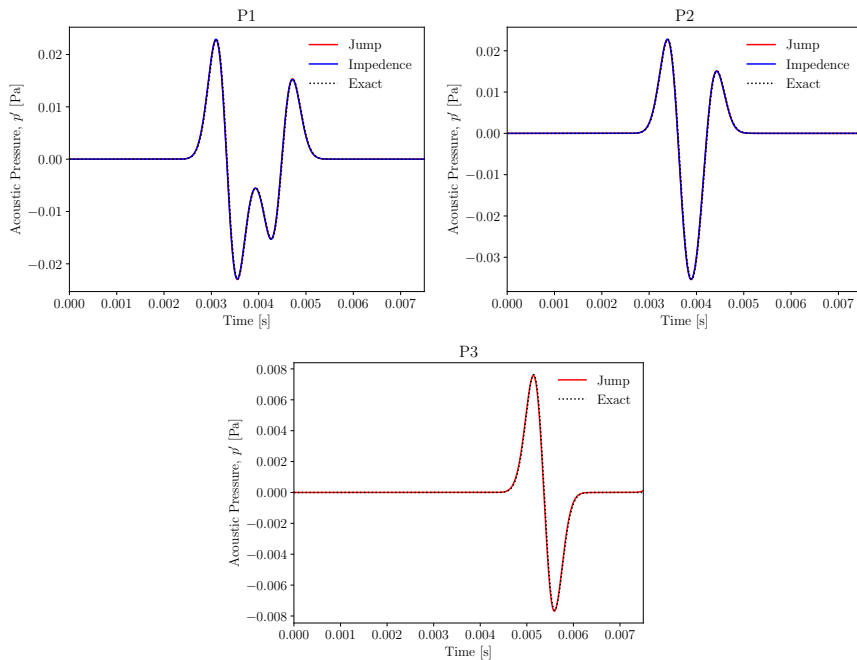


Figure 5.3: Comparison of the computed numerical solution for the transmission problem and impedance problem with the exact solution computed at $P1 = (0, 0, -0.2L_\ell)$, $P2 = (0, 0, -0.1L_\ell)$, $P3 = (0, 0, 0.5L_r)$, where $L_\ell = 1$ m and $L_r = 0.2$ m.

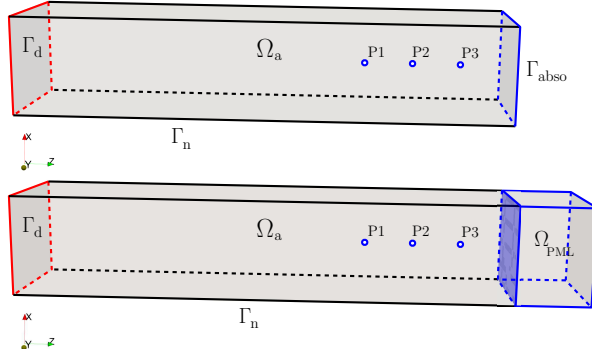


Figure 5.4: (a) Setup with Absorbing conditions. (b) Setup with PML conditions.

Section 2.3.3 and we verify the effectiveness of the Perfectly Matched Layer (PML) introduced in Section 2.3.3. We consider a finite domain $\Omega_a = (-L, L)^2 \times (-L_\ell, 0)$, with a Dirichlet datum imposed at the surface Γ_d :

$$g(t) = -2 \frac{\pi^2}{c_0^2} f_0 (t f_0 - 1) \exp\left(-\pi^2 (t f_0 - 1)^2\right),$$

see Figure 4.4. On the lateral wall we impose a homogeneous Neumann condition. To simulate an unbounded domain at the discrete level at $z = 0$ we impose a fully transmittive boundary conditions to model the infinite boundary domain. The first one is the absorbing condition introduced in Section 2.3.3, and hence we impose on Γ_{abs} that

$$\frac{1}{\rho_0} \nabla p' \cdot \mathbf{n} = -\frac{1}{\rho_0 c_0} \frac{\partial p'}{\partial t},$$

while the second one is the PML, introduced in Section 2.3.3, see Figure 4.4. We denote with $\Omega_{\text{PML}} = (-L, L)^2 \times (0, L_{\text{PML}})$ the domain of the PML, where L_{PML} is the length of the layer and where we employed the inverse damping $\sigma(y) = \frac{c_0}{L_{\text{PML}} - y}$. We solve the PML problem employing two lengths, $L_{\text{PML}} = 0.15$ m and $L_{\text{PML}} = 0.2$ m. The domain has been discretized with $\Delta x = 0.05$ m and with a polynomial degree $r = 3$. We employ an explicit Leap Frog time advancing scheme, with $\Delta t = 10^{-5}$ s and we simulate up to $T = 0.075$ s. The acoustic solution is recorded in three probes $P1 = (0, 0, -0.3L_\ell)$, $P2 = (0, 0, -0.2L_\ell)$, $P3 = (0, 0, -0.1L_\ell)$. From Figure 4.5 we note that overall the PML and the absorbing conditions have the same effect

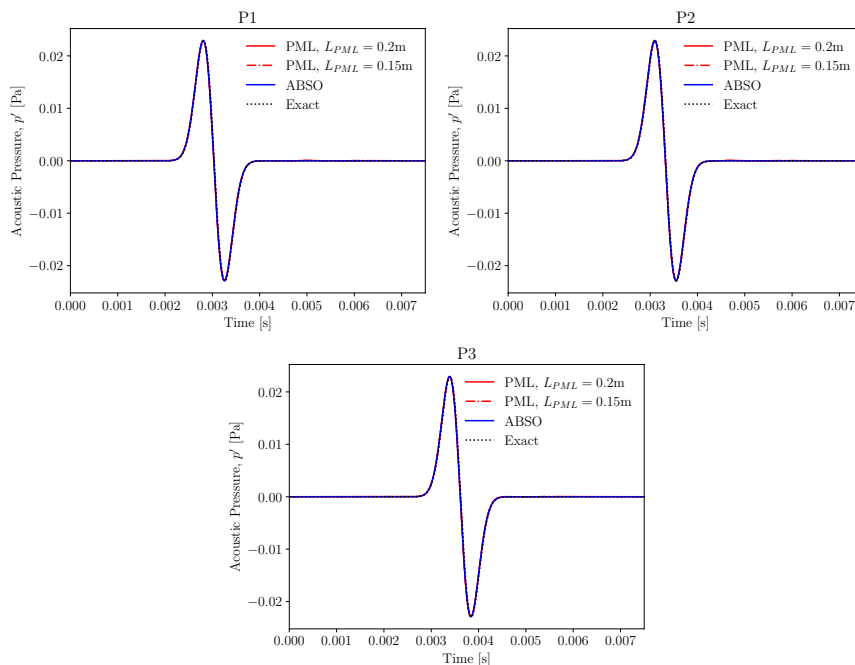


Figure 5.5: Computed numerical solutions at the probes P1, P2, P3 computed with the PML with a length of $L_{PML} = 0.15\text{ m}$, $L_{PML} = 0.2\text{ m}$, the absorbing condition and the exact solution.

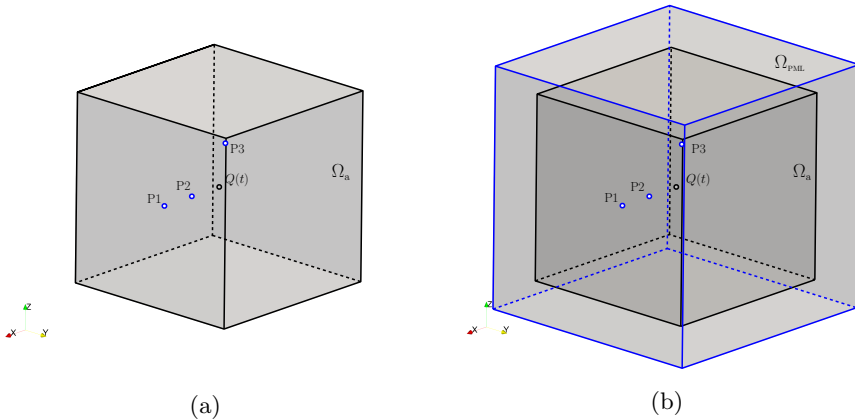


Figure 5.6: (a) Computational domain for the case with the absorbing boundary conditions. On the whole external boundary domain $\partial\Omega_a$ the characteristic impedance is imposed. (b) Computational domain for the case with the perfectly matched layer. In blue, the domain of the Ω_{PML} surrounding the whole acoustic domain.

for this kind of problem. As already discussed in Section 2.3.3, the absorbing conditions are very effecting for normal incident wave, like this case. Indeed, for this case, the overall increased computational cost introduced by the PML is not justifiable.

5.4 Monopole Sound Source

We consider now the sound generated by a monopole in an unbounded domain. As already discussed in Section 2.3.2, this problem has an analytical solution. As for the previous test case, we consider two different free field boundary conditions, the absorbing condition described in Section 2.3.3 and Perfectly Matched Layer, described in Section 2.3.3. We assess their performance on a bounded three-dimensional domain. In particular, we consider a cubic domain $\Omega_a = (-L, L)^3$, where $L = 0.5$ m, with an acoustic monopole $f(\mathbf{x}, t) = Q(t)\delta(\mathbf{x})$ with volume acceleration $Q(t) = \sin(2\pi f_0 t)$, see Figure 4.6. We simulate up to a final time $T = 0.1$ s. The analytical solution is given by

$$p'(\mathbf{x}, t) = \frac{1}{4\pi|\mathbf{x}|} \sin(2\pi(k|\mathbf{x}| - f_0 t)),$$

where $f_0 = 1000$ Hz, and $k = \frac{f_0}{c_0} = 2.915 \text{ m}^{-1}$ is the wavenumber. We consider the speed of sound in the air $c_0 = 343 \text{ m s}^{-1}$, and the respective wave length of the solution is $\lambda = \frac{c_0}{f_0} = 0.343 \text{ m}$. The grid has been designed in order to resolve accurately enough the wavelength of the signal and hence the domain Ω_a has been discretized with $\Delta x = 0.05 \text{ m}$ employing elements with $r = 3$. The time domain has been discretized with an explicit Leap Frog scheme, with $\Delta t = 10^{-5} \text{ s}$. Given the domain Ω_a , we extend the geometry in each direction, obtaining a layer with $L = 0.15 \text{ m}$. We denote hence with $\Omega_{PML} = ((-(L + L_{PML}), -L) \cup (L, (L + L_{PML})))^3$ the PML domain, where $L_{PML} = 0.15 \text{ m}$. We next compare the effectiveness of the two boundary conditions. While in the previous section the PML did not show relevant improvements with respect to the absorbing boundary condition, in this example we show that PML for non normal incident wave propagation problems has to be preferred. For both cases, we compute the solution in three probes $P1 = (0.4L, 0, 0)$, $P2 = (0.8L, 0, 0)$, $P3 = (0.9L, 0.9L, 0.9L)$ (displayed in Figure 4.6) and together with the analytical solution, see Figure 4.7. In the probes P1 and P2 both the boundary conditions are accurate enough, although a small error is introduced by the absorbing condition. This is due to the fact that, as already discussed in Section 2.3.3, these conditions are optimal in the case of normal planar incident wave. The probe P3 is in the corner of the domain. Here the impedance matching condition totally fails to absorb the incoming wave. The impinging wave at the corner is not normal to the boundary and a reflected wave is introduced, see Figure 4.7c. As a consequence, the quality of the wave fronts deteriorates, see Figure 4.8. The same can be noticed in the wave fronts closer to the boundary in Figure 4.9. The solution obtained with the PML is much smoother, further showing the effectiveness of the damping incoming from the additional layer. Notably, no reflection is introduced by the PML. The simulations were run on 32 cores on a E5-4610 v2 @2.3GHz with 1.2TB RAM. The computational time for the case with the absorbing conditions is 962 s for a case with 226981 degrees of freedom, while for the PML is 1760 s, for a case with 493039 degrees of freedom. However, the high quality of the obtained results fully justify the computational cost.

Remark 5.4.1 When dealing with a monopole sound source at the discrete level, given an element $K \in \mathcal{T}_a$, we need to integrate the

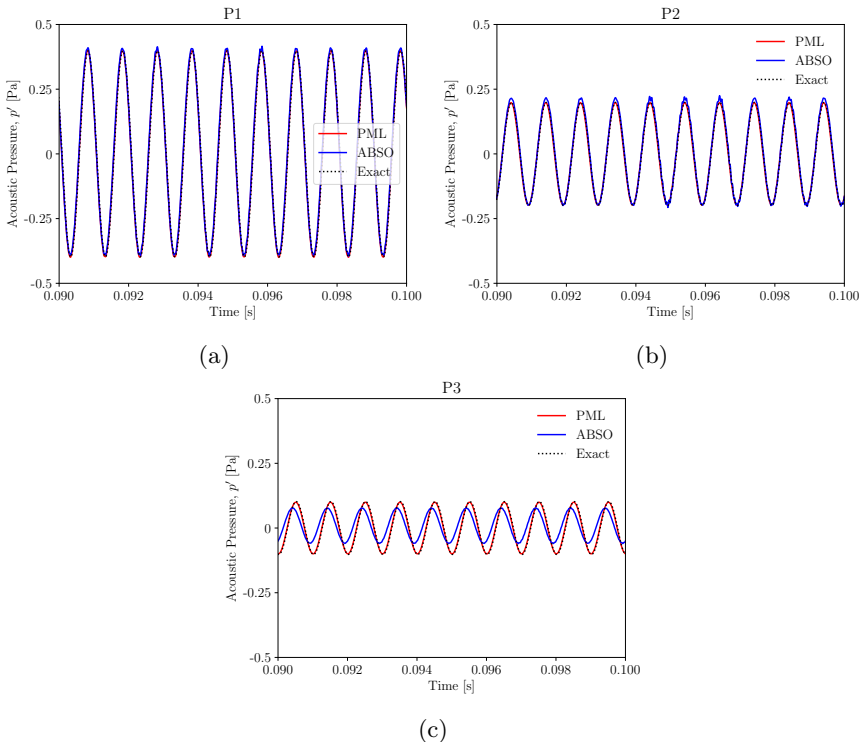


Figure 5.7: Computed numerical solutions for the case with absorbing boundary conditions and the PML compared with the analytical solution in three probes of interest.

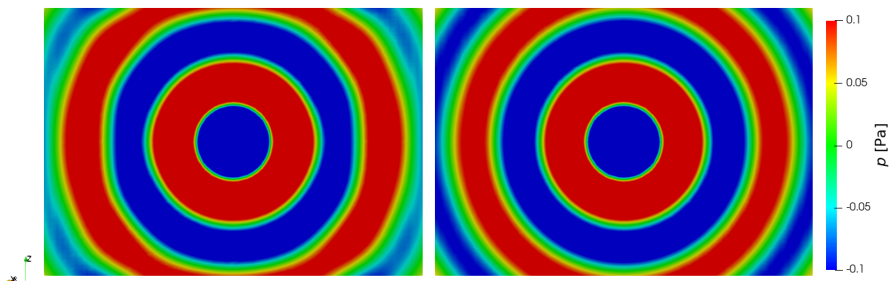


Figure 5.8: Snapshot for $T = 0.1$ s cut with a plane $\mathbf{n} = (-1, 1, 0)$. On the left, solution obtained with the absorbing condition. On the right, solution obtained with the PML. Notice on the corner of the slice the different behaviours of the computed numerical solutions.

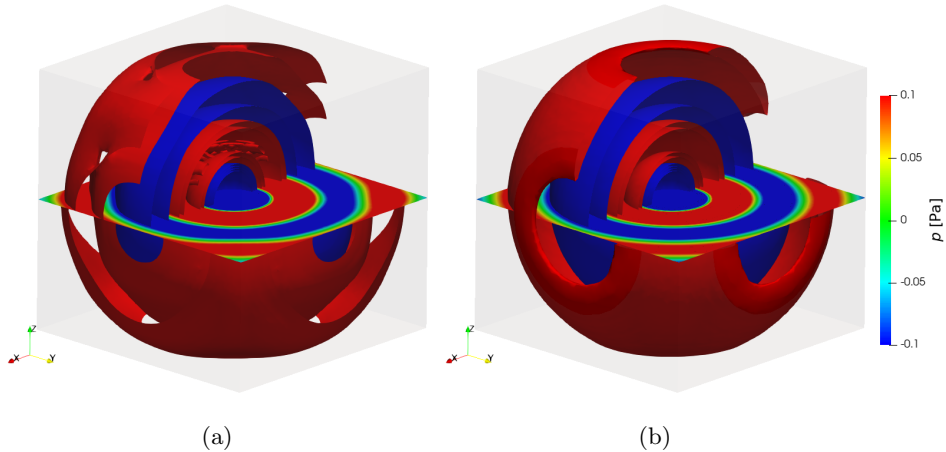


Figure 5.9: (a) Snapshot of the numerical solution computed employing the absorbing boundary conditions. (b) Snapshot of the numerical solution computed employing the PML. For both the snapshots, the shown contour levels are $p' = -0.5, -0.375, -0.25, -0.125, 0.125, 0.25, 0.375, 0.5$ (acoustic pressure in Pa). Notice at the corner of the domains the differences between the computed numerical solutions.

following:

$$I = \int_K f(\mathbf{x})\delta(\mathbf{x})\phi_{a,i}(\mathbf{x})d\mathbf{x} \quad \text{with } \phi_{a,i}(\mathbf{x}) \in V_a,$$

where $\delta(\cdot)$ is the Dirac delta. Now, instead of computing numerically the integral 4.4.1, we just employ the definition of the δ and we obtain $I = f(0)$. The value $f(0)$ is then added to the respective node at the discrete level. This strategy is perfect when the monopole is exactly located in one of the degrees of freedom of the computational grid. If the monopole is not located exactly at that point, we take the nearest degree of freedom.

5.5 Anechoic Chamber

In the previous Sections we have presented a set of numerical tests to assess the performance of the AeroSPEED acoustic solver and to verify the behaviour of some specific features, like the absorbing conditions, the impedance boundary conditions and the PML. We apply now the acoustic solver in a real, even if still simple, acoustic problem, with the future objective to apply our numerical tool in more complex scenarios

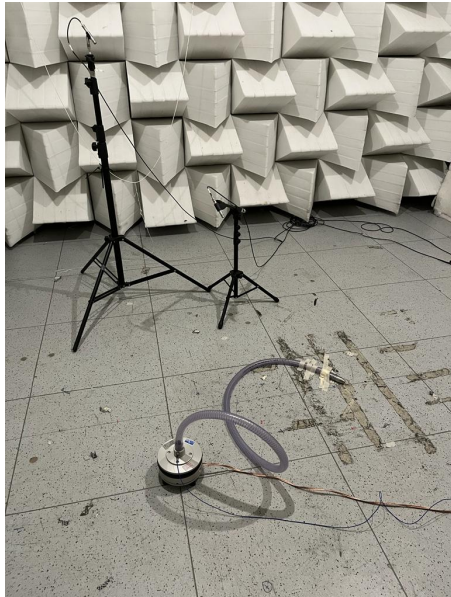
where there is no analytical solution.

Open-field acoustic measurements can be challenging due to the influence of various outdoor factors that affect the reproducibility of experiments. Background noise, as well as atmospheric conditions such as wind, humidity, and temperature can be difficult to control in open environments. Anechoic chambers are acoustically isolated rooms that provide a controlled environment to perform accurate and reproducible measurements. We want to characterize the noise emitted by an omnidirectional sound source called q-source [135], that can be modelled analytically as a monopole. We first perform an experimental campaign in which we extract the sound pressure at two microphones in the anechoic chamber. Then, we employ our acoustic solver to numerically solve the same problem. Finally, we compare the obtained results with the analytical solution. We remark again that, although the problem here is very simple, it is fundamental to understand what are the limitations of the employed acoustic hardware and to compare the numerical and the analytical solutions. This overall characterization of the q-source in a controlled setting is particularly relevant in view of future usage in complicated context, such as the scattering of tyre grooves, where the geometry is complex. In such cases, there is no analytical solution available, and only a computational model can assist in distinguishing any spurious frequencies that might be introduced by the hardware employed during the experiment.

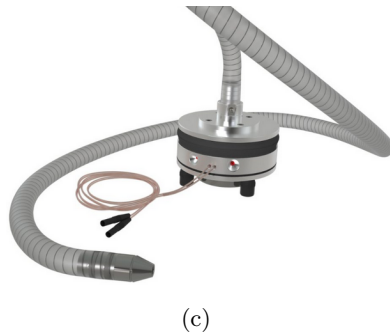
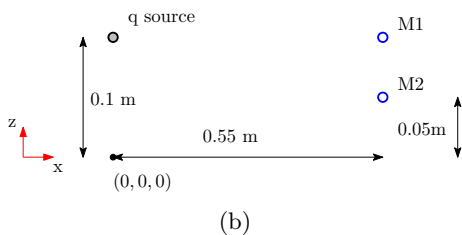
5.5.1 Experimental Setup

The experimental campaign was conducted in the anechoic chamber at the inter-departmental Polimi Sound and Vibration Laboratory (PSVL) of Politecnico di Milano. The main objective is to understand how the q-source behaves in the environment of the anechoic chamber. The size of the room is $4\text{ m} \times 4\text{ m} \times 4\text{ m}$ and during the tests it is in a semi-anechoic configuration, meaning that of the six walls only the floor is purely reflective, while the remaining walls absorb the acoustic waves minimizing spurious reflections and mimicking free field conditions. The measurement setup is sketched in Figure 4.10.

By denoting with $(0, 0, 0)$ the floor centre of the room, the q-source is placed at $\mathbf{x}_q = (0, 0, 0.1\text{ m})$. Next, we place two microphones M1, M2 at $(0, 0.55\text{ m}, 0.1\text{ m})$ and $(0, 0.55\text{ m}, 0.05\text{ m})$, respectively. The q-source should be an omnidirectional source, but due to the nature of the hardware some directivity is expected due to a nozzle at the end



(a)



(c)

Figure 5.10: (a) Q-source placed inside the anechoic room, alongside the employed microphones. (b) Schematic representation of the experimental setup. (c) The employed sound generator, the q-source.

of the q-source, see Figure 4.10c. A white noise input is given to the q-source and it is recorded and employed in the computational and analytical model as described in the next Section. The data was acquired at 25 kHz for 20 s.

5.5.2 Sound Source

As already mentioned, we measure the voltage input given to the q-source. This allows us to reproduce the same forcing term both in the computational model and in the analytical model. However, we need to process the source term in order to make it more coherent with the computational strategy, see Figure 4.11. First, instead of the 20 s of acquisition of the experimental data, we consider only the last two seconds. Then, given the voltage $q(t)$ we perform a Fast Fourier Transform, obtaining in the frequency domain $q(\omega)$. Now, we convert the acquired data with the sensitivity map given by the producer of the q-source from Volt to Volume Acceleration, obtaining $Q(\omega)$. Next, we apply a low pass filter, where we select as cut off frequency 2000 Hz

obtaining $\widehat{Q}(\omega)$. In the computational model, we take into account this choice, providing a computational grid that must resolve up to 2000 Hz. Next, we perform an inverse Fast Fourier Transform obtaining the final time dependent volume acceleration $\widehat{Q}(t)$. In Figure 4.12 we plot an extract of the input signal $q(t)$ and the filtered signal $\widehat{Q}(t)$. Last, we interpolate the obtained data from 25 kHz to 100 kHz required by the CFL for the acoustic simulation.

5.5.3 Analytical Model

Let $\Omega = \mathbb{R}^2 \times (0, \infty)$ and let Γ_b be the plane $z = 0$. The acoustic problem in the anechoic chamber can be formulated as follows:

$$\begin{aligned} \frac{1}{c_0^2} \frac{\partial^2 p'}{\partial t^2} - \Delta p' &= \rho_0 Q(t) \delta(\mathbf{x} - \mathbf{x}_q), && \text{in } \Omega_a \times (0, T], \\ \frac{\partial p'}{\partial \mathbf{n}} &= 0, && \text{on } \Gamma_b \times (0, T], \\ p'(\mathbf{x}, 0) &= 0, && \mathbf{x} \in \Omega_a, \\ \frac{\partial p'}{\partial t}(\mathbf{x}, 0) &= 0, && \mathbf{x} \in \Omega_a, \end{aligned} \quad (5.3)$$

where $\rho_0 = 1.225 \text{ Pa}$ is the density of the air and $c_0 = 343 \text{ m s}^{-1}$ is the speed of sound. Problem (4.3) cannot be solved by directly employing the fundamental solution described in Section 2.3.2, because of the floor Γ_b . With the objective to extend the problem on the whole \mathbb{R}^3 , we introduce a mirror image of the monopole at $-\mathbf{x}_q$ in order to reproduce the effect of the purely reflective boundary Γ_b , see Figure 4.13. Now, we can apply the strategy introduced in Section 2.3.2. Let us denote with r_1 the distance between the monopole and the microphone M1, $r_1 = |\mathbf{x}_q - \mathbf{x}_1|$ and with $r_2 = |-\mathbf{x}_q - \mathbf{x}_1|$ the distance between the mirrored monopole and the microphone M1. The solution computed at M1 is:

$$p'(\mathbf{x}_1, t) = \frac{Q(t)}{4\pi r_1} \exp(-jkr_1) + \frac{Q(t)}{4\pi r_2} \exp(-jkr_2),$$

and we compute the frequency response function:

$$T(\mathbf{x}_1) = \frac{p'(\mathbf{x}_1, t)}{Q(t)} = \frac{1}{4\pi r_1} \exp(-jkr_1) + \frac{1}{4\pi r_2} \exp(jkr_2).$$

The solution for the second microphone M2 is analogous.

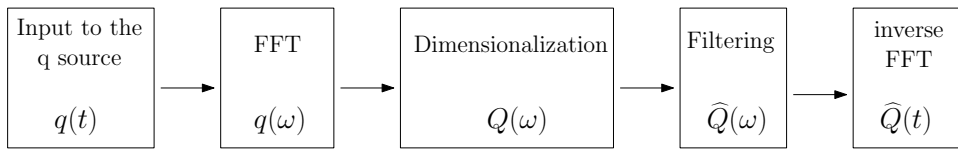


Figure 5.11: Scheme of the processing of the voltage input measured from the q -source. The final employed signal is $Q(\mathbf{x}, t)$.

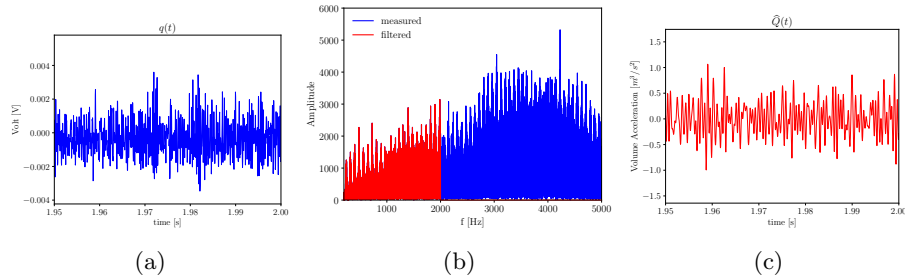


Figure 5.12: (a) Extract of the input source $q(t)$. (b) Comparison between the source spectra before and after the application of a low pass filter. (c) Extract of the input source after the filtering operation $\hat{Q}(t)$.

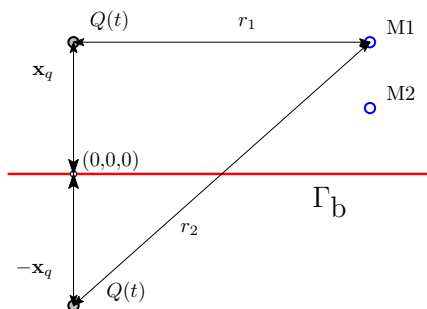


Figure 5.13: Sketch of the mirroring strategy. We added a specular source and we employ it to compute the effect of the floor Γ_b .

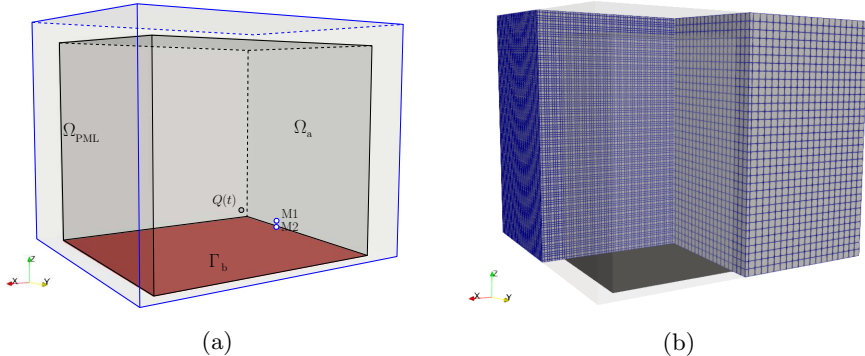


Figure 5.14: Computational model of the anechoic chamber. (a) Sketch of the computational domain with the boundary conditions. In red, the Neumann boundary. In blue, the hull of the PML. (b) Discretization of the computational domain. On the clip xz we show the computational grid with the degrees of freedom. On the clip yz we show the elements of the grid.

5.5.4 Computational Setup

Instead of solving the whole domain of the anechoic room, we decide to simulate a smaller domain to reduce the computational cost. We consider $\Omega_a = (-L_\Delta, L) \times (-L_\Delta, L) \times (0, L)$, with $L = 1$ m and $L_\Delta = 0.15$ m, see Figure 4.14a. On the floor, Neumann boundary conditions are imposed to model the semi-anechoic configuration of the chamber. Next, we extend the domain by including the PML hull in order to guarantee full absorbing at the boundaries. The PML domain extends for 0.15 m in each normal direction. The whole computational domain has been discretized with $\Delta x = 0.05$ m, employing a polynomial degree of $r = 3$ and by fixing the $\Delta t = 10^{-5}$ s. We simulated until $T = 2$ s. The time scheme is Leap Frog. In the PML region we placed three acoustic elements, as can be noticed from 4.14b. We highlight that with $\Delta x = 0.05$ m and being the minimum wave length at $\lambda_{\min} = c_0/2000$ Hz = 0.1715 m, we are placing at least three elements of degree $r = 3$ per wave-length.

5.5.5 Acoustic Results

For the validation of the results the frequency response function between the input (the q-source) and the output (microphone M1 and M2). The obtained results are reported in Figure 4.15. The numerical results are aligned with the analytical model. There is an important misalignment between the experimental measured data and the com-

puted numerical and analytical solutions. In fact, we believe that the hardware of the q-source, made basically by little tubes inside the nozzle, introduces spurious resonances that deteriorate the quality of the measurements. The effect of these resonances, however, are in the range of the precision of the instrument, that from the product data sheet is ± 2 dB.

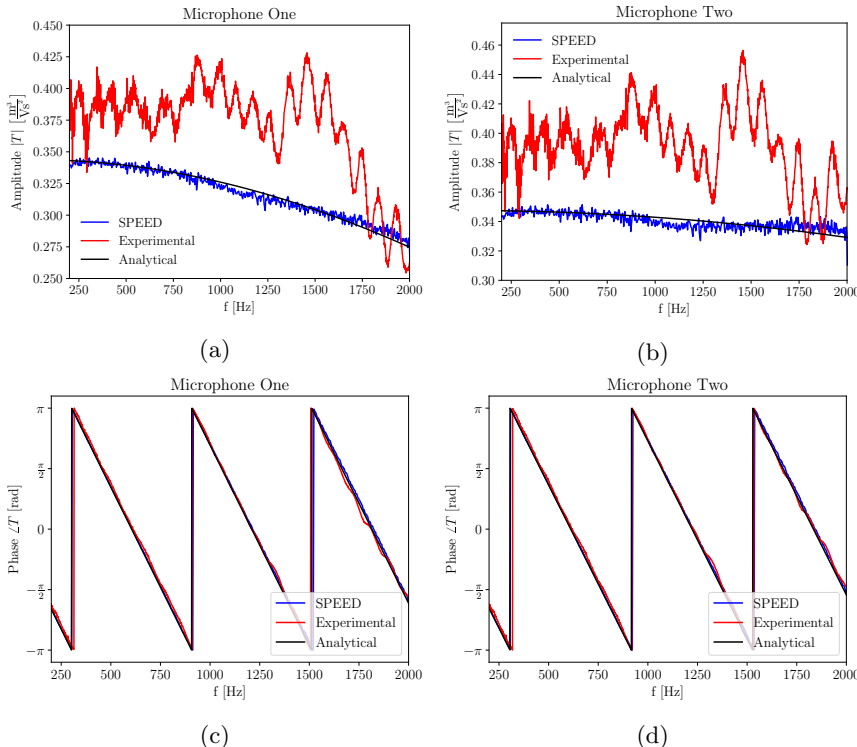


Figure 5.15: Comparison of the computed numerical data with SPEED, the measured data and the analytical frequency response function. (a) Amplitude of the frequency response function computed at microphone M1. (b) Amplitude of the frequency response function computed at microphone M2. (c) Phase of the frequency response function computed at microphone M1. (d) Phase of the frequency response function computed at microphone M2.

5.6 Noise Box

As a final test case, we consider the sound propagation in a confined real geometry that resembles the cockpit of a car and we compare the obtained numerical solution with the one provided by COMSOL Multiphysics®. The so called Noise Box (see Fig. 4.16) is a geometry that

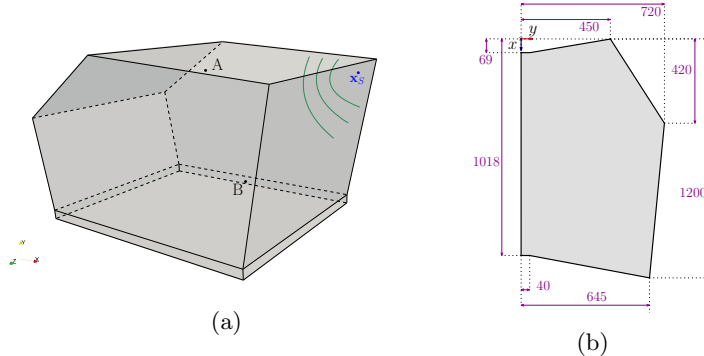


Figure 5.16: (a) Three-dimensional view of the domain of the Noise Box. A and B are the positions of the selected microphones, where $A = (0.424 \text{ m}, 0.595 \text{ m}, 0.151 \text{ m})$ and $B = (0.9 \text{ m}, 0.224 \text{ m}, 0.528 \text{ m})$. (b) Quoted computational domain of the Noise Box. The spanwise length is 0.825 m. In the figure, units are expressed in millimeters.

represents a simplified car cockpit, introduced in [89]. Each wall is modelled as a real solid wall, meaning that it will show partially reflective and partially absorbing behaviour, by setting a wall impedance of $Z = 32\,206 \text{ Pa s m}^{-1}$. As forcing term we consider a monopole sound source $f(\mathbf{x}, t) = \delta(\mathbf{x} - \mathbf{x}_S) \sin(2\pi f_0 t)$, where $\delta(\mathbf{x} - \mathbf{x}_S)$ is the Dirac delta centered in $\mathbf{x}_S = (1.15 \text{ m}, 0.595 \text{ m}, 0.065 \text{ m})$ and $f_0 = 162 \text{ Hz}$. We set the density of air to be $\rho_0 = 1.204 \text{ kg m}^{-3}$ and the speed of sound $c_0 = 343 \text{ m s}^{-1}$. For the space discretization we set the polynomial degree $r = 2$ and we fix $\Delta x = 0.04 \text{ m}$. For the time discretization we consider a Newmark scheme with $\gamma = 0.5$ and $\beta = 0.25$, with $\Delta t = 5 \times 10^{-6} \text{ s}$, with a final time of $T = 0.5 \text{ s}$. We solve for the same setup both with COMSOL and AeroSPEED and we compare the two results. From the results reported in Fig. 4.17a, we note the initial transient state, up to around $t \approx 0.05 \text{ s}$. The acoustic monopole is injecting energy in the system, that is not fully dissipated, up until $t \approx 0.1 \text{ s}$. After this transient, the system reaches a stationary regime, where the amount of energy dissipated by the system is balanced by the amount of energy injected. The numerical solution obtained with AeroSPEED perfectly matches the numerical solution obtained with COMSOL. In Fig. 4.18 we see the stationary pressure waves inside the Noise Box from different snapshots of the solution.

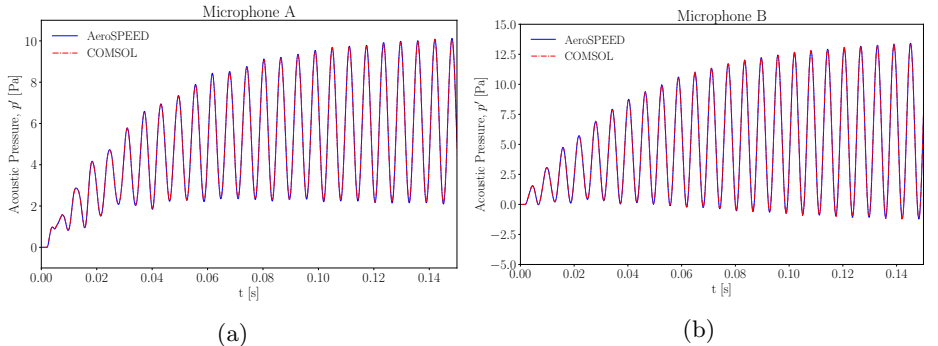


Figure 5.17: Computed acoustic pressure measured by microphone A and B with both AeroSPEED and COMSOL.

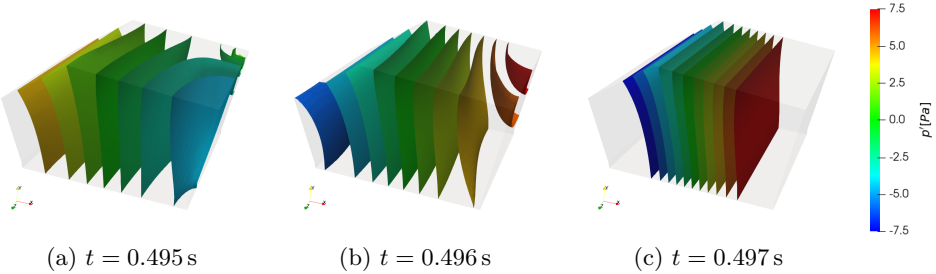


Figure 5.18: Snapshots of the computed pressure fluctuations $p' = p - \bar{p}$, where \bar{p} is the average pressure, inside the Noise Box, for $t = 0.495, 0.496, 0.497 \text{ s}$. The selected contour levels are from -7.5 Pa to 7.5 Pa with a step of 1.5 Pa .

5.7 Conclusions

In this chapter we gave an overview of the computational capabilities of the employed acoustic solver AeroSPEED. We first started by validating our acoustic solver with an industrial software, showing the advantages of the Spectral Element Method over a Lagrangian Finite Element method, in terms of accuracy versus efficiency. We then validated our implementation for impedance and absorbing boundary conditions and for the Perfectly Matched Layer. These boundary conditions are critical both to solve acoustics in confined real geometries and to solve free field problems. We then applied our solver to solve two real acoustic problems. The first one, aimed at providing and verifying a numerical tool for addressing the noise generated inside the anechoic room at PSVL. In the second case, we applied the acoustic solver to a confined geometry, the Noise Box.

Chapter 6

Numerical Results on Aeroacoustic Problems

In this chapter we solve aeroacoustic problems employing the segregated strategy. First, we solve a flow problem employing the open-source finite volume library OpenFOAM[76]. Then we employ the projection algorithm described in Section 2.8 combined with our intersection algorithm described in Section 2.9 to project the noise source coming from the flow problem onto the acoustic space. The accuracy of the projection method combined with the intersection strategy has already been assessed in Section 3.6 and Section 2.9. Finally, we employ the acoustic DGSEM solver, whose performances have been shown in Chapter 4, to solve the inhomogeneous acoustic problem with the forcing term coming from the flow solution. In order to best assess the capabilities of our solver AeroSPEED, we solve problems with increasing difficulty. The first problem is a semi-analytical problem, where the two-dimensional flow solution is given by a potential flow solution, the corotating vortex pair. The rotating quadrupole analytical solution to the acoustic problem [108] is then compared with the computed numerical solution. Next, we focus our study on a simple two-dimensional laminar problem, namely the flow around a square cylinder. Next, we consider the turbulent three-dimensional flow around two tandem cylinders. This case is characterized by a high Reynolds number, and turbulence modelling is required in order to capture the most critical flow features. From an acoustic point of view, however, the problem is still considered two-dimensional. Finally, we simulate the flow around a wall mounted side view mirror. The problem is challenging since the

flow is fully three dimensional, highly unsteady and again turbulence modelling is mandatory. The computational cost of the flow problem is high. The inherited acoustic problem is also complex. The acoustic problem is three dimensional, and the expected noise is broadband and generated by the complex separated flow field past the bluff side view mirror geometry.

6.1 Potential Flow with Corotating Vortex Pair

We apply our hybrid aeroacoustic computational strategy to the corotating vortex pair problem [100]. For this two-dimensional test case, the flow solution can be computed analytically based on potential flow theory. Furthermore, an analytical expression for the pressure fluctuations is obtained at the far field, see [100] or [98] for a detailed derivation of the analytical solution. We assume that the flow field induced by the corotating vortex pair is inviscid and incompressible. This assumption allows us to employ a complex potential function $\Phi(z, t) : \mathbb{C} \times (0, T] \rightarrow \mathbb{C}$ to define the flow field, namely:

$$\Phi(z, t) = \frac{\Gamma}{2\pi i} \ln(z - b(t)) + \frac{\Gamma}{2\pi i} \ln(z + b(t)), \quad (6.1)$$

where Γ is the circulation, i is the imaginary unit and $b = r_0 \exp(i\omega t) \in \mathbb{C}$ are the rotating centres of the vortices, with ω denoting the rotational speed defined as $\omega = \Gamma/(4\pi r_0^2)$ and r_0 the distance from the origin, see Figure 5.1. We introduce the rotating Mach number $M_r = \Gamma/(4\pi r_0 c_0)$, where c_0 is the speed of the wave. The period of the rotating monopoles is $T_f = 8\pi^2 r_0^2/\Gamma$, while the emitted period of the acoustic wave is $T_a = T_f/2$. From the complex potential in eq. (5.1) we compute the two-dimensional fluid flow velocity $\mathbf{u} = [u; v]$ as

$$u - iv = \frac{\partial}{\partial z} \Phi(z, t), \quad (6.2)$$

and then we compute the Lighthill's stress tensor $\mathbf{t} = \rho_0(\mathbf{u} \otimes \mathbf{u})$. As discussed in [125], the far field solution for the pressure fluctuations $p' = p - \bar{p}$ is given by:

$$p'(z, t) = -\frac{\rho_0 c_0^2}{64\pi^3} \left(\frac{\Gamma}{r_0 c_0} \right)^4 [J_2(kr) \sin(2(\theta - \omega t)) + Y_2(kr) \cos(2(\theta - \omega t))],$$

where J_2 and Y_2 are respectively the first and second kind Bessel functions, $k = 2\omega/c_0$ and $z = r \exp(i\theta)$. As already showed in [85], a

$\Gamma \text{ [m s}^{-2}\text{]}$	M_r	$T_a \text{ [s]}$	$r_0 \text{ [m]}$
0.98696	0.0785397	40	1
$\rho_0 \text{ [kg m}^{-3}\text{]}$	$c_0 \text{ [m s}^{-1}\text{]}$	$\omega \text{ [s}^{-1}\text{]}$	$r_c \text{ [m]}$
1	1	0.0785397	0.2

Table 6.1: Parameters employed for the rotating vortex pair test case.

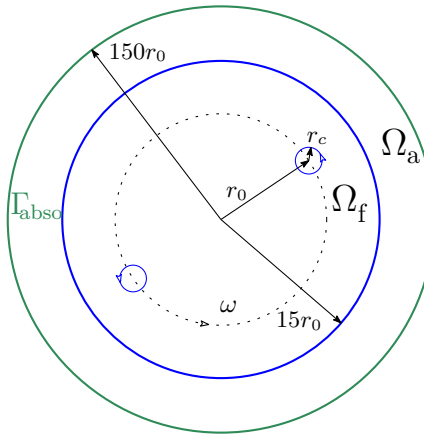


Figure 6.1: Sketch of the domain for the corotating vortex pair problem. The model is not to scale.

desingularization model is required in order to avoid numerical issues in representing the source vortices. Here, we employ the Scully model [131] getting

$$u_\theta(r_v) = \frac{\Gamma r_v}{2\pi(r_c^2 + r_v^2)}, \quad (6.3)$$

where r_c is the desingularized core radius, $u_\theta(r_v)$ is the tangential velocity and r_v is the distance from the vortex core center.

Fluid Setup

We consider the corotating vortex pair problem with the parameters summarized in Table 5.1. The fluid domain is a circle Ω_f with radius $15r_0$. The flow solution is computed by employing the complex velocity in eq. (5.2) and then the divergence of the Lighthill's tensor $\nabla \cdot \mathbf{T} = \rho_0 \nabla \cdot (\mathbf{u} \otimes \mathbf{u})$ is computed as a post-processing of the flow velocity. The solutions are saved at each time instant with time step $\Delta t_f = 0.02 \text{ s}$. Since the solution is periodic, we store the solutions up to T_a .

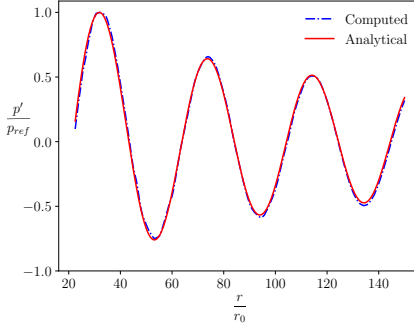


Figure 6.2: Comparison between the analytical far field solution and the computed numerical solution obtained with the hybrid approach and by employing the vortex core model. The results have been normalized with respect to $p_{ref} = \max(p - \bar{p})$ to take into account the energy disparity introduced by the vortex model.

Acoustic Setup

The acoustic domain Ω_a is a circle of radius $150r_0$. A circular domain has been chosen since the employed absorbing boundary conditions work better when the incident wave is orthogonal to the boundary, see [48]. On the external boundary Γ_{abs} absorbing conditions are imposed. We employ a polynomial degree $r = 2$ for the SE discretization. We consider a structured o-grid mesh with a total of 57 500 elements. Each vortex is resolved by at least 15 elements. For the time discretization, an implicit Newmark method is used, see for instance [78] or [13], with $\beta = 0.5$, $\alpha = 0.25$ and $\Delta t_a = 0.02$ s. In order to avoid spurious oscillation due to the non-consistent initial conditions, see [51] or [88], the following time ramp is multiplied to the source term $g(t) = \frac{1}{2} \left(1 - \cos \left(\pi \frac{t}{T_f} \right) \right)$, where $T_f = T_a$, up to T_f .

Numerical results

The numerical solution obtained with the proposed algorithm matches the analytical solution, as it is shown in Figure 5.2, where we sampled the pressure fluctuations p' along the line $y = 0$ with $x > 0$ at $T = 380$ s. The results obtained with the analytical solution have been normalized to a reference pressure $p_{ref} = \max(p')$ in order to take into account the desingularization effect in eq. (5.3), see for instance [126]. The acoustic field generated by a pair of corotating vortices is a rotating acoustic quadrupole as can be seen from Figure 5.3.

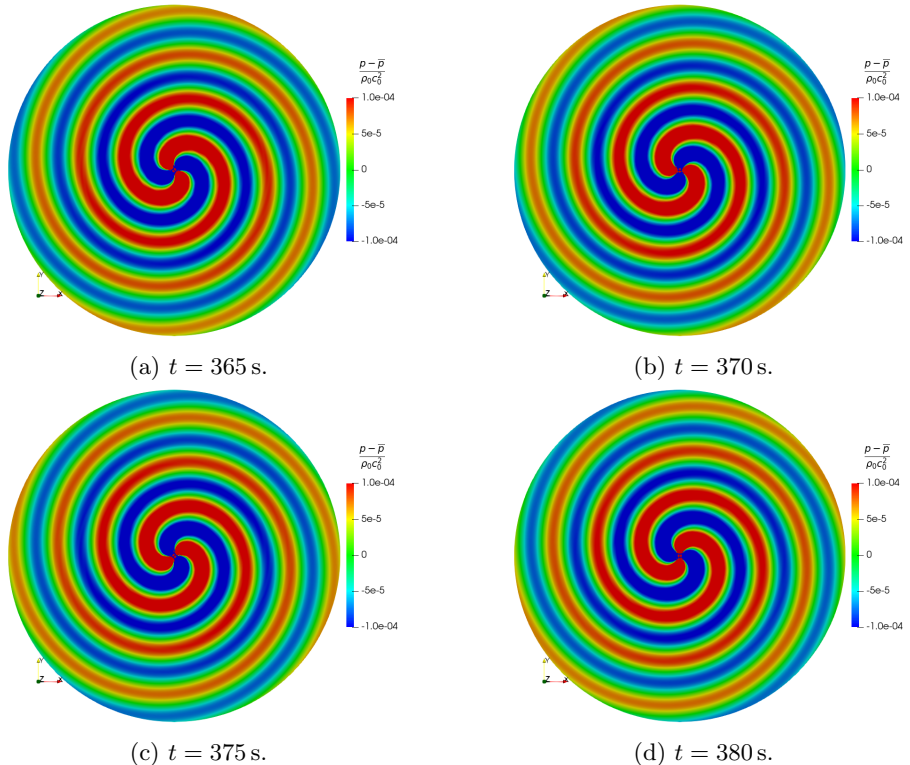


Figure 6.3: Snapshots of the computed numerical solution for the corotating vortex pair for $t = 365, 370, 375, 380$ s.

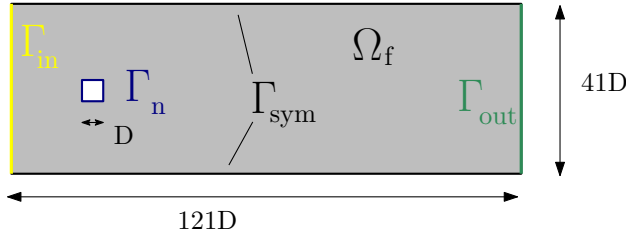


Figure 6.4: Computational domain for the flow problem. Here Γ_{in} denotes the inlet boundary condition, Γ_{out} denotes the outlet boundary condition, Γ_n is the Neumann boundary on the square cylinder and Γ_{sym} is the symmetric boundary.

	Γ_n	Γ_{sym}	Γ_{in}	Γ_{out}
$\mathbf{u} [\text{m s}^{-1}]$	$\mathbf{u} = \mathbf{0}$	$\mathbf{u} \cdot \mathbf{n} = 0$	$\mathbf{u} = (68.6, 0, 0)$	$(\nabla \mathbf{u}) \mathbf{n} = \mathbf{0}$
$p [\text{Pa}]$	$\nabla p \cdot \mathbf{n} = 0$	$\nabla(\mathbf{u} - (\mathbf{u} \cdot \mathbf{n})\mathbf{n}) \cdot \mathbf{n} = 0$ $\nabla p \cdot \mathbf{n} = 0$	$\nabla p \cdot \mathbf{n} = 0$	$p = 0$

Table 6.2: Boundary conditions for the laminar flow around a square cylinder. The boundary definitions are detailed in Figure 5.4.

6.2 Laminar Flow Around a Square Cylinder

We consider the case of a laminar flow around a square cylinder, see for instance the Direct Numerical Simulation (DNS) performed by [74] or the solution obtained with a Curle analogy in [140]. When a rigid squared cylinder is placed in a uniform flow, it exhibits strong vortex shedding, resulting in fluctuating forces on the cylinder due to the alternating pressure highs and drops at the wake. These forces generate pressure waves that propagate through the domain. For laminar flows, the main frequency radiated from the body is associated with the Strouhal number and the intensity of the observed noise is proportional to the fluctuation of the forces on the cylinder. The flow solution has been computed by employing the Pressure Implicit Splitting Operator (PISO) method implemented in OpenFOAM [149].

Fluid Setup

A laminar two-dimensional incompressible simulation of a fluid flow around a square cylinder is performed. Let $D = 3.28 \times 10^{-5} \text{ m}$ be the length of the square cylinder, $U = 68.7 \text{ m s}^{-1}$ be the inlet velocity and $\nu = 1.5 \times 10^{-5} \text{ m}^2 \text{ s}^{-1}$ the kinematic viscosity. The Reynolds number is $\text{Re} = 150$ and the Mach number is $\text{Ma} = 0.2$. The flow computational domain Ω_f is $(-20.5D, 100.5D) \times (-20.5D, 20.5D)$, see Figure 5.4. A

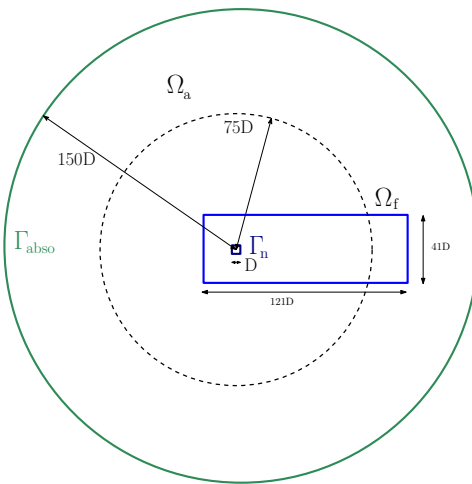


Figure 6.5: Computational domain of the flow problem and the acoustic problem. The square cylinder has a diameter $D = 3.28 \times 10^{-5}$ m and the fluid domain is a rectangle of size $121D \times 41D$. The acoustic domain is a circle of radius $150D$, centered at the centre of the square. The dotted line represent the sampled probes in the acoustic domain employed to compute the directivity, see Fig. 5.9.

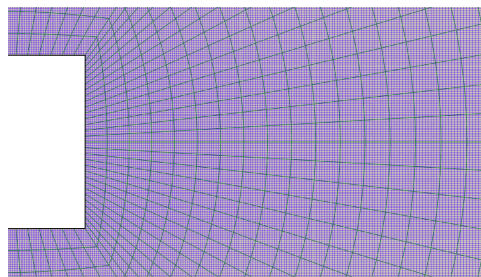


Figure 6.6: Detail of the acoustic (green) and fluid (blue) computational grids around the square cylinder for the aeroacoustic test case. A structured o-grid is employed for the acoustic problem and a structured h-grid is employed for the flow problem.

fixed velocity is prescribed at the inlet Γ_{in} . On the upper and lower wall Γ_{sym} symmetry conditions are employed. No slip conditions are applied on the cylinder walls Γ_n . Zero gradient pressure conditions are applied at the wall of the cylinder and at the inlet. On the outlet, the pressure is set to zero, while a zero gradient condition is imposed for the velocity, see Table 5.2 and Figure 5.4. A block structured h-grid around the square cylinder is used, employing 970 000 elements. In Fig. 5.6, a zoom of the fluid grid is shown. The computational time step is $\Delta t = 10^{-9}$ s.

Acoustic Setup

To minimize spurious reflections, the acoustic domain Ω_a is a circle of radius $150D$, with an internal square hole of side D , see Figure 5.5. On the external boundary Γ_{abs} , absorbing conditions are imposed. On the solid wall Γ_b homogeneous Neumann boundary conditions are imposed. The coupling region is given by $\Omega_a \cap \Omega_f = \Omega_f$. A smoothing function is employed in order to let the sound source term decay to avoid the well known spurious noise generation due to the abrupt domain cut on the wake, see for instance [108] or [94]. We used the following spatial smoothing function:

$$g(x) = \begin{cases} 1 & x < r_i, \\ \frac{1}{2} \left(1 + \cos(\pi \frac{x - r_i}{r_o - r_i}) \right) & x \geq r_i, \end{cases}$$

where r_i is the initial filtering position, while r_o is the end of the fluid domain. In this case, it is sufficient to apply the smooth function only downstream and along the x direction, so that $r_i = 65D$ and $r_o = 105.5D$. The fluid solution is sampled every 10 fluid time steps, meaning that $\Delta t_a = 10^{-8}$ s = $10\Delta t_f$. The expected main frequency is the Strouhal frequency. The acoustic discretization close to the square is of h-type, with $h_a = D/10$. Then the grid is structured and an o-type grid is employed. The polynomial degree chosen is $r = 4$. The whole acoustic grid has around 1 261 500 degrees of freedom. The main wavelength associated to the lift force is $\lambda \approx 32.5D$ and around 40 nodes per wavelength where placed in the far field. The acoustic simulation was run for 5×10^{-5} s, starting from a fluid time of $t_f = 10^{-4}$ s, hence with a fully developed flow field. A zoom of the acoustic grid is shown in Fig 5.6. Note that the acoustic element size is larger than the size of the fluid elements.

	St	\bar{C}_D	$C_{L,rms}$	$C_{L,peak}$
Experiments [109, 136]	0.148-0.155	1.4	-	-
Doolan [44]	0.156	1.44	0.296	-
Ali [140]	0.16	1.47	0.285	-
Inoue [74]	0.151	1.4	-	0.4
Current study	0.156	1.43	0.281	0.3976

Table 6.3: Comparison of the results on the laminar flow around the cylinder with analogous results available in the literature, at $Re = 150$.

Numerical Results

The flow around the squared cylinder at $Re = 150$ is laminar and it presents the Von Karman vortex street pattern. We define the drag and lift coefficients as $C_D = \frac{F_D}{\frac{1}{2}\rho_0 U^2 A}$ and $C_L = \frac{F_L}{\frac{1}{2}\rho_0 U^2 A}$ where F_D and F_L are the drag and lift forces, respectively, with $A = DH$, being H the width of the domain and having chosen $H = D$. The coefficients C_L and C_D are displayed in Figure 5.7. We consider the Strouhal number $St = f_0 \frac{D}{U}$, based on frequency f_0 of C_L . In Table 5.3 we compare our results with those available in the literature. The Strouhal number matches the results obtained by [44] and it is aligned with the experiments [109, 136] and the compressible DNS performed by [74]. The intensity of the noise emitted by the square cylinder depends mainly on the amplitude of the force fluctuations. Hence, during the flow computation we evaluate the root mean squared (rms) values. By defining \bar{C}_D, \bar{C}_L as the average of C_D (resp. C_L), we compute the rms values of the lift coefficient as $C_{L,rms} = \sqrt{(C_L - \bar{C}_L)^2}$ and we also identify $C_{L,peak} = \max(|C_L|)$. Again, from Table 5.3, we see that our results are in agreement with the ones available in literature. Finally, we compute the acoustic field, namely the noise induced by the flow around the square cylinder. From Figure 5.8, we see the characteristic dipole pattern, that is mainly due to the lift force acting on the cylinder. The results are comparable with the compressible simulations, presented for instance in [41] and [74]. To further validate our acoustic results, we computed the directivity from $p'_{rms} = \sqrt{(p - \bar{p})^2}$. The obtained directivity pattern is in good agreement with the references, see [74] and [140].

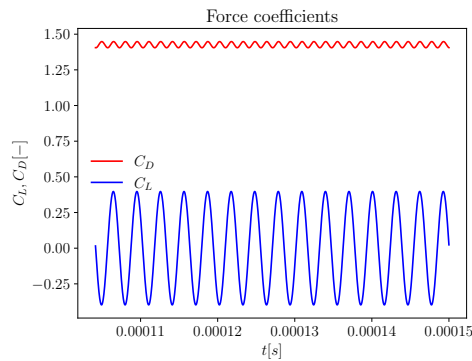


Figure 6.7: Computed lift C_L and drag C_D force coefficients.

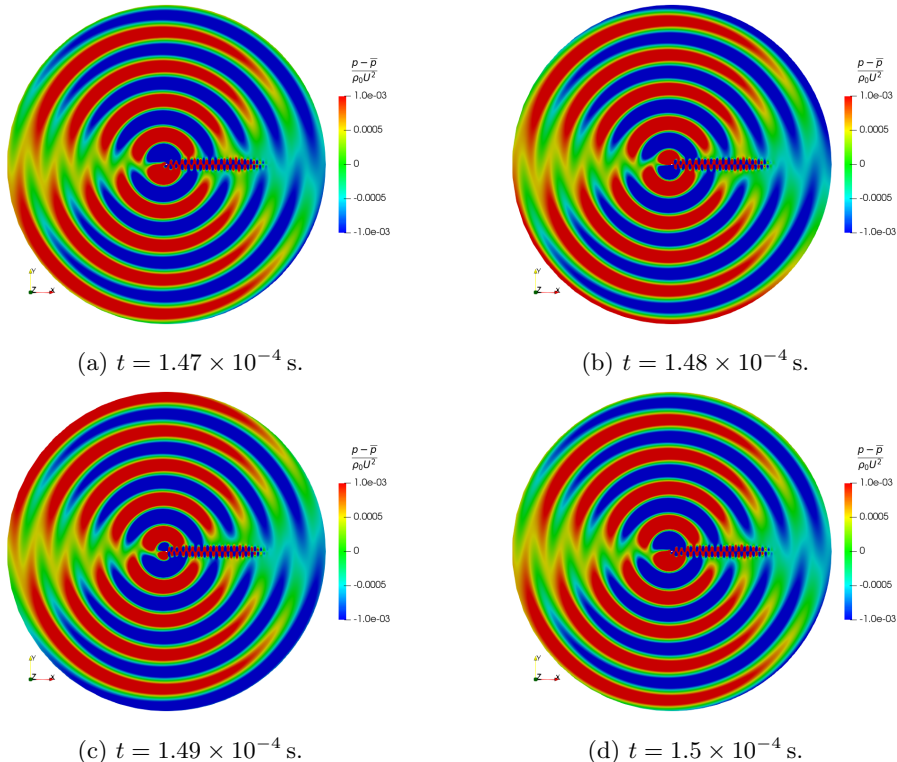


Figure 6.8: Snapshot of the computed acoustic pressure field at $t = 1.47 \times 10^{-4}$ s, 1.48×10^{-4} s, 1.49×10^{-4} s, 1.5×10^{-4} s.

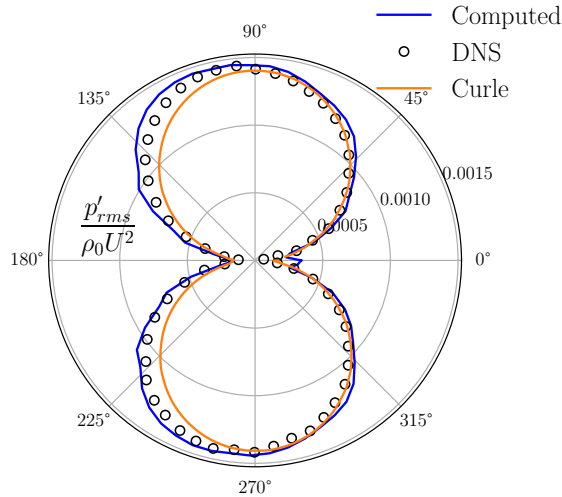


Figure 6.9: Directivity pattern. The adimensionalized p'_{rms} is sampled on a circumference of radius $75D$, see Fig. 5.5. Comparison with the DNS in [74] and the Curle computations of [140].

6.3 Turbulent Flow Around a Tandem Cylinder

The next aeroacoustic application is the noise generated by a tandem cylinder, a well-known test case that has been subject of a dedicated workshop [90]. The flow simulation has been performed with OpenFOAM [149], while the aeroacoustic coupling has been implemented in AeroSPEED [17]. Simulating the turbulent flow around two tandem cylinders at high Reynolds number is a challenging problem due to the unsteadiness and the complex flow structures that have to be captured. The separation point on the front cylinder moves on the surface, generating a shear layer that rolls up forming a periodic vortex shedding that impinges on the rear cylinder. As a result, a tonal and broadband noise is generated. Proper turbulence models are crucial to simulate at a reasonable computational cost such a complex physics.

Flow Setup

The tandem cylinder problem configuration involves two cylinders of equal diameter $D = 0.057\text{ m}$ aligned along the streamwise direction at a distance of $3.7D$. A sketch of the computational domain is reported in Fig. 5.10. At the inlet a fixed velocity of $U_\infty = 44\text{ m s}^{-1}$ is set, with $\nu = 1.51 \times 10^{-5}\text{ m}^2\text{ s}^{-1}$ corresponding to a Reynolds number $Re =$

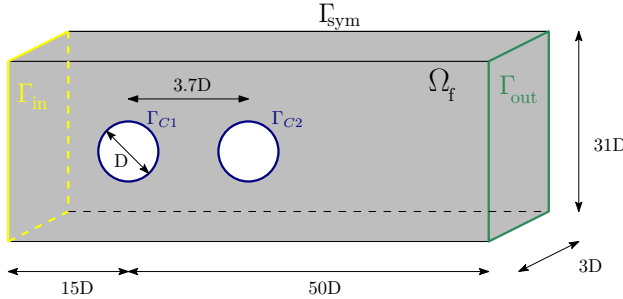


Figure 6.10: Computational domain for the flow problem. Γ_{in} denotes the inlet boundary. Γ_{out} denotes the outlet boundary. Γ_{C1} and Γ_{C2} are the front and rear cylinder's surface, respectively. Γ_{sym} denotes the remaining boundary.

	$\mathbf{u} [\text{m s}^{-1}]$	$p[\text{Pa}]$	ω	$k [\text{m}^2 \text{s}^{-2}]$
Γ_{in}	$\mathbf{u} = (44, 0, 0)$	$\nabla p \cdot \mathbf{n} = 0$	$\omega = 9.45$	$k = 2.904 \times 10^{-1}$
Γ_{out}	$(\nabla \mathbf{u}) \cdot \mathbf{n} = \mathbf{0}$	$p = 0$	$\nabla \omega \cdot \mathbf{n} = 0$	$\nabla k \cdot \mathbf{n} = 0$
Γ_{C1}	$\mathbf{u} = \mathbf{0}$	$\nabla p \cdot \mathbf{n} = 0$	ωWF	$kqRWF$
Γ_{C2}	$\mathbf{u} = \mathbf{0}$	$\nabla p \cdot \mathbf{n} = 0$	ωWF	$kqRWF$
Γ_{sym}	$\mathbf{u} \cdot \mathbf{n} = 0$ $\nabla(\mathbf{u} - (\mathbf{u} \cdot \mathbf{n})\mathbf{n}) \cdot \mathbf{n} = 0$	$\nabla p \cdot \mathbf{n} = 0$ $\nabla p \cdot \mathbf{n} = 0$	$\nabla \omega \cdot \mathbf{n} = 0$	$\nabla k \cdot \mathbf{n} = 0$

Table 6.4: Boundary conditions for the flow around the tandem cylinder. On the walls of the front and the rear cylinder wall functions (WF) are applied. ωWF is the wall function denoted as `omegaWallFunction` in OpenFOAM, see [115]. $kqRWF$ is the wall function denoted as `kqRWallFunction` in OpenFOAM.

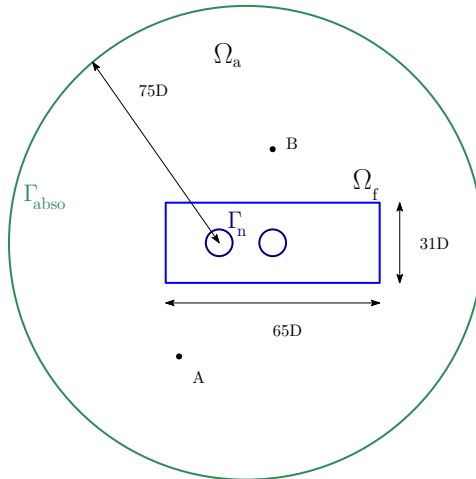


Figure 6.11: Aeroacoustics computational domain. The center of the computational domain is set at the center of the front cylinder. Microphone probes are located at $A = (-8.33D, 27.82D)$, and $B = (9.11D, 32.49D)$, with $D = 0.057\text{ m}$. We denote with Ω_a the acoustic domain, with Ω_f the fluid domain contained in Ω_a . We denote with Γ_{abso} the boundary of the external domain and with Γ_n the wall boundary of the tandem.

1.66×10^5 . On Γ_{C1} and Γ_{C2} , no slip conditions are imposed. At the outlet, a zero gradient condition is set. On the remaining boundaries, a symmetry condition is imposed, see Table 5.4 and see Figure 5.10. We choose a fixed time step of $\Delta t_f = 1.25 \times 10^{-5}\text{ s}$, we set the final time to $T = 0.35\text{ s}$, and we employ a second order backward difference formula. The height of the first cell near the wall corresponds to $y^+ \approx 30$, and proper wall functions are prescribed, see [137]. Following [62], we employ a DDES $k - \omega$ SST model to simulate the turbulent flow, see for instance [63] for more details. The unsteady DDES simulations has been initialized with a RANS solution obtained with the $k - \omega$ SST model. The initial values for the k and ω at the inlet have been chosen imposing a turbulence intensity of 1% and by employing as turbulent length scale the diameter D , see Table 5.4.

Acoustic Setup

Since the acoustic problem can be considered two-dimensional, we take as sound source only the average along the spanwise direction. A sketch of the computational domain for the aeroacoustic case is depicted in Fig. 5.11. On the cylinders $\Gamma_{C1} \cup \Gamma_{C2} = \Gamma_n$ rigid wall boundary con-

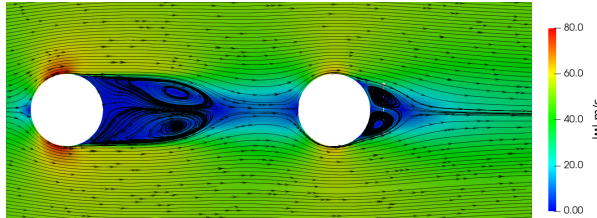


Figure 6.12: Average velocity magnitude $|\mathbf{u}|$ on the xy plane with streamlines.

ditions are imposed, while at the far field Γ_{abs} absorbing boundary conditions are considered. The fluid sound source is mapped each four time steps, namely the computational time step for the Lighthill's wave equation is $\Delta t_a = 5 \times 10^{-5}$ s. The chosen polynomial degree is $r = 2$ and the spacing at the far field is $\Delta x \approx 0.04$ m.

Flow Validation

The average flow field is characterized by a mostly symmetric recirculation regions after the cylinders, see Fig. 5.12. The first recirculation length is about two diameters D , aligned with the results of [62]. A visualization of the vortex structures in the instantaneous flow field, see Fig. 5.13, is made by employing the Q criterion, where $Q = \frac{1}{2} \left(\text{tr}(\nabla \mathbf{u})^2 + \text{tr}(\nabla \mathbf{u} \nabla \mathbf{u}) \right)$. In Fig. 5.14, we compare the prediction on the force coefficients with the results of a set of different numerical simulations collected in [90]. The results are quite heterogeneous due to the complexity of the problem and the numerous different strategies among the different research groups. We denote with C_D and C_L the mean drag and lift coefficients, and their root mean squared *rms* values as $\widetilde{C}_L, \widetilde{C}_D$, respectively. All the computed integral results are within the standard deviation from the literature data. For further comparison, we consider Fig. 5.15, where we plot the values of the pressure coefficient C_p along the cylinders and we compared it with the experiments [90], [105] and with the computations collected in [62]. The main differences are located in the aft of both cylinders, and are due to the prediction of a different pressure recovery, resulting in small shifts in the separation point locations. Overall, our flow predictions are aligned with the references.

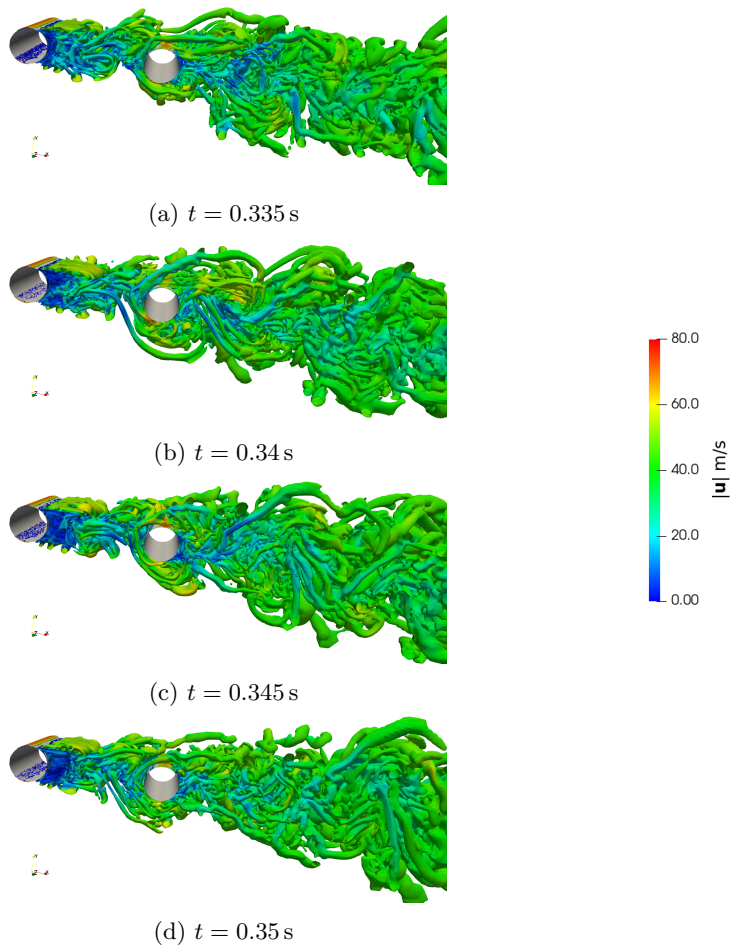


Figure 6.13: Different snapshots of the flow solution, with isosurfaces of $Q = 1000$ and colored with velocity magnitude.

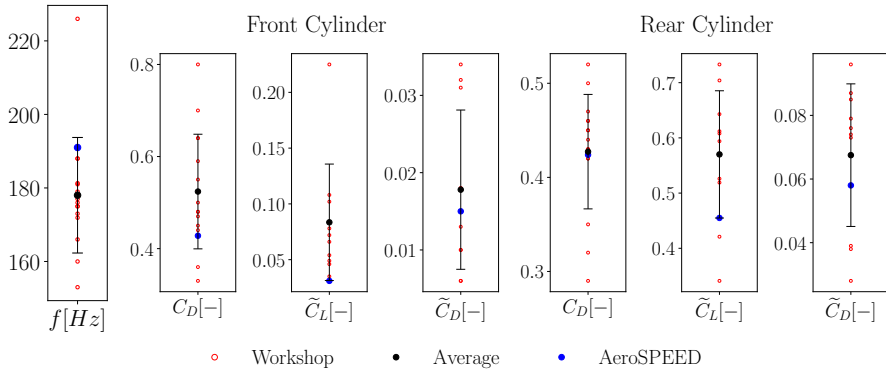


Figure 6.14: Comparison of the average drag forces and the *rms* for lift and drag of the two cylinders. With “Workshop” we denote the data taken from [90]. The lift frequency is common between the two cylinders. The bar is centred on the mean value of the available literature data, and the length of the bar is one standard deviation.

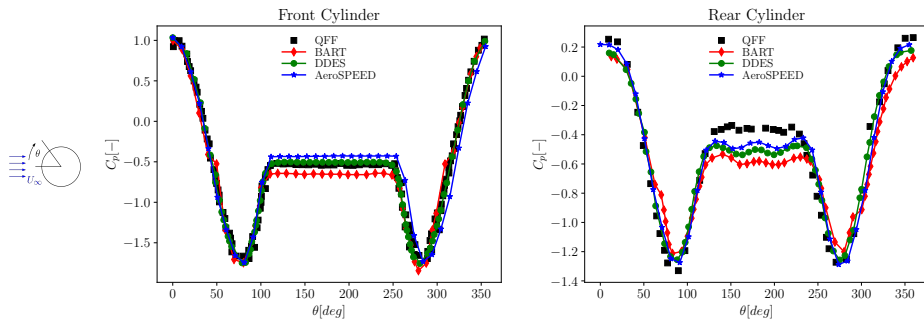


Figure 6.15: Average C_P distribution on the surface of the front and rear cylinders, where $C_P = \frac{\bar{p} - p_{ref}}{\frac{1}{2}\rho_0 U_\infty^2}$. With QFF we denote the data measured at the Quite Flow Facility [105], while BART denotes the Basic Aerodynamic Research Tunnel see [105] and with DDES we refer to the computed data in [62].

Aeroacoustic Validation

In Fig. 5.16, a snapshot of the pressure fluctuations induced by the tandem cylinder is shown. The acoustic pressure fluctuations are dominated by a dipole pattern induced by the lift force acting on the rear cylinder. As suggested by Fig. 5.14, the main contribution to the sound generation is indeed from the rear cylinder, being its \tilde{C}_L much larger than the front cylinder one. Also, we can observe the smaller structures coming from the flow compared with the larger wave lengths

solved by the acoustics. In Fig. 5.17 we compare the sound spectra obtained with different methodologies, such as the Curle method described in Section 2.4.4, another Curle analogy with a spanwise corrections proposed in [148], experimental data from QFF [90] and the results computed with AeroSPEED. We observe that, although all the aeroacoustic solutions predict the peak coming from the lift frequency of the rear cylinder, AeroSPEED better matches the *PSD* values of the experimental data.

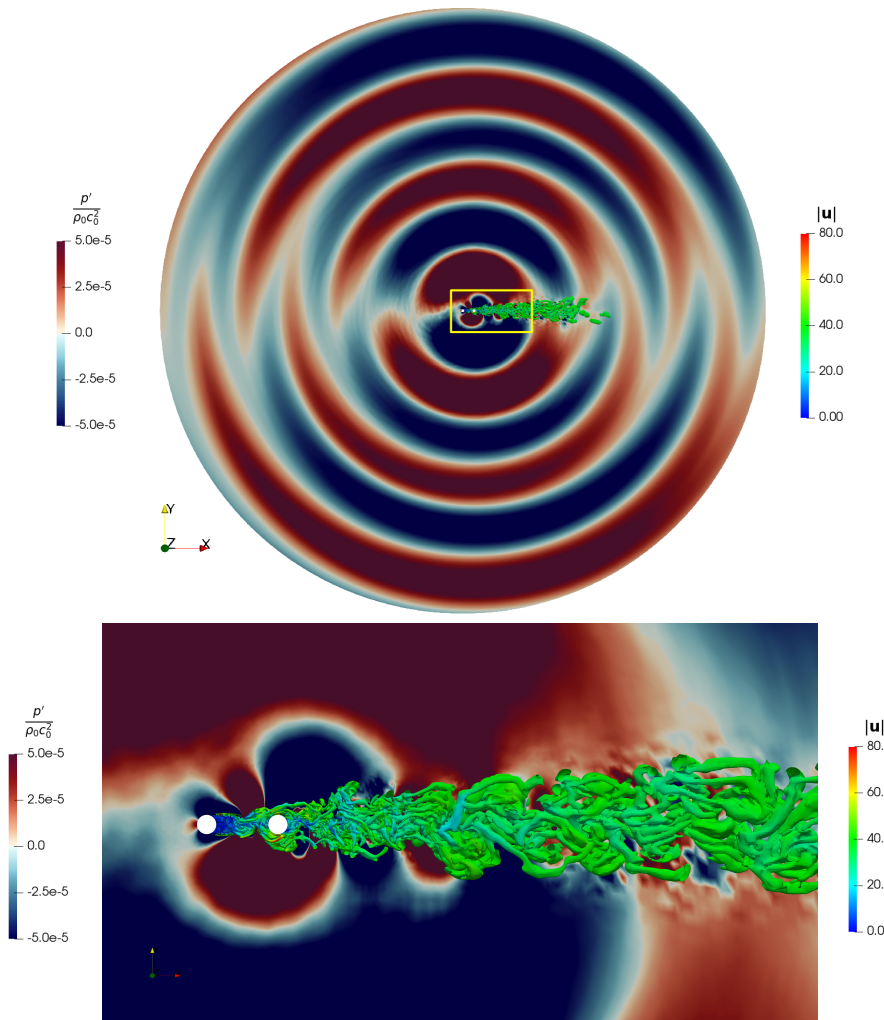


Figure 6.16: Snapshot of the fluctuating pressure (from the acoustic computations), and Q criterion colored with the velocity magnitude (from the flow computations).

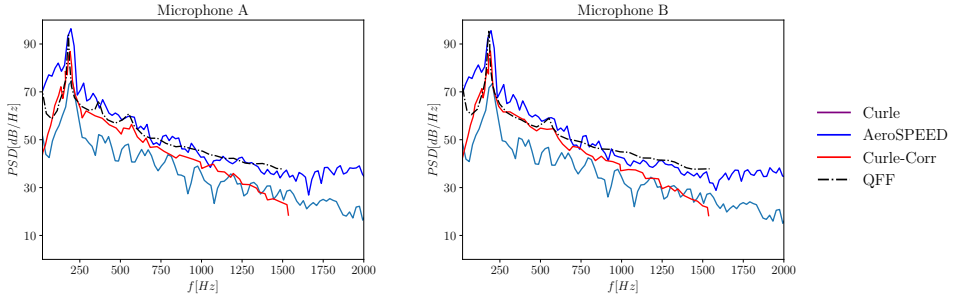


Figure 6.17: Comparison of the sound spectra at microphone A=(-8.33D,27.82D) and B=(9.11D, 32.49D). Curle and Curle-Corr denote the data computed in [148], while QFF denotes the experiment in [105].

6.4 Wall Mounted Side View Mirror

As a final test case, the case of a realistic geometry representing a wall mounted Side View Mirror (SVM) is considered. The benchmark of the SVM with this configuration was first studied in the two experimental works [72, 134] and then, it has been reproduced numerically by many research groups, see for instance [19], [154] and [147].

Fluid Setup

The SVM geometry is defined as a half cylinder with vertical axis with a quarter of a sphere on the top, see Figure 5.18. The cylinder has a diameter D and a height D and also the sphere has a diameter of D . The SVM is placed on a plate of dimension $(8D \times 12D)$. The center of the domain is at the front of the SVM, see Fig. 5.19b. Following [154], the whole computational domain for the flow computations is $\Omega_f = (-15D, 15D) \times (-14.5D, 30.5D) \times (0, 15D)$, see Fig. 5.19a. Uniform velocity with a magnitude of 39 m s^{-1} is imposed at the inlet, see Table 5.5. As for the previous test case, we employ a DDES turbulence model. The DDES computations have been initialized with a steady RANS, with the same boundary conditions described in Table 5.5. The imposed inlet values for the k and ω have been obtained by selecting a turbulence intensity 1% and imposing a turbulent length of 0.2 m. We consider a diameter $D = 0.2 \text{ m}$, resulting in a Reynolds number of $Re = 5.2 \times 10^5$. The timestep was set to $\Delta t = 10^{-5} \text{ s}$. At the wall of the SVM we solve the boundary layer, so no wall model is applied and a $y^+ \approx 1$ is kept. From [19] solving the boundary layer on the edges of

	\mathbf{u} [m s ⁻¹]	p [Pa]	ω	k [m ² s ⁻²]
Γ_{in}	$\mathbf{u} = (0, 39, 0)$	$\nabla p \cdot \mathbf{n} = 0$	$\omega = 2.381$	$k = 2.267 \times 10^{-1}$
Γ_{out}	$(\nabla \mathbf{u}) \mathbf{n} = \mathbf{0}$	$\nabla p \cdot \mathbf{n} = 0$	$\nabla \omega \cdot \mathbf{n} = 0$	$\nabla k \cdot \mathbf{n} = 0$
Γ_{plate}	$\mathbf{u} = \mathbf{0}$	$\nabla p \cdot \mathbf{n} = 0$	ω_{WF}	k_{qRWF}
Γ_{mirror}	$\mathbf{u} \cdot \mathbf{n} = \mathbf{0}$	$\nabla p \cdot \mathbf{n} = 0$	$\nabla \omega \cdot \mathbf{n} = 0$	$\nabla k \cdot \mathbf{n} = 0$
Γ_n	$\nabla(\mathbf{u} - (\mathbf{u} \cdot \mathbf{n})\mathbf{n}) \cdot \mathbf{n} = 0$ $(\nabla \mathbf{u}) \mathbf{n} = \mathbf{0}$	$\nabla p \cdot \mathbf{n} = 0$	$\nabla \omega \cdot \mathbf{n} = 0$	$\nabla k \cdot \mathbf{n} = 0$

Table 6.5: Boundary condition for the flow around a side view mirror problem. ω_{WF} is the wall function denoted as `omegaWallFunction` in OpenFOAM, see [115]. k_{qRWF} is the wall function denoted as `kqRWallFunction` in OpenFOAM. The boundary are defined in Figure 5.19a.



Figure 6.18: Geometry of the Side View Mirror.

the SVM seems critical in order to have accurate aeroacoustic predictions. At the wall of the plate we apply a wall function, compare with Table 5.5, and we keep a $y^+ \approx 30$. The size of the cells downstream of the side view mirror is 0.002 m. This choice is aligned with other choices in literature, see for [154]. The whole computational grid has a block structure with 24 079 350 elements, and it has been generated using Ansys IcemCFD software [7], see Figure 5.21.

Acoustic Setup

The aeroacoustic source term is taken from a smaller part of the flow grid close to the SVM geometry, where most of the vortical structures generating the noise are found. We denote with $\Omega_f^{\text{aero}} = (-7.5D, 7.5D) \times (-7.5D, 12.5D) \times (0, 7.5D)$ the aeroacoustic source domain, see Figure 5.20. The computational domain for the acoustic problem is $\Omega_a = (-8D, 8D) \times (-7.5D, 12.5D) \times (0, 10D)$, see Figure 5.22. At the

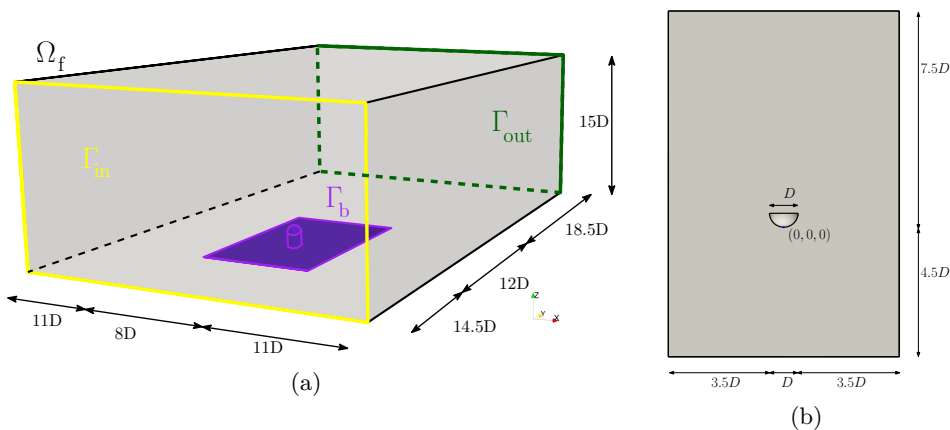


Figure 6.19: (a) Computational domain for the flow problem. (b) Geometry of the plate.

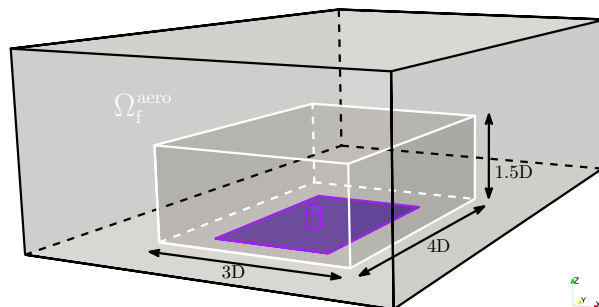


Figure 6.20: Computational support of the aeroacoustic source for the acoustic problem.

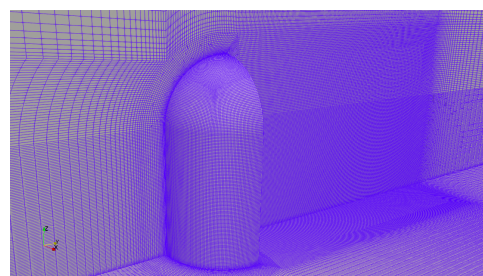


Figure 6.21: Close-up of the side-view mirror with the discretization of the flow problem.

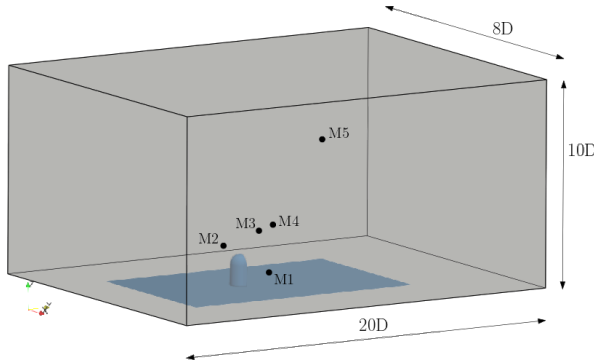


Figure 6.22: Acoustic domain. The microphones M₁, M₂, M₃, M₄, M₅ are employed for the acoustic validation.

external boundary we have applied the absorbing conditions described in Section 2.3.3, while on the plate wall and on the SVM walls we applied Neumann boundary conditions. The flexibility of the DGSEM in dealing with complex geometries is exploited here. We use low order spectral elements close to the object, and high order spectral elements far from the object, see Figure 5.23. In fact, we identify four different refinement regions. The first region is the inner region, close to the SVM. In this region we employ a non structured and low order $r = 1$ discretization strategy with $\Delta x = 5 \times 10^{-3}$ m, allowing us to easily capture the geometry of the SVM. In the downstream region, Cartesian and $r = 2$ elements are employed, with $\Delta x = 10^{-2}$ m. Since this is still the core of the aeroacoustic coupling, we still want to keep a low degree, due to the results presented in Theorem 3.3.1. Outside of the domain, we have a first transition region in which we employ $r = 3$ elements but with $\Delta x = 2.5 \times 10^{-2}$ m. Here the higher frequency components are still resolved. Finally, the discretization is halved in the free field region with $\Delta x = 5 \times 10^{-2}$ m, but we keep employing $r = 3$ elements. The whole acoustic grid has 10 011 805 degrees of freedom. We solved the acoustic problem employing $\Delta t = 10^{-5}$ s, employing a second order implicit Newmark scheme with coefficients $\gamma = 0.5$ and $\beta = 0.25$.

Flow Results

The flow field around the SVM at this regime is highly unsteady and complex. From the average velocity field in Figure 5.25 and the contour plots in Figure 5.27, we notice a horse shoe vortex in front of the

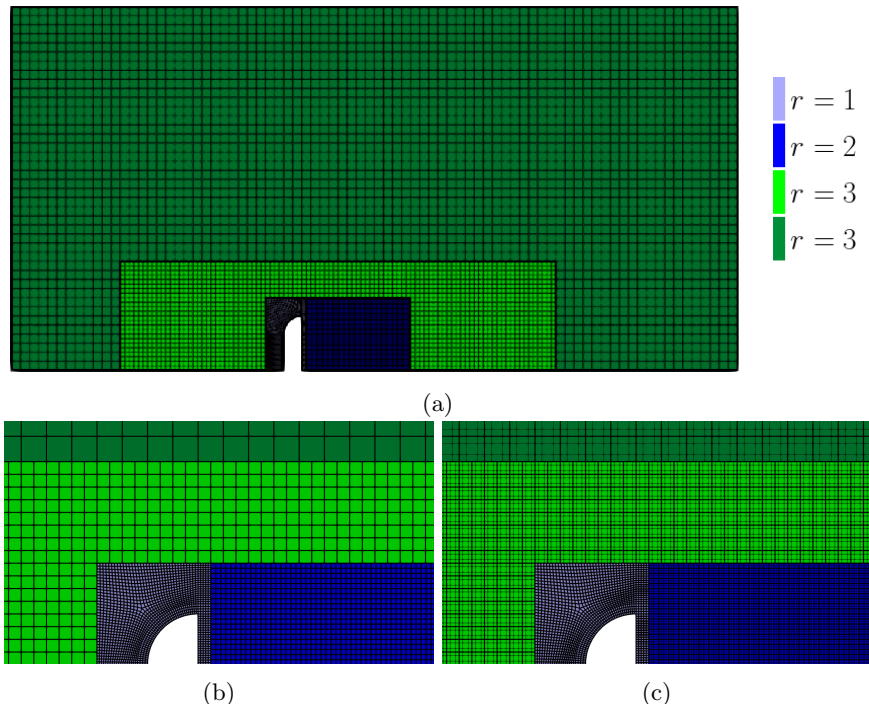
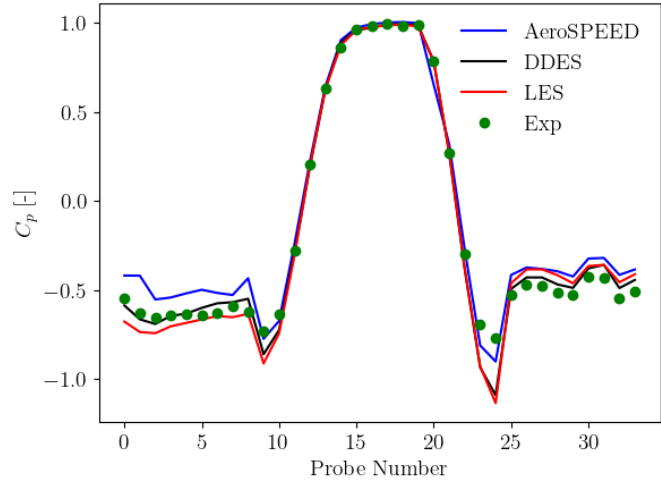
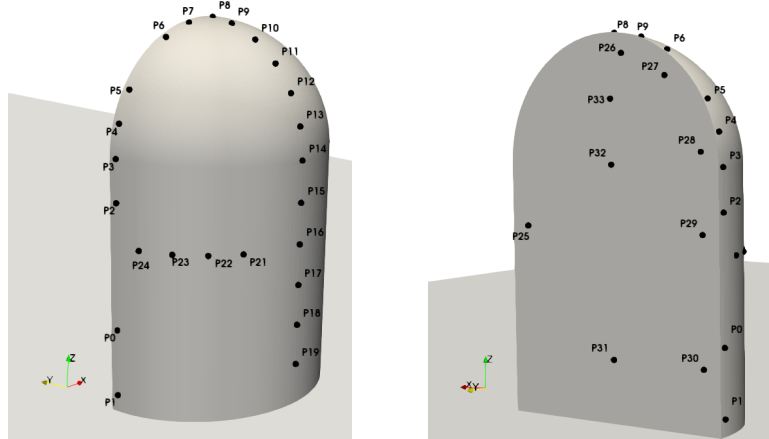


Figure 6.23: Slice of the acoustic domain at the yz mid plane. (•) Inner region.
(●) Downstream near field region. (●) Transition region (●) Free field region. (a) Description of the discretization strategy. Only the elements are shown. (b) Close up to the mirror geometry. Only the elements are shown. (c) Close up to the mirror geometry. Elements and degrees of freedom are shown.



(a)



(b)

Figure 6.24: (a) Id of each measurements probes vs pressure coefficient C_p . DDES refers to [154], Exp denotes the experiments performed in [72], LES denotes the computations in [19]. (b) Position of the probes on the geometry of the SVM.

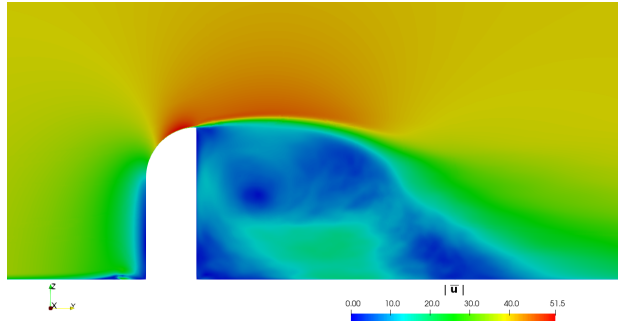


Figure 6.25: Snapshot of the averaged field on the zy mid plane.

cylinder. Then, in the downstream zone, we notice a large recirculation region and a shear layer instability, as displayed in the snapshots of the instantaneous flow velocity in Figure 5.26 and the average flow field Figure 5.25. This shear layer is the main responsible for the noise generation. The flow results are compared with literature data. First, we compute the pressure coefficients C_p on probes distributed along the wall of the SVM. The pressure coefficients and probes locations are displayed in Figure 5.24. Next, we compare the computed numerical results downstream, see Figure 5.28 with wall pressure measurements. In Figure 5.28a a slight mismatched is noted as the frequency is increased. The pressure probe is located at $S119 = (0, 0.2 \text{ m}, 0)$ on one of the sides of the SVM, and the cause of the mismatch could be related to not enough grid resolution. In Figure 5.28b the probe is placed downstream at $S123 = (-0.1418 \text{ m}, 0.4978 \text{ m}, 0)$ and there is a good accordance between the simulated data and the experimental reference.

Acoustic Results

Finally, we compute the acoustic solution with AeroSPEED. The sound signal is broadband. From Figure 5.29 we notice that the highest pressure fluctuations are located in the recirculation region after the side view mirror. We sampled the numerical solution at probes M1 to M5, see Figure 5.30 and Table 5.8. The probes from M1 to M4 are placed quite close to the side-view mirror, while M5 is placed at the far field. A rather good agreement of the spectra for the different probes is observed, in particular for the far field probe M5.

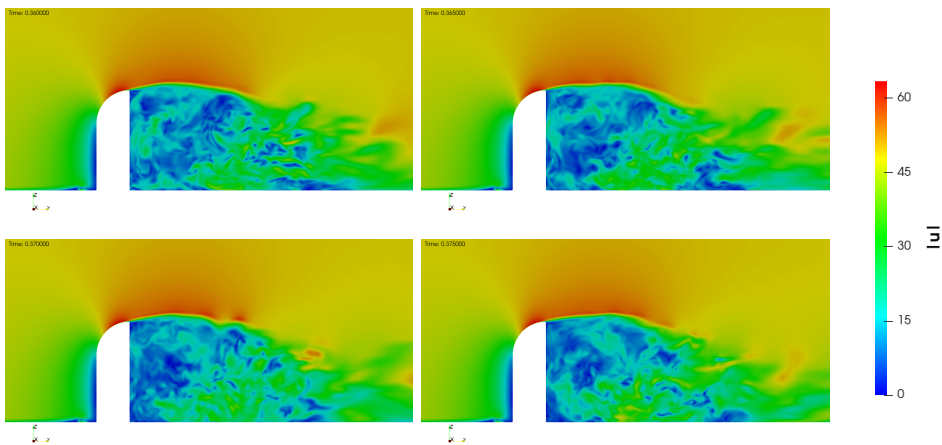


Figure 6.26: Snapshots of the instantaneous flow field on the zy mid plane.

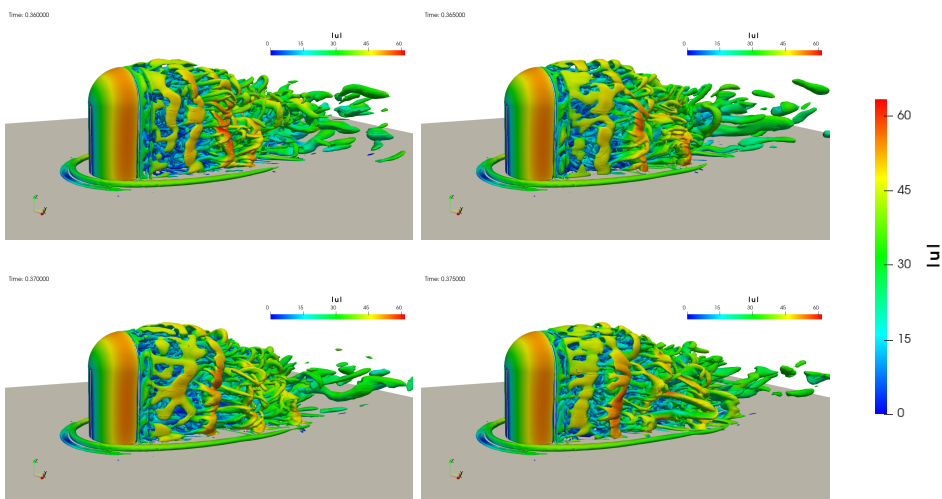


Figure 6.27: Snapshots of the instantaneous flow field, Q criterion.

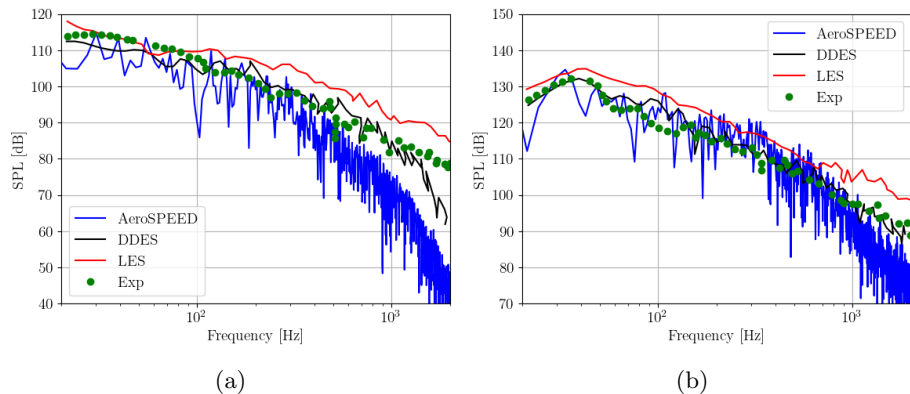


Figure 6.28: Near field probes from the CFD computation. DDES refers to the computation performed in [154], LES refers to the computation perfomed in [19], while Exp refers to the experiment in [72].

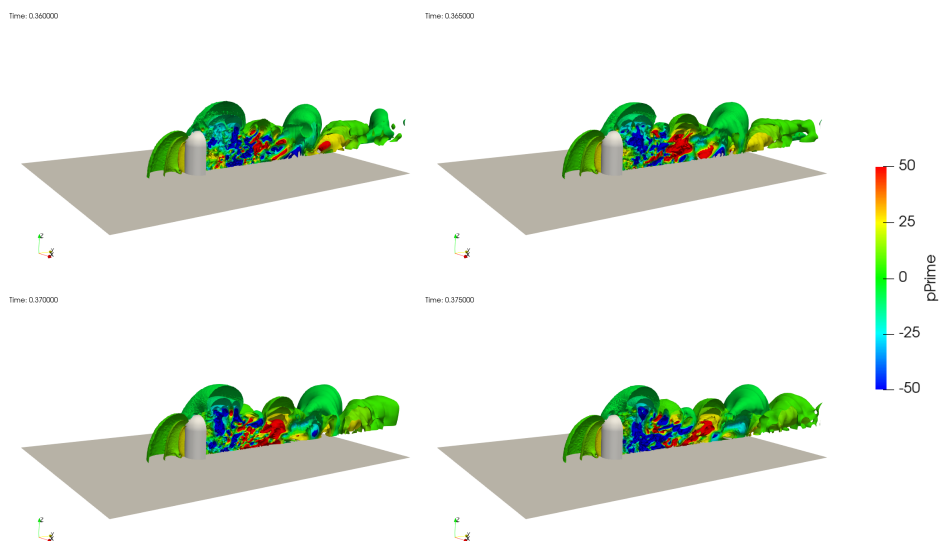


Figure 6.29: Countour plot of the acoustic field.

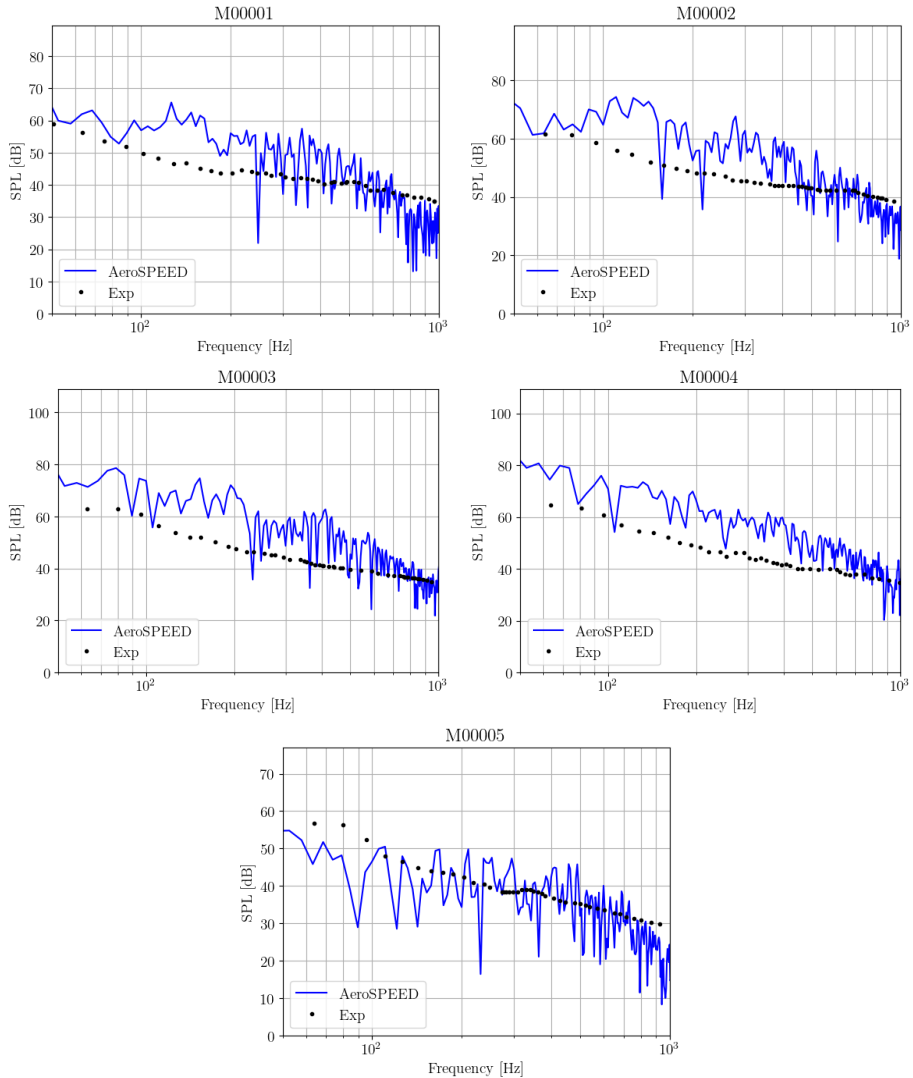


Figure 6.30: Computed pressure fluctuations acquired at the microphone M1, M2, M3, M4, M5 see Table 5.8, compared from the reference values of the experimental data in [72].

Probes	<i>x</i>	<i>y</i>	<i>z</i>
S0	-0.0998	0.094	0.0667
S1	-0.0998	0.094	0.0133
S2	-0.0998	0.094	0.1667
S3	-0.0998	0.094	0.2
S4	-0.0964	0.094	0.2258
S5	-0.0864	0.094	0.2499
S6	-0.0499	0.094	0.2864
S7	-0.0258	0.094	0.2964
S8	0.0	0.094	0.2998
S9	0.0	0.0741	0.2966
S10	0.0	0.05	0.2866
S11	0.0	0.0293	0.2707
S12	0.0	0.0134	0.25
S13	0.0	0.0034	0.2259
S14	0.0	0.0	0.2
S15	0.0	0.0	0.1667
S16	0.0	0.0	0.1333
S17	0.0	0.0	0.1
S18	0.0	0.0	0.0667
S19	0.0	0.0	0.0333
S20	-0.0259	0.034	0.1333
S21	-0.05	0.0134	0.1333
S22	-0.0707	0.0293	0.1333
S23	-0.0866	0.05	0.1333
S24	-0.0966	0.0741	0.1333
S25	0.085	0.1	0.15
S26	-0.0111	0.1	0.2843
S27	-0.0517	0.1	0.2674
S28	-0.0843	0.1	0.2111
S29	-0.085	0.1	0.15
S30	-0.085	0.1	0.05
S31	0.0	0.1	0.05
S32	0.0	0.1	0.2
S33	0.0	0.1	0.25

Table 6.6: Position of the probes for the computation of the pressure coefficient C_p . The microphone positions are taken from [72].

	<i>x</i>	<i>y</i>	<i>z</i>
S111	0.0850	0.1	0.1167
S114	-0.0850	0.1	0.1167
S116	0.0	-0.12	0.0
S119	0.0	0.2	0.0
S121	-0.1209	0.2989	0.0
S122	-0.1314	0.3984	0.0
S123	-0.1418	0.4978	0.0

Table 6.7: Position of the probes for the computation of the flow spectra. The microphone positions are taken from [72].

	<i>x</i>	<i>y</i>	<i>z</i>
M1	0.2469	-0.248	0.446
M4	0.5	0.1	0.2
M10	0.0	0.453	0.5458
M11	-0.2469	0.453	0.446
M14	1.4345	0.1	1.615

Table 6.8: Microphone positions for the acoustic computations. The microphone positions are taken from [72].

Chapter 7

Conclusions and Future Perspectives

The impact of noise, and in particular aeroacoustic noise, on human well-being has gained more and more attention in the past years. From ground and air transportation, HVAC systems, wind turbines, or architectural design, aeroacoustic noise impacts the everyday quality of life of citizens. Many research efforts have been devoted to the characterization of aeroacoustic noise. Many of these endeavours emphasize the development of high-fidelity numerical tools to facilitate the prediction of aeroacoustic noise and the design of effective noise reduction solutions.

In this work, we extended the acoustic solver SPEED [95], a high order three-dimensional DGSEM solver for inhomogeneous acoustic problems, by implementing impedance boundary conditions and the Perfectly Matched Layer. After having extensively tested the acoustic solver, we tackled the aeroacoustic problem by employing a segregated strategy. We have hence developed AeroSPEED, a high order DGSEM numerical software to solve the segregated aeroacoustic problem based on the Lighthill's wave equation with the objective of providing high fidelity solutions to the aeroacoustic problem. First, we solve a flow problem employing OpenFOAM, an open-source software based on the finite volume method that is largely used both in industry and in the academy. The CFD solver has been used to simulate both laminar and turbulent flows, using RANS and LES turbulence models available in the library. In the hybrid aeroacoustic setting, the sound source, computed from the CFD solution, is projected onto the acoustic grid, and

finally we solve an inhomogeneous acoustic wave propagation problem employing AeroSPEED. The main novelty of the coupling method is in the intergrid projection method that explicitly computes the intersection between the two non-nested polyhedral acoustic and flow grids. The intersection algorithm was shown to be accurate and scalable. Then, the intersected elements are employed for the computation of the projected solution, in combination with a quadrature free formula to compute the integrals over the polyhedral elements coming from the intersection. We next analysed the error introduced by the projection method, providing a priori estimates with numerical tests that validated our theoretical results. Then, we considered the Lighthill's acoustic wave equation and we provided a theoretical error analysis for the fully discrete analyses of the error, by taking also into account the aforementioned projection error. Again, the theoretical estimates have been validated with numerical results. Finally, the aeroacoustic solver have been largely tested on several benchmarks showing its accuracy and computational capabilities.

7.1 Main Outcomes

A high order acoustic solver for aeroacoustic problem has been described and fully analysed. Next, we highlight and summarize the key findings and novelties of this work as follows.

- The proposed FV-DGSEM has proved to be a viable discretization strategy for the hybrid Lighthill's aeroacoustic analogy. It was already shown that DGSEM was a practical approach for Direct Noise Computations [61], or the FV-DGSEM [126] on Cartesian nested grid. In this work, we generalized the approach to generic polyhedral grids for the flow problem.
- We proposed a novel intersection strategy for polyhedral grids. The interpolation presented in [79] is extended with a conservative interpolation based on the intersection of tetrahedral grids in [128]. In this work, we generalize the approach reframing the conservative interpolation as a projection method and generalizing the quadrature rule employed for the computation of the projection method. The presented intersection algorithm is able to intersect arbitrary polyhedral grids.
- The intersection strategy was shown to be accurate and scalable with the numerical tests presented in Section 2.9.

- An a priori error estimate for the projection error for the coupling between the acoustic and flow problem has been proved. The projection error for the coupling between the acoustic and flow problem has been analysed and numerical results validate the fully discrete error.
- An a priori error estimate for the fully discrete acoustic problem with projected source has been proved. The fully discrete acoustic problem with projected source has been analysed and numerical results validate the fully discrete error.
- Our computational strategy has been tested on relevant test cases, with strong focus on the validation of both the flow and the acoustic results. A large set of numerical tests have been presented to show the capabilities of both the acoustic and the aeroacoustic solvers.

7.2 Perspective and Future Developments

Several aspects can extend the work carried out in this thesis and should be further investigated.

- We limited ourselves to the Lighthill's acoustic wave equation, but the employed aeracoustic model could be improved. Indeed, there are many other aeroacoustic models that should be explored and compared in more detail, like the PCWE [157] where the sound source is given by the derivative of the pressure or the Möring [99] analogy where the sound source depends on the vorticity.
- The proposed computational strategy has been applied successfully to different aero-acoustic problems with fixed geometries. However, the most interesting noise phenomena are emitted by moving objects, like for instance the fan noise or the noise coming from the rotor of an helicopter. The current projection strategy is very accurate, but may become computationally unaffordable if the geometrical intersection between the two moving grids has to be computed at each time step. For cases like the fan noise, the computational grid could be kept fixed by taking an observer that moves with the fan. Being able to solve this kind of problem is critical, also considering the impact on the large number of applications, like for instance the next generation of high bypass ratio turbofan.

- We believe that our current analysis for the SEM acoustic problem with projection could be easily extended to the DGSEM case, giving further insights on the best discretization strategies to minimize both the projection error and to further enhance the numerical strategy.
- We already discussed in the introduction how high order polyhedral methods, like PolyDG [13, 10, 9], had a great impact in the wave propagation by providing also a flexible tool to tackle problems with complex geometries. Our current computational strategy can be easily extended also to the PolyDG framework since the proposed intersection method works for general polyhedra.
- An important recent trend in solving the time dependent wave equation is to employ also space-time discretization methods. Space-time methods are nowadays viable even for large problems thanks to the large improvements of computational capabilities of the last decades. We believe that our computational strategy could benefit from employing an ad-hoc space-time solver, and exploit high order in time discretization.

Bibliography

- [1] R. A. Adams. *Sobolev Spaces*. Pure and Applied Mathematics, Vol. 65. Academic Press, 1975.
- [2] P. C. Africa, M. Salvador, P. Gervasio, L. Dede', and A. M. Quarteroni. "A matrix-free high-order solver for the numerical solution of cardiac electrophysiology". In: *Journal of Computational Physics* 478 (2023). ISSN: 0021-9991. doi: [10.1016/j.jcp.2023.111984](https://doi.org/10.1016/j.jcp.2023.111984).
- [3] European Environment Agency. *Noise pollution and health*. Publications Office, 2022. URL: <https://www.eea.europa.eu/publications/zero-pollution/health/noise-pollution>.
- [4] M. Ainsworth. "Discrete Dispersion Relation for hp -Version Finite Element Approximation at High Wave Number". In: *SIAM Journal on Numerical Analysis* 42.2 (2004), pp. 553–575. doi: [10.1137/S0036142903423460](https://doi.org/10.1137/S0036142903423460).
- [5] M. Ainsworth, P. Monk, and W. Muniz. "Dispersive and Dissipative Properties of Discontinuous Galerkin Finite Element Methods for the Second-Order Wave Equation". In: *J. Sci. Comput.* 27 (2006), pp. 5–40. doi: [10.1007/s10915-005-9044-x](https://doi.org/10.1007/s10915-005-9044-x).
- [6] Z. Aladirany, R. Cottreau, M. Laforest, and S. Prudhomme. "Optimal error analysis of the spectral element method for the 2D homogeneous wave equation". In: *Computers and Mathematics with Applications* 119 (2022), pp. 241–256. ISSN: 0898-1221. doi: [10.1016/j.camwa.2022.05.038](https://doi.org/10.1016/j.camwa.2022.05.038).
- [7] *Ansys ICEM CFD*. URL: <https://www.ansys.com/>.
- [8] P. Antonietti, P. Houston, G. Pennesi, and E. Süli. "An agglomeration-based massively parallel non-overlapping additive Schwarz preconditioner for high-order discontinuous Galerkin methods on polytopic grids". In: *Mathematics of Computation* 89 (2019), p. 1. doi: [10.1090/mcom/3510](https://doi.org/10.1090/mcom/3510).
- [9] P. F. Antonietti, M. Botti, and I. Mazzieri. "On Mathematical and Numerical Modelling of Multiphysics Wave Propagation with Polytopal Discontinuous Galerkin Methods: a Review". In: *Vietnam Journal of Mathematics* 50 (2022). doi: [10.1007/s10013-022-00566-3](https://doi.org/10.1007/s10013-022-00566-3).
- [10] P. F. Antonietti, M. Botti, I. Mazzieri, and S. Nati Poltri. "A High-Order Discontinuous Galerkin Method for the Poro-elasto-acoustic Problem on Polygonal and Polyhedral Grids". In: *SIAM Journal on Scientific Computing* 44 (2022), B1–B28. doi: [10.1137/21M1410919](https://doi.org/10.1137/21M1410919).
- [11] P. F. Antonietti, P. Houston, and G. Pennesi. "Fast Numerical Integration on Polytopic Meshes with Applications to Discontinuous Galerkin Finite Element Methods". In: *Journal of Scientific Computing* 77.3 (2018), pp. 1339–1370. doi: [10.1007/s10915-018-0802-y](https://doi.org/10.1007/s10915-018-0802-y).
- [12] P. F. Antonietti, I. Mazzieri, N. Dal Santo, and A. M. Quarteroni. "A high-order discontinuous Galerkin approximation to ordinary differential equations with applications to elastodynamics". In: *IMA Journal of Numerical Analysis* 38.4 (2017), pp. 1709–1734. ISSN: 0272-4979. doi: [10.1093/imanum/drw062](https://doi.org/10.1093/imanum/drw062).
- [13] P. F. Antonietti, I. Mazzieri, M. Muhr, V. Nikolić, and B. Wohlmuth. "A High-order Discontinuous Galerkin Method for Nonlinear Sound Waves". In: *Journal of Computational Physics* 415 (2020), p. 109484. ISSN: 0021-9991. doi: [10.1016/j.jcp.2020.109484](https://doi.org/10.1016/j.jcp.2020.109484).

- [14] P. F. Antonietti, I. Mazzieri, A. M. Quarteroni, and F. Rapetti. “Non-conforming high order approximations of the elastodynamics equation”. In: *Computer Methods in Applied Mechanics and Engineering* 209–212 (2012), pp. 212–238. ISSN: 0045-7825. DOI: [10.1016/j.cma.2011.11.004](https://doi.org/10.1016/j.cma.2011.11.004).
- [15] D. N. Arnold. “An Interior Penalty Finite Element Method with Discontinuous Elements”. In: *SIAM Journal on Numerical Analysis* 19.4 (1982), pp. 742–760. DOI: [10.1137/0719052](https://doi.org/10.1137/0719052).
- [16] D. N. Arnold, F. Brezzi, B. Cockburn, and L. D. Marini. “Unified Analysis of Discontinuous Galerkin Methods for Elliptic Problems”. In: *SIAM Journal on Numerical Analysis* 39.5 (2002), pp. 1749–1779. DOI: [10.1137/S0036142901384162](https://doi.org/10.1137/S0036142901384162).
- [17] A. Artoni, P. F. Antonietti, R. Corradi, I. Mazzieri, N. Parolini, D. Rocchi, P. Schito, and F. F. Semeraro. “AeroSPEED: A High Order Acoustic Solver for Aeroacoustic Applications”. In: *Finite Volumes for Complex Applications X—Volume 1, Elliptic and Parabolic Problems*. Cham: Springer Nature Switzerland, 2023, pp. 39–55. DOI: [10.1007/978-3-031-40864-9_3](https://doi.org/10.1007/978-3-031-40864-9_3).
- [18] A. Artoni, P. F. Antonietti, I. Mazzieri, N. Parolini, and D. Rocchi. “A hybrid finite volume - spectral element method for aeroacoustic problems”. In: *Computers & Mathematics with Applications* 155 (2024), pp. 193–208. ISSN: 0898-1221. DOI: <https://doi.org/10.1016/j.camwa.2023.12.004>. URL: <https://www.sciencedirect.com/science/article/pii/S0898122123005540>.
- [19] J. Ask and L. Davidson. “The Sub-Critical Flow Past a Generic Side Mirror and its Impact on Sound Generation and Propagation”. In: *12th AIAA/CEAS Aeroacoustics Conference (27th AIAA Aeroacoustics Conference)*. DOI: [10.2514/6.2006-2558](https://doi.org/10.2514/6.2006-2558).
- [20] I. Babuška, B. A. Szabo, and I. N. Katz. “The p -Version of the Finite Element Method”. In: *SIAM Journal on Numerical Analysis* 18.3 (1981), pp. 515–545. DOI: [10.1137/0718033](https://doi.org/10.1137/0718033).
- [21] S. Balay, S. Abhyankar, M. F. Adams, S. Benson, J. Brown, P. Brune, K. Buschelman, E. Constantinescu, L. Dalcin, A. Dener, V. Eijkhout, J. Faibussowitsch, W. D. Gropp, V. Hapla, T. Isaac, P. Jolivet, D. Karpeev, D. Kaushik, M. G. Knepley, F. Kong, S. Kruger, A. May, L. C. McInnes, R. T. Mills, L. Mitchell, T. Munson, J. E. Roman, K. Rupp, P. Sanan, J. Sarich, B. F. Smith, S. Zampini, H. Zhang, and J. Zhang. *PETSc/TAO Users Manual*. Tech. rep. ANL-21/39 - Revision 3.20. Argonne National Laboratory, 2023. DOI: [10.2172/1968587](https://doi.org/10.2172/1968587).
- [22] C. Bernardi and Y. Maday. “Polynomial interpolation results in Sobolev spaces”. In: *Journal of Computational and Applied Mathematics* 43.1 (1992), pp. 53–80. ISSN: 0377-0427. DOI: [https://doi.org/10.1016/0377-0427\(92\)90259-Z](https://doi.org/10.1016/0377-0427(92)90259-Z). URL: <https://www.sciencedirect.com/science/article/pii/037704279290259Z>.
- [23] C. Bernardi and Y. Maday. “Spectral methods”. In: *Techniques of Scientific Computing (Part 2)*. Vol. 5. Handbook of Numerical Analysis. Elsevier, 1997, pp. 209–485. DOI: [10.1016/S1570-8659\(97\)80003-8](https://doi.org/10.1016/S1570-8659(97)80003-8).
- [24] T. D. Blacker, S. J. Owen, M. L. Staten, W. R. Quadros, B. Hanks, Brett W. Clark, Ray J. Meyers, C. Ernst, K. Merkley, R. Morris, C. McBride, Clinton J. Stimpson, M. Plooster, and S. Showman. “CUBIT geometry and mesh generation toolkit 15.1 user documentation”. In: (2016). DOI: [10.2172/1430472](https://doi.org/10.2172/1430472).
- [25] R. Bozak and R. P. Dougherty. “Measurement of noise reduction from acoustic casing treatments installed over a subscale high bypass ratio turbofan rotor”. In: *2018 AIAA/CEAS aeroacoustics conference*. 2018, p. 4099. DOI: [10.2514/6.2018-4099](https://doi.org/10.2514/6.2018-4099).
- [26] S. C. Brenner and L. R. Scott. *The Mathematical Theory of Finite Element Methods*. Vol. 15. Texts in Applied Mathematics. Springer, 2008. DOI: [10.1007/978-0-387-75934-0](https://doi.org/10.1007/978-0-387-75934-0).
- [27] K. S. Brentner and F. Farassat. “Modeling aerodynamically generated sound of helicopter rotors”. In: *Progress in Aerospace Sciences* 39.2 (2003), pp. 83–120. ISSN: 0376-0421. DOI: [10.1016/S0376-0421\(02\)00068-4](https://doi.org/10.1016/S0376-0421(02)00068-4).

- [28] M. Brink, S. Mathieu, and S. Rüttener. "Lowering urban speed limits to 30 km/h reduces noise annoyance and shifts exposure-response relationships: Evidence from a field study in Zurich". In: *Environment International* 170 (2022), p. 107651. ISSN: 0160-4120. DOI: [10.1016/j.envint.2022.107651](https://doi.org/10.1016/j.envint.2022.107651).
- [29] R. Brionnaud, M. Chávez Modena, G. Trapani, and D. M. Holman. "Direct Noise Computation with a Lattice-Boltzmann Method and Application to Industrial Test Cases". In: *22nd AIAA/CEAS Aeroacoustics Conference*. DOI: [10.2514/6.2016-2969](https://doi.org/10.2514/6.2016-2969).
- [30] A. Cangiani, Z. Dong, E. Georgoulis, and P. Houston. *hp-Version Discontinuous Galerkin Methods on Polygonal and Polyhedral Meshes*. 2017. ISBN: 978-3-319-67671-5. DOI: [10.1007/978-3-319-67673-9](https://doi.org/10.1007/978-3-319-67673-9).
- [31] C. Canuto, M. Hussaini, A. M. Quarteroni, and T. Zang. *Spectral Methods: Fundamentals in Single Domains*. Vol. 23. 2006. ISBN: 978-3-540-30725-9. DOI: [10.1007/978-3-540-30726-6](https://doi.org/10.1007/978-3-540-30726-6).
- [32] C. Canuto, M. Hussaini, A. M. Quarteroni, and T. Zang. *Spectral Methods in Fluid Dynamic*. Vol. 57. 1988. ISBN: 978-3-540-52205-8. DOI: [10.1007/978-3-642-84108-8](https://doi.org/10.1007/978-3-642-84108-8).
- [33] C. Canuto, M. Y. Hussaini, A. M. Quarteroni, and T. Zang. *Spectral Methods: Evolution to Complex Geometries and Applications to Fluid Dynamics*. 2007. DOI: [10.1007/978-3-540-30726-6](https://doi.org/10.1007/978-3-540-30726-6).
- [34] C. Canuto and A. M. Quarteroni. "Approximation Results for Orthogonal Polynomials in Sobolev Spaces". In: *Mathematics of Computation* 38.157 (1982), pp. 67–86. ISSN: 00255718, 10886842. (Visited on 10/06/2023).
- [35] S. Caro, Y. Detandt, J. Manera, F. Mendonça, and R. Toppinga. "Validation of a New Hybrid CAA Strategy and Application to the Noise Generated by a Flap in a Simplified HVAC Duct". In: *15th AIAA/CEAS Aeroacoustics Conference (30th AIAA Aeroacoustics Conference)* (2009). DOI: [10.2514/6.2009-3352](https://doi.org/10.2514/6.2009-3352).
- [36] E. B. Chin, J. B. Lasserre, and N. Sukumar. "Numerical integration of homogeneous functions on convex and nonconvex polygons and polyhedra". In: *Computational Mechanics* 56.6 (2015), pp. 967–981. DOI: [10.1007/s00466-015-1213-7](https://doi.org/10.1007/s00466-015-1213-7).
- [37] Y. Chu, Y. Shin, and S. Lee. "Aerodynamic Analysis and Noise-Reducing Design of an Outside Rear View Mirror". In: *Applied Sciences* 8.4 (2018). ISSN: 2076-3417. DOI: [10.3390/app8040519](https://doi.org/10.3390/app8040519).
- [38] European Commission, Directorate-General for Mobility, Transport, Directorate-General for Research, and Innovation. *Flightpath 2050 – Europe's vision for aviation – Maintaining global leadership and serving society's needs*. Publications Office, 2011. DOI: [10.2777/50266](https://doi.org/10.2777/50266).
- [39] D. G. Crighton, A. P. Dowling, J. E. Ffowcs-Williams, M. Heckl, F. G. Leppington, and J. F. Bartram. "Modern Methods in Analytical Acoustics Lecture Notes". In: *The Journal of the Acoustical Society of America* 92.5 (1992), pp. 3023–3023. ISSN: 0001-4966. DOI: [10.1121/1.404334](https://doi.org/10.1121/1.404334).
- [40] N. Curle and M. J. Lighthill. "The influence of solid boundaries upon aerodynamic sound". In: *Proceedings of the Royal Society of London. Series A. Mathematical and Physical Sciences* 231.1187 (1955), pp. 505–514. DOI: [10.1098/rspa.1955.0191](https://doi.org/10.1098/rspa.1955.0191).
- [41] V. D'Alessandro, M. Falone, L. Giannicchele, and S. Montelpare. "A low-storage Runge-Kutta OpenFOAM solver for compressible low-Mach number flows: aeroacoustic and thermo-fluid dynamic applications". In: *E3S Web of Conferences* 128 (2019), p. 10001. DOI: [10.1051/e3sconf/201912810001](https://doi.org/10.1051/e3sconf/201912810001).
- [42] P. di Francescantonio. "A New Boundary Integral Formulation for the Prediction of Sound Radiation". In: *Journal of Sound and Vibration* 202.4 (1997), pp. 491–509. ISSN: 0022-460X. DOI: [10.1006/jsvi.1996.0843](https://doi.org/10.1006/jsvi.1996.0843).
- [43] Z. Dong and E. Georgoulis. "Robust Interior Penalty Discontinuous Galerkin Methods". In: *Journal of Scientific Computing* 92 (2022). DOI: [10.1007/s10915-022-01916-6](https://doi.org/10.1007/s10915-022-01916-6).
- [44] C. J. Doolan. "Flat-Plate Interaction with the Near Wake of a Square Cylinder". In: *AIAA Journal* 47.2 (2009), pp. 475–479. DOI: [10.2514/1.40503](https://doi.org/10.2514/1.40503).

- [45] J. Douglas and T. Dupont. "Interior Penalty Procedures for Elliptic and Parabolic Galerkin Methods". In: *Lecture Notes in Physics*, Berlin Springer Verlag. Vol. 58. 1976, p. 207. DOI: [10.1007/BFb0120591](https://doi.org/10.1007/BFb0120591).
- [46] S. Duczek and H. Gravenkamp. "Mass lumping techniques in the spectral element method: On the equivalence of the row-sum, nodal quadrature, and diagonal scaling methods". In: *Computer Methods in Applied Mechanics and Engineering* 353 (2019), pp. 516–569. ISSN: 0045-7825. DOI: [10.1016/j.cma.2019.05.016](https://doi.org/10.1016/j.cma.2019.05.016).
- [47] D. Eberly. *Robust and Error-Free Geometric Computing*. London: CRC Press, 2020.
- [48] B. Engquist and A. Majda. "Absorbing boundary conditions for the numerical simulation of waves". English (US). In: *Mathematics of Computation* 31.139 (1977), pp. 629–651. DOI: [10.2307/2005997](https://doi.org/10.2307/2005997).
- [49] *Ensight*. URL: <https://dav.lbl.gov/archive/NERSC/Software/ensight/doc/Manuals/UserManual.pdf>.
- [50] A. Epikhin, I. Evdokimov, M. Krashenin, M. Kalugin, and S. Strijhak. "Development of a Dynamic Library for Computational Aeroacoustics Applications Using the OpenFOAM Open Source Package". In: *Procedia Computer Science* 66 (2015). 4th International Young Scientist Conference on Computational Science, pp. 150–157. ISSN: 1877-0509. DOI: [10.1016/j.procs.2015.11.018](https://doi.org/10.1016/j.procs.2015.11.018).
- [51] M. Escobar. "Finite Element Simulation of Flow-Induced Noise using Sighthill's Acoustic Analogy". In: *Ph.D. Thesis* (2007).
- [52] L. C. Evans. *Partial Differential Equations*. Graduate studies in mathematics. American Mathematical Society, 2010. ISBN: 9780821849743. URL: https://books.google.it/books?id=XnuOo_EJrcQC.
- [53] R. Ewert and W. Schröder. "Acoustic perturbation equation based on flow decomposition via source filtering". In: *Journal of Computational Physics* 188 (2003), pp. 365–398. DOI: [10.1016/S0021-9991\(03\)00168-2](https://doi.org/10.1016/S0021-9991(03)00168-2).
- [54] E. Faccioli, F. Maggio, R. Paolucci, and A. M. Quarteroni. "2D and 3D elastic wave propagation by a pseudo-spectral domain decomposition method". In: *Journal of Seismology* 1 (1997), pp. 237–251. DOI: [10.1023/A:1009758820546](https://doi.org/10.1023/A:1009758820546).
- [55] F. Fahy and T. Rossing. "Foundations of Engineering Acoustics". In: *Journal of The Acoustical Society of America* 111 (2002), pp. 1142–1142. DOI: [10.1121/1.1445786](https://doi.org/10.1121/1.1445786).
- [56] F. Farassat and M. K. Myers. "Extension of Kirchhoff's formula to radiation from moving surfaces". In: *Journal of Sound and Vibration* 123.3 (1988), pp. 451–460. ISSN: 0022-460X. DOI: [10.1016/S0022-460X\(88\)80162-7](https://doi.org/10.1016/S0022-460X(88)80162-7).
- [57] S. Fechter, F. Hindenlang, H. Frank, C. Munz, and G. Gassner. "Discontinuous Galerkin Schemes for the Direct Numerical Simulation of Fluid Flow and Acoustics". In: *18th AIAA/CEAS Aeroacoustics Conference (33rd AIAA Aeroacoustics Conference)*. DOI: [10.2514/6.2012-2187](https://doi.org/10.2514/6.2012-2187).
- [58] J. E. Ffowcs Williams, D. L. Hawkings, and M. J. Lighthill. "Sound generation by turbulence and surfaces in arbitrary motion". In: *Philosophical Transactions of the Royal Society of London. Series A, Mathematical and Physical Sciences* 264.1151 (1969), pp. 321–342.
- [59] D. Flad, H. Frank, A. Beck, and C. Munz. "A Discontinuous Galerkin Spectral Element Method for the direct numerical simulation of aeroacoustics". In: 2014. DOI: [10.2514/6.2014-2740](https://doi.org/10.2514/6.2014-2740).
- [60] S. Forte, L. Preziosi, and M. Vianello. *Meccanica dei Continui*. 2019. ISBN: 9788847039858. URL: <http://lib.ugent.be/catalog/ebk01:410000007823571>.
- [61] H. M. Frank and C. Munz. "Direct aeroacoustic simulation of acoustic feedback phenomena on a side-view mirror". In: *Journal of Sound and Vibration* 371 (2016), pp. 132–149. DOI: [10.1016/j.jsv.2016.02.014](https://doi.org/10.1016/j.jsv.2016.02.014).
- [62] B. Greschner, D. Eschricht, C. Mockett, and F. Thiele. "Turbulence Modelling Effects on Tandem Cylinder Interaction Flow and Analysis of Installation Effects on Broadband Noise Using Chimera Technique". In: *30th AIAA Applied Aerodynamics Conference*. DOI: [10.2514/6.2012-3033](https://doi.org/10.2514/6.2012-3033).

- [63] M. Gritskevich, A. Garbaruk, J. Schütze, and F. Menter. “Development of DDES and IDDES Formulations for the $k - \omega$ Shear Stress Transport Model”. In: *Flow, Turbulence and Combustion* 88 (2012). DOI: [10.1007/s10494-011-9378-4](https://doi.org/10.1007/s10494-011-9378-4).
- [64] M. Grote and D. Schoetzau. “Optimal Error Estimates for the Fully Discrete Interior Penalty DG Method for the Wave Equation”. In: *J. Sci. Comput.* 40 (2009), pp. 257–272. DOI: [10.1007/s10915-008-9247-z](https://doi.org/10.1007/s10915-008-9247-z).
- [65] M. J. Grote and I. Sim. “Efficient PML for the wave equation”. In: *Preprint* (2010).
- [66] P. Hachenberger and L. Kettner. “3D Boolean Operations on Nef Polyhedra”. In: *CGAL User and Reference Manual*. 5.4. CGAL Editorial Board, 2022.
- [67] O. Hadad, S. Kröller-Schön, A. Daiber, and T. Münzel. “The cardiovascular effects of noise”. en. In: *Dtsch. Arztebl. Int.* 116.14 (2019), pp. 245–250. DOI: [10.3238/arztebl.2019.0245](https://doi.org/10.3238/arztebl.2019.0245).
- [68] M. M. Haines, S. A. Stansfeld, R. F. S. Job, B. Berglund, and J. Head. “Chronic aircraft noise exposure, stress responses, mental health and cognitive performance in school children”. In: *Psychological Medicine* 31.2 (2001), 265–277. DOI: [10.1017/S0033291701003282](https://doi.org/10.1017/S0033291701003282).
- [69] J. C. Hardin and D. S. Pope. “An acoustic/viscous splitting technique for computational aeroacoustics”. In: *Theoretical and Computational Fluid Dynamics* 6.5-6 (1994), pp. 323–340. DOI: [10.1007/BF00311844](https://doi.org/10.1007/BF00311844).
- [70] M. Helper. “General Aspects of Vehicle Aeroacoustics”. In: *Conference: Lecture Series Road Vehicle Aerodynamics* (2005).
- [71] J. Hesthaven and T. Warburton. “Nodal Discontinuous Galerkin Methods: Algorithms, Analysis, and Applications”. In: vol. 54. 2007. DOI: [10.1007/978-0-387-72067-8](https://doi.org/10.1007/978-0-387-72067-8).
- [72] R. Hoeld, A. Brenneis, A. Eberle, V. Schwarz, and R. Siegert. “Numerical simulation of aeroacoustic sound generated by generic bodies placed on a plate. I - Prediction of aeroacoustic sources”. In: *5th AIAA/CEAS Aeroacoustics Conference and Exhibit*. DOI: [10.2514/6.1999-1896](https://doi.org/10.2514/6.1999-1896).
- [73] O. Inoue and N. Hatakeyama. “Sound generation by a two-dimensional circular cylinder in a uniform flow”. In: *Journal of Fluid Mechanics* 471 (2002), 285–314. DOI: [10.1017/S0022112002002124](https://doi.org/10.1017/S0022112002002124).
- [74] O. Inoue, M. Mori, and N. Hatakeyama. “Aeolian tones radiated from flow past two square cylinders in tandem”. In: *Physics of Fluids* 18.4 (2006). DOI: [10.1063/1.2187446](https://doi.org/10.1063/1.2187446).
- [75] R. I. Issa, A. D. Gosman, and A. P. Watkins. “The computation of compressible and incompressible recirculating flows by a non-iterative implicit scheme”. In: *Journal of Computational Physics* 62.1 (1986), pp. 66–82. DOI: [10.1016/0021-9991\(86\)90100-2](https://doi.org/10.1016/0021-9991(86)90100-2).
- [76] H. Jasak. “Error Analysis and Estimation for the Finite Volume Method with Applications to Fluid Flows”. In: *Ph.D. Thesis, Imperial College* (1996).
- [77] B. Kaltenbacher, M. Kaltenbacher, and I. Sim. “A modified and stable version of a perfectly matched layer technique for the 3D second order wave equation in time domain with an application to aeroacoustics”. In: *Journal of computational physics* 235 (2013), pp. 407–422. DOI: [10.1016/j.jcp.2012.10.016](https://doi.org/10.1016/j.jcp.2012.10.016).
- [78] M. Kaltenbacher. *Numerical simulation of mechatronic sensors and actuators*. Vol. 2. Springer, 2007. DOI: [10.1007/978-3-642-40170-1](https://doi.org/10.1007/978-3-642-40170-1).
- [79] M. Kaltenbacher, M. Escobar, S. Becker, and I. Ali. “Computational Aeroacoustics based on Lighthill’s Acoustic Analogy”. In: *Computational Acoustics of Noise Propagation in Fluids - Finite and Boundary Element Methods*. Berlin, Heidelberg: Springer Berlin Heidelberg, 2008, pp. 115–142. DOI: [10.1007/978-3-540-77448-8_5](https://doi.org/10.1007/978-3-540-77448-8_5).
- [80] M. Kaltenbacher, M. Escobar, S. Becker, and I. Ali. “Numerical simulation of flow-induced noise using LES/SAS and Lighthill’s acoustic analogy”. In: *International Journal for Numerical Methods in Fluids* 63.9 (2010), pp. 1103–1122. DOI: [10.1002/fld.2123](https://doi.org/10.1002/fld.2123).
- [81] G. Karypis and V. Kumar. “A Fast and High Quality Multilevel Scheme for Partitioning Irregular Graphs”. In: *SIAM Journal on Scientific Computing* 20.1 (1998), pp. 359–392. DOI: [10.1137/S1064827595287997](https://doi.org/10.1137/S1064827595287997).

- [82] M. Kessler and S. Wagner. “Source-time dominant aeroacoustics”. In: *Computers and Fluids* 33.5 (2004). Applied Mathematics for Industrial Flow Problems, pp. 791–800. ISSN: 0045-7930. DOI: [10.1016/j.compfluid.2003.06.012](https://doi.org/10.1016/j.compfluid.2003.06.012).
- [83] W. Kim and S. Menon. “A new dynamic one-equation subgrid-scale model for large eddy simulations”. In: *33rd Aerospace Sciences Meeting and Exhibit*. DOI: [10.2514/6.1995-356](https://doi.org/10.2514/6.1995-356).
- [84] B. Launder and D. B. Spalding. “The numerical computation of turbulent flows”. In: *Comput. Methods Appl. Mech. Eng.* 103 (1974), pp. 456–460.
- [85] D. J. Lee and S. O. Koo. “Numerical study of sound generation due to a spinning vortex pair”. In: *AIAA Journal* 33.1 (1995), pp. 20–26. DOI: [10.2514/3.12327](https://doi.org/10.2514/3.12327).
- [86] M. J. Lighthill. “On sound generated aerodynamically II. Turbulence as a source of sound”. In: *Proceedings of the Royal Society of London. Series A. Mathematical and Physical Sciences* 222.1148 (1954), pp. 1–32. DOI: [10.1098/rspa.1954.0049](https://doi.org/10.1098/rspa.1954.0049).
- [87] M. J. Lighthill and M. H. A. Newman. “On sound generated aerodynamically I. General theory”. In: *Proceedings of the Royal Society of London. Series A. Mathematical and Physical Sciences* 211.1107 (1952), pp. 564–587. DOI: [10.1098/rspa.1952.0060](https://doi.org/10.1098/rspa.1952.0060).
- [88] Y. S. K. Liow, B. T. Tan, M. C. Thompson, and K. Hourigan. “Sound generated in laminar flow past a two-dimensional rectangular cylinder”. In: *Journal of Sound and Vibration* 295.1 (2006), pp. 407–427. DOI: [10.1016/j.jsv.2006.01.014](https://doi.org/10.1016/j.jsv.2006.01.014).
- [89] L. Liu, F. Ripamonti, R. Corradi, and Z. Rao. “Design and Characterization of a Test Bench For Interior Noise Investigations”. In: *The International Journal of Acoustics and Vibration* 27 (2022), pp. 245–256. DOI: [10.20855/ijav.2022.27.31866](https://doi.org/10.20855/ijav.2022.27.31866).
- [90] D. Lockard. “Summary of the Tandem Cylinder Solutions from the Benchmark problems for Airframe Noise Computations-I Workshop”. In: (2011). DOI: [10.2514/6.2011-353](https://doi.org/10.2514/6.2011-353).
- [91] D. A. Lysenko and I. S. Ertesväg. “Assessment of algebraic subgrid scale models for the flow over a triangular cylinder at $Re = 45000$ ”. In: *Ocean Engineering* 222 (2021), p. 108559. ISSN: 0029-8018. DOI: [10.1016/j.oceaneng.2020.108559](https://doi.org/10.1016/j.oceaneng.2020.108559).
- [92] Y. Maday and A. T. Patera. “Spectral element methods for the incompressible Navier-Stokes equations”. In: *IN: State-of-the-art surveys on computational mechanics (A90-47176 21-64)*. New York. 1989, pp. 71–143.
- [93] F. Maggio and A. M. Quarteroni. “Acoustic wave simulation by spectral methods”. In: *East-West Journal of Numerical Mathematics* 2 (1994).
- [94] P. Martínez-Lera and C. Schram. “Correction techniques for the truncation of the source field in acoustic analogies”. In: *The Journal of the Acoustical Society of America* 124 (6 2008). DOI: [10.1121/1.2999555](https://doi.org/10.1121/1.2999555).
- [95] I. Mazzieri, M. Stupazzini, R. Guidotti, and C. Smerzini. “SPEED: SPectral Elements in Elastodynamics with Discontinuous Galerkin: a non-conforming approach for 3D multi-scale problems”. In: *International Journal for Numerical Methods in Engineering* 95.12 (2013), pp. 991–1010. DOI: [10.1002/nme.4532](https://doi.org/10.1002/nme.4532).
- [96] F. Menter. “Zonal Two Equation $k - \omega$ Turbulence Models For Aerodynamic Flows”. In: *23rd Fluid Dynamics, Plasmadynamics, and Lasers Conference*. DOI: [10.2514/6.1993-2906](https://doi.org/10.2514/6.1993-2906).
- [97] F. Menter, M. Kuntz, and R. B. Langtry. “Ten years of industrial experience with the SST turbulence model”. In: *Heat and Mass Transfer* 4 (2003).
- [98] B. E. Mitchell, S. K. Lele, and P. Moin. “Direct computation of the sound from a compressible co-rotating vortex pair”. In: *Journal of Fluid Mechanics* 285 (1995), 181–202. DOI: [10.1017/S0022112095000504](https://doi.org/10.1017/S0022112095000504).
- [99] W. Möhring. “On vortex sound at low Mach number”. In: *Journal of Fluid Mechanics* 85.4 (1978), 685–691. DOI: [10.1017/S0022112078000865](https://doi.org/10.1017/S0022112078000865).
- [100] E. A. Muller and F. Obermeier. “The spinning vortices as a source of sound”. In: *AGARD CP-22 22* (1967).
- [101] COMSOL Multiphysics. *Introduction to COMSOL multiphysics®*. 1998.

- [102] C. Munz, M. Dumbser, and S. Roller. "Linearized acoustic perturbation equations for low Mach number flow with variable density and temperature". In: *Journal of Computational Physics* 224.1 (2007), pp. 352–364. ISSN: 0021-9991. DOI: [10.1016/j.jcp.2007.02.022](https://doi.org/10.1016/j.jcp.2007.02.022).
- [103] N. Murad, J. Naser, F. Alam, and S. Watkins. "Computational fluid dynamics study of vehicle A-pillar aero-acoustics". In: *Applied Acoustics* 74.6 (2013), pp. 882–896. ISSN: 0003-682X. DOI: [10.1016/j.apacoust.2012.12.011](https://doi.org/10.1016/j.apacoust.2012.12.011).
- [104] E. Nesbitt. "Current engine noise and reduction technology". In: *CEAS Aeronautical Journal* 10.1 (2019), pp. 93–100. doi: [10.1007/s13272-019-00381-6](https://doi.org/10.1007/s13272-019-00381-6).
- [105] D. Neuhart, L. Jenkins, M. Choudhari, and M. Khorrami. "Measurements of the Flowfield Interaction Between Tandem Cylinders". In: *15th AIAA/CEAS Aeroacoustics Conference (30th AIAA Aeroacoustics Conference)*. DOI: [10.2514/6.2009-3275](https://doi.org/10.2514/6.2009-3275).
- [106] A. Niemöller, M. Schlottke-Lakemper, M. Meinke, and W. Schröder. "Jet Noise Prediction for Chevron Nozzles using a Direct-Hybrid CFD/CAA Method". In: ICCFD10-237. 2018.
- [107] M. P. Norton and D. G. Karczub. "Fundamentals of Noise and Vibration Analysis for Engineers". In: 2nd ed. Cambridge University Press, 2003. DOI: [10.1017/CBO9781139163927](https://doi.org/10.1017/CBO9781139163927).
- [108] A. A. Oberai, F. Roknaldin, and T. J. R. Hughes. "Computational procedures for determining structural-acoustic response due to hydrodynamic sources". In: *Computer Methods in Applied Mechanics and Engineering* 190.3 (2000), pp. 345–361. DOI: [10.1016/S0045-7825\(00\)00206-1](https://doi.org/10.1016/S0045-7825(00)00206-1).
- [109] A. Okajima. "Strouhal numbers of rectangular cylinders". In: *Journal of Fluid Mechanics* 123 (1982), pp. 379–398. DOI: [10.1017/S0022112082003115](https://doi.org/10.1017/S0022112082003115).
- [110] S. P. Oliveira and S. A. Leite. "Error analysis of the spectral element method with Gauss-Lobatto-Legendre points for the acoustic wave equation in heterogeneous media". In: *Applied Numerical Mathematics* 129 (2018), pp. 39–57. ISSN: 0168-9274. DOI: [10.1016/j.apnum.2018.02.007](https://doi.org/10.1016/j.apnum.2018.02.007).
- [111] *OpenFOAM*. URL: <https://dl.openfoam.com/source/v2012/>.
- [112] A. T. Patera. "A spectral element method for fluid dynamics: Laminar flow in a channel expansion". In: *Journal of Computational Physics* 54.3 (1984), pp. 468–488. ISSN: 0021-9991. DOI: [10.1016/0021-9991\(84\)90128-1](https://doi.org/10.1016/0021-9991(84)90128-1).
- [113] V. Pauz, A. Niemoeller, M. H. Meinke, and W. Schröder. "Numerical analysis of chevron nozzle noise". In: *23rd AIAA/CEAS Aeroacoustics Conference*. DOI: [10.2514/6.2017-3853](https://doi.org/10.2514/6.2017-3853).
- [114] S. B. Pope. *Turbulent Flows*. Cambridge University Press, 2000. DOI: [10.1017/CBO9780511840531](https://doi.org/10.1017/CBO9780511840531).
- [115] M. Popovac and K. Hanjalic. "Compound Wall Treatment for RANS Computation of Complex Turbulent Flows and Heat Transfer". In: *Flow, Turbulence and Combustion*, 78 (2) 78 (2007). DOI: [10.1007/s10494-006-9067-x](https://doi.org/10.1007/s10494-006-9067-x).
- [116] A. Powell. "Theory of Vortex Sound". In: *The Journal of the Acoustical Society of America* 36.1 (1964), pp. 177–195. ISSN: 0001-4966. DOI: [10.1121/1.1918931](https://doi.org/10.1121/1.1918931).
- [117] A. M. Quarteroni. *Numerical models for differential problems; 1st ed.* Milano: Springer, 2009. DOI: [10.1007/978-88-470-5522-3](https://doi.org/10.1007/978-88-470-5522-3).
- [118] W. H. Reed and T. R. Hill. "Triangular mesh methods for the neutron transport equation". In: (1973). URL: <https://www.osti.gov/biblio/4491151>.
- [119] B. Rivière and M. Wheeler. "Discontinuous finite element methods for acoustic and elastic wave problems". In: *Contemporary Mathematics* 329 (2003). DOI: [10.1090/conm/329/05862](https://doi.org/10.1090/conm/329/05862).
- [120] W. De Roeck and W. Desmet. *Accurate CAA-Simulations Using a Low-Mach Aerodynamic/Acoustic Splitting Technique*. DOI: [10.2514/6.2009-3230](https://doi.org/10.2514/6.2009-3230).
- [121] S. Roller, T. Schwartzkopff, R. Fortenbach, M. Dumbser, and C. Munz. "Calculation of low Mach number acoustics: a comparison of MPV, EIF and linearized Euler equations". In: *ESAIM: M2AN* 39.3 (2005), pp. 561–576. DOI: [10.1051/m2an:2005016](https://doi.org/10.1051/m2an:2005016).

- [122] G. Romani and D. Casalino. "Rotorcraft blade-vortex interaction noise prediction using the Lattice-Boltzmann method". In: *Aerospace Science and Technology* 88 (2019), pp. 147–157. ISSN: 1270-9638. DOI: [10.1016/j.ast.2019.03.029](https://doi.org/10.1016/j.ast.2019.03.029).
- [123] S. Salsa. *Partial Differential Equations in Action: From Modelling to Theory*. UNITEXT. Springer International Publishing, 2016. ISBN: 9783319312385. URL: <https://books.google.it/books?id=bdkyDQAAQBAJ>.
- [124] L. Sanders, E. Manoha, M. Murayama, Y. Yokokawa, K. Yamamoto, and T. Hirai. "Lattice-Boltzmann Flow Simulation of a Two-Wheel Landing Gear". In: *22nd AIAA/CEAS Aeroacoustics Conference*. DOI: [10.2514/6.2016-2767](https://doi.org/10.2514/6.2016-2767).
- [125] M. Schlottke-Lakemper. "A direct-hybrid method for aeroacoustic analysis". In: *Ph.D. Thesis* (2017).
- [126] M. Schlottke-Lakemper, M. Meinke, and W. Schröder. "A Hybrid Discontinuous Galerkin-Finite Volume Method for Computational Aeroacoustics". In: *New Results in Numerical and Experimental Fluid Mechanics X*. Cham: Springer International Publishing, 2016, pp. 743–753. DOI: [10.1007/978-3-319-27279-5_65](https://doi.org/10.1007/978-3-319-27279-5_65).
- [127] S. Schoder and M. Kaltenbacher. "Hybrid Aeroacoustic Computations: State of Art and New Achievements". In: *Journal of Theoretical and Computational Acoustics* 27.04 (2019). DOI: [10.1142/S2591728519500208](https://doi.org/10.1142/S2591728519500208).
- [128] S. Schoder, A. Wurzinger, C. Junger, M. Weitz, C. Freidhager, K. Roppert, and M. Kaltenbacher. "Application Limits of Conservative Source Interpolation Methods Using a Low Mach Number Hybrid Aeroacoustic Workflow". In: *Journal of Theoretical and Computational Acoustics* 29.01 (2021), p. 2050032. DOI: [10.1142/S2591728520500322](https://doi.org/10.1142/S2591728520500322).
- [129] C. Schwab. *P- and hp- finite element methods : theory and applications in solid and fluid mechanics*. 1998.
- [130] T. Schwartzkopff, C. Munz, and E. Toro. "Ader: A High-Order Approach for Linear Hyperbolic Systems in 2D". In: *Journal of Scientific Computing* 17 (2002), pp. 231–240. DOI: [10.1023/A:1015160900410](https://doi.org/10.1023/A:1015160900410).
- [131] M. Scully. "Computation of helicopter rotor wake geometry and its influence on rotor harmonic airloads". In: (1975).
- [132] J. H. Seo and Y. Moon. "The Linearized Perturbed Compressible Equations for Aeroacoustic Noise Prediction at Very Low Mach Numbers". In: *Aiaa Journal - AIAA J* 43 (2005), pp. 1716–1724. DOI: [10.2514/1.3001](https://doi.org/10.2514/1.3001).
- [133] M. Shur, P. R. Spalart, M. Strelets, and A. Travin. "Detached-eddy simulation of an airfoil at high angle of attack". In: *Engineering Turbulence Modelling and Experiments 4*. Ed. by W. Rodi and D. L. Oxford: Elsevier Science Ltd, 1999, pp. 669–678. ISBN: 978-0-08-043328-8. DOI: [10.1016/B978-008043328-8/50064-3](https://doi.org/10.1016/B978-008043328-8/50064-3).
- [134] R. Siegert, V. Schwarz, and J. Reichenberger. "Numerical simulation of aeroacoustic sound generated by generic bodies placed on a plate. II - Prediction of radiated sound pressure". In: *5th AIAA/CEAS Aeroacoustics Conference and Exhibit*. DOI: [10.2514/6.1999-1895](https://doi.org/10.2514/6.1999-1895).
- [135] Siemens, ed. *Q-source*. URL: <https://www.qsources.be/simcenter-qsources/q-mhf-2/>.
- [136] A. Sohankar, C. Norberg, and L. Davidson. "Simulation of three-dimensional flow around a square cylinder at moderate Reynolds numbers". In: *Physics of Fluids* 11.2 (1999), pp. 288–306. DOI: [10.1063/1.869879](https://doi.org/10.1063/1.869879).
- [137] D. B. Spalding. "A Single Formula for the ‘Law of the Wall’". In: *Journal of Applied Mechanics* 28.3 (1961), pp. 455–458. ISSN: 0021-8936. DOI: [10.1115/1.3641728](https://doi.org/10.1115/1.3641728).
- [138] *SPEED*. URL: <https://speed.mox.polimi.it/>.
- [139] M. Stupazzini, S. Lee, D. Komatitsch, J. Tromp, E. Casarotti, and A. Piersanti. "CUBIT and Seismic Wave Propagation Based Upon the Spectral-Element Method: An Advanced Unstructured Mesher for Complex 3D Geological Media". In: *Proceedings of the 16th International Meshing Roundtable* (2007). DOI: [10.1007/978-3-540-75103-8_32](https://doi.org/10.1007/978-3-540-75103-8_32).

- [140] M. Sukri Mat Ali, C. J. Doolan, and V. Wheatley. “The sound generated by a square cylinder with a splitter plate at low Reynolds number”. In: *Journal of Sound and Vibration* 330.15 (2011), pp. 3620–3635. ISSN: 0022-460X. DOI: <https://doi.org/10.1016/j.jsv.2011.03.008>.
- [141] S. H. El Tahry. “K-epsilon equation for compressible reciprocating engine flows”. In: *Journal of Energy* 7 (1983), pp. 345–353. URL: <https://api.semanticscholar.org/CorpusID:122676550>.
- [142] C. K. W. Tam and J. C. Webb. “Dispersion-Relation-Preserving Finite Difference Schemes for Computational Acoustics”. In: *Journal of Computational Physics* 107.2 (1993), pp. 262–281. ISSN: 0021-9991. DOI: [10.1006/jcph.1993.1142](https://doi.org/10.1006/jcph.1993.1142).
- [143] M. E. Taylor. *Partial Differential Equations I, Basic Theory*. New York: Springer, 1996. DOI: [10.1007/978-1-4419-7055-8](https://doi.org/10.1007/978-1-4419-7055-8).
- [144] F. L. Teixeira and W. C. Chew. “Complex space approach to perfectly matched layers: a review and some new developments”. In: *International Journal of Numerical Modelling: Electronic Networks, Devices and Fields* 13.5 (2000), pp. 441–455. DOI: [10.1002/1099-1204\(200009/10\)13:5<441::AID-JNM376>3.0.CO;2-J](https://doi.org/10.1002/1099-1204(200009/10)13:5<441::AID-JNM376>3.0.CO;2-J).
- [145] The CGAL Project. *CGAL User and Reference Manual*. 5.5.1. CGAL Editorial Board, 2022. URL: <https://doc.cgal.org/5.5.1/Manual/packages.html>.
- [146] P. A. Thompson. *Compressible-Fluid Dynamics*. New York N.Y: McGraw-Hill, 1988.
- [147] A. Tosh, M. Caraeni, and D. Caraeni. “A Hybrid Computational Aeroacoustic Method For Low Speed Flows”. In: 2018. DOI: [10.2514/6.2018-4096.c1](https://doi.org/10.2514/6.2018-4096.c1).
- [148] M. Weinmann, R. D. Sandberg, and C. Doolan. “Tandem cylinder flow and noise predictions using a hybrid RANS/LES approach”. In: *International Journal of Heat and Fluid Flow* 50 (2014), pp. 263–278. ISSN: 0142-727X. DOI: [10.1016/j.ijheatfluidflow.2014.08.011](https://doi.org/10.1016/j.ijheatfluidflow.2014.08.011).
- [149] H. G. Weller, G. Tabor, H. Jasak, and C. Fureby. “A tensorial approach to computational continuum mechanics using object-oriented techniques”. In: *Computers in Physics* 12.6 (1998), pp. 620–631. DOI: [10.1063/1.168744](https://doi.org/10.1063/1.168744).
- [150] M. P. Wernet and J. E. Bridges. “Characterization of Chevron Nozzle Performance”. In: *Technical Memorandum (TM)*. URL: <https://ntrs.nasa.gov/citations/20210020164>.
- [151] D. C. Wilcox. “Comparison of two-equation turbulence models for boundary layers with pressure gradient”. In: *AIAA Journal* 31.8 (1993), pp. 1414–1421. DOI: [10.2514/3.11790](https://doi.org/10.2514/3.11790).
- [152] J. Ye, M. Xu, P. Xing, Y. Cheng, D. Meng, Y. Tang, and M. Zhu. “Investigation of aerodynamic noise reduction of exterior side view mirror based on bionic shark fin structure”. In: *Applied Acoustics* 182 (2021), p. 108188. ISSN: 0003-682X. DOI: [10.1016/j.apacoust.2021.108188](https://doi.org/10.1016/j.apacoust.2021.108188).
- [153] A. Yoshizawa and K. Horiuti. “A Statistically-Derived Subgrid-Scale Kinetic Energy Model for the Large-Eddy Simulation of Turbulent Flows”. In: *Journal of The Physical Society of Japan* 54 (1985), pp. 2834–2839. DOI: [10.1143/JPSJ.54.2834](https://doi.org/10.1143/JPSJ.54.2834).
- [154] L. Yu, S. Diasinos, and B. Thornber. “A fast transient solver for low-Mach number aerodynamics and aeroacoustics”. In: *Computers and Fluids* 214 (2021), p. 104748. DOI: [10.1016/j.compfluid.2020.104748](https://doi.org/10.1016/j.compfluid.2020.104748).
- [155] E. Zampieri and L. Pavarino. “An explicit second order spectral element method for acoustic waves”. In: *Advances in Computational Mathematics* 25 (2006), pp. 381–401. DOI: [10.1007/s10444-004-7626-z](https://doi.org/10.1007/s10444-004-7626-z).
- [156] W. Zheng and H. Qi. “On Friedrichs–Poincaré-type inequalities”. In: *Journal of Mathematical Analysis and Applications* 304 (2005), pp. 542–551. DOI: [10.1016/j.jmaa.2004.09.066](https://doi.org/10.1016/j.jmaa.2004.09.066).
- [157] P. Šidlof, S. Zörner, and A. Hüppé. “A hybrid approach to the computational aeroacoustics of human voice production”. In: *Biomechanics and modeling in mechanobiology* 14 (2014). DOI: [10.1007/s10237-014-0617-1](https://doi.org/10.1007/s10237-014-0617-1).